Interfacing Silicon-Based Quantum Dots with Proteins for Biological and Sensing Applications

by

Christopher Jay T. Robidillo

A thesis submitted in partial fulfilment of the requirements for
the degree of

Doctor of Philosophy

Department of Chemistry

University of Alberta

Abstract

This dissertation presents the preparation of functional bioinorganic hybrids from silicon-based quantum dots (SiQDs) and enzymes and the use of SiQDs and green fluorescent protein as ratiometric photoluminescent sensors for nerve agents.

Chapter 2 discusses the preparation of water-soluble acid-terminated SiQDs and their functionalization with enzymes through the amide coupling reaction. The resulting bioinorganic hybrids exhibited the unique photoluminescent properties characteristic of SiQDs and preserved the catalytic activities of the enzymes. Although kinetic analysis of the activities of the free enzymes and the hybrids revealed that the conjugation lowered the affinity of the enzymes for their substrates, the immobilized enzymes remained sufficiently active to carry out their intended catalytic functions.

Chapter 3 details the conjugation of enzymes to alkene-terminated SiQDs (*ene*-SiQDs) using the thiol–ene 'click' reaction. Cysteine-containing enzymes were reacted with *ene*-SiQDs in the presence of a photoinitiator and ultraviolet light. This bioconjugation strategy mitigates the formation of unwanted side products and the multimerization of enzyme molecules, which typically are observed in amide coupling reactions. The synthesized hybrids manifested the characteristic indirect bandgap emission of SiQDs and the catalytic activities of the conjugated enzymes. Moreover, the hybrids showed potential use as sensors for the detection of chemicals that serve as the substrates of the immobilized enzymes.

Chapter 4 demonstrates the use of SiQDs and mAmatrine1.2 (mAm), a green fluorescent protein, as ratiometric photoluminescent sensors for the detection of the toxicologically potent nitrophenyl-containing nerve agents paraoxon (PX) and parathion (PT); they quench SiQD photoluminescence selectively via a dynamic quenching mechanism. The

sensing platform exhibited micromolar limits of detection for PX and PT, was unaffected by the presence of organic and inorganic interferents, and was selective for PX and PT. Moreover, paper-based sensors based upon SiQDs and mAm were developed as litmus test kits for the quick and convenient detection of PX and PT.

Lastly, an appendix, which shows the estimation of the concentration of the SiQDs discussed in Chapter 4 has been included at the end of this thesis.

Preface

This dissertation is an original work by Christopher Jay T. Robidillo (C. J. T. Robidillo) under the supervision of Professor Jonathan G. C. Veinot (J. G. C. Veinot).

Chapter 2 of this thesis has been published as Robidillo, C. J. T.; Islam, M. A.; Aghajamali, M.; Faramus, A.; Sinelnikov, R.; Zhang, X.; Boekhoven, J.; Veinot, J. G. C. *Langmuir* **2018**, *34 (22)*, 6556–6569. I was responsible for formulating the research concept, designing and executing the experiments, collecting and analyzing the data, and preparing the manuscript. M. A. Islam, M. Aghajamali, A. Faramus, R. Sinelnikov, and X. Zhang assisted in collecting and analyzing the data. J. Boekhoven assisted in analyzing the data and preparing the manuscript. J. G. C. Veinot was the supervisory author and was involved in designing the experiments, analyzing the data, and preparing the manuscript.

Chapter 3 of this dissertation has been published as Robidillo, C. J. T.; Aghajamali, M.; Faramus, A.; Sinelnikov, R.; Veinot, J. G. C. *Nanoscale* **2018**, *10*, 18706–18719. I was responsible for formulating the research concept, designing and executing the experiments, collecting and analyzing the data, and preparing the manuscript. M. Aghajamali, A. Faramus, and R. Sinelnikov assisted in collecting and analyzing the data. J. G. C. Veinot was the supervisory author and was involved in designing the experiments, analyzing the data, and preparing the manuscript.

Chapter 4 of this thesis has been published as Robidillo, C. J. T.; Wandelt, S.; Dalangin, R.; Zhang, L.; Yu, H. Y.; Meldrum, A.; Campbell, R. E.; Veinot, J. G. C. *ACS Appl. Mater. Interfaces* **2019**, *11*, 33478–33488. I was responsible for formulating the research concept, designing and executing the experiments, collecting and analyzing the data, and preparing the manuscript. S. Wandelt, R. Dalangin, L. Zhang, and H. Y. Yu assisted in collecting and analyzing the data. A. Meldrum and R. E. Campbell assisted in analyzing the data and preparing the manuscript. J. G. C. Veinot was the supervisory author and was involved in designing the experiments, analyzing the data, and preparing the manuscript.

"He has made everything beautiful in its time."

–Ecclesiastes 3:11

Acknowledgements

This work would not have been completed without the help and guidance of many individuals.

I would like to extend my sincerest gratitude to my research supervisor, Professor Jonathan G. C. Veinot. Thank you so much, Jon, for giving me the freedom and opportunity to pursue new lines of research and for guiding me along the way. Your encouragement and direction made all this possible.

I am very grateful to my co-supervisor from the Technische Universität München (TUM), Professor Job Boekhoven, for his guidance and invaluable suggestions. Acknowledgements are due as well to my supervisory committee members, Professors Michael Serpe and Christopher Cairo, for their time and comments. In addition, I am very thankful to my external examiner, Professor Michael Sailor, for his invaluable input.

I would like to thank Dr. Maryam Aghajamali, my mon amie and mentor, for training me in the lab and, more importantly, for helping make my research journey more enjoyable and fun.

I am thankful to my friends, both within the Veinot Group and without, for the pleasure of their company and their invaluable help. Special thanks to Rochelin Dalangin, Radhika Chakraberty, Hanh Tran, Vivian Guzman, Ahmed Elmenoufy, Zach Zhang, Albert Rosana, Kelsey Deutsch, Emmett Yu, Alyxandra Thiessen, and Drs. Christina Gonzalez, Regina Sinelnikov, Angelique Faramus, Amirul Islam, Nduka Ikpo, and John Washington.

I am grateful for the technical expertise of Wayne Moffat, Jennifer Jones, Dr. Shihong Xu, and Dr. Anqiang He; thank you so much for your expert assistance!

I also would like to acknowledge the wonderful staff of the Chemistry Department and the Alberta/Technical University of Munich International Graduate School for Hybrid Functional Materials (ATUMS) who had, in one way or another, assisted me during my stay in the program. Thank you, Anita Weiler, Esther Moibi, Laura Pham, and Kelly Fowler! Special mention to our amazing ATUMS coordinator, Leah Veinot; thank you so much, Leah!

I have gained a very good friend in the course of writing this thesis: Dr. Anna Jordan. Thank you so much, Anna, for painstakingly correcting my drafts — you have the eyes of a hawk! Also, your cookies are most delectable!

I would like to acknowledge Alberta Innovates for the scholarship that supported me during my studies and the Natural Sciences and Engineering Research Council of Canada (NSERC) Discovery Grant Program for the generous research funding.

I am sincerely grateful to my family for their unwavering support and unconditional love. Thank you so much Mama, Papa, Lola, Fatima, Oket, and Aidan! I will never trade you for anything in the world. You are my treasure on earth.

Most of all, words cannot express my deepest gratitude to my Lord and Savior Jesus Christ for giving me the grace, fortitude, and wisdom to accomplish all this. This one is for You, Lord.

Ad majórem Dei glóriam.

For the greater glory of God.

Table of Contents

List of Tables

List of Figures

List of Schemes

List of Abbreviations and Symbols

a.u.	Arbitrary unit
A549	Human lung carcinoma
Acet	Sodium acetate
ACh	Acetylcholine
AChE	Acetylcholine esterase
acid-*Ox*SiNPs	Acid-terminated *Ox*SiNPs
acid-SiQDs	Acid-terminated SiQDs
ADH	Alcohol dehydrogenase
ADH-*Ox*SiNPs	Alcohol dehydrogenase-conjugated *Ox*SiNPs
ADH-SiNCs	Alcohol dehydrogenase-conjugated SiNCs
AFM	Atomic force microscopy
Ala	Alanine
ala-SiQDs	Alanine-conjugated SiQDs
alkyl-SiQDs	Alkyl-coated SiQDs
amine SiNPs	Amine-terminated SiNPs
amine-SiQDs	Amine-terminated SiQDs
anti-HSA-B/P-SiQDs	Anti-HSA-conjugated *B/P*-SiQDs
APTES	(3-Aminopropyl)trimethoxysilane
Arg	Arginine
AuNP(R)s	Gold nanoparticles/nanorods
B/P-SiQDs	Boron- and phosphorous-doped SiQDs
BSE/SEM	Backscattered scanning electron microscopy
Cit	Sodium citrate
Cl-SiNPs	Chloride-terminated SiNPs
CP	Chlorpyrifos
DCC	*N,N′*-Dicyclohexylcarbodiimide
DLS	Dynamic light scattering
DMSO	Dimethylsulfoxide
DNA	Deoxyribonucleic acid
DNA-SiQDs	DNA-conjugated SiQDs
DNT	Dinitrotoluene
DSA	Dissipative self-assembly
dsDNA-SiQDs	Double-stranded DNA-conjugated SiQDs
DZ	Diazinon
EDC	1-Ethyl-3-(3-dimethylaminopropyl)carbodiimide
EDX	Energy-dispersive X-ray spectroscopy
ELPs	Elastin-like polypeptides
ene-SiNCs	Alkene-terminated SiNCs
ene-SiQDs	Alkene-terminated SiQDs
Enz-*Ox*SiNPs	Enzyme-conjugated silicon-based nanoparticles
enz-SiNCs	Enzyme-conjugated SiNCs

eV	Electron-volt
F127	Pluronic® triblock copolymer
Fln-DNA	Fluorescein-functionalized oligonucleotide
Fln-DNA-SiQDs	Fluorescein-functionalized oligonucleotide-coated SiQDs
fol-SiQDs	Folate-conjugated SiQDs
FRET	Förster/fluorescence resonance energy transfer
FTIR	Fourier transform infrared spectroscopy
FTY	Fentanyl
Gal SiNPs	Galactose-conjugated SiNPs
GFP	Green fluorescent protein
Gg3,dye-SiQDs	Gg3- and dye-conjugated SiQDs
Glc	Glucose
Glu SiNPs	Glucose-conjugated SiNPs
GOx	Glucose oxidase
GOx-*Ox*SiNPs	Glucose oxidase-conjugated *Ox*SiNPs
HEPES	4-(2-Hydroxyethyl)-1-piperazineethanesulfonic acid
HHL-5	Human immortalized hepatocytes
HHMP	2-Hydroxy-4'-(2-hydroxyethoxy)-2-methylpropiophenone
H-NMR	Proton nuclear magnetic resonance spectroscopy
HOBt	Hydroxybenzotriazole
HOMO	Highest occupied molecular orbital
H-SiNCs	Hydride-terminated silicon nanocrystals
H-SiNPs	Hydride-terminated silicon nanoparticles
H-SiQDs	Hydride-terminated silicon quantum dots
HSQ	Hydrogen silsesquioxane
IC_{50}	Half maximal inhibitory concentration
IgG-SiQDs	IgG-conjugated SiQDs
kDa	Kilodalton
K_M	Michaelis–Menten constant
K_{SV}	Stern-Volmer constant
Lac SiNPs	Lactose-conjugated SiNPs
LD_{50}	Median lethal dose
LOD	Limit of detection
Lse	Lactase
Lse-SiNCs	Lactase-conjugated SiNCs
LSS	Long Stokes shift
LUMO	Lowest unoccupied molecular orbital
Lys	Lysine
MA	Malonic acid
mAm	mAmetrine 1.2
man-SiQDs	Mannose-conjugated SiQDs
Man SiNPs	Mannose-conjugated SiNPs
MDCK	Normal kidney epithelium cells
miR-21	MicroRNA 21

miR-155	MicroRNA 155
MT	Malathion
MTS	3-(4,5-Dimethylthiazol-2-yl)-5-(3-carboxymethoxyphenyl)-2-(4-sulfophenyl)-2H-tetrazolium)
MWCO	Molecular weight cutoff
NAD^+	Nicotinamide adenine dinucleotide sodium salt
NHS	*N*-Hydroxysuccinimide
NTA	Nitrilotriacetic acid
ONPG	*o*-Nitrophenyl-β-D-galactopyranoside
OPEs	Organic esters of phosphoric acid
Osu-SiQDs	*N*-Hydroxysuccinimide-functionalized SiQDs
*Ox*SiNPs	Oxide-rich silicon-based nanoparticles
*ox*TMB	Oxidized TMB
PAGE	Polyacrylamide gel electrophoresis
Panc-1	Pancreatic cancer
PEG	Polyethylene glycol
PETN	Pentaerythritol tetranitrate
PL	Photoluminescence
PLAL	Pulsed laser ablation in liquid
PN	*p*-Nitrophenol
proA	*Staphylococcus aureus* protein A
proA-SiQDs	protein A-conjugated SiQDs
PT	Parathion
PX	Paraoxon
QDs	Quantum dots
RDX	Cyclotrimethylene trinitramine
RGB	Red/green/blue
SDS	Sodium dodecyl sulfate
SEM	Scanning electron microscopy
SiNCs	Silicon nanocrystals
SiNPs	Silicon nanoparticles
SiNWs	Silicon nanowires
SiQDs	Silicon-based quantum dots
ssDNA-SiQDs	Single-stranded DNA-conjugated SiQDs
SSO	Single-stranded oligonucleotide
SSO-SiQDs	Single-stranded oligonucleotide-conjugated SiQDs
styrene-SiQDs	Styrene-coated SiQDs
Suc	Sucrose
sulfo-NHS	*N*-Hydroxysulfosuccinimide
TDBA-OSu	4’-[3-(Trifluoromethyl-3H-diazirin-3-yl)]-benzoic acid *N*-hydroxysuccinimide ester
TEM	Transmission electron microscopy
TGA	Thermogravimetric analysis
THC	Tetrahydrocannabinol

THF	Tetrahydrofuran
Thiazolyl blue	3-(4,5-Dimethylthiazol-2-yl)-2,5-diphenyltetrazolium bromide
TMB	3,3',5,5'-Tetramethylbenzidine
TNT	Trinitroluene
T_t	Transition temperature
Use	Urease
Use-SiNCs	Urease-conjugated SiNCs
UV	Ultraviolet
Vis	Visible
XPS	X-ray photoelectron spectroscopy
τ	Excited-state lifetime

Chapter 1

Introduction

1.1 Bioconjugation of Silicon-Based Quantum Dots

Quantum dots are semiconductor nanoparticles that exhibit size-dependent photoluminescence (PL).[1,2] This unique property results from quantum confinement, a phenomenon that occurs when the diameter of the semiconductor nanoparticles approaches the Bohr exciton radius of their charge carriers.[3,4] Their brightness, large absorption cross-section, photostability, tailorable surface chemistry, and water-dispersibility make them attractive for applications, such as bioimaging and biosensing in biology and medicine.[5] The most studied and commercially available quantum dots are comprised of combinations of elements from groups II and VI (e.g., CdSe, CdTe),[6–8] groups IV and VI (e.g., PbS, PbSe),[9,10] or groups III and V (e.g., InP, GaP)[11] of the periodic table. The surfaces of these nanoparticles have been modified successfully with biologically relevant molecules, such as proteins, carbohydrates, and nucleic acids, for targeted drug delivery and cell-specific biological staining.[12] Though a great body of literature had demonstrated the potential utility of these quantum dots for biomedical applications successfully, the well-established cytotoxicity of heavy metals like lead and cadmium poses a serious hurdle on their actual implementation in real-life applications.[13–15]

Silicon-based quantum dots (SiQDs) are indirect bandgap semiconductor nanoparticles that offer the same advantages as heavy-metal-based quantum dots but are non-toxic and biocompatible.[16] Moreover, SiQDs, being derived from silicon, the second most abundant element on the earth's crust,[17] offer a more cost-effective alternative to heavy-metal-based quantum dots. In addition, nanoscale silicon is reported to decompose into silicic acid, which is readily excreted in the urine.[18] Depending on the exact route employed for their synthesis, blue or blue-green photoluminescent SiQDs exhibiting nanosecond PL lifetimes, possibly emitting from excited surface states, and red or orange-red photoluminescent SiQDs emitting from a bandgap transition and exhibiting longer excited-state lifetimes (i.e., microseconds) have been reported in the literature.[19,20] Unlike heavy-metal-based quantum dots, the colour of light emitted by SiQDs greatly depends on the chemical groups present on their surfaces.[21]

Most bottom-up methods (i.e., solution-based methods) for SiQD synthesis, such as hydride reduction of silicon halide precursors[22] and metathesis reactions involving Zintl salts,[23–25] give rise to blue or blue-green emitting particles. On the other hand, methods like laser pyrolysis of silanes[26–28] and thermal disproportionation of hydrogen silsesquioxane[29,30] yield red or orange-red emitting particles upon etching with hydrogen fluoride and capping with organic ligands. Interested readers are directed to excellent reviews by Veinot,[31]Tilley,[32] and Gooding[33] for a discussion of the different chemical routes for the preparation and surface passivation of SiQDs.

Nanoparticles intended for biomedical applications must be modified or functionalized with biological molecules for biorecognition and specific cellular targeting. The paucity of literature on bioconjugation of SiQDs compared to that of heavy-metal-based quantum dots can be attributed to factors such as the difficulty in preparing water-dispersible and water-stable SiQDs and the unique surface chemistry of silicon.[34] It must be mentioned that silicon nanoparticles undergo oxidation and decomposition upon exposure to air and water.[18,32,35] Nonetheless, some strategies have been developed to overcome these challenges. For example, SiQDs have been passivated with monolayer coatings consisting of polar organic groups, such as alkylamines[22] and alkylcarboxylic acids,[27] which serve to protect the quantum dots against oxidation and degradation and render them soluble in water. SiQDs also have been encapsulated within functionalized phospholipid micelles[26] and amphiphilic polymers[28,36] in order to protect them from decomposition and make them dispersible in aqueous environments. Recently, the Veinot group has developed procedures for passivating the SiQD surface with mixed organic ligands consisting of methyl undecanoate[37] and poly(ethylene oxide), which render the SiQDs soluble in water and stable against oxidation without compromising their characteristic red photoluminescence and microsecond lifetimes. These and other advances have set the stage for the preparation of bioinorganic hybrids from SiQDs and biomolecules via bioconjugation reactions in aqueous media.

Scheme 1-1 summarizes the strategies that have been employed for the conjugation of biomolecules to SiQDs. The first strategy involves the passivation of SiQDs with alkyl groups that bear appropriate functional group handles for bioconjugation, such as an amine, carboxylic acid, and alkene group. In some instances, the SiQDs are coated either with poly(ethylene

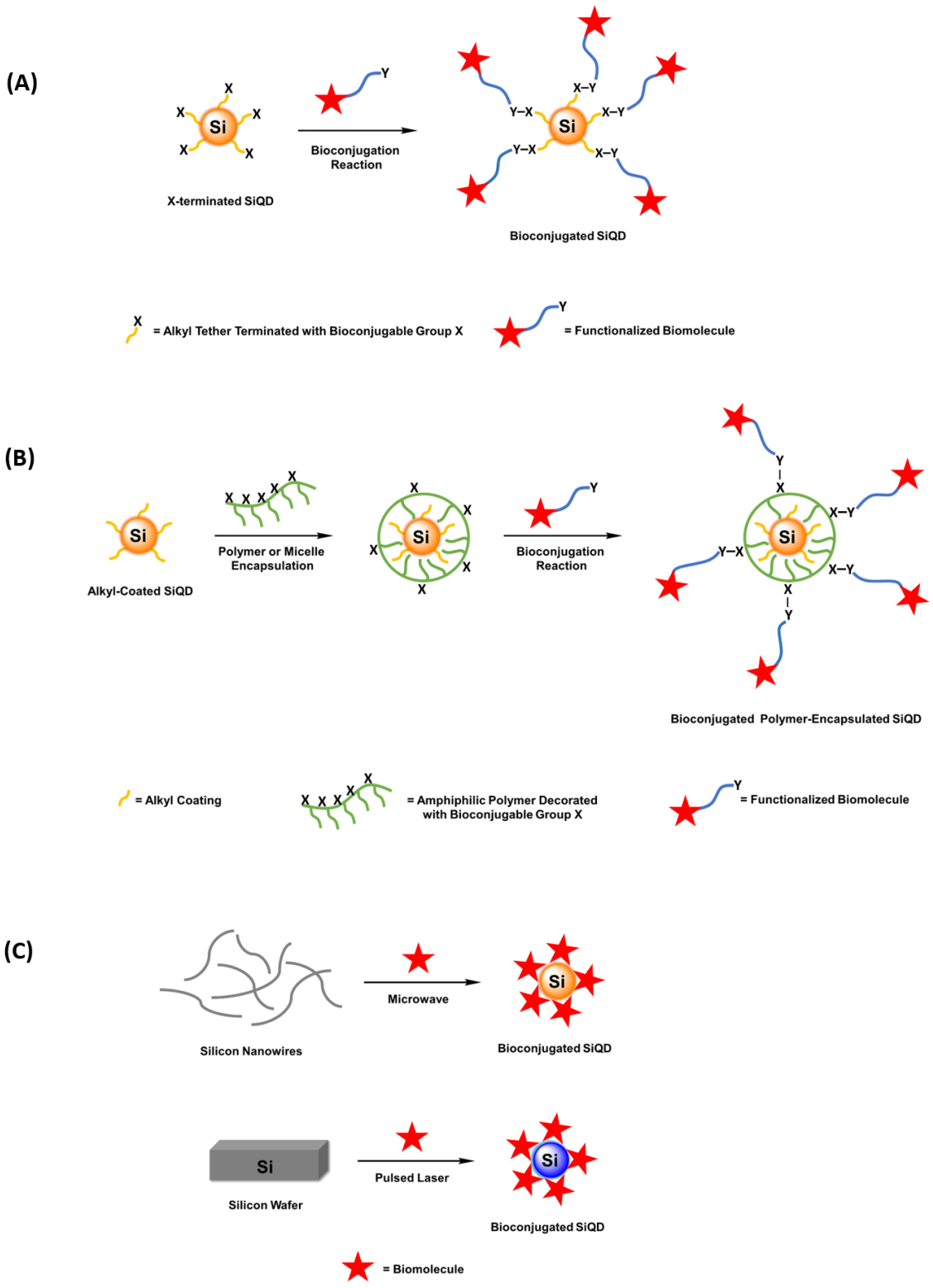

Scheme 1-1. (A) Bioconjugation of SiQDs terminated with bioconjugable functional groups. **(B)** Encapsulation of SiQDs with polymers decorated with bioconjugable groups, followed by bioconjugation. **(C)** One-pot synthesis and bioconjugation of SiQDs.

oxide) terminated with bioconjugable groups or with a mixture of poly(ethylene oxide) and alkylamines or alkylcarboxylic acids. Poly(ethylene oxide) is used to render the SiQDs soluble in water and to promote the biocompatibility of the resulting hybrids. Once installed, the bioconjugable groups are reacted with biomolecules derivatized with relevant functionalities (e.g., acid-functionalized sugars, thiolated deoxyribonucleic acid, etc.) through conjugation reactions, such as the amide coupling and thiol–ene reactions. In the second strategy, amphiphilic polymers decorated with bioconjugable groups are employed for the encapsulation and solubilization of hydrophobic alkyl-coated SiQDs and their subsequent bioconjugation. The last strategy involves the one-pot synthesis of biomolecule-conjugated SiQDs using microwave radiation or pulsed lasers. This strategy typically gives rise to hybrids where the biomolecules are either physically adsorbed on the SiQDs or chemically linked to the SiQD surface through some bonds.

SiQDs have been functionalized with a variety of biological molecules (e.g., carbohydrates, nucleic acids, lipids, and proteins) for bioimaging, biosensing, and other biomedical applications. To this end, SiQD surfaces have been modified with groups like carboxylic acids, amines, alkenes, and alkyl groups. Choi and co-workers conjugated multiple SiQDs to streptavidin, a protein, via the amide coupling chemistry.[38] As shown in Figure 1-1A, they have coated the surfaces of SiQDs with octyl groups through the photochemical hydrosilylation of octene with hydride-terminated silicon nanoparticles (*H*-SiNPs) obtained from the anodic HF etching of silicon wafers, followed by a nitrene-type C–H insertion reaction with 4-azido-2,3,5,6-tetrafluorobenzoic acid succinimidyl ester, a heterobifunctional linker, in the presence of UV light. The resulting material was reacted with the amine groups in streptavidin to afford streptavidin-conjugated SiQDs, wherein multiple quantum dots were linked to a streptavidin molecule through amide bonds upon displacement of the succinimidyl leaving group in a nucleophilic acyl substitution reaction. Successful coating with octyl groups, subsequent functionalization with the bi-linker succinimidyl ester, and conjugation with streptavidin were confirmed through Fourier transform infrared spectroscopy (FTIR). Native gel electrophoresis also showed that the bioinorganic hybrids elute faster than pure streptavidin, which is consistent with covalent attachment of streptavidin to the negatively charged SiQDs. In addition, capillary electrophoresis revealed that around 4–5 quantum dots are conjugated to one streptavidin molecule. However, the surface modifications altered the

PL of the silicon nanoparticles; the orange PL (λ_{em} = 600 nm) of *H*-SiNPs shifted to blue upon modification with octyl groups (λ_{em} = 400 nm) and streptavidin (λ_{em} = 450 nm) (Figure 1-1B). Nonetheless, as shown in Figure 1-1C, the streptavidin-conjugated SiQDs bind to biotin on biotin-coated polystyrene beads, demonstrating the biological activity of the immobilized streptavidin molecules.

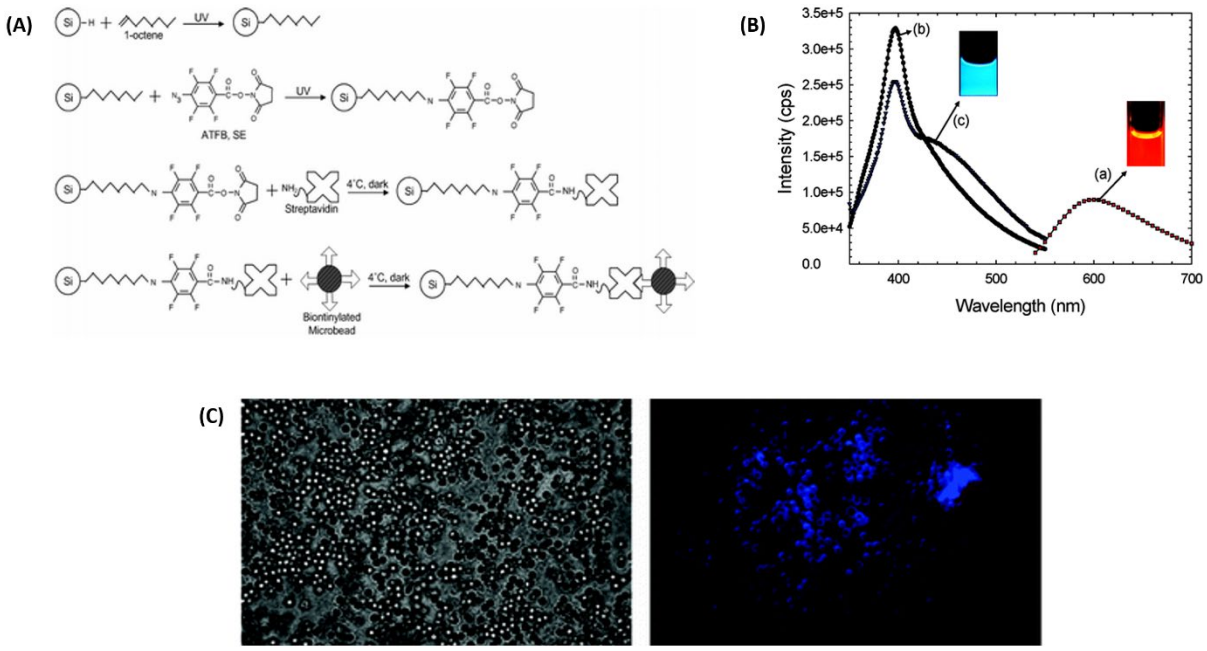

Figure 1-1. (A) Scheme showing the stepwise synthesis of streptavidin-conjugated SiQDs from *H*-SiNPs. **(B)** Photoluminescence spectra of (a) *H*-SiNPs, (b) octyl-coated SiQDs, and (c) streptavidin-conjugated SiQDs. **(C)** Phase (left) and fluorescence microscopy (right) images of 2 μm biotinylated polystyrene beads exposed to streptavidin-conjugated SiQDs. Adapted with permission from Choi, J.; Wang, N. S.; Reipa, V. *Bioconjugate Chem.* **2008**, *19* (3), 680–685. Copyright © 2008 American Chemical Society.

Erogbogbo et al. have synthesized water-dispersible SiQDs modified with carboxylic acid groups (*acid*-SiQDs) via thermal hydrosilylation of undecenoic acid in refluxing ethanol solution.[27] They conjugated the *acid*-SiQDs to amine-containing compounds through the amide coupling reaction. The surface carboxylic acid groups were converted first to an *O*-acylisourea via reaction with 1-ethyl-3-(3-dimethylaminopropyl)carbodiimide (EDC) and then converted to an amine-reactive and semi-stable succinimide ester via reaction with *N*-hydroxysulfosuccinimide (sulfo-NHS). The resulting sulfo-NHS-modified SiQDs underwent a nucleophilic acyl substitution with amine-containing compounds, lysine, folic acid, and antimesothelin, and the protein transferrin, to afford bioinorganic hybrids that

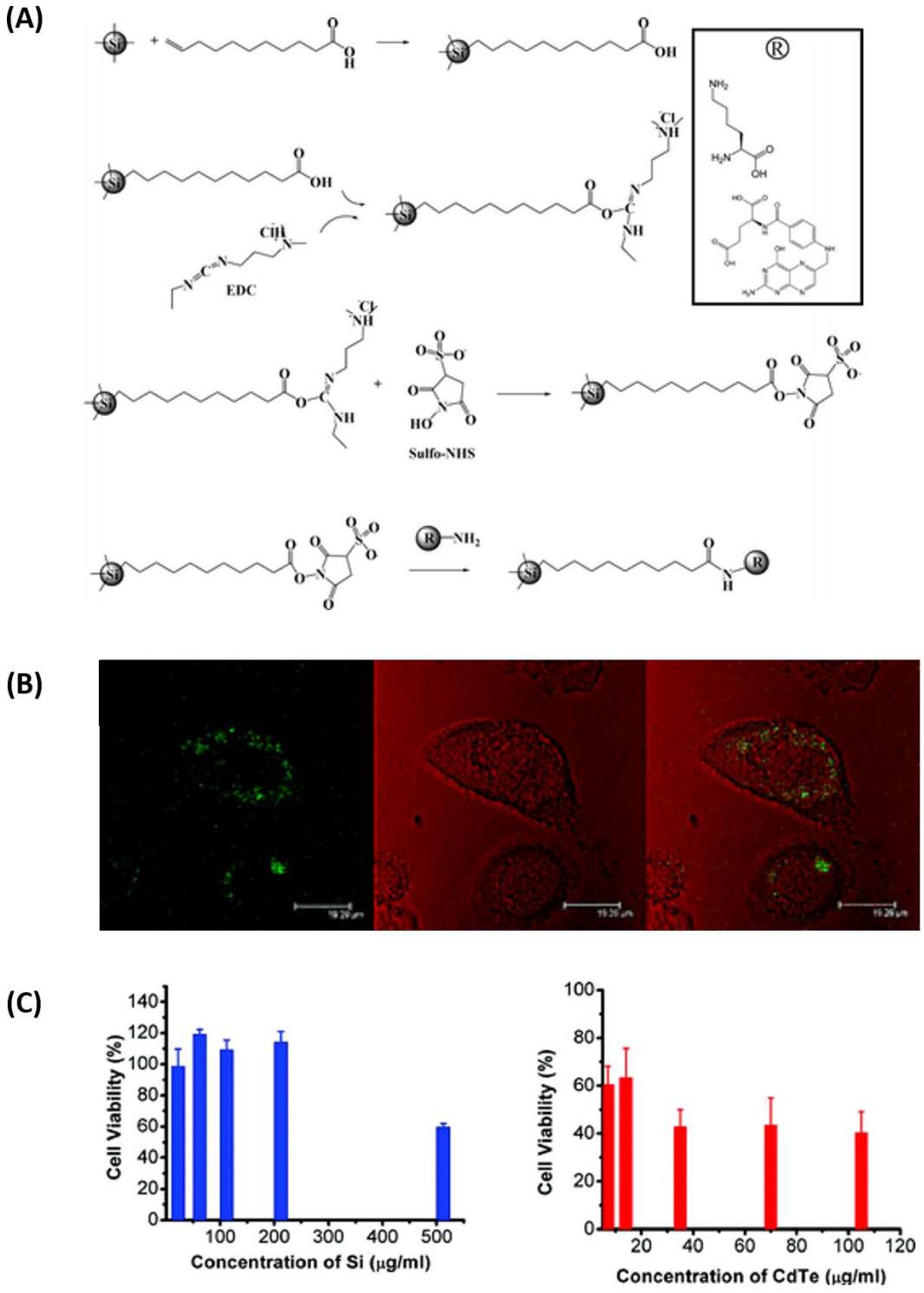

Figure 1-2. (A) Scheme showing the stepwise synthesis of bioconjugated SiQDs from *H*-SiNPs. **(B)** Confocal images of Panc-1 cells incubated with folate-conjugated SiQDs (left–right: luminescence, transmission, overlay images). **(C)** Cell viability of Panc-1 cells in the presence of *H*-SiNPs (left) and CdTe QDs (right) as measured using MTS assay. Adapted with permission from Erogbogbo, F.; Tien, C.-A.; Chang, C.-W.; Yong, K.-T.; Law, W.-C.; Ding, H.; Roy, I.; Swihart, M. T.; Prasad, P. N. *Bioconjugate Chem.* **2011**, *22* (6), 1081–1088. Copyright © 2011 American Chemical Society.

exhibited the biological activities of the conjugated molecules (Figure 1-2A). Successful biological functionalization was confirmed through the presence of amide A (N-H stretch, 3270 cm^{-1}), amide I (C=O stretch, 1635 cm^{-1}), and amide II (C-N stretch, 1550 cm^{-1}) peaks characteristic of the peptide bonds. The *acid*-SiQDs synthesized had a TEM diameter of 4–5 nm and a hydrodynamic diameter of 23 nm. The *acid*-SiQDs exhibited red emission (λ_{em} = 662 nm at an excitation wavelength of 350 nm) and a quantum yield of 15 ± 5%. Upon conjugation with lysine, the emission maximum blue-shifted to 645 nm, and the quantum yield dropped to 5 ± 3%. The photoluminescence of the lysine-conjugated SiQDs was stable for 11 days. The *acid*-SiQDs were conjugated to folate, antimesothelin, and transferrin (molecules with overexpressed receptors in tumours) in order to prepare bioinorganic hybrids that can be selectively taken up by cancer cells. As shown in Figure 1-2B, confocal imaging revealed that the folate-conjugated SiQDs were internalized readily by pancreatic cancer (Panc-1) cells. Lastly, the MTS [3-(4,5-dimethylthiazol-2-yl)-5-(3-carboxymethoxyphenyl)-2-(4-sulfophenyl)-2H-tetrazolium)] assay showed that hydride-terminated SiQDs are non-toxic compared to cysteine-capped CdTe quantum dots, with the former having an IC_{50} that is greater than 500 μg mL^{-1} and the latter an IC_{50} of ~40 μg mL^{-1} (Figure 1-2C).

Zhong et al. reported the large-scale synthesis of blue-photoluminescent SiQDs through the microwave-mediated reduction of (3-aminopropyl)trimethoxysilane (APTES) using sodium citrate as a reducing agent (Figure 1-3A).[39] TEM and DLS analyses revealed an average diameter of 2.2 ± 0.7 nm and a hydrodynamic diameter of ~3.86 nm for the synthesized *amine*-SiQDs. FTIR indicated the presence of amine groups on the quantum dot surface. PL quantum yield measurements showed that the *amine*-SiQDs have quantum efficiencies in the range of 20–25%. Moreover, the *amine*-SiQDs displayed superior photostability compared to fluorescent organic dyes and Cd-based quantum dots. In addition, cytotoxicity studies of *amine*-SiQDs on cervical carcinoma HeLa cell line yielded insignificant toxicity. As shown in Figure 1-3B, they have exploited the presence of the amine groups on the quantum dot surface in conjugating the *amine*-SiQDs to goat-antimouse IgG, a protein antibody, using EDC and NHS as amide coupling agents. The resulting goat-antimouse IgG-conjugated SiQDs (*IgG*-SiQDs) were used as an immunofluorescent cell label for targeting the nuclei of HeLa cells that were pre-treated with a nuclei-specific anti-hn RNP antibody. Laser scanning confocal immunofluorescence microscopy demonstrated that the *IgG*-SiQDs were localized in the cell

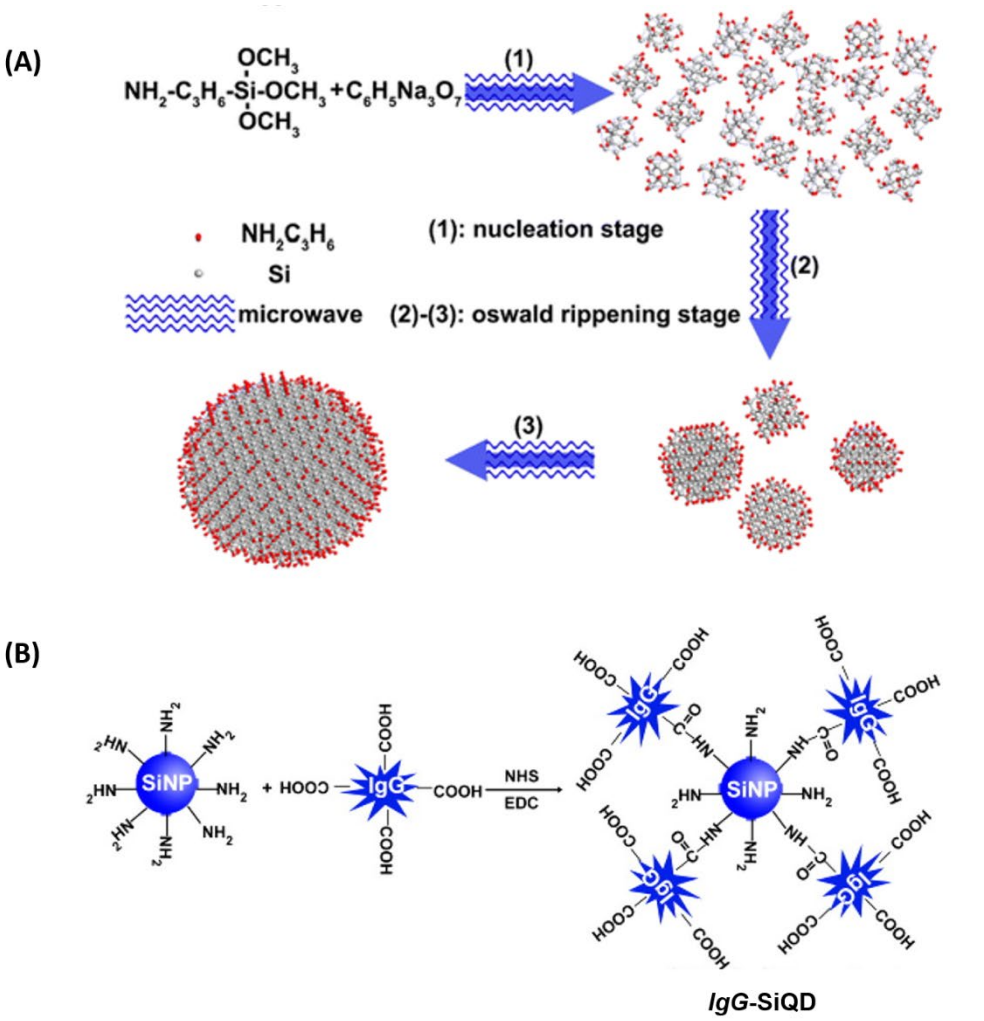

Figure 1-3. (A) Scheme showing the synthesis of *amine*-SiQDs from APTES and sodium citrate. **(B)** Scheme showing synthesis of *IgG*-SiQDs from amine-terminated SiQDs and IgG using EDC and NHS as coupling agents. **(C)** Scanning confocal immunofluorescent cell images of Hela cells incubated with *IgG*-SiQDs and fluorescein isothiocyanate (FITC). The leftmost image shows that cell nuclei are labelled by *IgG*-SiQDs, while the middle image shows that the cell microtubules are labelled by FITC. The rightmost image is a superposition of the two fluorescence images. Adapted with permission from Zhong, Y.; Peng, F.; Bao, F.; Wang, S.; Ji, X.; Yang, L.; Su, Y.; Lee, S.-T.; He, Y. *J. Am. Chem. Soc.* **2013**, *135* (22), 8350–8356. Copyright © 2013 American Chemical Society.

nuclei (Figure 1-3C) and were photostable, withstanding a 60 min long continuous observation, which suggests that the bioconjugated SiQDs can be employed for long-term biological imaging. However, the exact chemical nature and composition of the SiQDs prepared following this procedure have come into question recently, with some researchers independently providing strong evidence for the implausibility of sodium citrate as a reducing agent for APTES even under conditions of microwave irradiation,[40] and attributing the observed photoluminescence to carbon quantum dots obtained from the thermal decomposition of citrate.[41]

The same group reported the gram-scale preparation of *amine*-SiQDs through the reduction of APTES by 1,8-naphthalimide as a reducing agent (Figure 1-4A).[42] The particles synthesized exhibited tuneable blue–green PL (λ_{em} = 470–560 nm) and quantum yields of ~25%, were photostable, and showed stable PL intensity even upon continuous irradiation with high-power UV for a long time (>3 h). As in their previous work, they had conjugated the *amine*-SiQDs to goat-antimouse IgG following the same amide coupling chemistry and yielded *IgG*-SiQDs that have been used successfully in immunofluorescence cell imaging of the microtubules of HeLa cells (Figure 1-4B). Similarly, the reported *IgG*-SiQDs survived 2 h of continuous UV irradiation, pointing to their potential utility for long-term biological imaging.

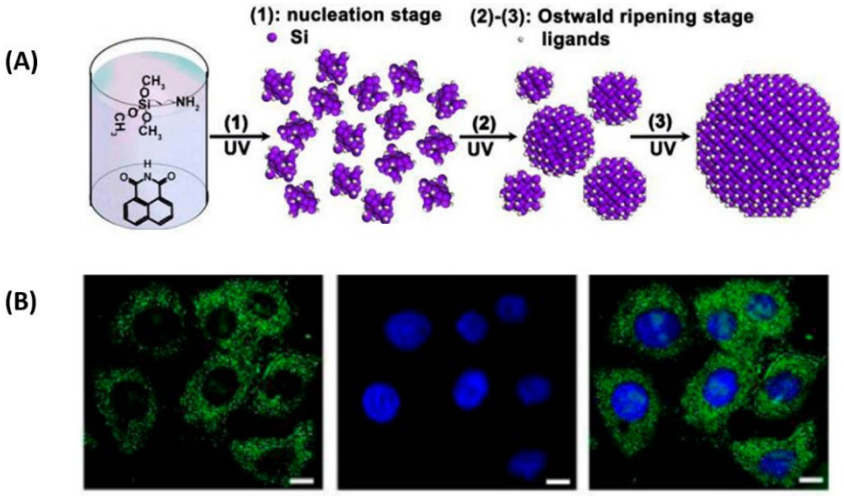

Figure 1-4. (A) Scheme showing the synthesis of *amine*-SiQDs from APTES and 1,8-naphthalimide. **(B)** Scanning confocal immunofluorescent cell images of Hela cells incubated with *IgG*-SiQDs and Hoechst nuclear stain. The leftmost image shows that microtubules are labelled by *IgG*-SiQDs, while the middle image shows that the cell nuclei are labelled by Hoechst stain. The rightmost image is a superposition of the two images. Adapted with permission from Zhong, Y.; Sun, X.; Wang, S.; Peng, F.; Bao, F.; Su, Y.; Li, Y.; Lee, S.-T.; He, Y. *ACS Nano* **2015**, *9* (6), 5958–5967. Copyright © 2015 American Chemical Society.

Figure 1-5A outlines the procedure used by Erogbogbo and co-workers in preparing water-dispersible SiQDs by encapsulation of multiple hydrophobic alkyl-coated SiQDs (*alkyl*-SiQDs) within poly(ethylene oxide) phospholipid micelles.[26] First, they synthesized *alkyl*-SiQDs by the UV-initiated hydrosilylation of styrene, octadecene, or ethyl undecylenate with *H*-SiNPs obtained from the laser-driven pyrolysis of silane. The resulting *alkyl*-SiQDs were embedded within the hydrophobic interior of poly(ethylene oxide) phospholipid micelles functionalized with carboxylic acid groups, folate, or biotin. TEM characterization of the micelle-encapsulated SiQDs revealed micelle diameters ranging from 50 to 120 nm and SiQD diameters of about 4 nm. Analysis of the optical spectra showed that the *alkyl*-SiQDs and the micelle-encapsulated *alkyl*-SiQDs have emission maxima at ~670 nm at an excitation wavelength of 350 nm. Micelle encapsulation of *styrene*-SiQDs caused a decrease in PL quantum yield from 17% to 2%. Figure 1-5B shows that the PL intensity of the SiQDs varied by less than 10% at physiologically relevant values of temperature (i.e., 25–40 °C). Similarly, the PL intensity of the SiQDs was stable from pH 4.0 to pH 10.0, varying by less than 10%. Carboxylic acid-functionalized micellar assemblies of *alkyl*-SiQDs were conjugated to the protein transferrin using EDC as a coupling agent. The resulting transferrin-conjugated micelle-encapsulated *alkyl*-SiQDs were used successfully in imaging pancreatic cancer (Panc-1) cells (Figure 1-5C). Consistent with the need for a biologically active molecule or group on the SiQD surface for cell staining, the micelle-encapsulated *alkyl*-SiQDs that contain neither amine nor transferrin were not internalized by the cells. The MTS assay indicated that the micelle-encapsulated *alkyl*-SiQDs did not induce cell death at the concentration used in imaging the cells (i.e., at ~8 μg mL^{-1}, mean cell viability was above 95% after 24 h and above 85% at 48 h).

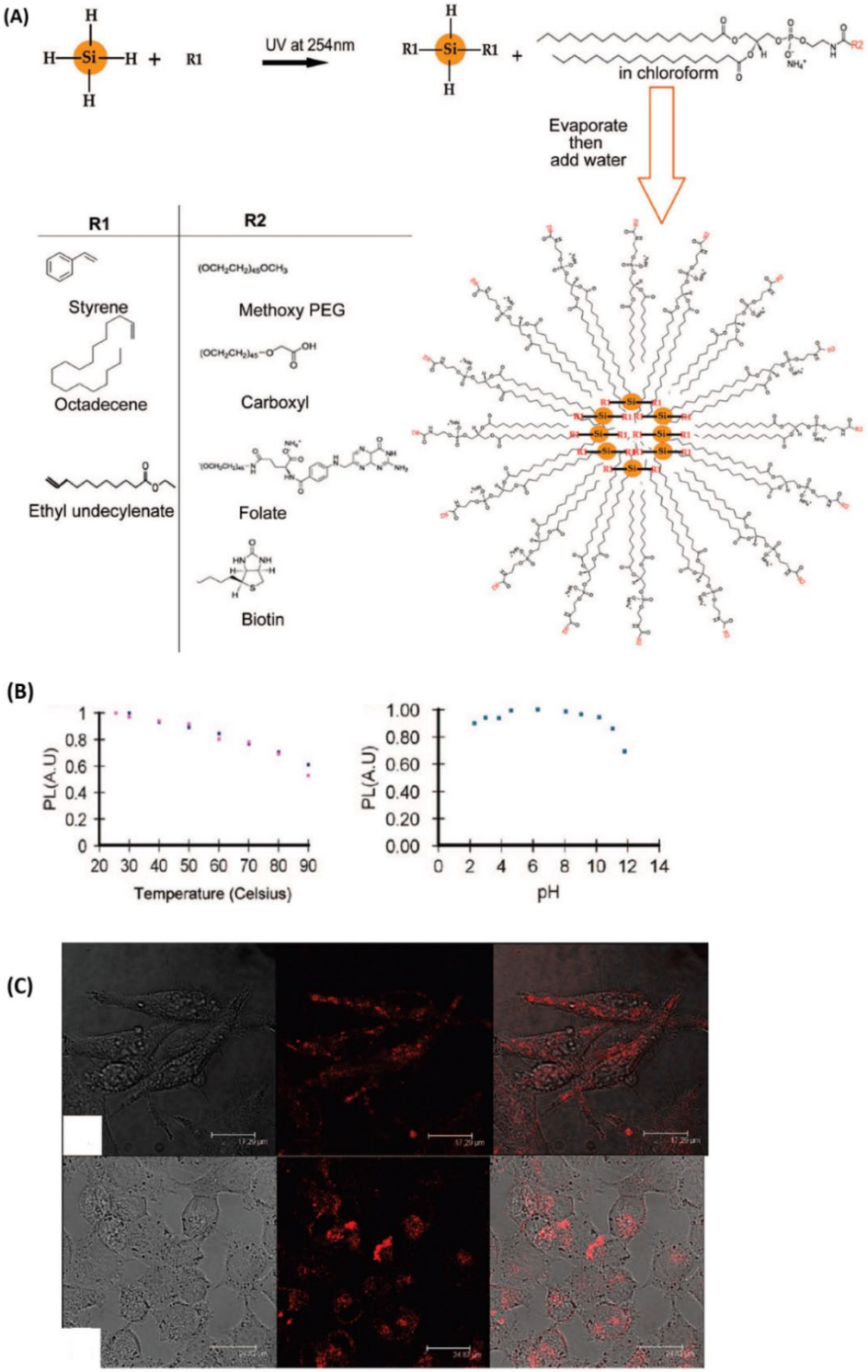

Figure 1-5. (A) Scheme showing the synthesis of micelle-encapsulated *alkyl*-SiQDs from *H*-SiNPs. **(B)** Plots of photoluminescence intensity of micelle-encapsulated *alkyl*-SiQDs versus temperature (left) and pH (right). **(C)** Confocal microscopy images of Panc-1 cells incubated with transferrin-conjugated micelle-encapsulated *alkyl*-SiQDs (left: transmission image, middle: luminescence image, right: overlay of the two images). Adapted with permission from Erogbogbo, F.; Yong, K.-T.; Roy, I.; Xu, G.; Prasad, P. N.; Swihart, M. T. *ACS Nano* **2008**, *2* (5), 873–878. Copyright © 2008 American Chemical Society.

May et al. employed an identical encapsulation procedure for preparing water-dispersible SiQDs using acid-modified Pluronic® triblock copolymer (F127) as an encapsulating agent.[28] Similarly, they synthesized *alkyl*-SiQDs via the UV-initiated hydrosilylation of ethyl undecylenate with *H*-SiNPs obtained from the laser pyrolysis of silane. The hydrophobic *alkyl*-SiQDS obtained were encapsulated within F127 micelles that were decorated with carboxylic acid groups. TEM characterization showed SiQDs with diameters of 5 nm and micelles with a diameter range of 20–200 nm. Moreover, the micelle-encapsulated *alkyl*-SiQDs exhibited red PL, with an emission maximum at around 670 nm at an excitation wavelength of 350 nm. The encapsulated SiQDs exhibited stable PL from pH 2.0 to pH 9.0 and manifested temperature-independent PL intensity. EDC and sulfo-NHS were used as coupling agents for covalently linking biologically active molecules like folic acid, anti-mesothelin, and anti-claudin-4 to the acid-terminated Pluronic®-encapsulated *alkyl*-SiQDs. As in the previous example, the resulting bioinorganic hybrids (e.g., anti-mesothelin-conjugated micelle-encapsulated *alkyl*-SiQDs and anti-claudin-4-conjugated micelle-encapsulated *alkyl*-SiQDs) were employed successfully in staining and imaging Panc-1 cells through confocal microscopy. Note that unconjugated micelle-encapsulated SiQDs did not stain the cells.

Das and co-workers also prepared folate-conjugated SiQDs for bioimaging.[36] They first synthesized the SiQDs via the thermal decomposition of chloro(dimethyl)octadecylsilane in 1,3,5-trimethylbenzene at 140 °C in the presence of octadecylamine as a surface-capping agent (Figure 1-6A). SiQDs of varying sizes and different emission colours were obtained, depending on the length of time that the silane precursor was heated. TEM imaging showed

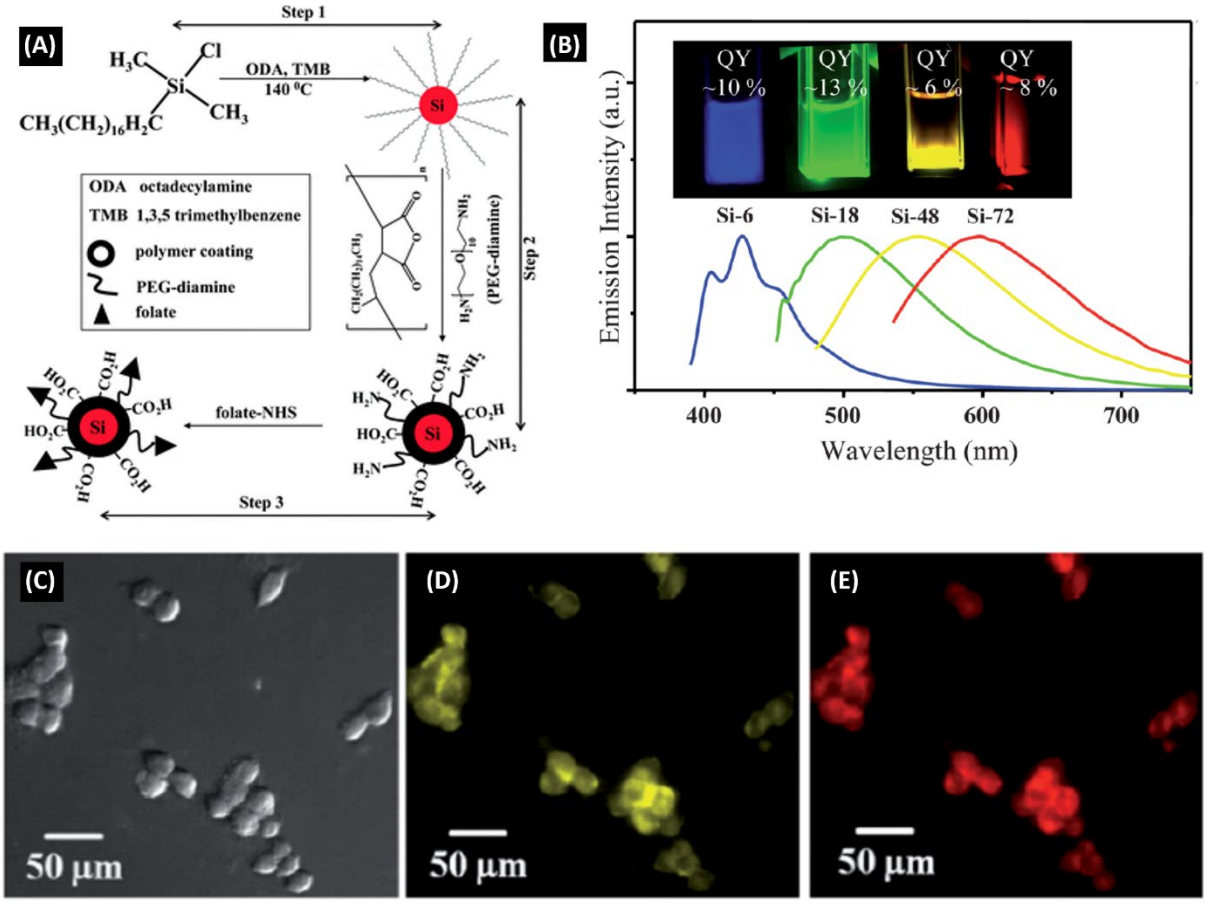

Figure 1-6. (A) Scheme showing the synthesis of SiQDs and *fol*-SiQDs. **(B)** Photoluminescence spectra of synthesized SiQDs (Si-6: 6 h, Si-18: 18 h, Si-48: 48 h, Si-72: 72 h). The inset shows the solutions of SiQDs under UV light and their corresponding quantum yields. Differential interference contrast image **(C)** and fluorescence images under blue **(D)** and green **(E)** light excitation of HeLa cells incubated with *fol*-SiQDs. Adapted with permission from Das, P.; Saha, A.; Ranjan Maity, A.; C. Ray, S.; R. Jana, N. *Nanoscale* **2013**, *5* (13), 5732–5737. Copyright © 2013 Royal Society of Chemistry.

that the particles obtained after heating the precursor for 6, 48, and 72 h, have diameters of ~1–2.5 nm, ~2–4 nm, and ~5–10 nm, respectively. Energy dispersive X-ray spectroscopy (EDX) confirmed the presence of silicon and oxygen, while FTIR indicated the presence of Si–O, Si–C, and alkyl groups that are consistent with successful capping of SiQDs by octadecylamine. XPS revealed the presence of Si(0) and silicon suboxides, alkyl carbon atoms, and silicon-bonded oxygen atoms, suggesting that the SiQDs consist of an elemental silicon core coated with an oxide shell and capped with alkyl groups. Figure 1-6B shows that the SiQDs exhibit emission colours ranging from blue to red and quantum yields ranging from 6 to 13%. The authors employed the red-emitting SiQDs in imaging cells by first rendering them water-soluble [through encapsulation with the lipophilic polymer polymaleic anhydride-alt-1-

octadecene and subsequent aminolysis with $H_2N(CH_2CH_2O)_nCH_2CH_2NH_2$)] and then conjugating the resulting amine-terminated SiQDs to folate (through the amide coupling reaction) (Figure 1-6A). The folate-conjugated SiQDs, *fol*-SiQDs, retained the red PL of the SiQDs and increased in hydrodynamic diameter from ~8 nm to ~18 nm after polymer coating and folate conjugation. As shown in Figure 1-6C–E, the *fol*-SiQDs were used successfully in imaging HeLa cells and cervical cancer positive tissue cells with overexpressed folate receptors. Control experiments showed that unconjugated polymer-coated SiQDs were not taken up by the two cell lines and that *fol*-SiQDs were not internalized by cells that do not have folate receptors.

Yanagawa and co-workers have employed the amide coupling and epoxide ring-opening reactions in preparing bioinorganic hybrids from antibodies and boron- and phosphorous-doped SiQDs (*B/P*-SiQDs).[43] The *B/P*-SiQDs consist of a crystalline silicon core encapsulated in a negatively charged boron- and phosphorous-doped amorphous shell that renders the all-inorganic SiQDs soluble in water in the absence of any passivating organic surface groups. However, the relative chemical inertness of the amorphous shell renders the *B/P*-SiQDs unreactive to conventional bioconjugation reactions. In order to overcome this, the authors have coated the *B/P*-SiQDs with a layer of amine- or epoxide-functionalized silicon oxide via silane-condensation chemistry [i.e., using (3-aminopropyl)dimethylethoxysilane or (3-glycidyloxypropyl)trimethoxysilane)] (Figure 1-7A–B). The resulting amine- or epoxide-coated *B/P*-SiQDs (*amine-B/P*-SiQDs or *epox-B/P*-SiQDs) were reacted with IgG antibodies through the amide coupling reaction or the amine-mediated epoxide ring-opening reaction in order to afford IgG-conjugated *B/P*-SiQDs (*IgG-B/P*-SiQDs) (Figure 1-7C). TEM, DLS, and polyacrylamide gel electrophoretic (PAGE) analysis of the bioinorganic hybrids revealed that multiple SiQDs were attached to a single IgG molecule through its heavy and light chains. Furthermore, experimental evidence suggests that the antibodies and the SiQDs formed cross-linked structures. TEM also revealed that the crystalline core of the bioinorganic hybrids has a diameter of ~4.2 nm. Coating the *B/P*-SiQDs with silanes and conjugation with IgG did not alter the PL emission of the SiQDs; the quantum dots still exhibited near infrared emission with a maximum at ~830 nm at an excitation wavelength of 400 nm. In order to confirm that the IgG antibody retains its biological activity and thus demonstrate the utility of the bioinorganic hybrids in fluorescent immunoassay, the binding of *IgG-B/P*-SiQDs to an

influenza virus NP antigen-coated plate was monitored (Figure 1-7D). As shown in Figure 1-7E, compared to the anti-HSA-conjugated *B/P*-SiQDs (*anti-HSA-B/P*-SiQDs) negative controls, the *IgG-B/P*-SiQDs showed significant binding to NP-coated plate, confirming that the IgG antibodies retain their biological activity upon bioconjugation.

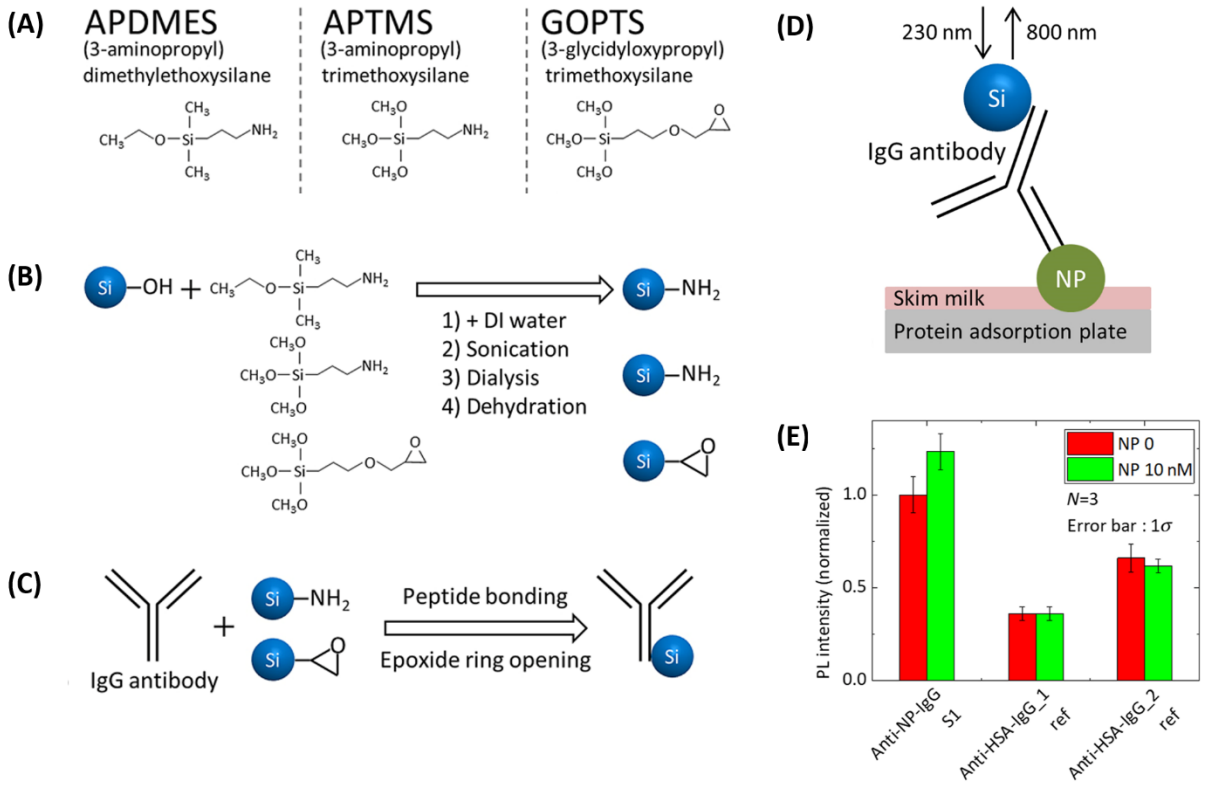

Figure 1-7. (A) Functionalized silanes used in coating the *B/P*-SiQDs. **(B)** Condensation reaction used in coating the *B/P*-SiQDs. **(C)** Bioconjugation of *amine-B/P*-SiQDs or *epox-B/P*-SiQDs to IgG antibody through the amide coupling reaction or epoxide ring opening reaction. Fluorescence immunoassay scheme **(D)** and fluorescence immunoassay results **(E)** for *IgG-B/P*-SiQDs and *anti-HSA-B/P*-SiQDs (negative controls). Adapted with permission from Yanagawa, H.; Inoue, A.; Sugimoto, H.; Shioi, M.; Fujii, M. *MRS Commun.* **2019**, *9* (3), 1079–1086. Copyright © 2019 Cambridge University Press.

Nucleic acids, such as deoxyribonucleic acid (DNA), also have been conjugated to SiQDs through the amide coupling reaction. Figure 1-8A shows the scheme employed by Wang and co-workers in modifying the surface of SiQDs with a succimidyl ester via two consecutive photochemical reactions: the UV-mediated hydrosilylation of 1-octene with *H*-SiNPs obtained from the lateral electrochemical anodization of silicon wafers, followed by the carbene insertion reaction of the photoactivatable diazirine cross-linker 4'-[3-(trifluoromethyl-3H-diazirin-3-yl)]-benzoic acid *N*-hydroxysuccinimide ester (TDBA-OSu)

into the methyl groups of the resulting octyl-capped SiQDs.[44] DNA-conjugated SiQDs (*DNA*-SiQDs) were prepared by reacting the succimidyl ester-modified SiQDs with amine-terminated single-stranded DNA in a nucleophilic substitution reaction. The ssDNA-conjugated SiQDs (*ssDNA*-SiQDs) were allowed to hybridize with complementary ssDNA strands to form double-stranded DNA-conjugated SiQDs (*dsDNA*-SiQDs). As shown in Figure 1-8B, PAGE confirmed the hybridization of *ssDNA*-SiQDs with complementary ssDNA strands; the diffused band in Lane 3 corresponds to *dsDNA*-SiQDs, while the band at the same running positions in Lanes 2 and 3 correspond to unhybridized *ssDNA*-SiQDs. TEM analysis showed that the SiQDs have a distribution of diameters ranging from one to two nanometers. Spectral characterization revealed that the *ssDNA*-SiQDs have a PL maxima at ~400 nm and ~450 nm (i.e., blue emission) at an excitation wavelength of 300 nm. The quantum yield of *ssDNA*-SiQDs measured relative to a quinine sulfate standard was 0.08. Of note, the dilute solution of *ssDNA*-SiQDs was stable and did not exhibit any significant decrease in PL intensity after a week of dispersion in water.

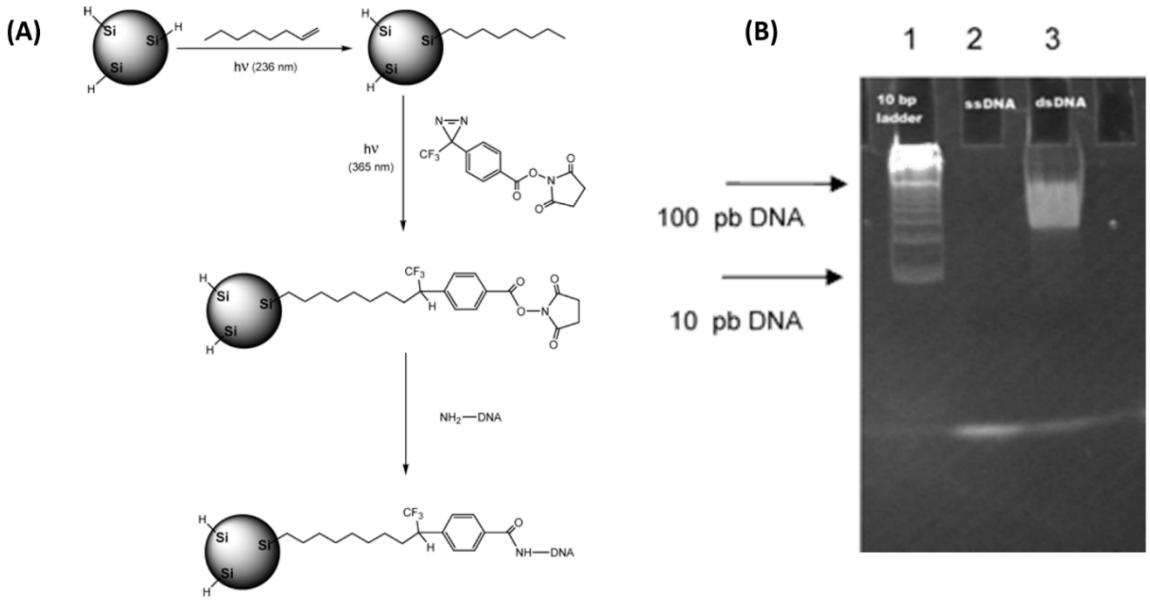

Figure 1-8. (A) Scheme showing the synthesis of *ssDNA*-SiQDs from *H*-SiNPs **(B)** Polyacrylamide gel electrophoretic profiles of *ssDNA*-SiQDs (Lane 2) and *dsDNA*-SiQDs (Lane 3). Lane 1 consists of 10 base pairs DNA ladder. Adapted from Wang, L.; Reipa, V.; Blasic, J. *Bioconjugate Chem.* **2004**, *15* (2), 409–412. Not subject to US copyright.

Ruizendaal et al. prepared *DNA*-SiQDs following the procedure depicted in Figure 1-9A–B.[45] They prepared alkene-terminated SiQDs (*ene*-SiQDs) via the oxidation of magnesium silicide with bromine and the subsequent reaction of the resulting *H*-SiNPs with butenyl magnesium bromide (Figure 1-9A). TEM revealed a size of 2.4 ± 0.5 nm for the *ene*-SiQDs, while H-NMR and XPS confirmed successful butenyl functionalization. Steady-state photoluminescence measurements showed that the *ene*-SiQDs exhibited green emission (λ_{em} = 525 nm at an excitation wavelength of 430 nm) and a quantum yield of 1.8% at an excitation wavelength of 366 nm. The lifetime obtained from time-resolved fluorescence spectroscopy of the SiQDs was in the nanosecond regime, which is consistent with SiQDs emitting from excited surface states. The *ene*-SiQDs were reacted with thiol-functionalized organic compounds, such as thioacetic acid, by means of a thiol–ene reaction to afford *acid*-SiQDs (Figure 1-9A), which then were conjugated to amine-terminated single-stranded DNA using EDC and NHS as amide coupling reagents (Figure 1-9B). Fluorescent dye-labelled single-stranded DNA with a sequence complementary to the immobilized ssDNA strands were allowed to hybridize with the ssDNA-conjugated SiQDs (*ssDNA*-SiQDs) and form double-stranded DNA SiQD hybrids (*dsDNA*-SiQDs) (Figure 1-9C). The successful covalent immobilization of ssDNA on the SiQDs was confirmed through agarose gel electrophoresis and absorption and fluorescence spectroscopy. Figure 1-9D shows the electrophoretic profiles of the *dsDNA*-SiQDs. The band identified by arrow II in Lanes 2–4 indicates that a single quantum dot contains a maximum of two to three covalently linked DNA strands.

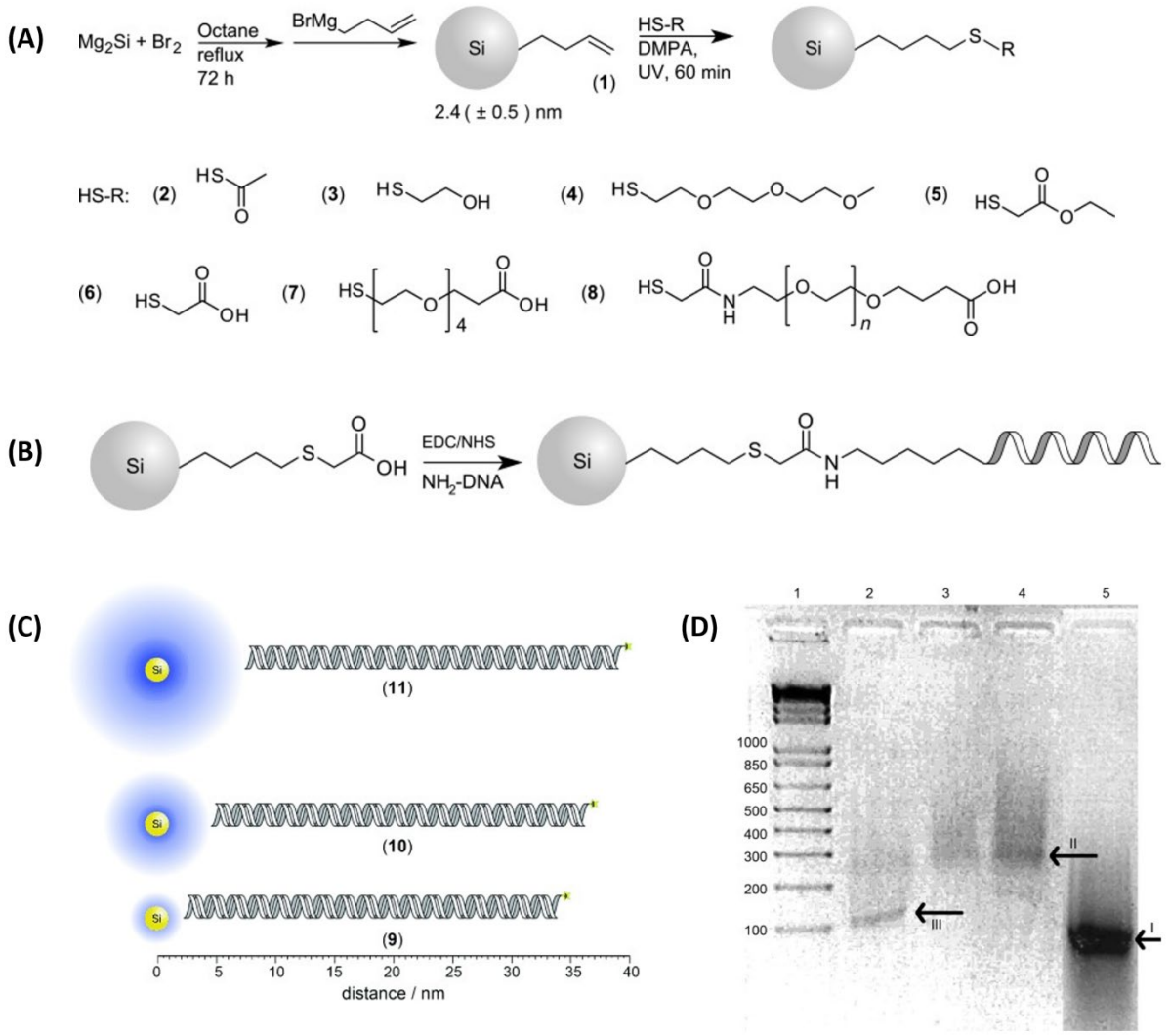

Figure 1-9. (A) Scheme showing synthesis of *ene*-SiQDs and other functionalized SiQDs through a photochemical thiol–ene reaction. **(B)** Scheme showing the synthesis of *ssDNA*-SiQDs. **(C)** *dsDNA*-SiQDs with varying lengths of thiol linkers (EO) tethers (9: thioglycolic acid; 10: $(EO)_4$, EO = ethylene oxide; 11: $(EO)_n$. **(D)** Agarose gel electrophoretic profiles of *dsDNA*-SiQDs (Lane 2: 9, Lane 3: 10, Lane 4: 11) and unconjugated double-stranded DNA (Lane 5). Lane 1 consists of a DNA ladder. Adapted with permission from Ruizendaal, L.; Pujari, S. P.; Gevaerts, V.; Paulusse, J. M. J.; Zuilhof, H. *Chem. Asian J.* **2011**, *6* (10), 2776–2786. Copyright © 2011 Wiley VCH.

Carbohydrates also have been linked covalently to SiQDs through the amide coupling reaction. Figure 1-10A shows the synthetic route employed by Lai and co-workers in preparing bioinorganic hybrids consisting of SiQDs, an organic dye, and Gg3, the sugar moiety of a glycosphingolipid implicated in cancer.[46] They used these dual-fluorescent scaffolds in imaging B16F10 melanoma cells, a GM3-overexpressing cancer cell line, to probe the ultraweak carbohydrate interactions between Gg3 and GM3, a sugar moiety of surface

glycosphingolipid present in B16F10 cancer cells. First, they synthesized *acid*-SiQDs by nucleophilic substitution reaction of bromide-terminated SiQDs with 3-butenylmagnesium bromide, followed by oxidation of the alkene moieties into carboxylic acids using $NaIO_4/RuCl_3$ as an oxidizing agent. XPS analysis confirmed the presence of Si and C in the hybrids. The quantum dots have a TEM diameter of 4 ± 1 nm and a molecular weight of 10.5 kDa, according to analytical ultracentrifugation measurements. An amine-functionalized dye (ATTO-647N) and amine-functionalized sugars (e.g., glucose, lactose, or Gg3) were linked to the acid-SiQDs using EDC and hydroxybenzotriazole (HOBt) as amide coupling agents. The resulting decrease in the negative values of the zeta potential of the *acid*-SiQDs after reaction is consistent with successful immobilization of the dye and carbohydrate moieties on the quantum dot surface. Furthermore, the presence of the conjugated sugars was confirmed by H-NMR. It was estimated that 8.3 Gg3 residues were immobilized on one SiQD. The uptake of SiQDs conjugated to Gg3 and dye (*Gg3,dye*-SiQDs) by the B16F10 melanoma cell line was investigated using flow cytometry. The results revealed that B16F10 cells selectively uptake *Gg3,dye*-SiQDs, suggesting that overexpressed GM3 sugars on B16F10 cells mediate successful nanoparticle internalization. The utility of *Gg3,dye*-SiQDs for bioimaging was evaluated further using confocal microscopy (Figure 1-10B–G). The B16F10 cells successfully internalized the *Gg3,dye*-SiQDs, as confirmed by the detection of the intrinsic blue photoluminescence of the SiQDs and the purple fluorescence of the appended organic dye.

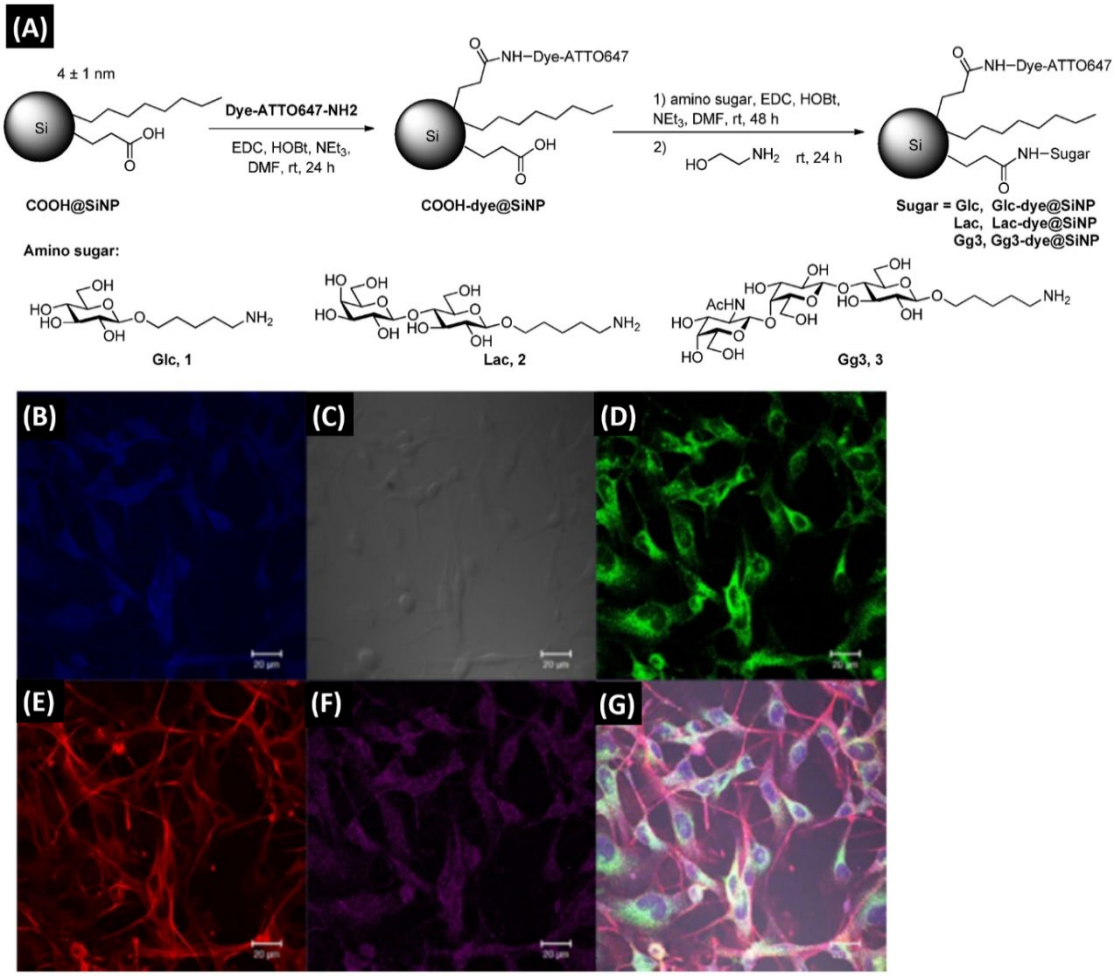

Figure 1-10. (A) Scheme showing synthesis of *ene*-SiQDs and other functionalized SiQDs through a photochemical thiol–ene reaction. Differential interference contrast and confocal microscopy images of B16F10 cells showing **(B)** intrinsic blue PL of *Gg3,dye*-SiQDs, **(C)** normal B16F10 cell morphology, **(D)** early endosomes stained with anti-EEA1 antibody (green), **(E)** actin cytoskeleton stained with Alexa 555-labeled phalloidin (red), and **(F)** purple fluorescence of the ATTO-647N dye conjugated to the SiQDs. **(G)** Overlay of images B–F. Adapted with permission from Lai, C.-H.; Hütter, J.; Hsu, C.-W.; Tanaka, H.; Varela-Aramburu, S.; De Cola, L.; Lepenies, B.; Seeberger, P. H. *Nano Lett.* **2016**, *16* (1), 807–811. Copyright © 2016 American Chemical Society.

Ahire et al. employed amine-terminated SiQDs (amine SiNPs) in preparing carbohydrate-conjugated SiQDs for bioimaging applications. They coated SiQDs with amine groups by reacting *H*-SiNPs obtained from electrochemical alcoholic HF etching of a porous silicon layer with allylamine in the presence of H_2PtCl_6 as catalyst (Figure 1-11A).[47] The resulting amine SiNPs had a mean TEM size of 4.6 nm and exhibited blue PL, having an emission maximum at around 450 nm (Figure 1-11B) and a PL quantum yield of 22% (λ_{ex} = 360 nm). Acid-functionalized sugars (galactose, mannose, glucose, or lactose) were attached covalently to the amine SiNPs through the amide coupling chemistry using EDC and

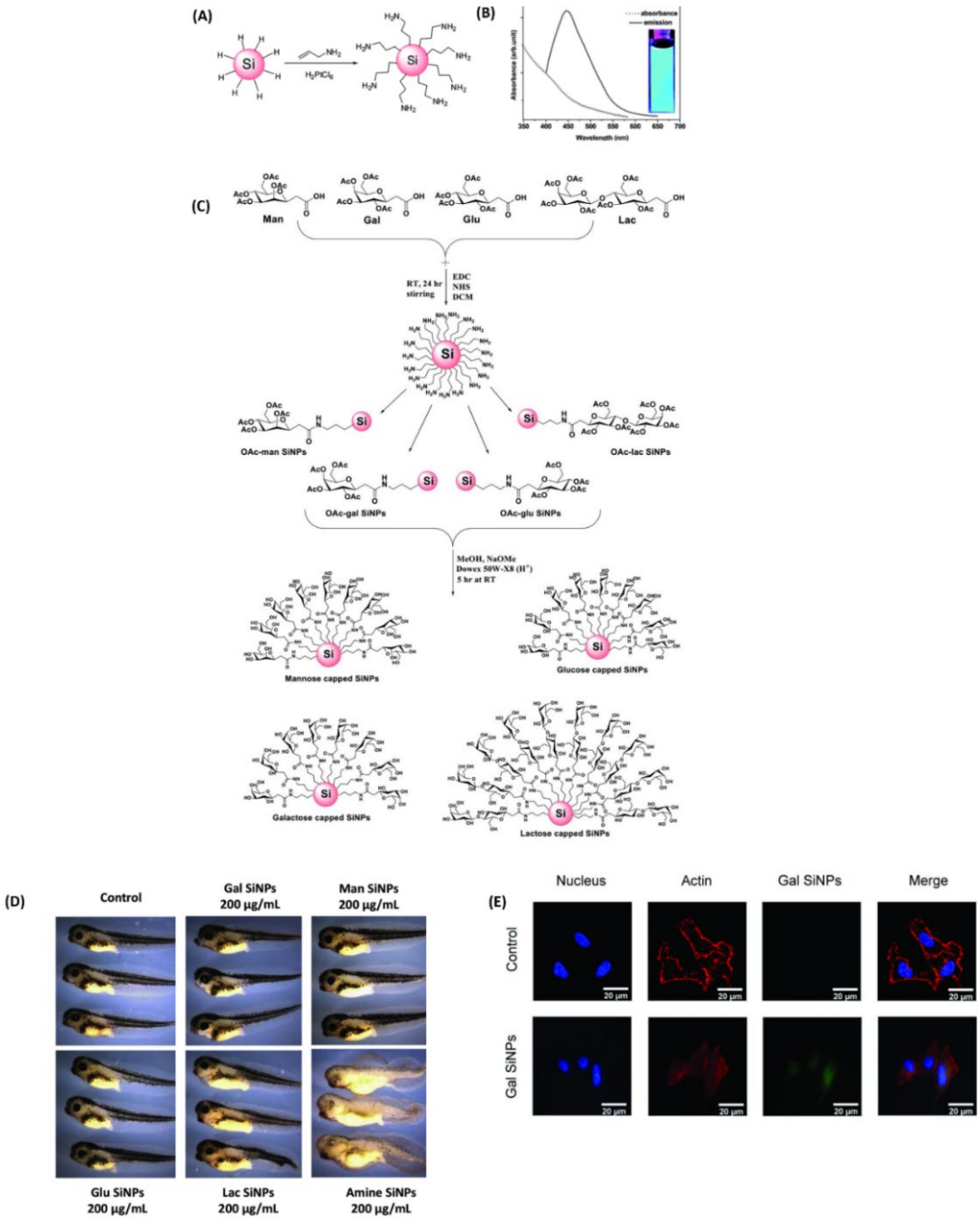

Figure 1-11. (A) Scheme showing the synthesis of amine SiNPs through a platinum-catalyzed hydrosilylation of allylamine with *H*-SiNPs. **(B)** Absorbance and emission spectra of amine SiNPs. **(C)** Scheme showing the synthesis of carbohydrate-conjugated SiQDs using the amide coupling chemistry. **(D)** *X. laevis* embyos exposed to different carbohydrate-conjugated SiQDs. **(E)** Confocal microscopy images of A549 cells incubated in the presence and absence (control) of Gal SiNPs. The blue fluorescence is due to a DAPI nuclear stain while the red fluorescence is due to actin staining. The green photoluminescence comes from Gal SiNPs. Adapted with permission from Ahire, J. H.; Wang, Q.; Coxon, P. R.; Malhotra, G.; Brydson, R.; Chen, R.; Chao, Y. *ACS Appl. Mater. Interfaces* **2012**, *4* (6), 3285–3292 and Ahire, J. H.; Behray, M.; Webster, C. A.; Wang, Q.; Sherwood, V.; Saengkrit, N.; Ruktanonchai, U.; Woramongkolchai, N.; Chao, Y. *Adv. Healthc. Mater.* **2015**, *4* (12), 1877–1886. Copyrights © 2012 American Chemical Society and © 2015 Wiley VCH, respectively.

NHS as coupling agents (Figure 1-11C).[48] An MTT assay revealed that the carbohydrate-conjugated SiQDs (Gal SiNPs, Man SiNPs, Glu SiNPs, Lac SiNPs), unlike the amine SiNPs, were non-cytotoxic, exhibiting no toxicity to three mammalian cell lines: A549 (human lung carcinoma), HHL-5 (human immortalized hepatocytes), and MDCK (normal kidney epithelium cells). As shown in Figure 1-11D, an in vivo assay using *X. laevis* embryos as model revealed that, consistent with the results of the in vitro toxicity assay, the carbohydrate-conjugated SiQDs did not cause any significant death or embryonic malformations at concentrations as high as 200 μg mL^{-1}. Moreover, the Gal SiNPs were internalized by A549 cells and successfully used in imaging the cell cytoplasm (Figure 1-11E). Also, the carbohydrate-conjugated SiQDs were taken up by cancer cells more readily than by normal cells, which suggests that they can be employed for targeted treatment of tumors.

In a separate work, Ahire and co-workers synthesized mannose-conjugated SiQDs from amine-terminated SiQDs and acid-functionalized mannose through the amide coupling reaction using *N,N′*-Dicyclohexylcarbodiimide (DCC) as a coupling agent (Figure 1-12A).[49] They tested the biological activity of the resulting mannose-conjugated SiQDs by monitoring their interaction with concanavalin A, a mannose-specific carbohydrate-binding protein that has four binding sites for mannose (Figure 1-12B). The mannose-conjugated SiQDs underwent visible aggregation in the presence of concanavalin A. This concanavalin A-mediated aggregation caused a decrease in the PL intensity of the SiQDs and their cross-linking, as seen through TEM (Figure 1-12C). Also, like the carbohydrate-conjugated SiQDs discussed above, Ahire et al. successfully employed these bioconjugated SiQDs for imaging cancer cells (Figure 1-12D). Together, these confirm that the mannose molecules retain their biological activity upon immobilization on the SiQDs and point to the potential utility of carbohydrate-conjugated SiQDs as tools, not only for bioimaging, but also in understanding carbohydrate-receptor interactions, which play crucial roles in endocytosis, intercellular communication, and biochemical processes implicated in cancer development and metastasis.

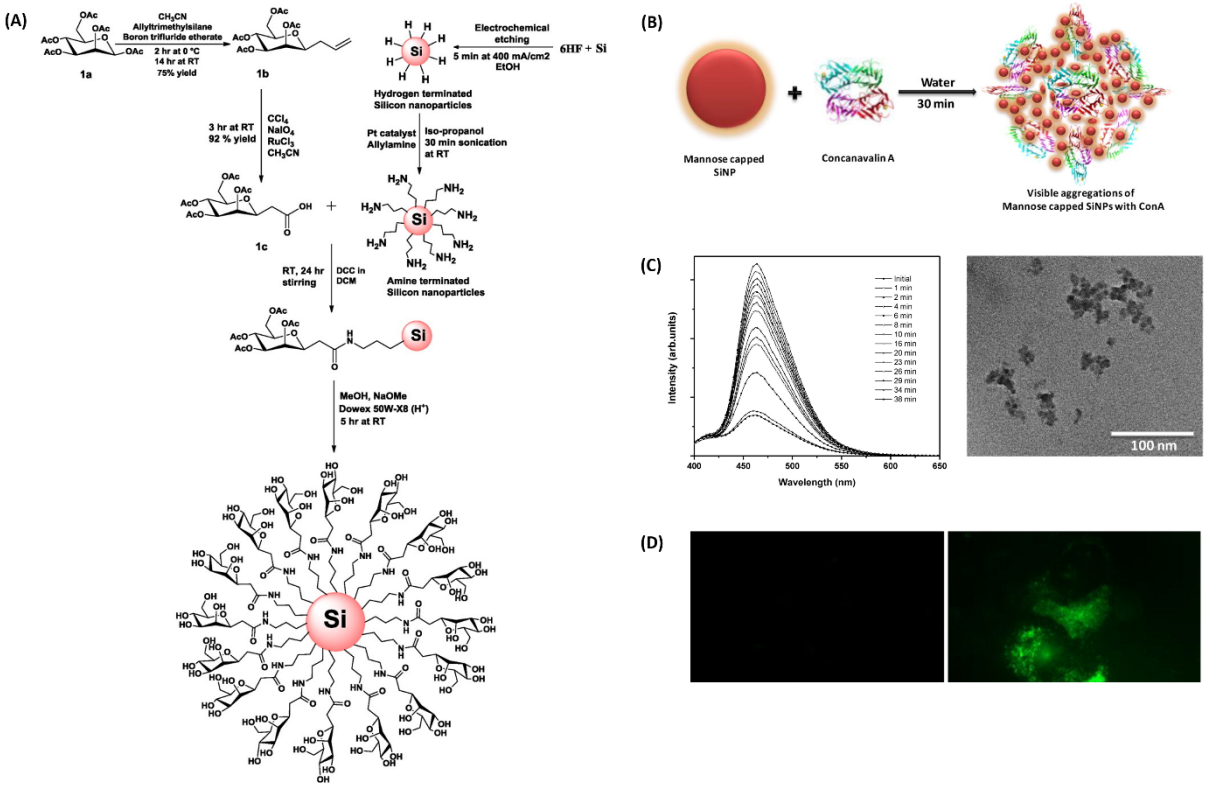

Figure 1-12. (A) Scheme showing the synthesis of mannose-conjugated SiQDs through the amide coupling chemistry. **(B)** Scheme showing the cross-linking of mannose-conjugated SiQDs induced by concanavalin A. **(C)** Photoluminescence spectra of mannose-conjugated SiQDs at different times after addition of concanavalin A (left) and TEM image (right) of aggregated mannose-conjugated SiQDs. **(D)** Fluorescence images of MCF-7 cells in the absence (left) and presence (right) of mannose-conjugated SiQDs. Adapted with permission from Ahire, J. H.; Chambrier, I.; Mueller, A.; Bao, Y.; Chao, Y. *ACS Appl. Mater. Interfaces* **2013**, *5* (15), 7384–7391. Copyright © 2013 American Chemical Society.

The thiol–ene 'click' reaction also has been utilized in the covalent conjugation of biomolecules to SiQDs. This reaction has become popular with bioconjugate chemists because of its high reaction yield, its insensitivity to the presence of oxygen, its functional group tolerance, and the chemical robustness of the resulting thioether linkage.[50,51] Su and co-workers, for instance, coated SiQDs with oligonucleotides and prepared DNA-conjugated SiQDs for micro-RNA detection.[52] They first prepared *ene*-SiQDs via the reactive high-energy ball milling of silicon wafer with 1,8-octadiene, followed by the photochemical thiol–ene reaction with thiol-terminated fluorescein-functionalized oligonucleotide (Fln-DNA) (Figure 1-13A). The *ene*-SiQDs and SiQDs coated with fluorescein-functionalized oligonucleotide (*Fln-DNA*-SiQDs) were characterized through TEM and atomic force microscopy (AFM),

revealing diameters of 3 nm and 10 nm, respectively. The increased diameter upon DNA functionalization is consistent with successful conjugation. PAGE also confirmed successful

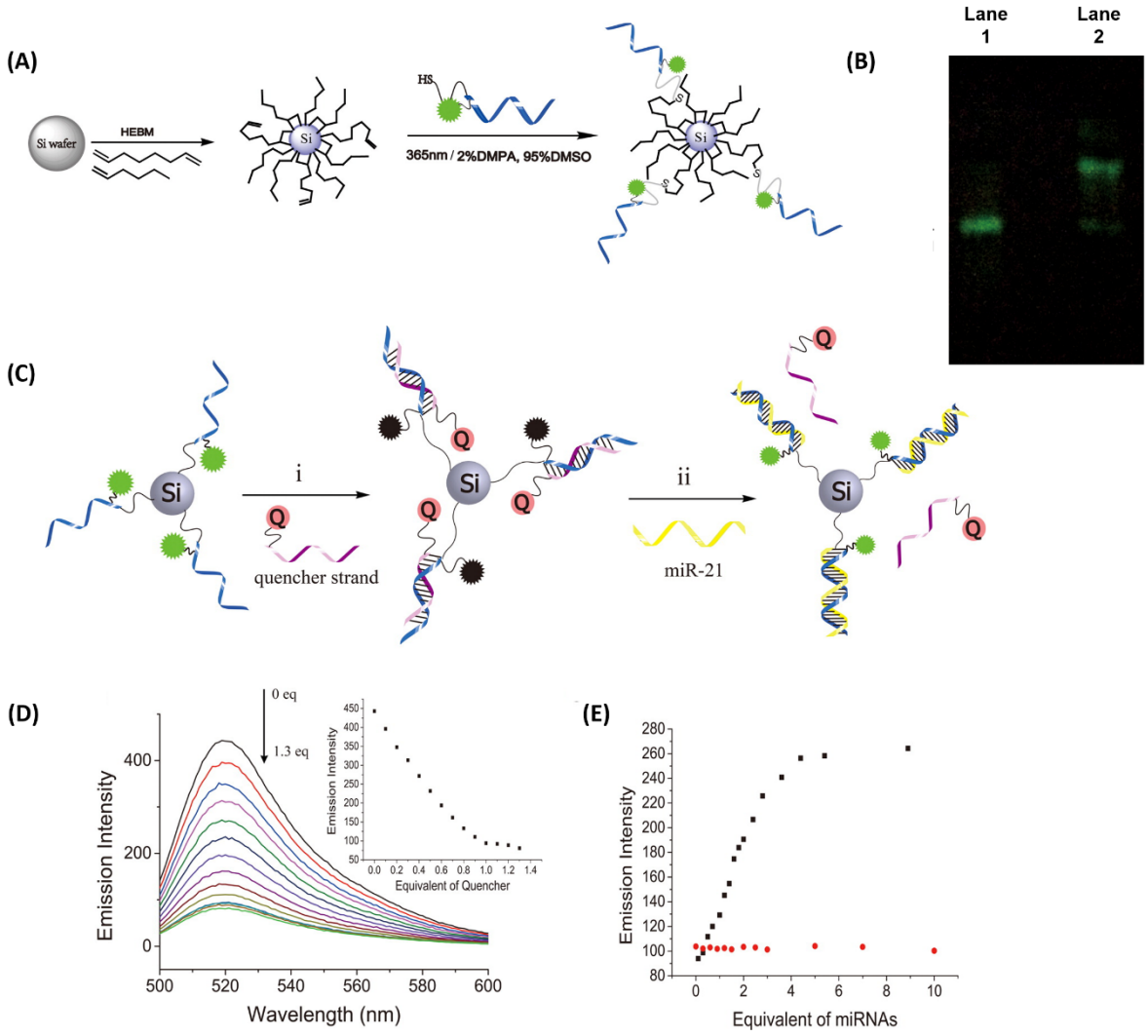

Figure 1-13. (A) Scheme showing the synthesis of ene-SiQDs and *Fln-DNA*-SiQDs. **(B)** Polyacrylamide gel electrophoretic profiles of unconjugated DNA (Lane 1) and *Fln-DNA*-SiQDs (Lane 2) visualized via excitation of fluorescein (λ_{ex} = 254 nm). **(C)** Scheme showing the detection of miR-21 using *Fln-DNA*-SiQDs. **(D)** Fluorescence spectra of *Fln-DNA*-SiQDs in the presence of increasing equivalents of quencher strand (Inset: Plot of fluorescence intensity versus equivalent of quencher strand). **(E)** Plots of fluorescence intensity versus equivalent of miR-21 (black) and miR-155 (red). Adapted with permission from Su, X.; Kuang, L.; Battle, C.; Shaner, T.; Mitchell, B. S.; Fink, M. J.; Jayawickramarajah, J. *Bioconjugate Chem.* **2014**, *25* (10), 1739–1743.

DNA conjugation; the band corresponding to *Fln-DNA*-SiQDs travelled a shorter distance compared to Fln-DNA (Figure 1-13B). Absorption spectroscopy revealed an estimate of 4–5 DNA strands per SiQD. It is worth mentioning that the SiQDs that they synthesized exhibit

blue PL with a minimal quantum yield (QY = 2%) at around 420 nm. The authors used the SiQD scaffold as a sensor for detecting microRNA 21 (miR-21), a noncoding RNA that is overexpressed in many forms of cancer. As shown in Figure 1-13C, their sensing strategy involves pairing up the DNA strands on the SiQDs with complementary single-stranded DNA that bear groups that quench the fluorescence of the fluorescein dye. Figure 1-13D shows that the fluorescence intensity of the fluorescein dye decreases in the presence of increasing concentration of the quencher strand. The analyte is detected by displacement of the quencher DNA strand by miR-21, which has a greater affinity for the DNA strands on the *Fln-DNA*-SiQDs than the quencher strand. This displacement leads to the recovery of fluorescein fluorescence, the intensity of which is proportional to the amount of miR-21 (Figure 1-13E). The method is highly specific for miR-21, as demonstrated by the failure of a microRNA with a noncomplementary sequence (miR-155) to switch on the fluorescence of the system (Figure 1-13E).

Zhai and co-workers conjugated the sugar mannose and the amino acid alanine to SiQDs through a nucleophilic substitution reaction between chloride-terminated silicon nanoparticles (*Cl*-SiNPs) and the hydroxyl and amino groups of functionalized mannose and alanine, respectively (Figure 1-14A).[53] They have obtained the *Cl*-SiNPs from the reaction between phosphorous pentachloride, PCl_5, and *H*-SiNPs. Direct addition of functionalized mannose and alanine to a solution containing *Cl*-SiNPs, followed by neutralization and deprotection, afforded mannose-conjugated SiQDs (*man*-SiQDs) and alanine-conjugated SiQDs (*ala*-SiQDs). FTIR confirmed successful bioconjugation through the detection of peaks characteristic of the functionalized biomolecules. XPS also revealed the presence of an intact Si(0) core and silicon suboxides. In the case of *ala*-SiQDs, the detection of N in XPS is consistent with successful alanine conjugation. TEM imaging showed that the diameters of *man*-SiQDs and *ala*-SiQDs are 2.6 ± 0.6 nm and 2.7 ± 0.5 nm, respectively. On the other hand, DLS analysis revealed a hydrodynamic diameter of 87.3 nm for both bioconjugated SiQDs. Aqueous dispersions of *man*-SiQDs and *ala*-SiQDs exhibited blue PL, with emission maxima at ~415 and 400 nm upon excitation with 350 nm UV light and quantum yields of 13% and 17%, respectively. Figure 1-14B–G shows the uptake of *man*-SiQDs and *ala*-SiQDs by MCF-7 human breast cancer cells, which demonstrate the utility of the bioconjugated SiQDs for bioimaging.

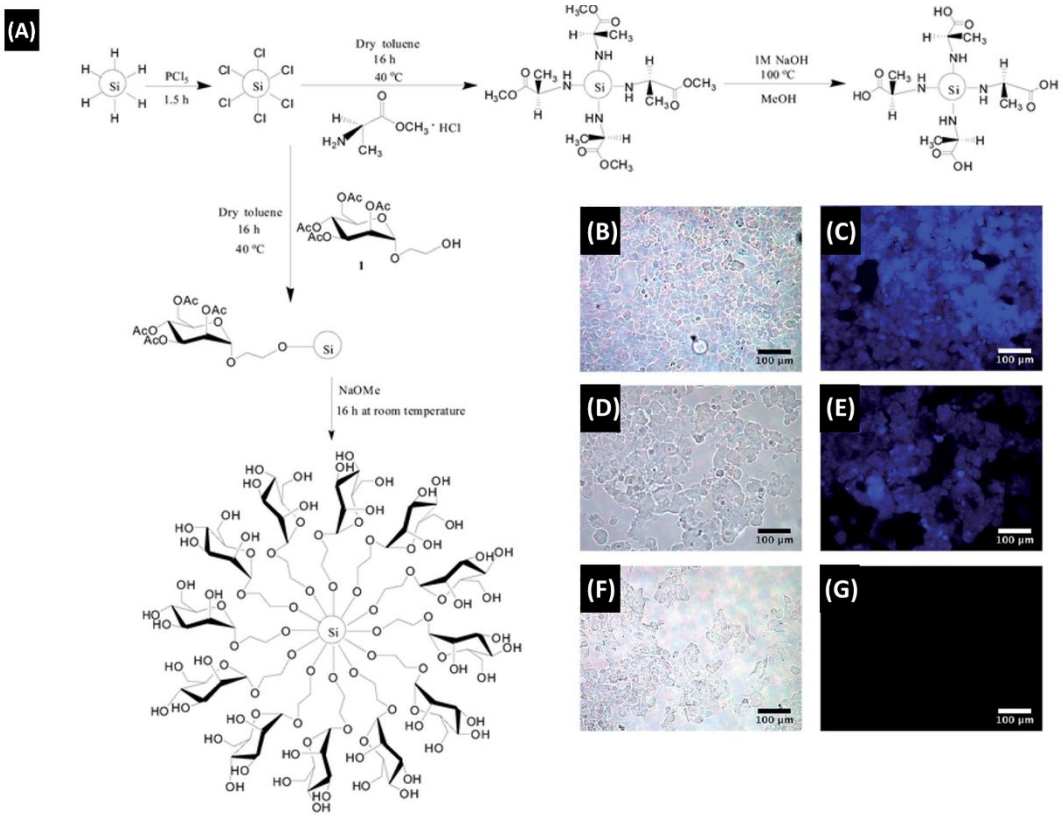

Figure 1-14. (A) Scheme showing the synthesis of *man*-SiQDs and *ala*-SiQDs from *Cl*-SiNPs and functionalized mannose and alanine through nucleophilic substitution. Images of MCF-7 cells incubated with: *man*-SiQDs without **(B)** and with **(C)** fluorescence, *ala*-SiQDs without **(D)** and with **(E)** fluorescence, and control (without SiQDs) without **(F)** and with **(G)** fluorescence. Adapted from Zhai, Y.; Dasog, M.; B. Snitynsky, R.; K. Purkait, T.; Aghajamali, M.; H. Hahn, A.; B. Sturdy, C.; L. Lowary, T.; C. Veinot, J. G. C. *J. Mater. Chem. B* **2014**, *2* (47), 8427–8433. Copyright © 2014 Royal Society of Chemistry.

One-pot methods for the synthesis of biomolecule-conjugated SiQDs also have been reported in the literature. These methods are top-down procedures that typically involve the formation of SiQDs from the breakdown of bigger silicon structures, such as silicon nanowires (SiNWs) and silicon wafers. Zhong and co-workers prepared SiQDs coated with Immunoglobulin G, IgG, as hydrophilic ligands via the thermal degradation of SiNWs under microwave irradiation.[54] The authors irradiated a solution of SiNWs and IgG for a short period of time (5–10 min) and at low temperature (30 °C) in order to prevent protein denaturation. TEM analysis showed that the IgG-conjugated SiQDs, *IgG*-SiQDs, have an average diameter of 3.17 ± 0.53 nm, while DLS revealed that they have a hydrodynamic diameter of ~40 nm. These values suggest that each SiQD is bonded to around four IgG molecules. Successful conjugation was confirmed by FTIR through the presence of functional groups present in IgG.

The *IgG*-SiQDs showed red PL (λ_{em} = 630 nm) (Figure 1-15A–B) and were highly dispersible in water. The SiQDs manifested robust pH stability, exhibiting stable PL in the pH range of 4.0–12.0, which was believed to be the result of the buffering action of the acidic and basic groups present in the IgG coating of the SiQDs. Moreover, the *IgG*-SiQDs exhibited a much superior long-term photostability compared to fluorescein isothiocyanate (FITC), an organic fluorescent dye, and Cd-based QDs (CdTe QDs and core-shell CdSe/ZnS QDs). The *IgG*-SiQDs also can be stored for more than three months without losing their PL. The utility of the bioinorganic hybrids for immunofluorescence imaging has been confirmed by treating HeLa cells with a microtubule-specific anti-tubulin antibody, which attaches to the microtubules of the HeLa cells. *IgG*-SiQDs bind to the anti-tubulin antibody as a result of antigen–antibody interactions, thus specifically staining the microtubules of the HeLa cells through its red photoluminescence (Figure 1-15C–D). While this observation supports successful coating of the SiQDs with IgG molecules, this does not provide any insight into the exact chemical nature of the bonds or the interactions that hold the IgG molecules in place around the SiQDs. Nonetheless, the water-dispersibility, red photoluminescence, and photostability of the *IgG*-SiQDs make them an attractive platform for long-term immunofluorescent cell imaging.

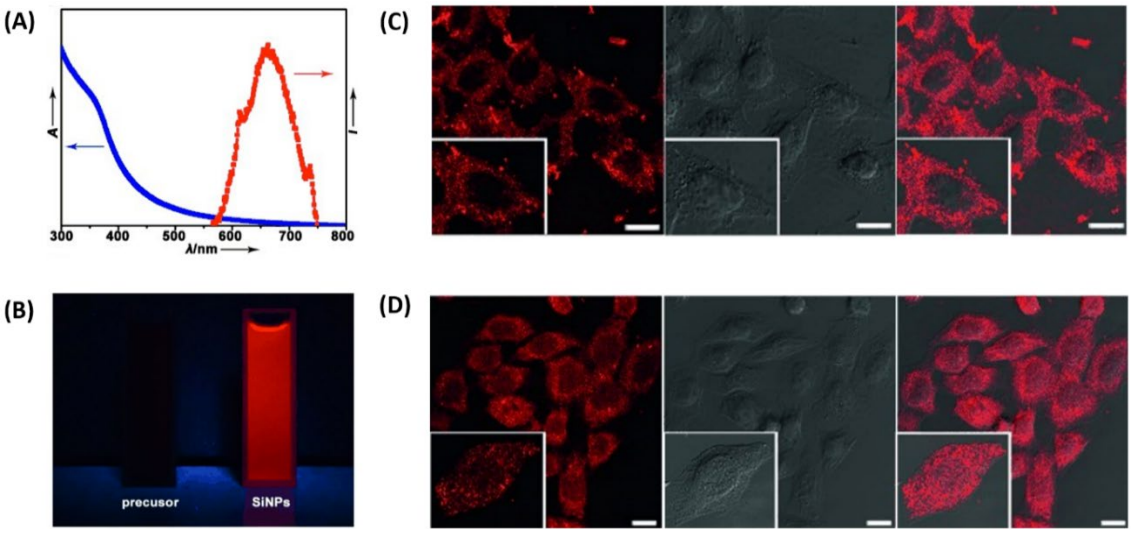

Figure 1-15. (A) Absorption and photoluminescence spectra of *IgG*-SiQDs. **(B)** Solutions containing SiNWs and IgG (left) and *IgG*-SiQDs (right) under UV illumination (365 nm). Confocal microscopy and bright field images which show that **(C)** *IgG*-SiQDs specifically stained the microtubules of Hela cells (red PL), while **(D)** unconjugated SiQDs were non-specifically taken up by the Hela cells (left: fluorescence image, middle: bright-field image, right: overlay of the two images). Adapted with permission from Zhong, Y.; Peng, F.; Wei, X.; Zhou, Y.; Wang, J.; Jiang, X.; Su, Y.; Su, S.; Lee, S.-T.; He, Y. *Angew. Chem., Int. Ed.* **2012**, *51* (34), 8485–8489. Copyright © 2012 Wiley VCH.

Bagga et al. employed the technique called pulsed laser ablation in liquid (PLAL) in synthesizing bioconjugated SiQDs. They exposed silicon wafers immersed in an aqueous solution of *Staphylococcus aureus* protein A (proA), an antibody-binding protein, to a femtosecond-pulsed infrared laser in order to synthesize photoluminescent protein A-conjugated SiQDs (*proA*-SiQDs) (Figure 1-16A).[55] The *proA*-SiQDs obtained have a TEM diameter of 8 nm, which is smaller compared to the 15 nm diameter of SiQDs obtained from PLAL of silicon wafers in pure water. This difference in size is attributed to the size quenching effect caused by proA molecules as they capped the nascent SiQDs during nanoparticle nucleation and growth. The *proA*-SiQDs exhibited blue-green photoluminescence (λ_{em} = 475 nm) at an excitation wavelength of 400 nm. The number of proA molecules coated on each SiQD was estimated by ultracentrifugation, UV/Vis spectroscopy, and inductively coupled plasma optical emission spectrometry (ICP-OES). The amount of protein A on each SiQD was estimated at 0.76 pmol nm^{-2}, corresponding to about five proA molecules per SiQD. ProA molecules were reported to have significant binding affinity to SiQD surfaces. In fact, SiQDs synthesized through pulsed-laser ablation in a solution lacking proA showed affinity for proA molecules. The utility of the *proA*-SiQDs for cell staining and bioimaging was demonstrated by allowing an anti-vinculin antibody to bind to the antigen vinculin, a cytoskeletal protein present in human fibroblasts. The addition of the anti-vinculin antibody, which binds to vinculin through its Fab region and to proA through its Fc region and *proA*-SiQDs, allows labelling and imaging of human fibroblast cells, as depicted in Figure 1-16B and demonstrated in Figure 1-16C through confocal imaging. The biocompatibility of *proA*-SiQDs was studied using real-time impedance analysis and quantified in terms of the dynamic cell index (CI), which provides information on cell status, such as morphology, cell viability, and cell spreading (Figure 1-16D). CI values obtained for HeLa cells in the presence of *proA*-SiQDs were not significantly different from those of the negative control (i.e., HeLa cells in the absence of nanoparticles). On the contrary, HeLa cells incubated with CdSe quantum dots showed diminished CI values. These results clearly indicate that, unlike the CdSe quantum dots, *proA*-SiQDs are non-toxic and biocompatible.

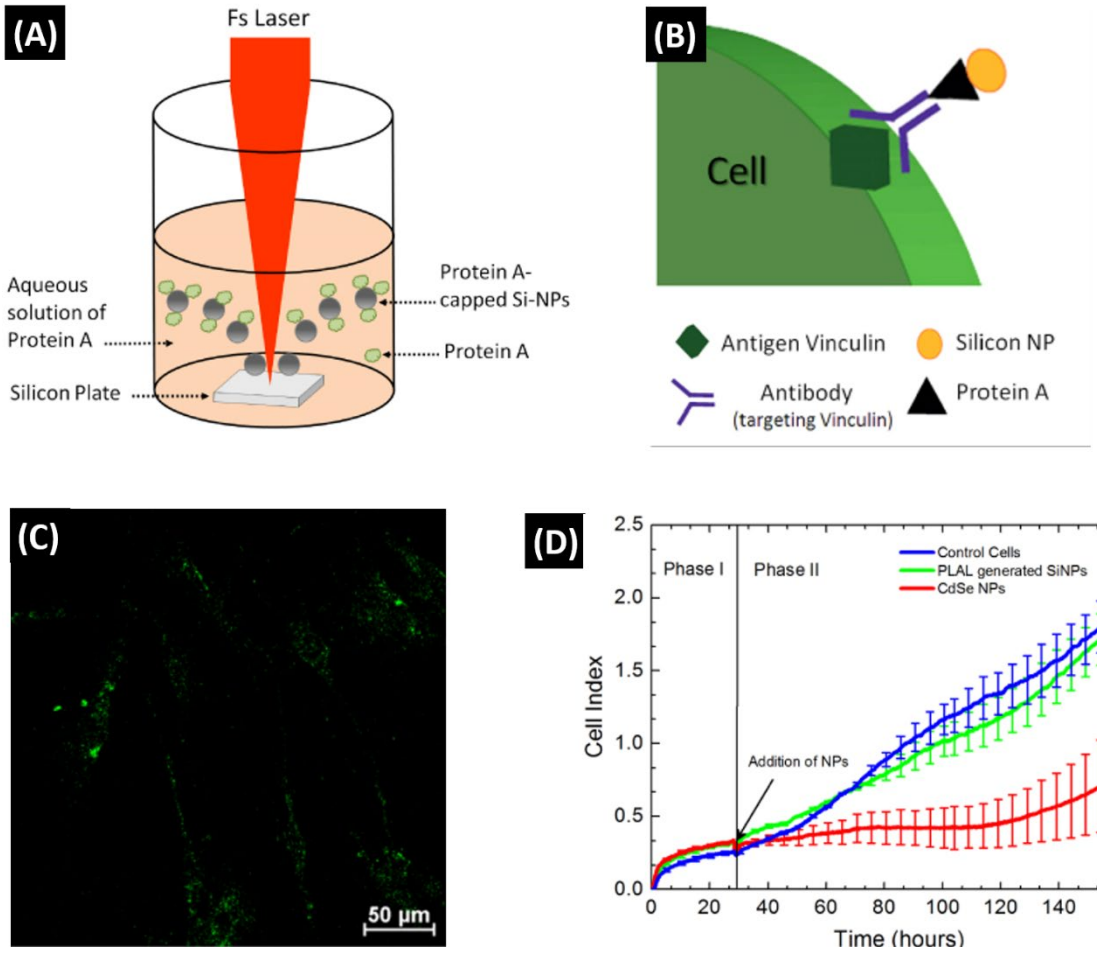

Figure 1-16. (A) Scheme showing the synthesis of *proA*-SiQDs through femtosecond-pulsed laser ablation of a silicon wafer. **(B)** Scheme showing the interaction between vinculin, anti-vinculin antibody, and *proA*-SiQDs. **(C)** Fluorescence image of human fibroblast cells stained with *proA*-SiQDs. **(D)** Cellular response curve for Hela cells in the presence of PLAL generated SiNPs (*proA*-SiQDs) and CdSe NPs, as monitored through real-time cell electronic sensing (Phase I: cell attachment and spreading, Phase II: exponential growth phase). Adapted with permission from Bagga, K.; Barchanski, A.; Intartaglia, R.; Dante, S.; Marotta, R.; Diaspro, A.; Sajti, C. L.; Brandi, F. *Laser Phys. Lett.* **2013**, *10* (6), 065603. Copyright © 2013 Astro Ltd. Reproduced by permission of IOP Publishing. All rights reserved.

In-situ bioconjugation of SiQDs using femtosecond PLAL of silicon wafers also has been used in the preparation of DNA oligonucleotide-conjugated SiQDs. Similar to the synthesis of *proA*-SiQDs, Intartaglia and co-workers ablated silicon wafers in a solution containing singe-stranded oligonucleotide (SSO) and obtained particles (*SSO*-SiQDs) with an average diameter of 3.5 ± 0.8 nm, as measured through TEM.[56] Of note, consistent with the size quenching effect of the biomolecules on the nanoparticles, the SiQDs obtained from ablating Si wafers in the absence of SSO have significantly larger diameters (i.e., <100 nm). Micro-probe Raman spectroscopy was used in order to investigate the chemical nature of the

bond between the SiQDs and the SSO. The analysis showed that the SSO becomes linked covalently at defect sites on the SiQDs through Si–C/Si–CH bonds. The shift in absorption maximum observed when the SiQDs were prepared in the presence of SSO is consistent with a decrease in size of the SiQDs (Figure 1-17A). The *SSO*-SiQDs exhibited blue-green PL, with an emission maximum at 450 nm at an excitation wavelength of 350 nm (Figure 1-17B). Moreover, the *SSO*-SiQDs have a relative photoluminescence quantum efficiency of 0.4%, as measured against Alexa 405 as reference dye standard. Ultracentrifugation and UV/vis analysis revealed that the *SSO*-SiQDs contain 1.5 SSO per SiQD, corresponding to an SSO surface density of 66 pmol cm^{-2}. Zeta potential measurements showed that the charge on the *SSO*-SiQD surface and that on the unconjugated SiQDs did not differ significantly, which suggests sufficient electrostatic stabilization of the particles. These results point to the potential utility of *SSO*-SiQDs in biomedical applications, such as vectors for nucleic acid delivery.

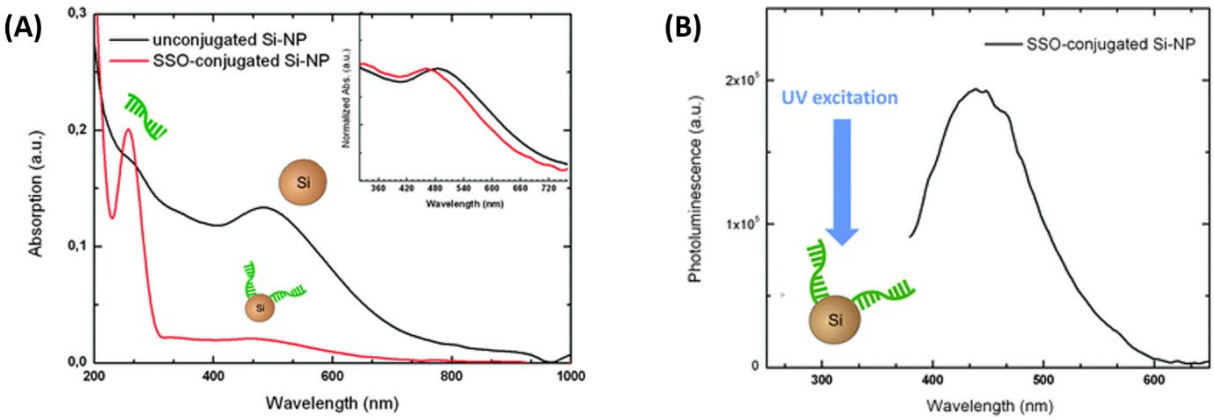

Figure 1-17. (A) Absorption spectra of SiQDs prepared in the absence (unconjugated Si-NP) and presence (SSO-conjugated Si-NP) of SSO (Inset: Normalized absorption spectra). **(B)** PL spectrum of *SSO*-SiQDs (SSO-conjugated Si-NP). Adapted with permission from Intartaglia, R.; Barchanski, A.; Bagga, K.; Genovese, A.; Das, G.; Wagener, P.; Fabrizio, E. D.; Diaspro, A.; Brandi, F.; Barcikowski, S. *Nanoscale* **2012**, *4* (4), 1271–1274.. Copyright © 2012 Royal Society of Chemistry.

The biocompatibility and non-toxicity of SiQDs coupled with the natural abundance of silicon make the bioinorganic hybrids obtained from SiQDs and biological molecules attractive platforms for applications in bioimaging and biosensing. However, as the relative paucity of literature on bioconjugated SiQDs suggests, a few challenges have to be overcome for this material to reach its full potential. Firstly, studies on how to manipulate a SiQD surface without compromising or altering its photoluminescence (e.g., emission colour and quantum yield)

must be performed in order to prepare functional and tailor-made photoluminescent bioconjugated SiQDs with predictable photoluminescence properties. Secondly, synthetic and purification strategies aimed at the preparation of SiQDs with higher quantum yields and narrower spectral bandwidths must be identified and optimized in order to come up with bioconjugated SiQDs that have brighter and sharper photoluminescence. Thirdly, reproducible, large-scale, and high-yielding methods for the synthesis of SiQDs functionalized with relevant molecular handles have to be developed in order to provide bioconjugated SiQDs in quantities sufficient for rigorous biological testing. Also, in the case of one-pot synthesis of bioinorganic SiQD hybrids, a thorough investigation of the exact chemical nature of the bonds or interactions that hold the immobilized biomolecules in place around the SiQDs must be performed in order to predict its behaviour in biological systems reliably and prevent untoward and unexpected biological responses. Lastly, SiQDs decorated with multiple biologically active molecules have to be synthesized in order to render the bioinorganic hybrids more successful in performing their intended functions. For example, aside from tumor-targeting motifs, biomolecules that promote the escape of internalized therapeutic SiQDs from endosomal capture and lysosomal degradation must be attached to the SiQDs at the same time that drugs or therapeutic enzymes are immobilized on the SiQD surface in order to enhance their performance and increase their therapeutic potency. This can be done through orthogonal bioconjugate chemistries, such as the amide coupling and thiol–ene reactions and other reactions like the Staudinger ligation, azide–alkyne cycloaddition, and nitrone dipole cycloaddition.

In conclusion, bioinorganic hybrids prepared from SiQDs and relevant biomolecules provide veritable biocompatible and cheaper alternatives to toxic heavy-metal-based quantum dots (e.g., Cd-based and Pb-based quantum dots) for biomedical applications. As such, this promising material may find its way soon into the market in the form of medicines for personalized therapy, biosensors for disease detection, and other products related to disease diagnosis and treatment.

1.2 Chemical Sensing Using Silicon-Based Quantum Dots

Silicon-based quantum dots (SiQDs), like their toxic counterparts, the heavy-metal-based quantum dots, have been used as sensors for the detection of different substances.[12,57–60] The general sensor design involves either one of four phenomena: electron transfer, Förster/fluorescence resonance energy transfer (FRET), formation of a ground-state non-photoluminescent complex, or photocurrent generation.[57,61] Scheme 1-2 depicts detection mechanisms that either involve transfer of energy or transfer of electrons.

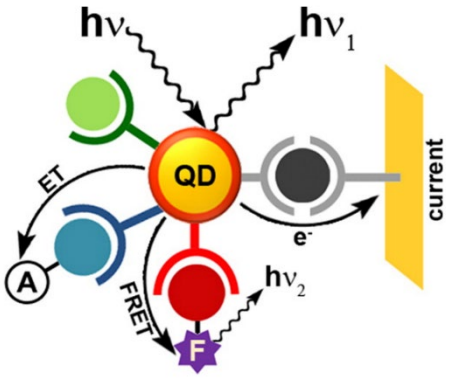

Scheme 1-2. Scheme showing the quantum dot sensing mechanisms that involve energy or electron transfer. Reprinted with permission from Freeman, R.; Girsh, J.; Willner, I. *ACS Appl. Mater. Interfaces* **2013**, *5* (8), 2815–2834. Copyright © 2013 American Chemical Society.

Electron transfer results in quenching of the quantum dot (QD) PL by disrupting electron-hole recombination. This process is critically dependent on the energy alignment of the band edges of the QDs and the lowest unoccupied molecular orbital (LUMO) or highest occupied molecular orbital (HOMO) of the quenching species. Shown in Scheme 1-3 are two possible scenarios. In the first case, where the quencher acts as an electron acceptor (i.e., oxidizing agent), the conduction band edge of the QD is higher in energy than that of the LUMO of the quencher.[62,63] In the second case, where the quencher acts as an electron donor (i.e., reducing agent), the valence band edge of the QD is lower in energy than the HOMO of the quencher.[62,63] The efficiency of electron transfer is affected by the oxidation–reduction properties of the QDs, which, in turn, depend on the presence of traps and charges on the QD surface.[64] It is important to note that the quenching of QD PL in this case involves a reaction between photoexcited QDs and the quencher molecules and is, therefore, an example of dynamic quenching, where the excited state lifetimes of the QDs are diminished.[65]

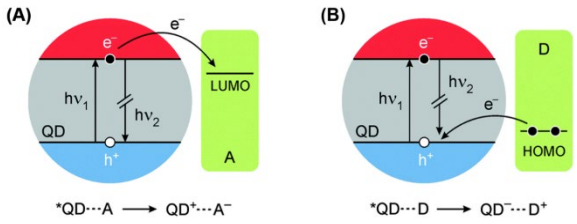

Scheme 1-3. Scheme depicting the transfer of electron **(A)** from a photoexcited quantum dot to an acceptor molecule (A) and **(B)** from a donor molecule (D) to a photoexcited quantum dot. Reprinted with permission from Silvi, S.; Credi, A. *Chem. Soc. Rev.* **2015**, *44* (13), 4275–4289. Copyright © 2015 Royal Society of Chemistry.

The QD PL also can be quenched through a phenomenon called Förster/fluorescence resonance energy transfer (FRET). This process entails the 'radiationless' transfer of energy from an excited fluorophore to an acceptor molecule, resulting in decreased fluorescence intensity of the donor (Figure 1-19).[61,66] The efficiency of this process largely depends on the distance of separation between the donor and acceptor and their relative orientation, as well as on the overlap between the emission spectrum of the donor and the absorption spectrum of the acceptor.[60,66] As FRET efficiency is determined by the inverse sixth power of the distance between the donor and acceptor, it occurs only when the donor is in very close proximity to the acceptor (i.e., separation distance of 2–8 nm).[66] Scheme 1-4 shows FRET from a photoexcited quantum dot to a molecular acceptor and vice versa.[63] As in the case of electron transfer, this quenching mechanism provides an effective alternative relaxation pathway for photoexcited QDs, leading to shortened QD lifetimes.[66]

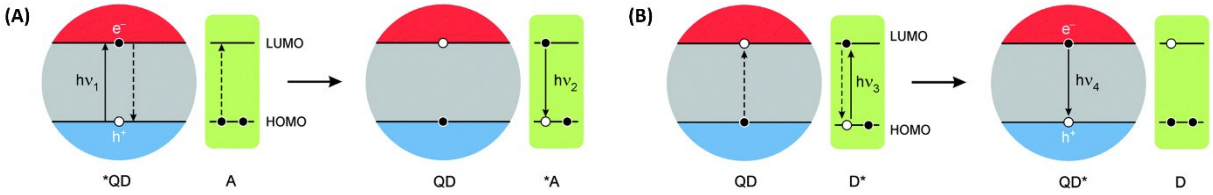

Scheme 1-4. Scheme depicting FRET **(A)** from a photoexcited quantum dot to an acceptor molecule (A) and **(B)** from a donor molecule (D) to a quantum dot. Adapted with permission from Silvi, S.; Credi, A. *Chem. Soc. Rev.* **2015**, *44* (13), 4275–4289. Copyright © 2015 Royal Society of Chemistry.

As mentioned above, electron transfer and FRET are dynamic quenching mechanisms, where the quencher reacts with photoluminescent species after it has been excited with light. PL quenching also can occur via a static quenching mechanism. In this case, the

photoluminescent species react with a quencher prior to excitation and form a non-photoluminescent complex that has an altered spectral absorption profile.[65]

Analyte detection using QDs also has been accomplished through generation of a photocurrent. This sensor design involves the covalent immobilization of QDs on an electrode surface. Upon exposure to light of appropriate wavelength, the conduction band electrons in photoexcited quantum dots become injected into the electrode, generating electrical currents,[61,67] whose behaviour and magnitude depend on the environment of the QDs, such as the presence and concentration of relevant (electro)chemically active analytes.[57]

SiQDs have been employed in the detection of heavy metals. For instance, Zhang and Yu employed blue-emitting SiQDs in the quantification of Hg^{2+} ions.[68] Hg^{2+} is believed to quench the PL of the SiQDs through interaction with the amine groups on the SiQD surface. Absorption and fluorescence lifetime measurements suggested that Hg^{2+} quenched the SiQD PL through both static and dynamic quenching mechanisms. The method is highly specific for Hg^{2+}, with an LOD of 50 nM. There are reports also on the detection of other heavy metals, like Cu^{2+}, using SiQDs as sensing platforms.[69–71]

Content and co-workers demonstrated that the PL of porous silicon films, which are emitted by silicon nanocrystallites, can be quenched by high-energy nitroaromatic compounds, such as dinitrotoluene (DNT) and trinitrotoluene (TNT).[72] They attributed the observed PL quenching to electron transfer from the excited silicon nanocrystallites to the nitroaromatic compounds and obtained a limit of detection (LOD) of 2 ppb and 1 ppb for DNT and TNT vapours, respectively. Likewise, Germanenko et al. showed that the PL of red-emitting SiQDs can be quenched by nitroaromatic compounds (e.g., 3,5-dinitrobenzonitrile, 1,4-dinitrobenzene, 2,4-dinitrotoluene, 2,6-dintrotoluene, etc.,) whose reduction potentials lie below the conduction band edge of the SiQDs.[73] Gonzalez and co-workers immobilized red-photoluminescent dodecyl-coated SiQDs on paper and employed the resulting sensor for the straightforward qualitative detection of explosives such as TNT, pentaerythritol tetranitrate (PETN), and cyclotrimethylene trinitramine (RDX) (Figure 1-18).[74] Like Content and Germanenko, they attributed the quenching of SiQD PL to an electron transfer mechanism where the quenchers act as oxidizing agents.

Figure 1-18. Detection of the high-energy compounds TNT, PETN, and RDX using red-photoluminescent SiQDs immobilized on filter paper. The images were taken while the paper sensors were exposed to a handheld UV lamp. Adapted with permission from M. Gonzalez, C.; Iqbal, M.; Dasog, M.; G. Piercey, D.; Lockwood, R.; M. Klapötke, T.; C. Veinot, J. G. C. *Nanoscale* **2014**, *6* (5), 2608–2612. Copyright © 2014 Royal Society of Chemistry.

Ban et al. used blue-photoluminescent amine-terminated SiQDs (*amine*-SiQDs) for the detection of TNT in water.[75] The authors rationalized the observed PL quenching on the basis of a FRET from the photoexcited SiQDs and the Meisenheimer complex that forms from the reaction between TNT molecules and the amine groups on the quantum dot surface. Their detection method had an LOD of 1 nM for TNT and was affected negligibly by common interfering metal cations (Scheme 1-5). Nguyen and co-workers employed SiQDs terminated with either alkyl groups or amine groups for sensing nitroaromatic compounds in the solid, solution, and vapour phases.[76] Consistent with previous reports, the PL of the red-photoluminescent alkyl-terminated SiQDs (*alkyl*-SiQDs) was quenched by nitroaromatics such as DNT, through electron transfer. Interestingly, the blue-photoluminescent amine-coated SiQDs were not as responsive to the nitroaromatic compounds as the *alkyl*-SiQDs and the previously reported *amine*-SiQDs. This possibly is due to the unavailability of the amine groups on the SiQDs for Meisenheimer complex formation, as they are covalently linked to the silicon atoms on the quantum dot surface.[57]

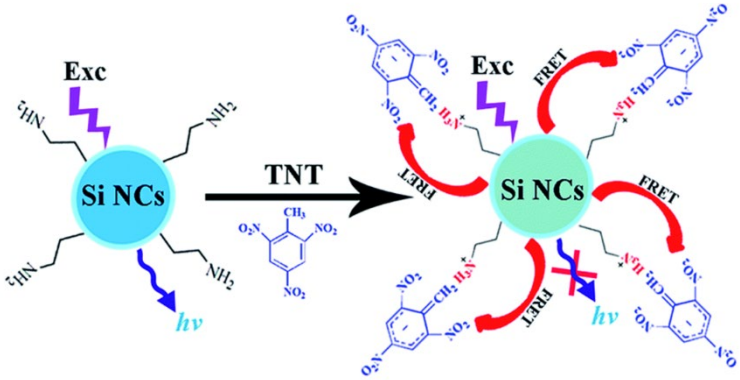

Scheme 1-5. Scheme showing FRET from the SiQDs to the Meisenheimer complex formed from the TNT molecules and the amine groups on the quantum dot surface. Reprinted with permission from Ban, R.; Zheng, F.; Zhang, J. *Anal. Methods* **2015**, *7* (5), 1732–1737. Copyright © 2015 Royal Society of Chemistry.

Biologically relevant substances, such as ethanol, glucose, dopamine, and antibiotics also have been detected using SiQDs. Zhang et al. employed optical fibers coated with red-photoluminescent SiQDs for the detection of ethanol.[77] The exposure of these fibers to air, dry oxygen, water vapor, and ethanol resulted in predictable variations in PL intensity. This method afforded an LOD for ethanol of 380 ppm at an exposure time of 15 s. Yi and co-workers demonstrated the detection of glucose using blue-photoluminescent hydride-terminated SiQDs (*H*-SiQDs), which were synthesized via the phosphomolybdic acid-mediated electrochemical etching of bulk silicon.[78] The sensing mechanism involves the action of the enzyme glucose oxidase (GOx), which catalyzes the reaction between glucose and molecular oxygen, forming gluconic acid and hydrogen peroxide, H_2O_2. The subsequent oxidation of the photoexcited SiQDs by H_2O_2 causes a decrease in SiQD PL intensity, with a degree proportional to the concentration of glucose in the sample. The LOD for glucose using this method is 0.68 μM. The same group developed a colorimetric sensor for glucose by exploiting the peroxidase-like activity of *H*-SiQDs.[79] As in the previous methodology, their sensing strategy entails the oxidation of SiQDs by H_2O_2. The resulting electron-deficient SiQDs, in turn, oxidize the colorimetric agent 3,3',5,5'-tetramethylbenzidine (TMB) into oxidized TMB (*ox*TMB), which forms a blue-green solution (Scheme 1-6). This sensing strategy afforded an LOD of 0.05 μM for glucose, an order of magnitude smaller than the LOD for their previous method.

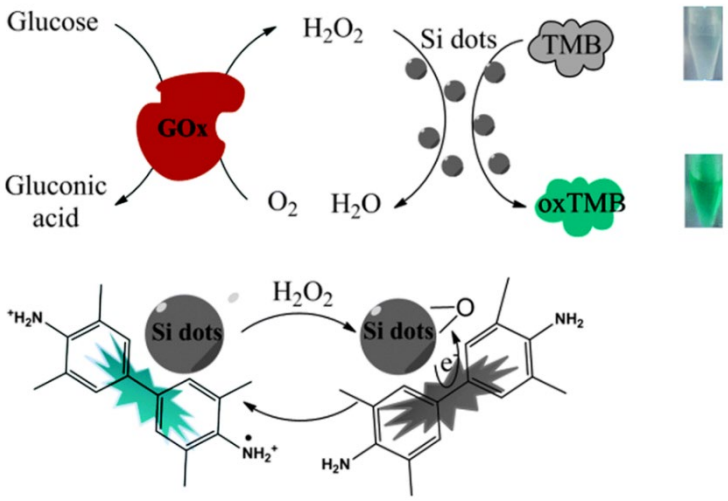

Scheme 1-6. Scheme depicting colorimetric detection of glucose mediated by the SiQDs. Reprinted with permission from Chen, Q.; Liu, M.; Zhao, J.; Peng, X.; Chen, X.; Mi, N.; Yin, B.; Li, H.; Zhang, Y.; Yao, S. *Chem. Commun.* **2014**, *50* (51), 6771–6774.. Copyright © 2014 Royal Society of Chemistry.

Dopamine, a hormone and a neurotransmitter, also has been detected using SiQDs. Blue-photoluminescent *amine*-SiQDs have been used by Zhang and co-workers for the detection of dopamine through dynamic quenching.[80] The mechanism of detection is thought to involve the facile oxidation of dopamine into its quinone, followed by quenching of SiQD PL through FRET from the quantum dot to the adsorbed quinone molecules (Scheme 1-7). The method showed high selectivity for dopamine and was affected only minimally by the presence of norepinephrine. This method was highly sensitive to dopamine, with an LOD that was as low as 0.3 nM. Lin and Wang reported the detection of tetracycline antibiotics using *amine*-SiQDs.[81] The tetracyclines were found to quench SiQD PL through static quenching, wherein the tetracycline molecules react with the functional groups (e.g., amines, etc.) on the SiQDs, forming non-emissive ground-state complexes. The LOD obtained for tetracycline, oxytetracycline, and chlortetracycline are 25.9, 20.4, and 28.3 nM, respectively.

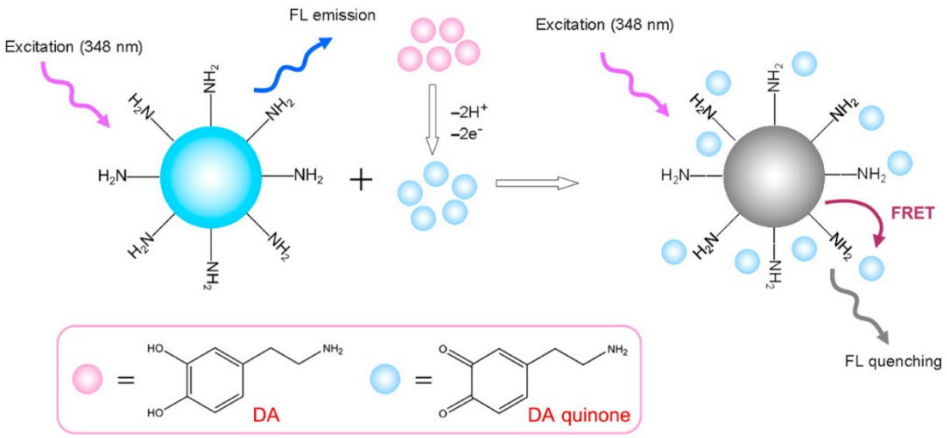

Scheme 1-7. Scheme depicting quenching of SiQD PL by dopamine through FRET. Reprinted with permission from Zhang, X.; Chen, X.; Kai, S.; Wang, H.-Y.; Yang, J.; Wu, F.-G.; Chen, Z. *Anal. Chem.* **2015**, *87* (6), 3360–3365. Copyright © 2015 American Chemical Society.

Yi et al. employed blue-photoluminescent *H*-SiQDs for the detection of pesticides.[82] Their sensing strategy entailed the concurrent use of the enzymes acetylcholine esterase (AChE) and choline oxidase (ChOx) and acetylcholine (ACh) as substrate. AChE first hydrolyzes Ach into acetic acid and choline (Ch). This is followed by the choline oxidase-catalyzed oxidation of Ch into a betaine and the concomitant production of H_2O_2. As before, the reaction of the photoexcited SiQDs with H_2O_2 results in the quenching of SiQD PL. Pesticides such as carbaryl, parathion, diazinon, and phorate inhibit the activity of AChE. Thus,

their presence leads to a diminished concentration of H_2O_2 and an increase in SiQD PL intensity. Scheme 1-8 summarizes the enzyme-mediated sensing strategy detailed in the preceding discussion. A plot of inhibition efficiency against the logarithm of pesticide concentration yielded straight lines, from which LODs of 7.25 x 10^{-9}, 3.25 x 10^{-8}, 6.76 x 10^{-8}, and 1.9 x 10^{-7} g L^{-1} were obtained for carbaryl, parathion, diazinon, and phorate, respectively.

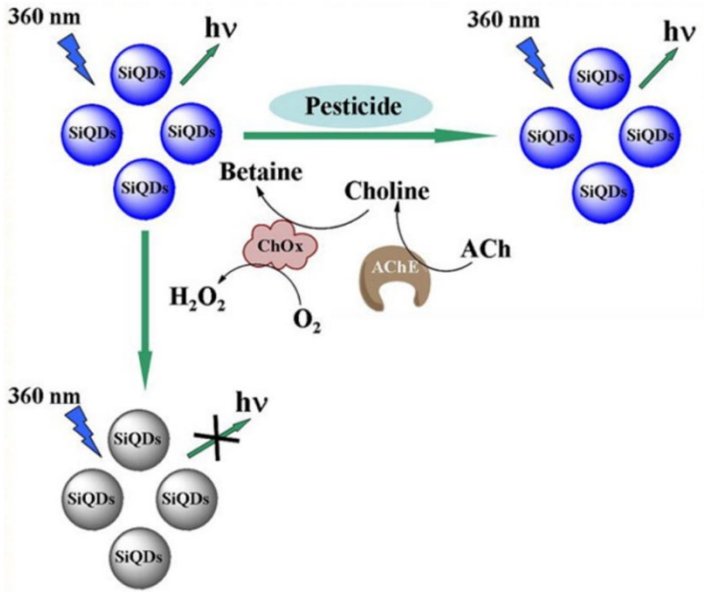

Scheme 1-8. Scheme showing the enzyme-mediated detection of pesticides using SiQDs. Adapted with permission from Yi, Y.; Zhu, G.; Liu, C.; Huang, Y.; Zhang, Y.; Li, H.; Zhao, J.; Yao, S. *Anal. Chem.* **2013**, *85* (23), 11464–11470. Copyright © 2013 American Chemical Society.

While a handful of studies have reported the use of SiQDs for the detection and quantification of different analytes successfully, the utility of SiQDs for sensing can be expanded further and improved upon. Firstly, sensing methods relying on the generation of photocurrents by electrode-immobilized SiQDs have to be explored in order to test their utility for detecting a more diverse group of electrochemically active analytes. Secondly, ratiometric (i.e., measurements relying on the use of two luminescent species) methods for analyte detection using SiQDs as one luminophore must be developed, as they could lead to the fabrication of more visually (i.e., naked eye) sensitive sensors. In addition, simultaneous detection of multiple analytes using mixtures of SiQDs of different PL emission or mixtures of SiQDs and other biologically compatible luminophores is another avenue for potential expansion. Lastly, convenient and straightforward detection methods that rely on direct

quenching of SiQD PL and which preclude the necessity for a cascade of reactions catalyzed by multiple enzymes must be developed in order to minimize methodological complexities that may compromise sensor performance.

1.3 References

(1) Alivisatos, A. P. Semiconductor Clusters, Nanocrystals, and Quantum Dots. *Science* **1996**, *271* (5251), 933–937.

(2) Brus, L. Quantum Crystallites and Nonlinear Optics. *Appl. Phys. A* **1991**, *53* (6), 465–474.

(3) Wang, Y.; Herron, N. Nanometer-Sized Semiconductor Clusters: Materials Synthesis, Quantum Size Effects, and Photophysical Properties. *J. Phys. Chem.* **1991**, *95* (2), 525–532.

(4) Weller, H. Colloidal Semiconductor Q-Particles: Chemistry in the Transition Region Between Solid State and Molecules. *Angew. Chem., Int. Ed.* **1993**, *32* (1), 41–53.

(5) Resch-Genger, U.; Grabolle, M.; Cavaliere-Jaricot, S.; Nitschke, R.; Nann, T. Quantum Dots versus Organic Dyes as Fluorescent Labels. *Nat. Methods* **2008**, *5* (9), 763–775.

(6) Peng, X.; Manna, L.; Yang, W.; Wickham, J.; Scher, E.; Kadavanich, A.; Alivisatos, A. P. Shape Control of CdSe Nanocrystals. *Nature* **2000**, *404* (6773), 59–61.

(7) Gerion, D.; Pinaud, F.; Williams, S. C.; Parak, W. J.; Zanchet, D.; Weiss, S.; Alivisatos, A. P. Synthesis and Properties of Biocompatible Water-Soluble Silica-Coated CdSe/ZnS Semiconductor Quantum Dots. *J. Phys. Chem. B* **2001**, *105* (37), 8861–8871.

(8) Rajh, T.; Micic, O. I.; Nozik, A. J. Synthesis and Characterization of Surface-Modified Colloidal Cadmium Telluride Quantum Dots. *J. Phys. Chem.* **1993**, *97* (46), 11999–12003.

(9) Semonin, O. E.; Johnson, J. C.; Luther, J. M.; Midgett, A. G.; Nozik, A. J.; Beard, M. C. Absolute Photoluminescence Quantum Yields of IR-26 Dye, PbS, and PbSe Quantum Dots. *J. Phys. Chem. Lett.* **2010**, *1* (16), 2445–2450.

(10) Zhang, J.; Gao, J.; Miller, E. M.; Luther, J. M.; Beard, M. C. Diffusion-Controlled Synthesis of PbS and PbSe Quantum Dots with In Situ Halide Passivation for Quantum Dot Solar Cells. *ACS Nano* **2014**, *8* (1), 614–622.

(11) Micic, O. I.; Sprague, J. R.; Curtis, C. J.; Jones, K. M.; Machol, J. L.; Nozik, A. J.; Giessen, H.; Fluegel, B.; Mohs, G.; Peyghambarian, N. Synthesis and Characterization of InP, GaP, and $GaInP_2$ Quantum Dots. *J. Phys. Chem.* **1995**, *99* (19), 7754–7759.

(12) Medintz, I. L.; Uyeda, H. T.; Goldman, E. R.; Mattoussi, H. Quantum Dot Bioconjugates for Imaging, Labelling and Sensing. *Nat. Mater.* **2005**, *4* (6), 435–446.

(13) Chen, N.; He, Y.; Su, Y.; Li, X.; Huang, Q.; Wang, H.; Zhang, X.; Tai, R.; Fan, C. The Cytotoxicity of Cadmium-Based Quantum Dots. *Biomaterials* **2012**, *33* (5), 1238–1244.

(14) Wani, A. L.; Ara, A.; Usmani, J. A. Lead Toxicity: A Review. *Interdiscip. Toxicol.* **2015**, *8* (2), 55–64.

(15) Martelli, A.; Rousselet, E.; Dycke, C.; Bouron, A.; Moulis, J.-M. Cadmium Toxicity in Animal Cells by Interference with Essential Metals. *Biochimie* **2006**, *88* (11), 1807–1814.

(16) Liu, J.; Erogbogbo, F.; Yong, K.-T.; Ye, L.; Liu, J.; Hu, R.; Chen, H.; Hu, Y.; Yang, Y.; Yang, J.; et al. Assessing Clinical Prospects of Silicon Quantum Dots: Studies in Mice and Monkeys. *ACS Nano* **2013**, *7* (8), 7303–7310.

(17) Meinardi, F.; Ehrenberg, S.; Dhamo, L.; Carulli, F.; Mauri, M.; Bruni, F.; Simonutti, R.; Kortshagen, U.; Brovelli, S. Highly Efficient Luminescent Solar Concentrators Based on Earth-Abundant Indirect-Bandgap Silicon Quantum Dots. *Nat. Photonics* **2017**, *11* (3), 177–185.

(18) Park, J.-H.; Gu, L.; Maltzahn, G. von; Ruoslahti, E.; Bhatia, S. N.; Sailor, M. J. Biodegradable Luminescent Porous Silicon Nanoparticles for in Vivo Applications. *Nat. Mater.* **2009**, *8* (4), 331–336.

(19) Dasog, M.; Yang, Z.; Regli, S.; Atkins, T. M.; Faramus, A.; Singh, M. P.; Muthuswamy, E.; Kauzlarich, S. M.; Tilley, R. D.; Veinot, J. G. C. Chemical Insight into the Origin of Red and Blue Photoluminescence Arising from Freestanding Silicon Nanocrystals. *ACS Nano* **2013**, *7* (3), 2676–2685.

(20) Sinelnikov, R.; Dasog, M.; Beamish, J.; Meldrum, A.; Veinot, J. G. C. Revisiting an Ongoing Debate: What Role Do Surface Groups Play in Silicon Nanocrystal Photoluminescence? *ACS Photonics* **2017**, *4* (8), 1920–1929.

(21) Dasog, M.; De los Reyes, G. B.; Titova, L. V.; Hegmann, F. A.; Veinot, J. G. C. Size vs Surface: Tuning the Photoluminescence of Freestanding Silicon Nanocrystals Across the Visible Spectrum via Surface Groups. *ACS Nano* **2014**, *8* (9), 9636–9648.

(22) Tilley, R. D.; Yamamoto, K. The Microemulsion Synthesis of Hydrophobic and Hydrophilic Silicon Nanocrystals. *Adv. Mater.* **2006**, *18* (15), 2053–2056.

(23) Manhat, B. A.; Brown, A. L.; Black, L. A.; Ross, J. B. A.; Fichter, K.; Vu, T.; Richman, E.; Goforth, A. M. One-Step Melt Synthesis of Water-Soluble, Photoluminescent, Surface-Oxidized Silicon Nanoparticles for Cellular Imaging Applications. *Chem. Mater.* **2011**, *23* (9), 2407–2418.

(24) Pettigrew, K. A.; Liu, Q.; Power, P. P.; Kauzlarich, S. M. Solution Synthesis of Alkyl- and Alkyl/Alkoxy-Capped Silicon Nanoparticles via Oxidation of Mg_2Si. *Chem. Mater.* **2003**, *15* (21), 4005–4011.

(25) Yang, C.-S.; Bley, R. A.; Kauzlarich, S. M.; Lee, H. W. H.; Delgado, G. R. Synthesis of Alkyl-Terminated Silicon Nanoclusters by a Solution Route. *J. Am. Chem. Soc.* **1999**, *121* (22), 5191–5195.

(26) Erogbogbo, F.; Yong, K.-T.; Roy, I.; Xu, G.; Prasad, P. N.; Swihart, M. T. Biocompatible Luminescent Silicon Quantum Dots for Imaging of Cancer Cells. *ACS Nano* **2008**, *2* (5), 873–878.

(27) Erogbogbo, F.; Tien, C.-A.; Chang, C.-W.; Yong, K.-T.; Law, W.-C.; Ding, H.; Roy, I.; Swihart, M. T.; Prasad, P. N. Bioconjugation of Luminescent Silicon Quantum Dots for Selective Uptake by Cancer Cells. *Bioconjugate Chem.* **2011**, *22* (6), 1081–1088.

(28) May, J. L.; Erogbogbo, F.; Yong, K.; Ding, H.; Law, W.; Swihart, T.; Prasad, P. N. Enhancing Silicon Quantum Dot Uptake by Pancreatic Cancer Cells via Pluronic® Encapsulation and Antibody Targeting. *J. Solid Tumors* **2012**, *2* (3), 24–37.

(29) Hessel, C. M.; Henderson, E. J.; Veinot, J. G. C. Hydrogen Silsesquioxane: A Molecular Precursor for Nanocrystalline Si−SiO2 Composites and Freestanding Hydride-Surface-Terminated Silicon Nanoparticles. *Chem. Mater.* **2006**, *18* (26), 6139–6146.

(30) Clark, R. J.; Aghajamali, M.; Gonzalez, C. M.; Hadidi, L.; Islam, M. A.; Javadi, M.; Mobarok, M. H.; Purkait, T. K.; Robidillo, C. J. T.; Sinelnikov, R.; et al. From Hydrogen Silsesquioxane to Functionalized Silicon Nanocrystals. *Chem. Mater.* **2017**, *29* (1), 80–89.

(31) Veinot, J. G. C. Synthesis, Surface Functionalization, and Properties of Freestanding Silicon Nanocrystals. *Chem. Commun.* **2006**, *40*, 4160–4168.

(32) McVey, B. F. P.; Tilley, R. D. Solution Synthesis, Optical Properties, and Bioimaging Applications of Silicon Nanocrystals. *Acc. Chem. Res.* **2014**, *47* (10), 3045–3051.

(33) Cheng, X.; B. Lowe, S.; J. Reece, P.; Justin Gooding, J. Colloidal Silicon Quantum Dots: From Preparation to the Modification of Self-Assembled Monolayers (SAMs) for Bio-Applications. *Chem. Soc. Rev.* **2014**, *43* (8), 2680–2700.

(34) Buriak, J. M. Organometallic Chemistry on Silicon and Germanium Surfaces. *Chem. Rev.* **2002**, *102* (5), 1271–1308.

(35) Doremus, R. H. Oxidation of Silicon by Water and Oxygen and Diffusion in Fused Silica. *J. Phys. Chem.* **1976**, *80* (16), 1773–1775.

(36) Das, P.; Saha, A.; Ranjan Maity, A.; C. Ray, S.; R. Jana, N. Silicon Nanoparticle Based Fluorescent Biological Label via Low Temperature Thermal Degradation of Chloroalkylsilane. *Nanoscale* **2013**, *5* (13), 5732–5737.

(37) Islam, M. A.; Sinelnikov, R.; Howlader, M. A.; Faramus, A.; Veinot, J. G. C. Mixed Surface Chemistry: An Approach to Highly Luminescent Biocompatible Amphiphilic Silicon Nanocrystals. *Chem. Mater.* **2018**, *30* (24), 8925–8931.

(38) Choi, J.; Wang, N. S.; Reipa, V. Conjugation of the Photoluminescent Silicon Nanoparticles to Streptavidin. *Bioconjugate Chem.* **2008**, *19* (3), 680–685.

(39) Zhong, Y.; Peng, F.; Bao, F.; Wang, S.; Ji, X.; Yang, L.; Su, Y.; Lee, S.-T.; He, Y. Large-Scale Aqueous Synthesis of Fluorescent and Biocompatible Silicon Nanoparticles and Their Use as Highly Photostable Biological Probes. *J. Am. Chem. Soc.* **2013**, *135* (22), 8350–8356.

(40) Oliinyk, B. V.; Korytko, D.; Lysenko, V.; Alekseev, S. Are Fluorescent Silicon Nanoparticles Formed in a One-Pot Aqueous Synthesis? *Chem. Mater.* **2019**, *31* (18), 7167–7172.

(41) L.Z. Ddungu, J.; Silvestrini, S.; Tassoni, A.; Cola, L. D. Shedding Light on the Aqueous Synthesis of Silicon Nanoparticles by Reduction of Silanes with Citrates. Faraday Discuss. **2020**, doi.org/10.1039/C9FD00127A.

(42) Zhong, Y.; Sun, X.; Wang, S.; Peng, F.; Bao, F.; Su, Y.; Li, Y.; Lee, S.-T.; He, Y. Facile, Large-Quantity Synthesis of Stable, Tunable-Color Silicon Nanoparticles and Their Application for Long-Term Cellular Imaging. *ACS Nano* **2015**, *9* (6), 5958–5967.

(43) Yanagawa, H.; Inoue, A.; Sugimoto, H.; Shioi, M.; Fujii, M. Antibody-Conjugated near-Infrared Luminescent Silicon Quantum Dots for Biosensing. *MRS Commun.* **2019**, *9* (3), 1079–1086.

(44) Wang, L.; Reipa, V.; Blasic, J. Silicon Nanoparticles as a Luminescent Label to DNA. *Bioconjugate Chem.* **2004**, *15* (2), 409–412.

(45) Ruizendaal, L.; Pujari, S. P.; Gevaerts, V.; Paulusse, J. M. J.; Zuilhof, H. Biofunctional Silicon Nanoparticles by Means of Thiol-Ene Click Chemistry. *Chem. Asian J.* **2011**, *6* (10), 2776–2786.

(46) Lai, C.-H.; Hütter, J.; Hsu, C.-W.; Tanaka, H.; Varela-Aramburu, S.; De Cola, L.; Lepenies, B.; Seeberger, P. H. Analysis of Carbohydrate–Carbohydrate Interactions Using Sugar-Functionalized Silicon Nanoparticles for Cell Imaging. *Nano Lett.* **2016**, *16* (1), 807–811.

(47) Ahire, J. H.; Wang, Q.; Coxon, P. R.; Malhotra, G.; Brydson, R.; Chen, R.; Chao, Y. Highly Luminescent and Nontoxic Amine-Capped Nanoparticles from Porous Silicon: Synthesis and Their Use in Biomedical Imaging. *ACS Appl. Mater. Interfaces* **2012**, *4* (6), 3285–3292.

(48) Ahire, J. H.; Behray, M.; Webster, C. A.; Wang, Q.; Sherwood, V.; Saengkrit, N.; Ruktanonchai, U.; Woramongkolchai, N.; Chao, Y. Synthesis of Carbohydrate Capped Silicon Nanoparticles and Their Reduced Cytotoxicity, In Vivo Toxicity, and Cellular Uptake. *Adv. Healthc. Mater.* **2015**, *4* (12), 1877–1886.

(49) Ahire, J. H.; Chambrier, I.; Mueller, A.; Bao, Y.; Chao, Y. Synthesis of D-Mannose Capped Silicon Nanoparticles and Their Interactions with MCF-7 Human Breast Cancerous Cells. *ACS Appl. Mater. Interfaces* **2013**, *5* (15), 7384–7391.

(50) Dondoni, A. The Emergence of Thiol–Ene Coupling as a Click Process for Materials and Bioorganic Chemistry. *Angew. Chem., Int. Ed.* **2008**, *47* (47), 8995–8997.

(51) Bertin, A.; Schlaad, H. Mild and Versatile (Bio-)Functionalization of Glass Surfaces via Thiol−Ene Photochemistry. *Chem. Mater.* **2009**, *21* (24), 5698–5700.

(52) Su, X.; Kuang, L.; Battle, C.; Shaner, T.; Mitchell, B. S.; Fink, M. J.; Jayawickramarajah, J. Mild Two-Step Method to Construct DNA-Conjugated Silicon Nanoparticles: Scaffolds for the Detection of MicroRNA-21. *Bioconjugate Chem.* **2014**, *25* (10), 1739–1743.

(53) Zhai, Y.; Dasog, M.; B. Snitynsky, R.; K. Purkait, T.; Aghajamali, M.; H. Hahn, A.; B. Sturdy, C.; L. Lowary, T.; C. Veinot, J. G. C. Water-Soluble Photoluminescent d -Mannose and l -Alanine Functionalized Silicon Nanocrystals and Their Application to Cancer Cell Imaging. *J. Mater. Chem. B* **2014**, *2* (47), 8427–8433.

(54) Zhong, Y.; Peng, F.; Wei, X.; Zhou, Y.; Wang, J.; Jiang, X.; Su, Y.; Su, S.; Lee, S.-T.; He, Y. Microwave-Assisted Synthesis of Biofunctional and Fluorescent Silicon Nanoparticles Using Proteins as Hydrophilic Ligands. *Angew. Chem., Int. Ed.* **2012**, *51* (34), 8485–8489.

(55) Bagga, K.; Barchanski, A.; Intartaglia, R.; Dante, S.; Marotta, R.; Diaspro, A.; Sajti, C. L.; Brandi, F. Laser-Assisted Synthesis OfStaphylococcus Aureusprotein-Capped Silicon Quantum Dots as Bio-Functional Nanoprobes. Laser *Phys. Lett.* **2013**, *10* (6), 065603.

(56) Intartaglia, R.; Barchanski, A.; Bagga, K.; Genovese, A.; Das, G.; Wagener, P.; Fabrizio, E. D.; Diaspro, A.; Brandi, F.; Barcikowski, S. Bioconjugated Silicon Quantum Dots from One-Step Green Synthesis. *Nanoscale* **2012**, *4* (4), 1271–1274.

(57) M. Gonzalez, C.; C. Veinot, J. G. C. Silicon Nanocrystals for the Development of Sensing Platforms. *J. Mater. Chem. C* **2016**, *4* (22), 4836–4846.

(58) Murphy, C. J. Peer Reviewed: Optical Sensing with Quantum Dots. *Anal. Chem.* **2002**, *74* (19), 520 A-526 A.

(59) Lin, C.-A. J.; Liedl, T.; Sperling, R. A.; Fernández-Argüelles, M. T.; Costa-Fernández, J. M.; Pereiro, R.; Sanz-Medel, A.; Chang, W. H.; Parak, W. J. Bioanalytics and Biolabeling with Semiconductor Nanoparticles (Quantum Dots). *J. Mater. Chem.* **2007**, *17* (14), 1343–1346.

(60) Lou, Y.; Zhao, Y.; Chen, J.; Zhu, J.-J. Metal Ions Optical Sensing by Semiconductor Quantum Dots. *J. Mater. Chem. C* **2014**, *2* (4), 595–613.

(61) Freeman, R.; Girsh, J.; Willner, I. Nucleic Acid/Quantum Dots (QDs) Hybrid Systems for Optical and Photoelectrochemical Sensing. *ACS Appl. Mater. Interfaces* **2013**, *5* (8), 2815–2834.

(62) Freeman, R.; Willner, I. Optical Molecular Sensing with Semiconductor Quantum Dots (QDs). *Chem. Soc. Rev.* **2012**, *41* (10), 4067–4085.

(63) Silvi, S.; Credi, A. Luminescent Sensors Based on Quantum Dot–Molecule Conjugates. *Chem. Soc. Rev.* **2015**, *44* (13), 4275–4289.

(64) Amelia, M.; Impellizzeri, S.; Monaco, S.; Yildiz, I.; Silvi, S.; Raymo, F. M.; Credi, A. Structural and Size Effects on the Spectroscopic and Redox Properties of CdSe Nanocrystals in Solution: The Role of Defect States. *ChemPhysChem* **2011**, *12* (12), 2280–2288.

(65) Fraiji, L. K.; Hayes, D. M.; Werner, T. C. Static and Dynamic Fluorescence Quenching Experiments for the Physical Chemistry Laboratory. *J. Chem. Educ.* **1992**, *69* (5), 424.

(66) Selvin, P. R. The Renaissance of Fluorescence Resonance Energy Transfer. *Nat. Struct. Biol.* **2000**, *7* (9), 730–734.

(67) Yue, Z.; Lisdat, F.; Parak, W. J.; Hickey, S. G.; Tu, L.; Sabir, N.; Dorfs, D.; Bigall, N. C. Quantum-Dot-Based Photoelectrochemical Sensors for Chemical and Biological Detection. *ACS Appl. Mater. Interfaces* **2013**, *5* (8), 2800–2814.

(68) Zhang, J.; Yu, S.-H. Highly Photoluminescent Silicon Nanocrystals for Rapid, Label-Free and Recyclable Detection of Mercuric Ions. *Nanoscale* **2014**, *6* (8), 4096–4101.

(69) Liao, B.; Wang, W.; Deng, X.; He, B.; Zeng, W.; Tang, Z.; Liu, Q. A Facile One-Step Synthesis of Fluorescent Silicon Quantum Dots and Their Application for Detecting Cu^{2+}. *RSC Adv.* **2016**, *6* (18), 14465–14467.

(70) Zhao, J.; Deng, J.; Yi, Y.; Li, H.; Zhang, Y.; Yao, S. Label-Free Silicon Quantum Dots as Fluorescent Probe for Selective and Sensitive Detection of Copper Ions. *Talanta* **2014**, *125*, 372–377.

(71) Campos, B. B.; Algarra, M.; Alonso, B.; Casado, C. M.; Jiménez-Jiménez, J.; Rodríguez-Castellón, E.; Esteves da Silva, J. C. G. Fluorescent Sensor for Cr(VI) Based in Functionalized Silicon Quantum Dots with Dendrimers. *Talanta* **2015**, *144*, 862–867.

(72) Content, S.; Trogler, W. C.; Sailor, M. J. Detection of Nitrobenzene, DNT, and TNT Vapors by Quenching of Porous Silicon Photoluminescence. *Chem. Eur. J.* **2000**, *6* (12), 2205–2213.

(73) Germanenko, I. N.; Li, S.; El-Shall, M. S. Decay Dynamics and Quenching of Photoluminescence from Silicon Nanocrystals by Aromatic Nitro Compounds. *J. Phys. Chem. B* **2001**, *105* (1), 59–66.

(74) M. Gonzalez, C.; Iqbal, M.; Dasog, M.; G. Piercey, D.; Lockwood, R.; M. Klapötke, T.; C. Veinot, J. G. C. Detection of High-Energy Compounds Using Photoluminescent Silicon Nanocrystal Paper Based Sensors. *Nanoscale* **2014**, *6* (5), 2608–2612.

(75) Ban, R.; Zheng, F.; Zhang, J. A Highly Sensitive Fluorescence Assay for 2,4,6-Trinitrotoluene Using Amine-Capped Silicon Quantum Dots as a Probe. *Anal. Methods* **2015**, *7* (5), 1732–1737.

(76) Nguyen, A.; Gonzalez, C. M.; Sinelnikov, R.; Newman, W.; Sun, S.; Lockwood, R.; Veinot, J. G. C.; Meldrum, A. Detection of Nitroaromatics in the Solid, Solution, and Vapor Phases Using Silicon Quantum Dot Sensors. *Nanotechnology* **2016**, *27* (10), 105501.

(77) Zhang, Z. H.; Lockwood, R.; Veinot, J. G. C.; Meldrum, A. Detection of Ethanol and Water Vapor with Silicon Quantum Dots Coupled to an Optical Fiber. *Sens. Actuators B Chem.* **2013**, *181*, 523–528.

(78) Yi, Y.; Deng, J.; Zhang, Y.; Li, H.; Yao, S. Label-Free Si Quantum Dots as Photoluminescence Probes for Glucose Detection. *Chem. Commun.* **2013**, *49* (6), 612–614.

(79) Chen, Q.; Liu, M.; Zhao, J.; Peng, X.; Chen, X.; Mi, N.; Yin, B.; Li, H.; Zhang, Y.; Yao, S. Water-Dispersible Silicon Dots as a Peroxidase Mimetic for the Highly-Sensitive Colorimetric Detection of Glucose. *Chem. Commun.* **2014**, *50* (51), 6771–6774.

(80) Zhang, X.; Chen, X.; Kai, S.; Wang, H.-Y.; Yang, J.; Wu, F.-G.; Chen, Z. Highly Sensitive and Selective Detection of Dopamine Using One-Pot Synthesized Highly Photoluminescent Silicon Nanoparticles. *Anal. Chem.* **2015**, *87* (6), 3360–3365.

(81) Lin, J.; Wang, Q. Role of Novel Silicon Nanoparticles in Luminescence Detection of a Family of Antibiotics. *RSC Adv.* **2015**, *5* (35), 27458–27463.

(82) Yi, Y.; Zhu, G.; Liu, C.; Huang, Y.; Zhang, Y.; Li, H.; Zhao, J.; Yao, S. A Label-Free Silicon Quantum Dots-Based Photoluminescence Sensor for Ultrasensitive Detection of Pesticides. *Anal. Chem.* **2013**, *85* (23), 11464–11470.

Chapter 2

Functional Bioinorganic Hybrids from Enzymes and Luminescent Silicon-Based Nanoparticles[1]

2.1 Introduction

Semiconductor nanoparticles (or quantum dots) possess properties — photostability, intense brightness, tunable emission spectra, and long photoluminescence lifetimes — that set them apart from conventional fluorescent organic dyes as more desirable biological photoluminescent probes and sensors.[1–4] Most commercially available quantum dots, however, consist of cadmium-containing group II–VI semiconductors (e.g., CdS, CdSe, and CdTe) that can release toxic cadmium ions when exposed to oxidative conditions or ultraviolet light.[3,5] Unlike these potentially toxic semiconductor quantum dots, photoluminescent silicon nanoparticles (SiNPs) are biodegradable and non-toxic.[6–10] Their emission is believed to result from strong quantum confinement effects exhibited by clusters of silicon atoms having dimensions less than the bulk Si Bohr exciton radius.[11,12] Quantum confinement effectively increases the probability of direct band gap electron-hole recombination and decreases the likelihood of phonon-assisted indirect band-gap transitions.[13] Notably, the photoluminescent signature of SiNPs can be tuned by varying their size and surface chemistry.[14–20]

It is not surprising then that the tailorable photoluminescent properties and biocompatibility of SiNPs have inspired considerable efforts directed at their preparation in a form that renders them suitable for biological applications. A number of studies have reported water-soluble SiNPs for bioimaging.[1,3,8,9,21–25] Water solubility/dispersibility in these instances has been achieved through surface oxidation,[3,14] introduction of hydrophilic functional groups (e.g., primary amine),[1] functionalization with water-soluble compounds,[22] grafting with hydrophilic polymers,[21] non-covalent coating with amphiphilic polymers,[26] and encapsulation in amphiphilic micelles.[8]

[1]The contents of this chapter have been copied and/or adapted from the following publication: Robidillo, C. J. T.; Islam, M. A.; Aghajamali, M.; Faramus, A.; Sinelnikov, R.; Zhang, X.; Boekhoven, J.; Veinot, J. G. C. *Langmuir* **2018**, *34*, 6556-6569. Copyright © 2018 American Chemical Society.

Biosensing and bioimaging probes have been fabricated from quantum dots and biological macromolecules through bioconjugate functionalization methodologies, with the most prominent being the amide coupling reaction.[27–29] This approach typically involves the formation of amide bonds between carboxylic acid residues on the surfaces of quantum dots and amine groups on biomolecules (or vice versa). Coupling agents, such as *N*-(3-dimethylaminopropyl)-*N′*-ethylcarbodiimide (EDC) and *N*-hydroxysuccinimide (NHS) commonly are used for this purpose. Several examples of cadmium-based quantum dots conjugated with proteins or nucleic acids prepared via amide coupling chemistry have been reported in the literature.[28,30] Potential challenges arise when applying this chemistry to Si nanomaterials because nitrogen containing reagents have been implicated in dramatic changes (i.e., quenching and spectral shifts) in their photoluminescence.[20] Still, a comparatively small number of researchers have employed this procedure to immobilize biological macromolecules on freestanding SiNPs. Erogbogbo et al. conjugated the glycoprotein transferrin with alkyl-passivated SiNPs coated with carboxylic acid-terminated phospholipid micelles, and used the resulting hybrids for bioimaging.[8] Ruizendaal and co-workers prepared SiNP-DNA conjugates using this chemistry.[31] In addition, Wang et al. have appended DNA to SiNP surfaces using a related NHS-ester coupling strategy.[32] Similarly, Choi and co-workers have conjugated streptavidin with SiNPs through the same procedure.[33] In most of these works, however, the carboxylic acid or the NHS-ester moieties are introduced onto the silicon quantum dot surface via lengthy multi-step procedures.

To the best of our knowledge, despite the demonstrated utility of the amide coupling reaction in conjugating biomolecules to surfaces, they have not yet been employed in the construction of functional bioinorganic freestanding silicon nanoparticle-enzyme hybrids. In this contribution, we show the preparation of a unique class of water-soluble photoluminescent oxide-rich silicon-based nanoparticles (*Ox*SiNPs), and their subsequent conjugation with enzymes through the amide coupling reaction.

2.2 Experimental Section

2.2.1 Chemicals

Commercial hydrogen silsesquioxane (HSQ, trade name Fox-17) dissolved in methyl isobutyl ketone was purchased from Dow Corning Corporation; the solvent was removed in vacuo, and the resulting white solid was used without further purification. Electronics grade hydrofluoric acid (49% $HF_{(aq)}$) was obtained from J. T. Baker. Allyloxy poly(ethylene oxide) methyl ether (9-12 ethylene oxide units, MW = 450-550 g mol^{-1}) (Gelest), undecenoic acid, poly(ethylene glycol) 2-aminoethyl ether biotin (Biotin-PEG-NH_2, ~77 ethylene oxide units, MW_{Ave} = 3400 g mol^{-1}) glucose oxidase (GOx, 10 kU, from *Aspergillus niger*), alcohol dehydrogenase (ADH, 30 kU, from *Saccharomyces cerevisiae*), horseradish peroxidase (~150 U mg^{-1}), *N*-(3-dimethylaminopropyl)-*N'*-ethylcarbodiimide (EDC), *N*-hydroxysulfosuccinimide (sulfo-NHS), glucose, phenol, 4-aminoantipyrine, nicotinamide adenine dinucleotide sodium salt (NAD^+), and 3-(4,5-dimethylthiazol-2-yl)-2,5-diphenyltetrazolium bromide (Thiazolyl blue) (Sigma Aldrich) were used as received without further purification. All other chemicals and solvents used were of analytical grade, unless otherwise indicated.

2.2.2 Preparation of Oxide-Embedded Silicon Nanocrystals

Oxide-embedded silicon nanocrystals were prepared following a well-established procedure developed in the Veinot laboratory.[34,35] Four grams of HSQ were transferred into a quartz boat, which was placed in a furnace (Sentro Tech. Corp.), heated to 1100 °C, and thermally processed at that temperature in an atmosphere of 5% H_2 and 95% Ar for 1 h. The amber-coloured composite obtained, which consisted of silicon nanocrystals (ca. 3 nm) embedded in an oxide matrix, was wetted with ethanol and ground using a mortar and pestle. The mixture was then transferred into a flask charged with glass beads, shaken for 6 h, and filtered through a hydrophilic membrane filter. The composite obtained was then stored in a standard glass vial and used as needed.

2.2.3 Synthesis of Hydride-Terminated Silicon Nanocrystals (*H*-SiNCs)

Hydride-terminated silicon nanocrystals were liberated from the oxide matrix through HF etching. Three hundred milligrams of the powdered composite were dispersed in a 9 mL solution consisting of 49% HF (**Note:** *HF is very corrosive. Handle it with extreme caution.*), 100% ethanol, and deionized water in a 1:1:1 volume ratio. The mixture was stirred for 40 min under ambient light and temperature conditions, and the liberated *H*-SiNCs (ca. 30 mg) were isolated through multiple extractions with toluene (3×, 15 mL) and multiple centrifugation–decantation cycles in toluene (3×, 3000 rpm).

2.2.4 Synthesis of Acid-Terminated Poly(ethylene oxide)-Coated Oxide-Rich Silicon-Based Nanoparticles (acid-*Ox*SiNPs)

Acid-terminated poly(ethylene oxide)-coated oxide-rich silicon-based nanoparticles were prepared through thermal hydrosilylation. The *H*-SiNCs obtained from etching 300 mg of the composite were dispersed in 2 mL undecenoic acid and 6 mL allyloxy poly(ethylene oxide) methyl ether in a Schlenk flask equipped with a magnetic stir bar. The mixture was then heated to 170 °C and stirred at that temperature for 4 h in an Ar atmosphere. Initial purification of the resulting water-soluble acid-*Ox*SiNPs was performed through extraction with 10 mL water and 10 mL hexane twice. Afterwards, the aqueous solution was dialyzed against 95% ethanol (2×) and then against deionized water (2×) using a regenerated cellulose dialysis tubing (Nominal MWCO = 12–14 kDa). The aqueous solution was transferred into a Centricon tube with a 30 kDa pore size membrane and subjected to centrifugal ultrafiltration using a J2-21 high-speed centrifuge (5000 rpm, 30 min), the resulting ultrafiltrate discarded, and the retentate further subjected to multiple centrifugal ultrafiltration steps in 10 mL mQ water (5000 rpm, 30 min, 5×). Finally, the retentate containing the acid-*Ox*SiNPs was diluted with mQ water in order to form 10 mL of solution.

2.2.5 Preparation of Biotin-Conjugated Silicon-Based Nanoparticles (Biotin-*Ox*SiNPs) from acid-*Ox*SiNPs

To a 2.0 mL solution of acid-*Ox*SiNPs in mQ water was added 4 mg EDC, 2 mg sulfo-NHS, and 4 mg Biotin-PEG-NH_2. The mixture was heated to 70 °C in a microwave reactor (Biotage

Initiator) and allowed to react for six hours. The solution was then transferred into a Centricon tube with a 10 kDa pore size membrane and subjected to centrifugal ultrafiltration using a J2-21 high-speed centrifuge (5000 rpm, 30 min), the resulting ultrafiltrate collected, and the retentate further subjected to centrifugal ultrafiltration twice in 1 mL mQ water (5000 rpm, 30 min). Finally, the retentate containing the Biotin-*Ox*SiNPs was diluted with mQ water in order to form 500 µL of solution.

2.2.6 Preparation of Enzyme-Conjugated Silicon-Based Nanoparticles (Enz-*Ox*SiNPs) from acid-*Ox*SiNPs

To a 5.0 mL solution of acid-*Ox*SiNPs in mQ water was added 5.0 mL phosphate buffer (0.1 M, pH 7.0), 10 mg EDC, and 5 mg sulfo-NHS. Ten microlitres of stock enzyme solution (6.7 kU/mL GOx or 15 kU/mL ADH) were added to the resulting solution after letting it stir for 30 min at 25 °C. The mixture was stirred for six more hours prior to purification. The solution was then transferred into a Centricon tube with a 100 kDa pore size membrane and subjected to centrifugal ultrafiltration using a J2-21 high-speed centrifuge (5000 rpm, 30 min), the resulting ultrafiltrate collected, and the retentate further subjected to multiple centrifugal ultrafiltration steps in 5 mL buffer (5000 rpm, 30 min, 5×). Finally, the retentate containing the Enz-*Ox*SiNPs was diluted with buffer in order to form 500 µL of solution.

2.2.7 Characterization of acid-*Ox*SiNPs and Enz-*Ox*SiNPs

Fourier transform infrared (FTIR) spectra of acid-*Ox*SiNPs and Enz-*Ox*SiNPs were obtained using a Nicolet Magna 750 IR spectrometer. X-ray photoelectron spectroscopy (XPS) analyses were carried out using a Kratos Axis Ultra instrument operating in energy spectrum mode at 210 W. Thin film samples for XPS were prepared by depositing a solution of the *Ox*SiNPs onto a small copper foil and drying in air. The base and operating chamber pressure of the instrument were kept at 10^{-7} Pa. A monochromatic Al Kα source (λ = 8.34 Å) was used to excite the samples, and the spectra were obtained with an electron takeoff angle of 90°. The charge neutralizer filament was used in order to minimize charging. Survey XP spectra were acquired using an elliptical spot with major and minor axis lengths of 2 and 1 mm, respectively, and a 160-eV pass energy with a step of 0.33 eV. CasaXPS software (VAMAS) was used to process high-resolution spectra. All spectra were corrected by calibration to the C 1s emission

(284.8 eV). A Shirley-type background was applied in order to remove most of the extrinsic loss structure.

Transmission electron microscopy (TEM) images were obtained using a JEOL 2010 TEM with LaB_6 filament at an accelerating voltage of 200 kV. Samples of *Ox*SiNPs were prepared by depositing a droplet of dilute solutions of *Ox*SiNPs onto a thin carbon-coated copper mesh. The nanoparticle size was averaged for 300 nanoparticles using Image J software (version 1.51). Dynamic light scattering (DLS) analyses were performed using a Malvern Zetasizer Nano S series equipped with a 633 nm laser. Diluted solutions of acid-*Ox*SiNPs and Enz-*Ox*SiNPs were equilibrated to 25 °C prior to data acquisition and scanned thrice.

Absorbance spectra of the samples were recorded using a SpectraMax® i3x multimode microplate reader. Photoluminescence spectra of the samples were obtained using a Varian Cary Eclipse fluorescence spectrometer (λ_{ex} = 350 nm). Photoluminescence stability experiments were performed by exposing acid-*Ox*SiNPs and Enz-*Ox*SiNPs to UV light (UV Trans-illuminator, λ_{ex} = 365 nm) and covering them with a nonreflective enclosure. Photoluminescence measurements were then carried out after 1, 2, 4, and 6 h. Photostability under ambient light conditions was monitored similarly in the absence of UV light. Photoluminescence intensities in photostability experiments were measured using a SpectraMax® i3x multimode microplate reader (λ_{ex} = 350 nm). Time-resolved photoluminescence spectroscopy was measured using an Argon ion laser with 351 nm emission wavelength, which was modulated by an acousto-optic modulator (response time ~50 ns) operated at a frequency of 200 Hz with a 50% duty cycle. The photoluminescence was fed into an optic fiber, passed through a 500 nm long-pass filter, and was then incident on a Hamamatsu H7422P-50 photomultiplier tube interfaced with a Becker-Hickl PMS-400A gated photon counter. The photoluminescence data were collected in 1 μs timesteps and a total of 10,000 sweeps were collected for a good signal-to-noise ratio. The luminescence decay lifetimes were calculated through lognormal fitting of the data.[36,37] Quantum yield measurements were performed using a home-built integrating sphere. Distilled water blank and sample solutions were transferred into a cuvette that was lowered into the integrating sphere on a magnetic holder. A 365 nm light emitting diode was used as the excitation source. The photoluminescence and excitation intensities were captured through a fiber attached to the sphere and analyzed with a calibrated Ocean Optics spectrometer. The quantum yield was

calculated using the equation $QY = (I_{PL,sample} - I_{PL,blank})/(I_{ex,blank} - I_{ex,sample})$, where I_{PL} is the integrated photoluminescence intensity and I_{ex} is the excitation intensity recorded inside the sphere. The measured samples have absorbances of 0.1–0.15 at 365 nm. The measurements were performed in quintuplicates.

2.2.8 Testing for Catalytic Activity of Enz-*Ox*SiNPs through Enzyme Activity Assays

2.2.8.1 Trinder's Assay for Glucose Oxidase Activity

To a vial containing 10 µL of glucose oxidase (67 U/mL), a vial containing 10 µL of ultrafiltrate, a vial containing 10 µL of solution of GOx-*Ox*SiNPs, and a vial containing 10 µL of phosphate buffer (0.1 M, pH 7.0), were added 100 µL of 8.5 mM 4-aminoantipyrine, 100 µL of 44 mM phenol, 10 µL of horseradish peroxidase (1.2 kU/mL), and 100 µL of 0.2 M glucose, respectively. The vials were then inspected visually and analyzed spectrophotometrically for the formation of a pink/red solution. The formation of a red quinoneimine dye (λ_{max} = 510 nm) indicates glucose oxidase activity. Absorbance spectra were obtained using a Cary 400 UV/Vis spectrometer.

2.2.8.2 Evaluation of the Michaelis–Menten Constant, K_M, of Free GOx and GOx-*Ox*SiNPs

Michaelis–Menten curves were constructed by plotting the initial reaction velocity, v_0 (i.e., rate of change of absorbance at 490 nm), of solutions containing 53 mM phenol, 0.8 mM 4-aminoantipyrine, 22 mU/mL horseradish peroxidase, 2.2 mU/mL pure glucose oxidase or fixed concentration of GOx-*Ox*SiNPs, and varying concentrations of glucose (0.0067–3.0 mM) in HEPES [4-(2-hydroxyethyl)-1-piperazineethanesulfonic acid] buffer (2.0 M, pH 7.0). The experiments were carried out in quadruplicates using a Thermoscientific Multiscan 60 microplate reader. Then, the curves were linearized into Lineweaver-Burk plots by graphing the reciprocal of the velocity against the reciprocal of the glucose concentration. The K_M of free GOx and GOx-*Ox*SiNPs were computed by taking the ratios of their respective slopes and y-intercepts.

2.2.8.3 Formazan Assay for Alcohol Dehydrogenase Activity

To a vial containing 20 µL of alcohol dehydrogenase (150 U/mL), a vial containing 20 µL of ultrafiltrate, a vial containing 20 µL of solution of ADH -*Ox*SiNPs, and a vial containing 20 µL of phosphate buffer (0.1 M, pH 7.0), were added 150 µL of 24 mM thiazolyl blue, 150 µL of 18 mM NAD^+, and 50 µL of absolute ethanol, respectively. Then, one mL of dimethyl sulfoxide (DMSO) was added to each vial after 4 h, after which the vials were inspected visually and analyzed spectrophotometrically for the formation of a purple solution. The formation of a purple formazan adduct (λ_{max} = 560 nm) indicates alcohol dehydrogenase activity. Absorbance spectra were obtained using a Cary 400 UV/Vis spectrometer.

2.2.8.4 Evaluation of the Michaelis–Menten Constant, K_M, of Free ADH and ADH-*Ox*SiNPs

Michaelis–Menten curves were constructed by plotting the initial reaction velocity, v_0 (i.e., rate of change of absorbance at 340 nm), of solutions containing 1.5 mM NAD^+, 60 U/mL pure alcohol dehydrogenase or fixed concentration of ADH-*Ox*SiNPs, and varying concentrations of ethanol (10–2000 mM) in phosphate buffer (0.1 M, pH 7.0). The experiments were carried out in quadruplicates using a SpectraMax® i3x multimode microplate reader. Then, the curves were linearized into Lineweaver–Burk plots by graphing the reciprocal of the velocity against the reciprocal of the ethanol concentration. The K_M of free ADH and ADH-*Ox*SiNPs were computed by taking the ratios of their respective slopes and y-intercepts.

2.3 Results and Discussion

For the present study, hydride-terminated silicon nanocrystals (*H*-SiNCs) were prepared via thermal disproportionation of hydrogen silsesquioxane (HSQ) at 1100 °C using a well-established procedure developed in the Veinot laboratory.[34,35,38] The *H*-SiNCs (ca. 3 nm) were liberated from the resulting SiNC/SiO_2 composite upon alcoholic HF-etching and were surface-modified with a mixture of hydrophilic poly(ethylene oxide) chains and carboxylic acid residues through thermal hydrosilylation at 170 °C (Figure 2-1A).[39] The poly(ethylene oxide) moieties render the SiNCs hydrophilic and resistant to nonspecific protein adsorption,[40–43] while the carboxylic acid groups provide the reactive platform necessary to facilitate

conjugation with enzymes. Hydrosilylation provided functionalization, however, the procedure also partially oxidized the SiNC core. Regardless, the unique optical properties (i.e., microsecond excited state lifetimes, emission colour) of the silicon core were not compromised. The Fourier transform infrared (FTIR) spectrum of the acid-terminated oxide-rich silicon-based nanoparticles (acid-*Ox*SiNPs) obtained is shown in Figure 2-1B. Consistent with surface functionalization, the Si-H_x related absorption at ca. 2100 cm^{-1} is diminished, however, this may also be due to partial surface oxidation of the nanoparticles as suggested by FTIR and X-ray photoelectron spectroscopy (XPS) (vide infra).[35]

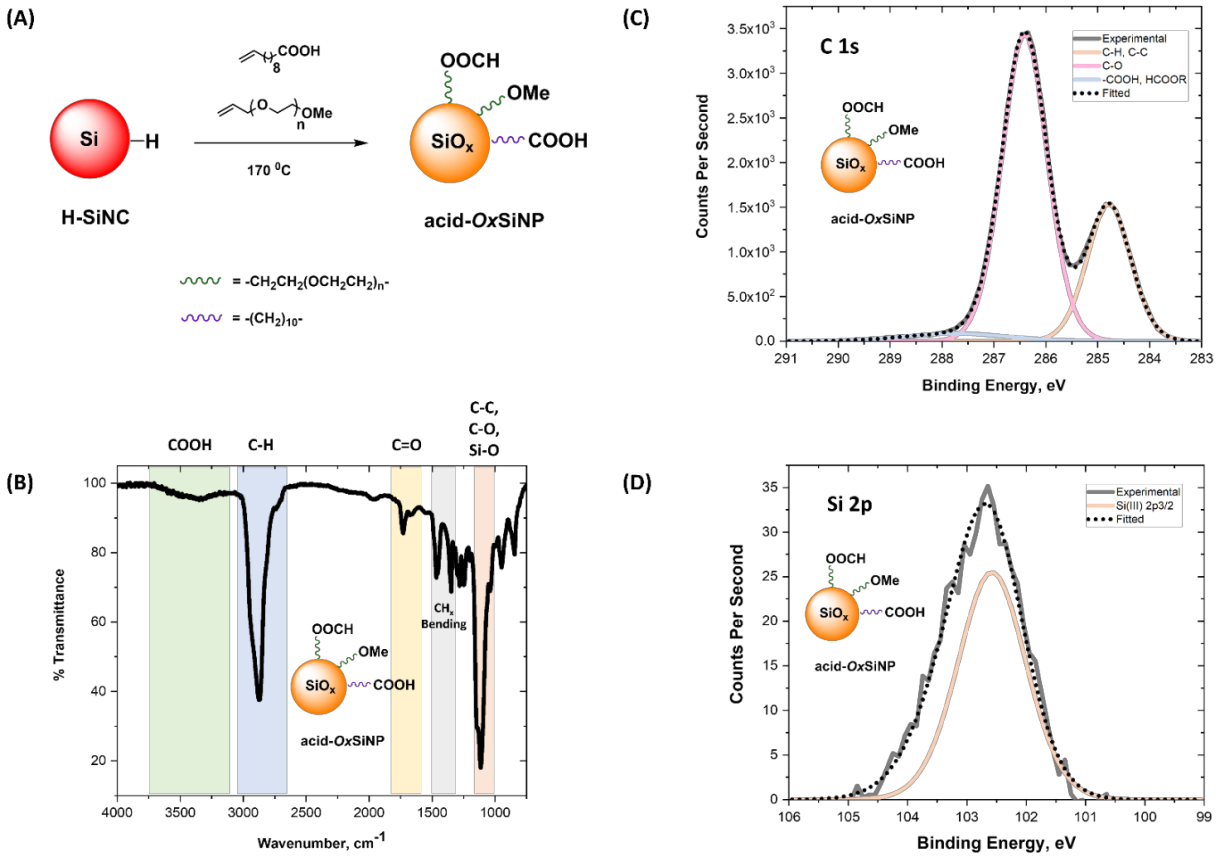

Figure 2-1. (A) Scheme showing thermal hydrosilylation of undecenoic acid and allyloxy poly(ethylene oxide) methyl ether with *H*-SiNCs (–OOCH is a formate ester group). **(B)** FTIR spectrum, **(C)** C 1s, and **(D)** Si 2p XP spectra of acid-*Ox*SiNPs (Si 2p1/2 peaks were omitted for clarity).

An absorption at ca. 1710 cm^{-1} confirms the presence of carboxylic acid carbonyl group,[44] however, this feature is obscured partially by an absorption at ca. 1730 cm^{-1} arising from surface-bonded poly(ethylene oxide) formate ester species appended to the

nanoparticles.[22] These esters result from the thermal oxidation of poly(ethylene oxide) during the hydrosilylation procedure and limit the quantitative determination of acid:poly(ethylene oxide) functionalization ratio.[45,46] The spectrum also shows a broad absorption at ca. 1100 cm^{-1} that arises from Si–O attributed to surface oxidation, as well as the C–C and C–O bonds in the undecanoic acid and poly(ethylene oxide) groups.[34] Characteristic aliphatic $–CH_x–$ vibrational bending features are noted in the 1475 to 1365 cm^{-1} region.[47,48] XPS analyses of acid-*Ox*SiNPs show C 1s emissions characteristic of aliphatic C–H and C–C carbons (284.8 eV), C–O carbons (286.4 eV), and carboxyl carbons (287.9 eV) arising from surface-bonded undecanoic acid and poly(ethylene oxide) ester groups (Figure 2-1C).[21,49,50] The Si 2p XP spectrum of acid-*Ox*SiNPs shown in Figure 2-1D indicates that the functionalized particles consist of silicon suboxides (102.4 eV), which is consistent with surface oxidation expected from the propensity of water to oxidize silicon.[44,51] This oxidation can be attributed to the purification steps that were performed in aqueous medium (e.g., extraction, dialysis, centrifugal ultrafiltration) and the dissolution and subsequent storage of the acid-*Ox*SiNPs in water. In contrast to the present *Ox*SiNPs, silicon nanoparticles purified via anhydrous techniques and dispersed in organic solvents display a relative abundance of Si(0).[15,47]

To further confirm the presence of reactive carboxylic acid residues on the luminescent nanoparticle surface, the acid-*Ox*SiNPs were reacted with amine-terminated biotin-functionalized poly(ethylene oxide) (Figure 2-2A). The resulting derivatization was confirmed by the detection of nitrogen through XPS (N 1s peak at ~399.6 eV; Figure 2-2B) as well as the characteristic biotin amide peak in FTIR (~1650 cm^{-1}; Figure 2-2C). The addition of fluorescently labeled avidin also caused the aggregation of Biotin-*Ox*SiNPs. All of these observations indicate successful biotinylation, which confirms the presence of carboxylic acid residues on the nanoparticle surface.

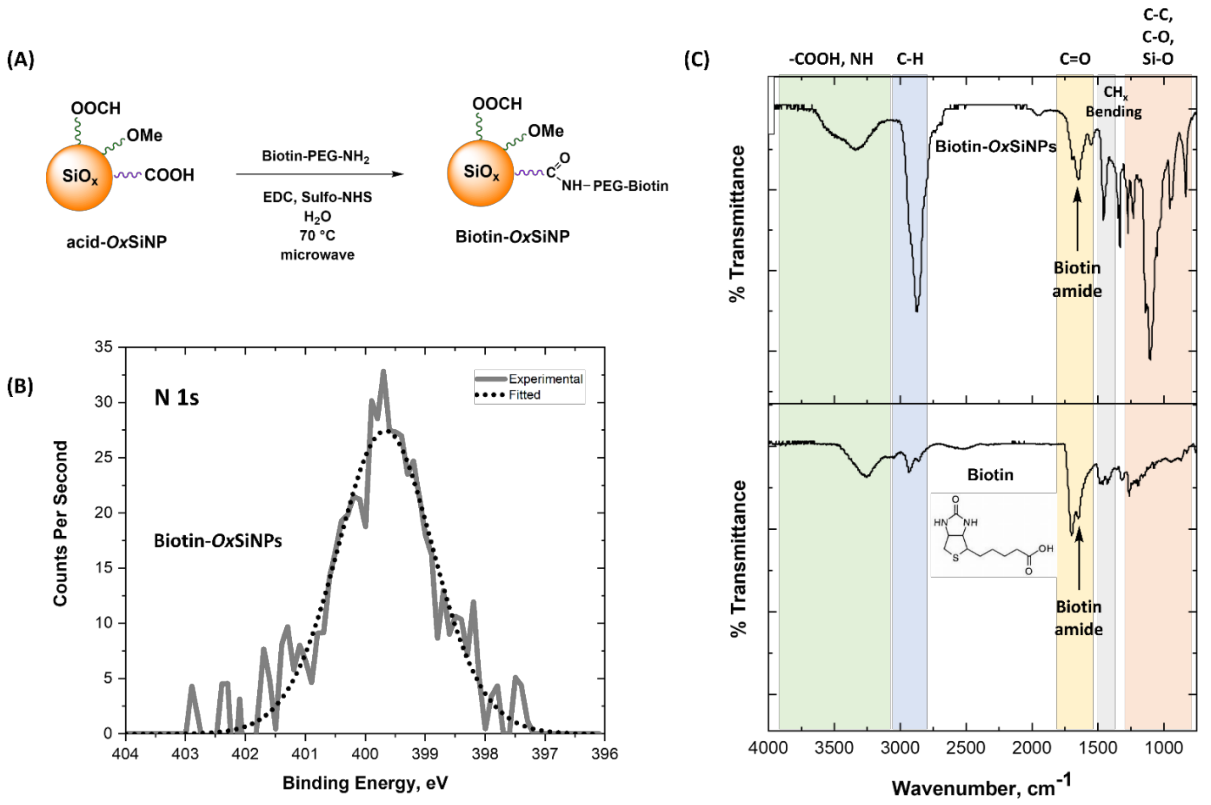

Figure 2-2. (A) Scheme showing coupling of Biotin-PEG-NH_2 with acid-*Ox*SiNPs via the amide coupling reaction. **(B)** N 1s XP spectrum of Biotin-*Ox*SiNPs. **(C)** FTIR spectrum of Biotin-*Ox*SiNPs and biotin.

Having water-compatible luminescent acid-*Ox*SiNPs in hand, we chose glucose oxidase (GOx) and alcohol dehydrogenase (ADH) as representative examples of enzymes for surface conjugation. Glucose oxidase is a 160 kDa homodimeric enzyme that catalyzes oxidation of glucose by molecular oxygen,[52,53] and alcohol dehydrogenase is a 150 kDa tetrameric protein that catalyzes the oxidation of ethanol into acetaldehyde using nicotinamide adenine dinucleotide (NAD^+) as an electron acceptor.[54–56] Scheme 2-1A shows the conjugation of these enzymes with the acid-*Ox*SiNPs through the amide coupling chemistry. These enzymes were covalently linked to acid-*Ox*SiNPs through their N-termini or the amine groups in their lysine side chains via EDC and sulfo-NHS coupling. Scheme 2-1B details the purification of the resulting hybrids. Briefly, the reaction mixture was transferred into a centrifugal ultrafiltration (Centricon) tube, which consists of a porous membrane, and centrifuged multiple times in order to separate the hybrids from unbound enzyme molecules. The hybrids are retained by the membrane (retentate) while the unbound enzyme molecules pass through the membrane pores (ultrafiltrate).

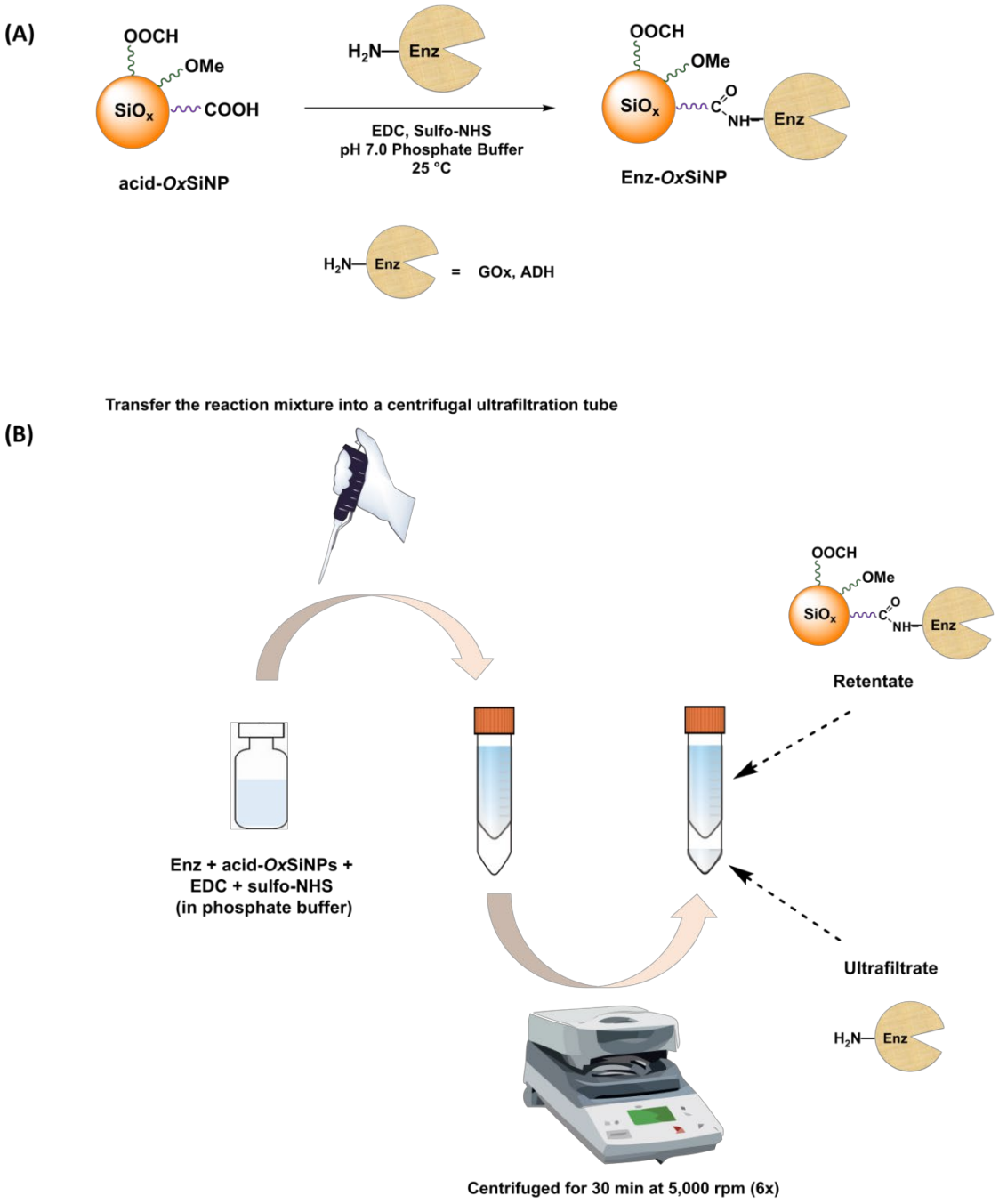

Scheme 2-1. (A) Bioconjugation of acid-*Ox*SiNPs with enzymes through the amide coupling reaction. **(B)** Purification of Enz-*Ox*SiNPs.

We have confirmed successful enzyme conjugation through FTIR and XPS. The presence of characteristic amide (peptide) bond features of the proteins centered at ca. 1640 cm^{-1} (C=O stretching) and 1540 cm^{-1} (amide N–H bending) in the FTIR spectra (Figure 2-3) of glucose oxidase-conjugated silicon-based nanoparticles (GOx-*Ox*SiNPs) and

alcohol dehydrogenase-conjugated silicon-based nanoparticles (ADH-*Ox*SiNPs) are consistent with acid-*Ox*SiNP–enzyme conjugation.[57,58] The C 1s region of the XP spectra of GOx-*Ox*SiNPs and ADH-*Ox*SiNPs (Figures 2-4A and 2-4D, respectively) also show features consistent with the target functionalization that are attributed readily to the presence of aliphatic carbon atoms (284.8 eV) as well as C–N and C–O carbon atoms (286.5 eV) and amide group carbon atoms (288.3 eV) of the enzymes.[59] In addition, expected emissions associated with conjugated enzymes are noted in the N 1s region (i.e., amide nitrogen at 399.7 eV; Figures 2-4B and 2-4E).[60] As expected, the Si 2p XP spectra of GOx-*Ox*SiNPs and ADH-*Ox*SiNPs (Figures 2-4C and 2-4F) are dominated by Si(III), as was in the case of acid-*Ox*SiNPs.

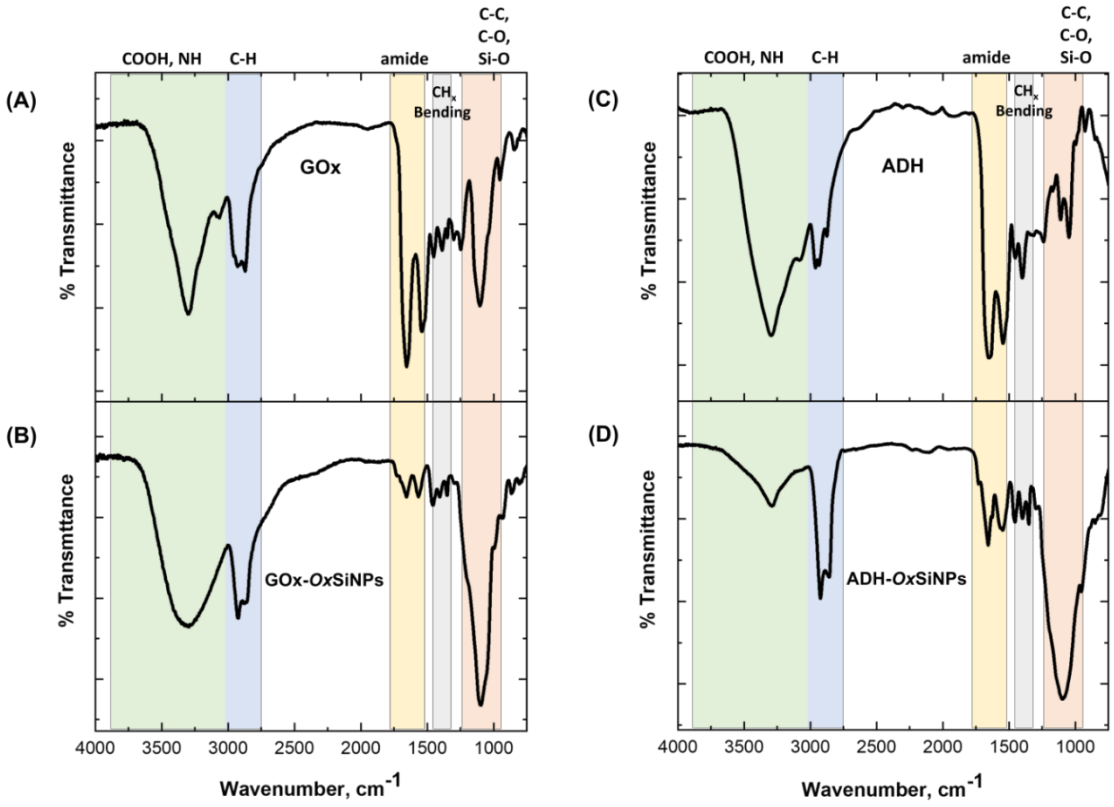

Figure 2-3. FTIR spectra of **(A)** GOx, **(B)** GOx-*Ox*SiNPs, **(C)** ADH, and **(D)** ADH-*Ox*SiNPs.

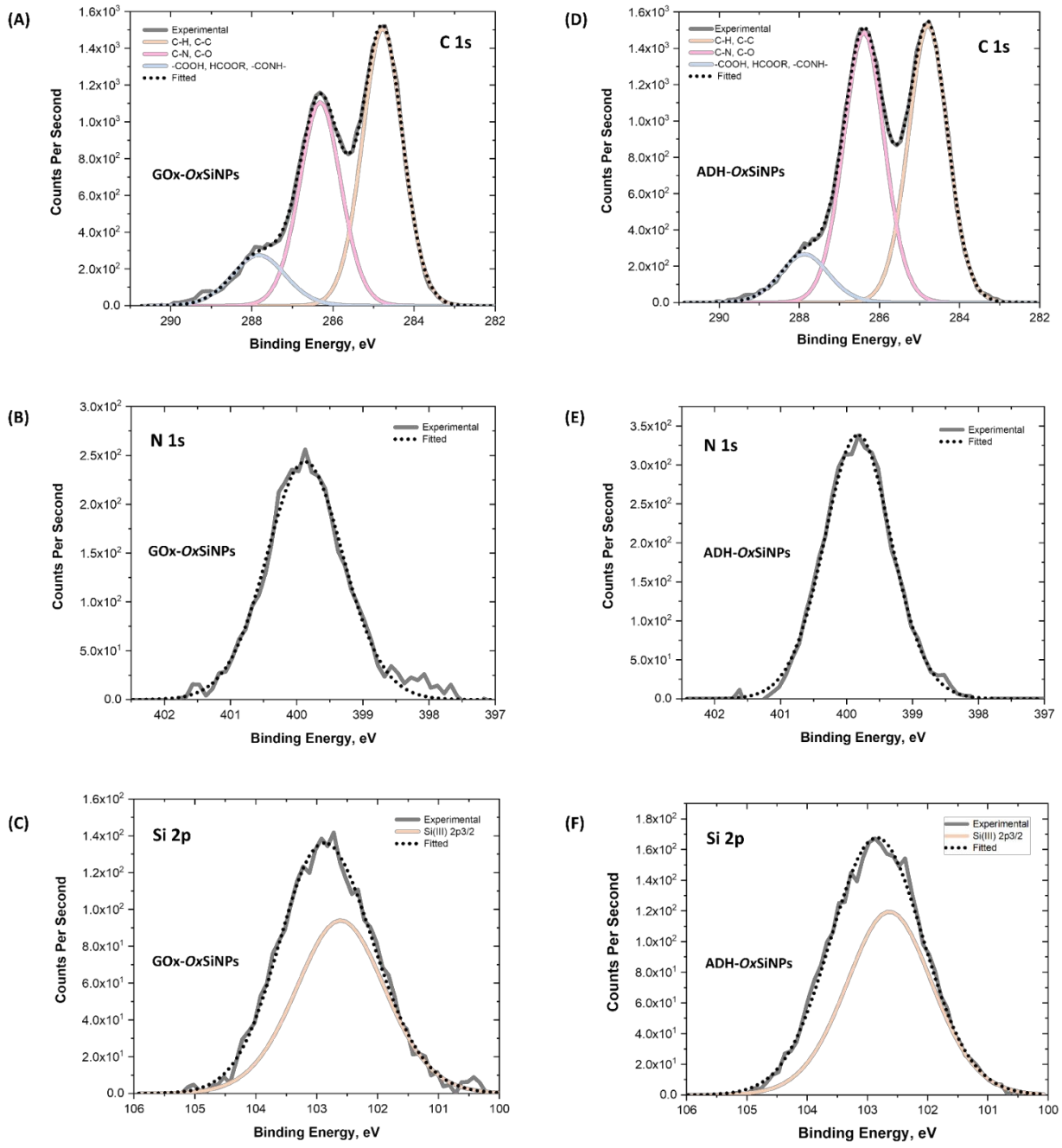

Figure 2-4. (A) C 1s, **(B)** N 1s, and **(C)** Si 2p XP spectra of GOx-*Ox*SiNPs, and **(D)** C 1s, **(E)** N 1s, **(F)** Si 2p XP spectra of ADH-*Ox*SiNPs (Si 2p1/2 peaks were omitted for clarity).

Dynamic light scattering (DLS) analyses of the acid-*Ox*SiNPs, GOx-*Ox*SiNPs, and ADH-*Ox*SiNPs show mean hydrodynamic diameters of 5.5, 10.5, and 10.3 nm, respectively (Figure 2-5). This increase in size upon enzyme conjugation is expected from the larger hydrated diameters of the enzyme-conjugated *Ox*SiNPs (Enz-*Ox*SiNPs) compared to that of the parent acid-*Ox*SiNPs. In addition, the hydrodynamic diameters of the Enz-*Ox*SiNPs approach the sum of the hydrodynamic diameters of the acid-*Ox*SiNPs and the corresponding enzymes (e.g., 7.3 nm for GOx and 6.4 nm for ADH), suggesting that each acid-*Ox*SiNP has been linked to only a single enzyme molecule. Transmission electron microscopy (TEM) and average shifted histogram[61] analyses (Figure 2-6) revealed Si-based core diameters of 4.8 ± 1.2 nm and 5.6 ± 1.6 nm for acid-*Ox*SiNPs and GOx-*Ox*SiNPs, respectively.

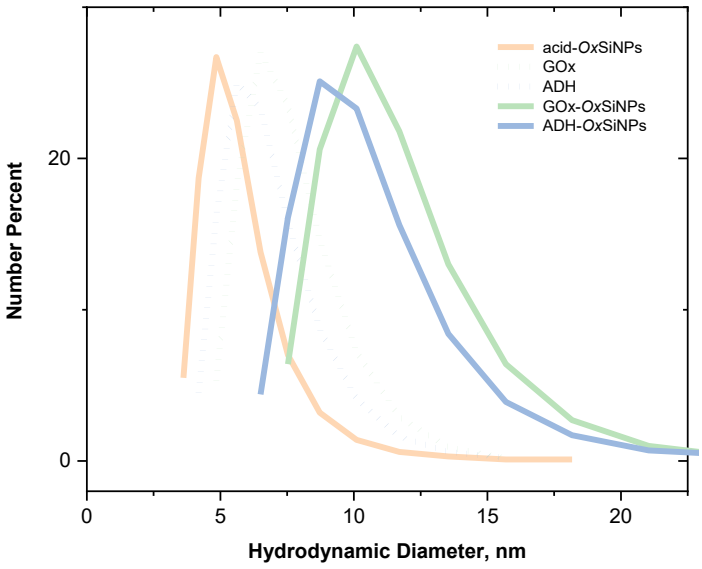

Figure 2-5. DLS size analysis of acid-*Ox*SiNPs, GOx, ADH, GOx-*Ox*SiNPs, and ADH-*Ox*SiNPs.

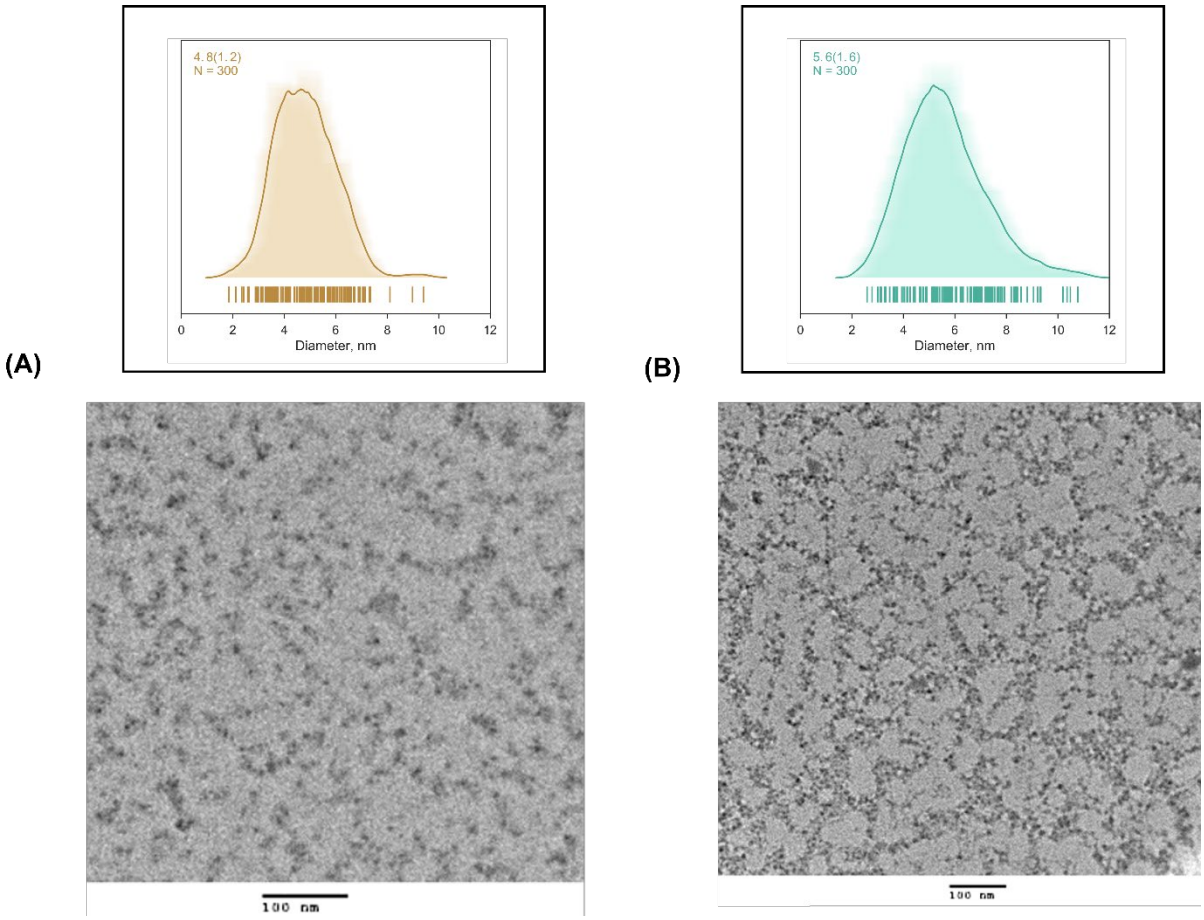

Figure 2-6. TEM images of **(A)** acid-*Ox*SiNPs and **(B)** GOx-*Ox*SiNPs. The insets show average shifted histograms of 300 nanoparticles.

As shown in Figure 2-7A, the water-soluble acid-*Ox*SiNPs and Enz-*Ox*SiNPs exhibit orange photoluminescence. Figure 2-7B shows that they exhibit significant absorption at wavelengths shorter than 400 nm. The photoluminescence maximum is blue-shifted (ca. 10 nm) after functionalization with enzymes (Figure 2-7C). This shift in photoluminescence maximum could arise from further oxidation resulting from the aqueous phase conjugation procedure. Oxide surface states have been implicated in preventing excited electrons from tunneling back to the bottom of the conduction band, causing radiative emission to occur with a slightly higher energy.[62] The acid-*Ox*SiNPs and Enz-*Ox*SiNPs also exhibit microsecond lifetimes (74–84 μs; Figure 2-8), and absolute quantum yields ranging from 23 to 30% (Table 2-1).

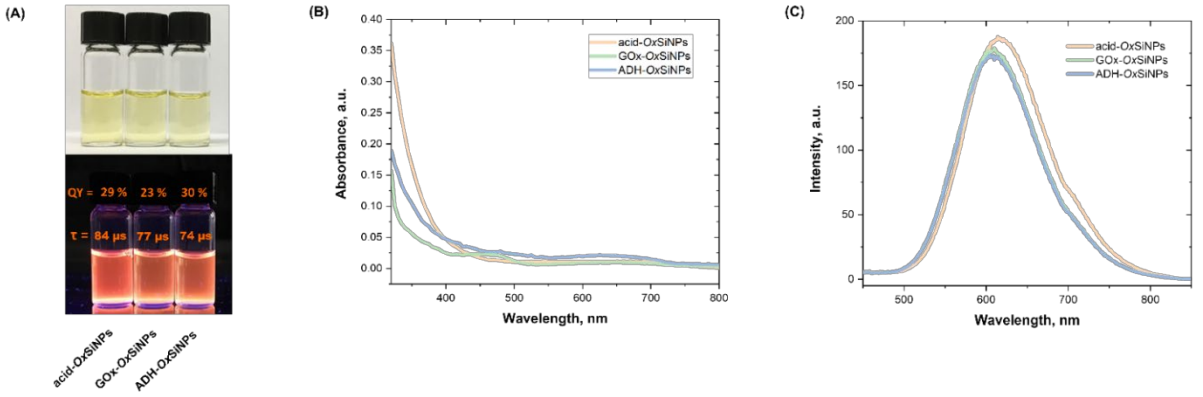

Figure 2-7. (A) Solutions of acid-*Ox*SiNPs, GOx-*Ox*SiNPs, and ADH-*Ox*SiNPs under ambient light conditions (top) and upon UV illumination (bottom). The functionalized *Ox*SiNPs exhibit orange photoluminescence and microsecond lifetimes. **(B)** Absorbance and **(C)** photoluminescence spectra of acid-*Ox*SiNPs, GOx-*Ox*SiNPs, and ADH-*Ox*SiNPs (λ_{ex} = 350 nm).

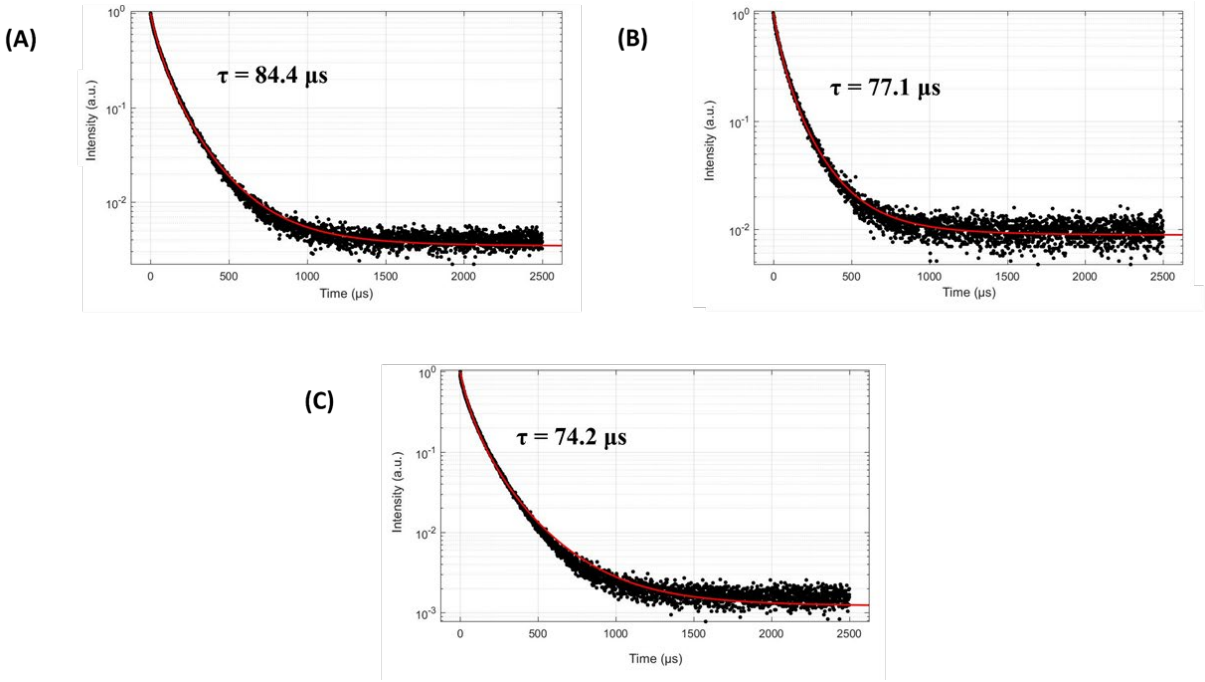

Figure 2-8. Photoluminescence decay plots of **(A)** acid-*Ox*SiNPs, **(B)** GOx-*Ox*SiNPs, and **(C)** ADH-*Ox*SiNPs. The lifetimes were calculated through lognormal fitting.

Table 2-1. Absolute Quantum Yields of acid-*Ox*SiNPs, GOx-*Ox*SiNPs, and ADH-*Ox*SiNPs (λ_{ex} = 365 nm)

Silicon-Based Nanoparticle	Absolute Quantum Yield, %
acid-*Ox*SiNP	28.8 ± 3.6
GOx-*Ox*SiNP	22.5 ± 1.3
ADH-*Ox*SiNP	30.2 ± 2.1

The photoluminescence intensities of acid-*Ox*SiNPs and Enz-*Ox*SiNPs under continuous UV illumination (λ = 365 nm) decreased with time (Figure 2-9A), which is consistent with the UV-induced oxidation of silicon nanoparticles observed by Hua et al. with their styrene-grafted silicon nanocrystals dispersed in toluene.[63]

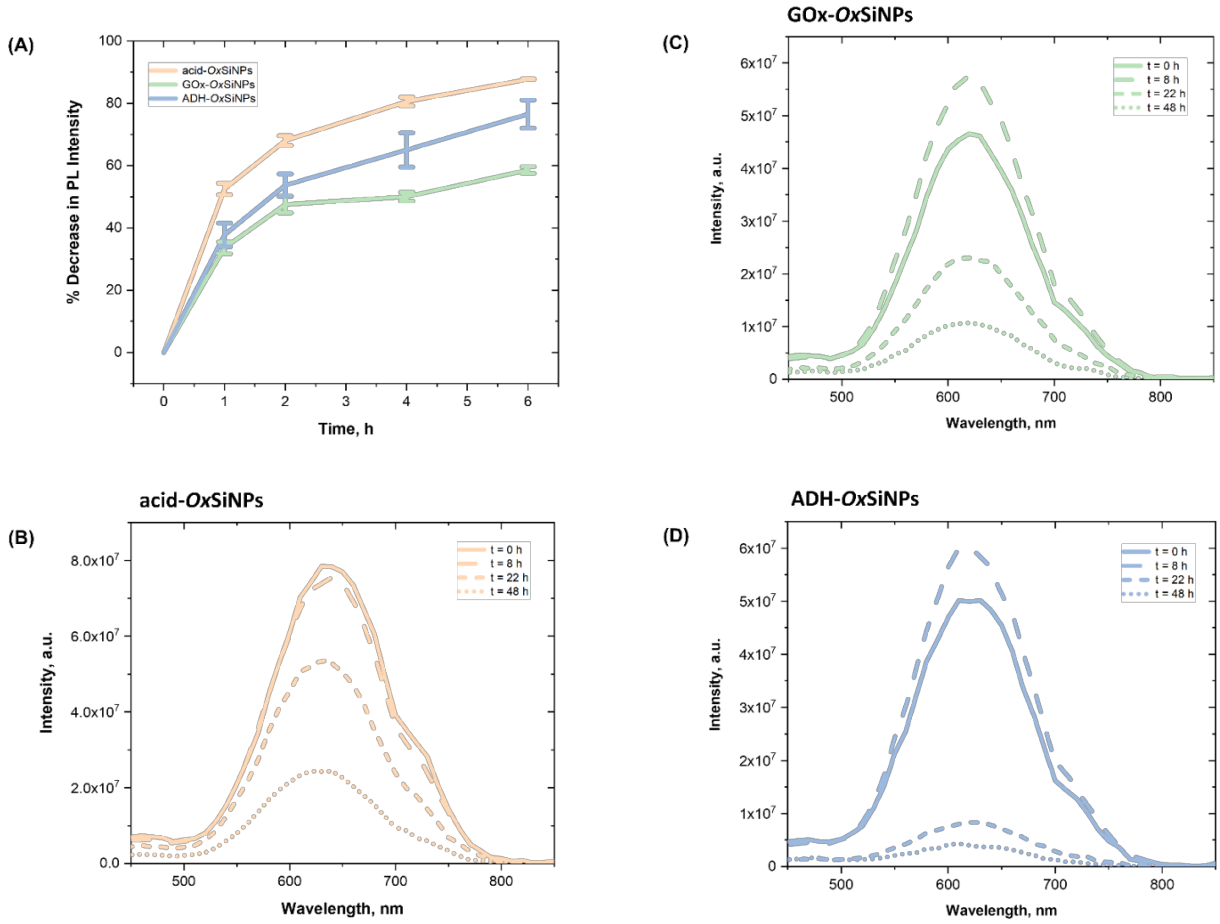

Figure 2-9. (A) % Decrease in photoluminescence intensity of acid-*Ox*SiNPs, GOx-*Ox*SiNPs, and ADH-*Ox*SiNPs as a function of time when they were subjected to continuous UV exposure. Photoluminescence spectra of **(B)** acid-*Ox*SiNPs, **(C)** GOx-*Ox*SiNPs, and **(D)** ADH-*Ox*SiNPs as a function of time under ambient light conditions.

The photoluminescence of their nanocrystals decreased by approximately 95% after 6 h. In comparison, the photoluminescence of our *Ox*SiNPs just decreased by 55–85% after the same time period. The greater relative photostability of our *Ox*SiNPs is notable since our nanoparticles were dispersed in water, which is known to cause degradation of silicon,[6] while theirs were dispersed in toluene. In contrast to that of acid-*Ox*SiNPs, the photoluminescence intensities of Enz-*Ox*SiNPs initially increased and then decreased with time under ambient

light conditions (Figures 2-9B to 2-9D). The origin of this observation is unknown; however, it may be related to the hydrophobic nature of the enzyme interior and is the subject of an ongoing study. The photoluminescence intensities of the Enz-*Ox*SiNPs reached values that are 49% (GOx-*Ox*SiNPs) and 17% (ADH-*Ox*SiNPs) of their original values after 22 h. These are lower than that of the acid-*Ox*SiNPs, which retained 68% of their original photoluminescence intensity after 22 h. Despite these losses in photoluminescence intensities, both the acid-*Ox*SiNPs and Enz-*Ox*SiNPs remain photoluminescent in phosphate buffer even after being left to stand at room temperature and in ambient light for more than three weeks. Also, the acid-*Ox*SiNPs can be stored in a -20 °C freezer with no observable loss in photoluminescence intensity after six months. An analogous observation was made by Dickinson and co-workers with undecyl-capped silicon nanocrystals dispersed in 1% (*v/v)* THF/phosphate buffer mixture. They have reported a decrease in the luminescence intensity of the silicon nanocrystals with time, which became pronounced a week after dispersion, but have also noted that the sols remain photoluminescent six months after initial preparation under ambient temperature conditions.[64] Their undecyl-capped silicon nanocrystals exhibited better photostability than the present *Ox*SiNPs, possibly because of the more hydrophobic nature of their nanocrystals' organic coating. Nonetheless, the relative stability displayed by the present *Ox*SiNPs and the persistence of their orange photoluminescence in aqueous medium are of note since silicon, as mentioned previously, is known to undergo decomposition on prolonged dispersion in water.[6]

Subsequently, the catalytic activity of the immobilized enzymes was evaluated. Glucose oxidase was tested using the Trinder's assay.[65,66] In this test, the enzyme peroxidase uses the hydrogen peroxide by-product of the glucose oxidase-catalyzed oxidation of glucose to couple phenol to 4-aminoantipyrine, leading to the formation of a pink/red aqueous solution of a quinoneimine dye that exhibits an absorption maximum at 510 nm (Figure 2-10A). The assay was performed by first adding phenol, 4-aminoantipyrine, and peroxidase, followed by glucose to vials containing the test samples (pure GOx, ultrafiltrate, retentate, and phosphate buffer blank). As shown in Figures 2-10B and 2-10C, the vials containing GOx-*Ox*SiNPs (retentate), unbound GOx (utrafiltrate), and pure GOx all provided pink/red solutions in the presence of the assay reagents consistent with the formation of the quinoneimine dye. No pink/red colour was observed with the phosphate buffer blank. These results are consistent with GOx remaining catalytically active following conjugation with the acid-*Ox*SiNPs.

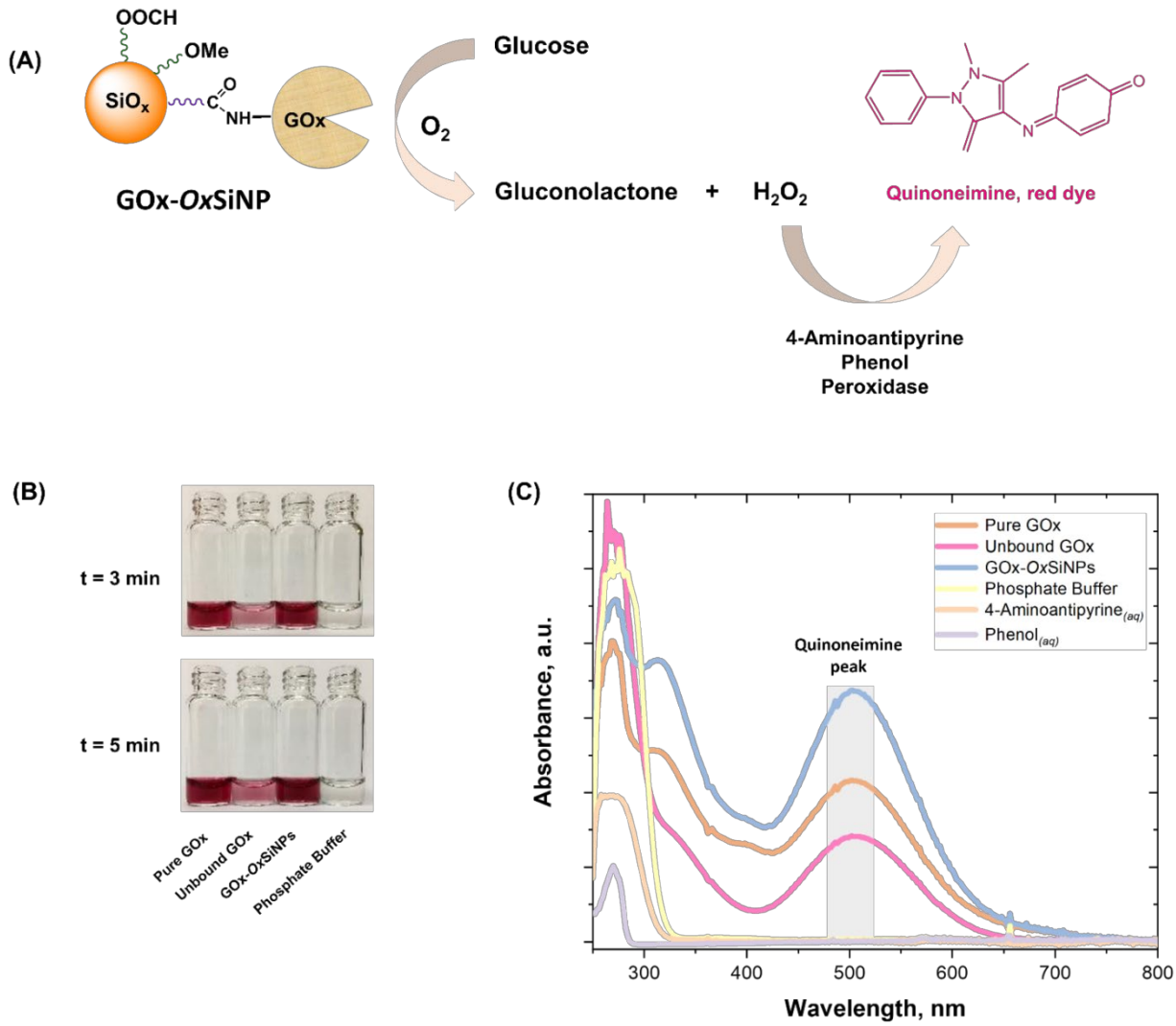

Figure 2-10. (A) Trinder's assay for GOx activity. **(B)** Photographs and **(C)** absorbance spectra of vials containing the assay reagents and tested samples.

The activity of glucose oxidase can be described mathematically by Michaelis–Menten kinetics,[67] a model of catalytic behavior wherein an enzyme acts on a single substrate molecule converting it to products by first forming an enzyme–substrate complex. A Michaelis–Menten curve (Figures 2-11A and 2-11C) is constructed by plotting the initial reaction velocity against the substrate concentration, yielding a hyperbolic curve that is asymptotic to the maximal value of velocity, v_{max}. The Michaelis–Menten constant, K_M, is a measure of the affinity of the enzyme for the substrate and can be obtained by transforming the Michaelis–Menten curve into a linear double reciprocal plot (Figures 2-11B and 2-11D). The K_M is calculated by taking the ratio of the slope of the generated line to its y-intercept.[68–70] Conflicting trends in K_M values

of surface-immobilized GOx and free GOx have been reported in the literature, with some studies showing a decrease in $K_{M,}$ while others showing an increase.[27,71,72] Here, we monitored the rate of formation of the quinoneimine dye (i.e., by measuring the change in absorbance at 490 nm with time) as a function of the concentration of glucose to obtain the K_M values for free GOx and GOx-*Ox*SiNPs. The K_M obtained for GOx-*Ox*SiNPs (1.60 ± 0.15 mM) is approximately seven times larger than that of free GOx (0.24 ± 0.09 mM), suggesting that conjugation of GOx with the acid-*Ox*SiNPs lowers its affinity for glucose. The reduction in affinity may result from partial deformation of its native three-dimensional structure upon surface immobilization. Despite this decrease in substrate affinity compared to the free enzyme, it is clear that sufficient enzyme activity remains to carry out its intended catalytic function.

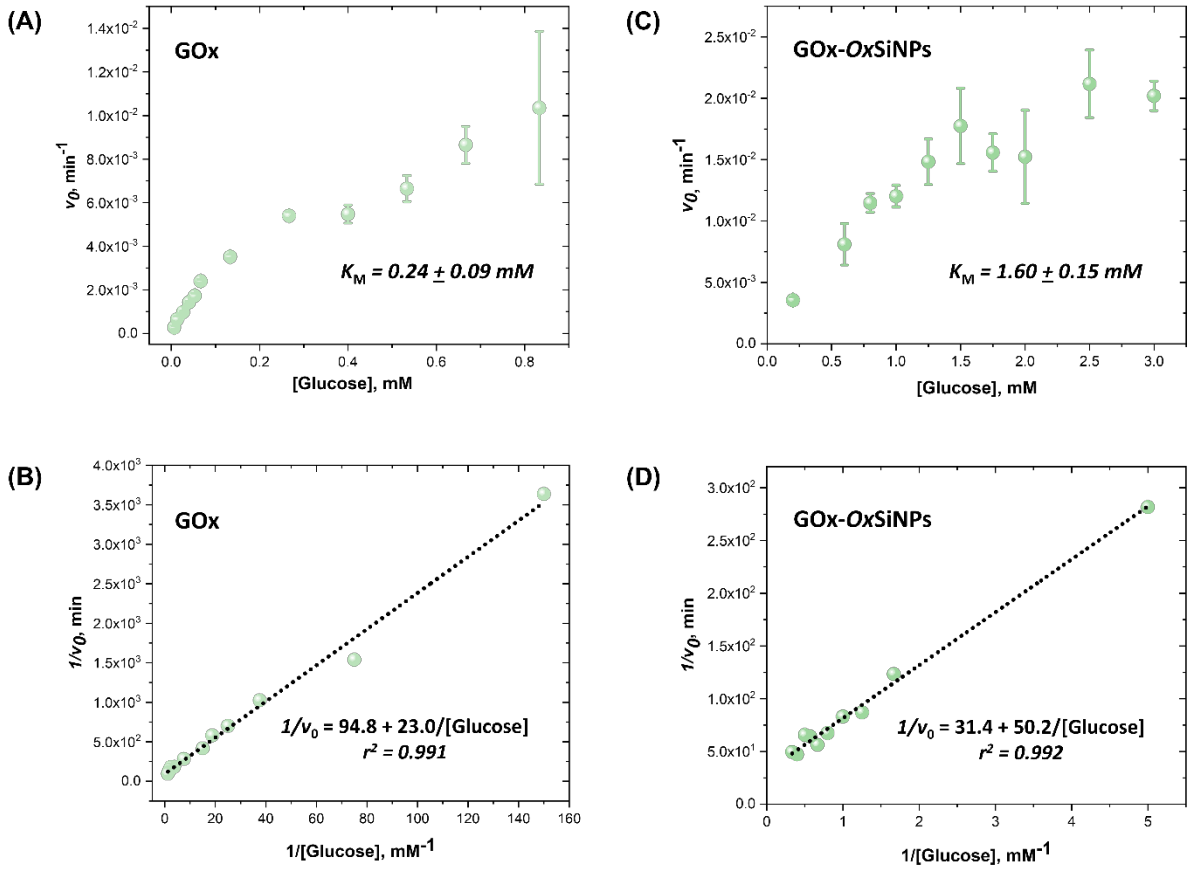

Figure 2-11. Michaelis–Menten curves of **(A)** GOx and **(C)** GOx-*Ox*SiNPs and their corresponding Lineweaver–Burk plots **(B, D)**.

Based upon the photoluminescence quenching observed by Yi et al. with the mixture of their unmodified blue-photoluminescent silicon nanocrystals, unbound GOx, and glucose,[73] we expected the H_2O_2 by-product from the oxidation of glucose by GOx to quench the *Ox*SiNP photoluminescence through electron-transfer as photoexcited electrons can, in principle, be transferred from the *Ox*SiNPs to the H_2O_2 molecules instead of undergoing electron-hole recombination and causing radiative emission. Our hybrids, however, did not manifest the same behavior, probably because of their silicon suboxide shell and poly(ethylene oxide) coating, which prevent effective contact with H_2O_2 molecules.

In addition, we evaluated the activity of surface-bonded alcohol dehydrogenase using the formazan assay that sees the formation of the intensely purple solution of formazan dye upon reduction of 3-(4,5-dimethylthiazol-2-yl)-2,5-diphenyltetrazolium bromide (Thiazolyl blue) by reduced nicotinamide adenine dinucleotide (NADH). NADH is produced from the reduction of nicotinamide adenine nucleotide (NAD^+), which is coupled to the alcohol dehydrogenase-catalyzed oxidation of ethanol into acetaldehyde (Figure 2-12A).[74,75] The formation of a purple solution upon addition of dimethyl sulfoxide (DMSO) to the mixture containing ADH-*Ox*SiNPs, NAD^+, thiazolyl blue, and ethanol suggests that the ADH molecules were conjugated with the acid-*Ox*SiNPs in their active form. Note that the formazan dye did not form upon addition of the assay reagents to phosphate buffer, as expected (Figure 2-12B). Figure 2-12C shows that the formazan dye has a maximum absorption at around 560 nm, while the unreacted thiazolyl blue absorbs at around 380 nm.

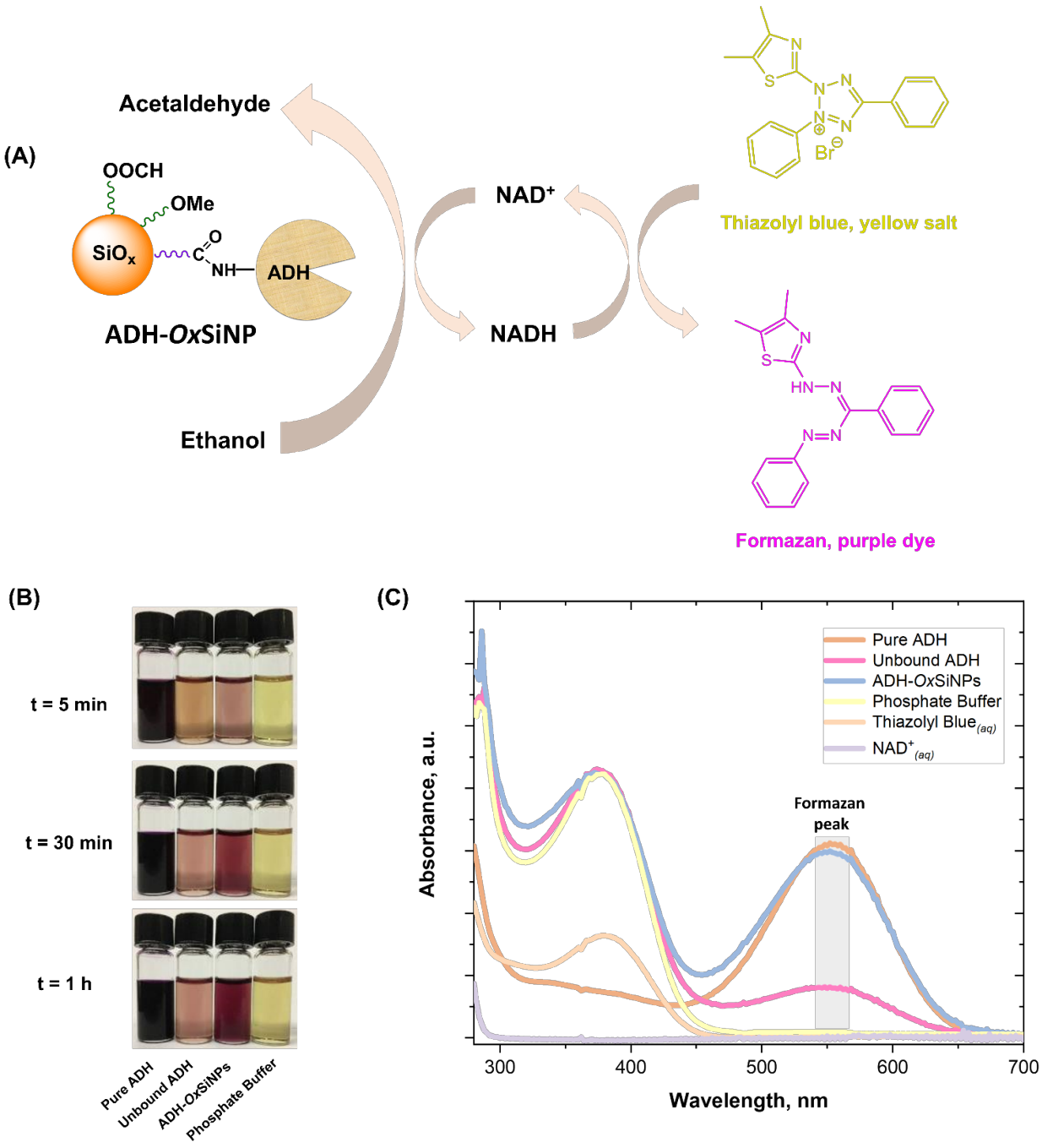

Figure 2-12. (A) Formazan assay for ADH activity. **(B)** Photographs and **(C)** absorbance spectra of vials containing the assay reagents and tested samples.

We have analyzed the kinetics of ethanol oxidation by free and surface-bound ADH by monitoring the rate at which NADH (λ_{max} = 340 nm) is formed (i.e., by measuring the change in absorbance at 340 nm with time) as a function of the concentration of ethanol[76] and construction of the corresponding Michaelis–Menten and Lineweaver–Burk plots (Figure

2-13). The K_M value obtained for ADH-*Ox*SiNPs (138.8 ± 6.8 mM) is four times larger than that for free ADH (35.3 ± 1.8 mM) suggesting that conjugation with the acid-*Ox*SiNPs lowers the enzyme's affinity for ethanol. This result is similar to what was observed with GOx and GOx-*Ox*SiNPs (vide supra).

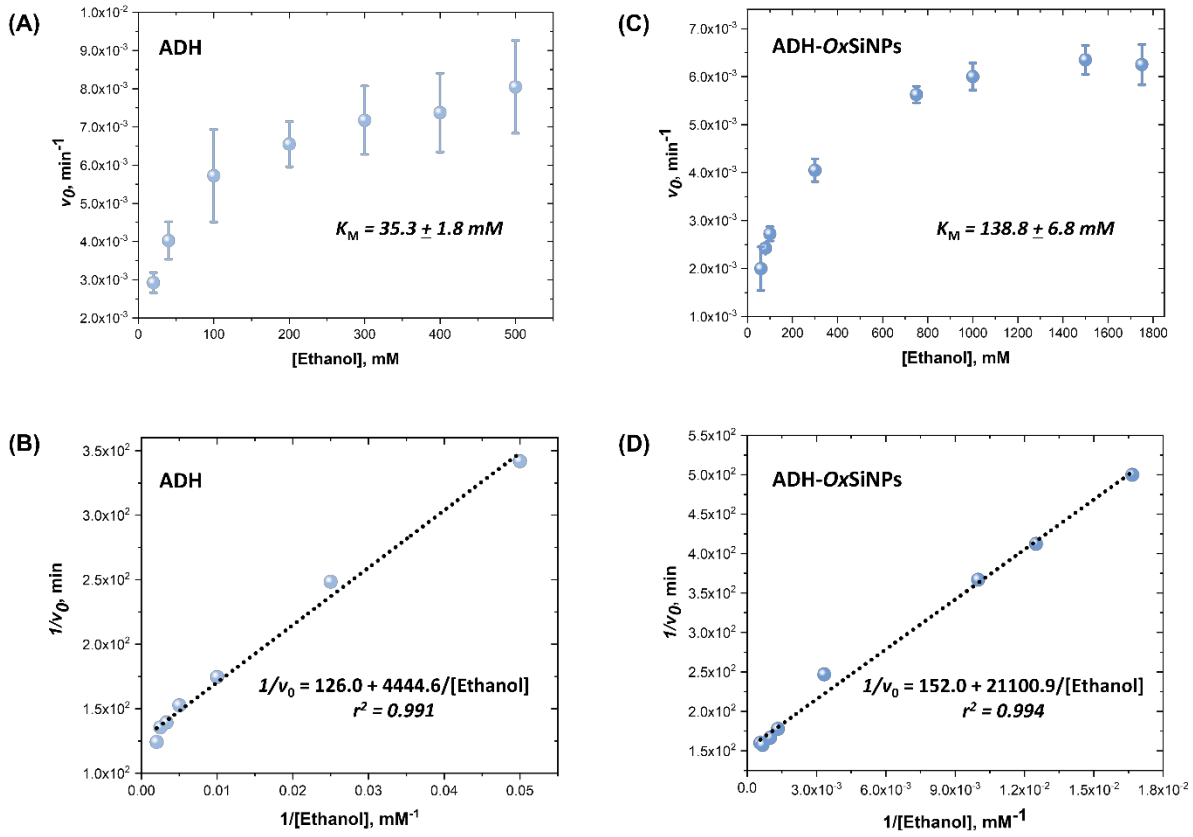

Figure 2-13. Michaelis–Menten curves of **(A)** ADH and **(C)** ADH-*Ox*SiNPs and their corresponding Lineweaver–Burk plots **(B, D)**.

The K_M values of GOx and ADH both increased by less than an order of magnitude upon their immobilization on the *Ox*SiNPs. This reduction in the enzymes' affinity for their respective substrates can be related to the size, shape, and surface composition of the *Ox*SiNPs, making it a property specific to the nanomaterial employed for conjugation. Regardless, both enzymes remain active upon conjugation with the acid-*Ox*SiNPs, thus affording catalytic photoluminescent bioinorganic hybrids.

2.4 Summary and Conclusions

This work demonstrates the preparation of functional bioinorganic hybrids exhibiting photoluminescent properties and substrate-specific catalytic activity from freestanding oxide-rich silicon-based nanoparticles and enzymes. The reported synthesis provides an expedient two-step route to bioconjugated silicon-based nanoparticles by precluding lengthy organic manipulations on the silicon surface. We have characterized the materials through FTIR, XPS, TEM, DLS, steady-state and time-resolved photoluminescence spectroscopy, and relevant enzyme activity assays, and confirmed the presence of groups characteristic of both nanoparticles and enzymes. The hybrids prepared are water-soluble, buffer-stable, and orange photoluminescent, which support their use for in vivo biomedical applications. The conjugated enzymes remain catalytically active upon immobilization on the silicon-based nanoparticles. The present catalytic hybrids potentially can be employed in simultaneous targeted enzyme-based therapy and real-time bioimaging (e.g., gated imaging) of diseased tissues through conjugation with suitable enzymes and decoration with appropriate biorecognition motifs.

2.5 References

(1) Warner, J. H.; Hoshino, A.; Yamamoto, K.; Tilley, R. Water-Soluble Photoluminescent Silicon Quantum Dots. *Angew. Chem.* **2005***, 117*, 4626-4630.

(2) Murray, C.; Norris, D. J.; Bawendi, M. G. Synthesis and Characterization of Nearly Monodisperse CdE (E = Sulfur, Selenium, Tellurium) Semiconductor Nanocrystallites. *J. Am. Chem. Soc.* **1993***, 115*, 8706-8715.

(3) Fujioka, K.; Hiruoka, M.; Sato, K.; Manabe, N.; Miyasaka, R.; Hanada, S.; Hoshino, A.; Tilley, R. D.; Manome, Y.; Hirakuri, K. Luminescent Passive-Oxidized Silicon Quantum Dots as Biological Staining Labels and Their Cytotoxicity Effects at High Concentration. *Nanotechnology* **2008***, 19*, 415102.

(4) Resch-Genger, U.; Grabolle, M.; Cavaliere-Jaricot, S.; Nitschke, R.; Nann, T. Quantum Dots versus Organic Dyes as Fluorescent Labels. *Nat. Methods* **2008***, 5*, 763.

(5) Derfus, A. M.; Chan, W. C.; Bhatia, S. N. Probing the Cytotoxicity of Semiconductor Quantum Dots. *Nano Lett.* **2004***, 4*, 11-18.

(6) Park, J.; Gu, L.; Von Maltzahn, G.; Ruoslahti, E.; Bhatia, S. N.; Sailor, M. J. Biodegradable Luminescent Porous Silicon Nanoparticles for in Vivo Applications. *Nat. Mater.* **2009***, 8*, 331.

(7) Zhong, Y.; Peng, F.; Bao, F.; Wang, S.; Ji, X.; Yang, L.; Su, Y.; Lee, S.; He, Y. Large-Scale Aqueous Synthesis of Fluorescent and Biocompatible Silicon Nanoparticles and Their Use as Highly Photostable Biological Probes. *J. Am. Chem. Soc.* **2013***, 135*, 8350-8356.

(8) Erogbogbo, F.; Yong, K.; Roy, I.; Xu, G.; Prasad, P. N.; Swihart, M. T. Biocompatible Luminescent Silicon Quantum Dots for Imaging of Cancer Cells. *ACS Nano* **2008***, 2*, 873-878.

(9) Osminkina, L. A.; Tamarov, K. P.; Sviridov, A. P.; Galkin, R. A.; Gongalsky, M. B.; Solovyev, V. V.; Kudryavtsev, A. A.; Timoshenko, V. Y. Photoluminescent Biocompatible Silicon Nanoparticles for Cancer Theranostic Applications. *J Biophotonics* **2012***, 5*, 529-535.

(10) Bhattacharjee, S.; Rietjens, I. M.; Singh, M. P.; Atkins, T. M.; Purkait, T. K.; Xu, Z.; Regli, S.; Shukaliak, A.; Clark, R. J.; Mitchell, B. S.; Alink, G. M.; Marcelis, A. T. M.; Fink, M. J.; Veinot, J. G. C.; Kauzlarich, S. M.; Zuilhof, H. Cytotoxicity of Surface-Functionalized Silicon and Germanium Nanoparticles: The Dominant Role of Surface Charges. *Nanoscale* **2013***, 5*, 4870-4883.

(11) Holmes, J. D.; Ziegler, K. J.; Doty, R. C.; Pell, L. E.; Johnston, K. P.; Korgel, B. A. Highly Luminescent Silicon Nanocrystals with Discrete Optical Transitions. *J. Am. Chem. Soc.* **2001***, 123*, 3743-3748.

(12) Wilcoxon, J.; Samara, G.; Provencio, P. Optical and Electronic Properties of Si Nanoclusters Synthesized in Inverse Micelles. *Phys. Rev. B* **1999***, 60*, 2704.

(13) Zhou, Z.; Brus, L.; Friesner, R. Electronic Structure and Luminescence of 1.1- and 1.4-nm Silicon Nanocrystals: Oxide Shell versus Hydrogen Passivation. *Nano Lett.* **2003***, 3*, 163-167.

(14) Kang, Z.; Liu, Y.; Tsang, C. H. A.; Ma, D. D. D.; Fan, X.; Wong, N.; Lee, S. Water-Soluble Silicon Quantum Dots with Wavelength-Tunable Photoluminescence. *Adv. Mater.* **2009***, 21*, 661-664.

(15) Dasog, M.; De los Reyes, Glenda B; Titova, L. V.; Hegmann, F. A.; Veinot, J. G. C. Size vs Surface: Tuning the Photoluminescence of Freestanding Silicon Nanocrystals Across the Visible Spectrum via Surface Groups. *ACS Nano* **2014***, 8*, 9636-9648.

(16) Hessel, C. M.; Reid, D.; Panthani, M. G.; Rasch, M. R.; Goodfellow, B. W.; Wei, J.; Fujii, H.; Akhavan, V.; Korgel, B. A. Synthesis of Ligand-Stabilized Silicon Nanocrystals with Size-Dependent Photoluminescence Spanning Visible to Near-Infrared Wavelengths. *Chem. Mater.* **2011***, 24*, 393-401.

(17) Veinot, J. G. C. Synthesis, Surface Functionalization, and Properties of Freestanding Silicon Nanocrystals. *Chem. Commun.* **2006**, 4160-4168.

(18) Maier-Flaig, F.; Rinck, J.; Stephan, M.; Bocksrocker, T.; Bruns, M.; Kübel, C.; Powell, A. K.; Ozin, G. A.; Lemmer, U. Multicolor Silicon Light-Emitting Diodes (SiLEDs). *Nano Lett.* **2013***, 13*, 475-480.

(19) Zou, J.; Baldwin, R. K.; Pettigrew, K. A.; Kauzlarich, S. M. Solution Synthesis of Ultrastable Luminescent Siloxane-Coated Silicon Nanoparticles. *Nano Lett.* **2004***, 4*, 1181-1186.

(20) Dasog, M.; Yang, Z.; Regli, S.; Atkins, T. M.; Faramus, A.; Singh, M. P.; Muthuswamy, E.; Kauzlarich, S. M.; Tilley, R. D.; Veinot, J. G. C. Chemical Insight into the Origin of Red and Blue Photoluminescence Arising from Freestanding Silicon Nanocrystals. *ACS Nano* **2013***, 7*, 2676-2685.

(21) Li, Z.; Ruckenstein, E. Water-Soluble Poly(acrylic acid) Grafted Luminescent Silicon Nanoparticles and Their Use as Fluorescent Biological Staining Labels. *Nano Lett.* **2004***, 4*, 1463-1467.

(22) Zhai, Y.; Dasog, M.; Snitynsky, R. B.; Purkait, T. K.; Aghajamali, M.; Hahn, A. H.; Sturdy, C. B.; Lowary, T. L.; Veinot, J. G. C. Water-Soluble Photoluminescent D-Mannose and L-Alanine

Functionalized Silicon Nanocrystals and Their Application to Cancer Cell Imaging. *J. Mater. Chem. B* **2014**, *2*, 8427-8433.

(23) Wu, S.; Zhong, Y.; Zhou, Y.; Song, B.; Chu, B.; Ji, X.; Wu, Y.; Su, Y.; He, Y. Biomimetic Preparation and Dual-Color Bioimaging of Fluorescent Silicon Nanoparticles. *J. Am. Chem. Soc.* 2015, *137*, 14726-14732.

(24) Henderson, E. J.; Shuhendler, A. J.; Prasad, P.; Baumann, V.; Maier-Flaig, F.; Faulkner, D. O.; Lemmer, U.; Wu, X. Y.; Ozin, G. A. Colloidally Stable Silicon Nanocrystals with Near-Infrared Photoluminescence for Biological Fluorescence Imaging. *Small* **2011**, *7*, 2507-2516.

(25) McVey, B. F.; Tilley, R. D. Solution Synthesis, Optical Properties, and Bioimaging Applications of Silicon Nanocrystals. *Acc. Chem. Res.* **2014**, *47*, 3045-3051.

(26) Hessel, C. M.; Rasch, M. R.; Hueso, J. L.; Goodfellow, B. W.; Akhavan, V. A.; Puvanakrishnan, P.; Tunnel, J. W.; Korgel, B. A. Alkyl Passivation and Amphiphilic Polymer Coating of Silicon Nanocrystals for Diagnostic Imaging. *Small* **2010**, *6*, 2026-2034.

(27) Wu, P.; He, Y.; Wang, H.; Yan, X. Conjugation of Glucose Oxidase onto Mn-Doped ZnS Quantum Dots for Phosphorescent Sensing of Glucose in Biological Fluids. *Anal. Chem.* **2010**, *82*, 1427-1433.

(28) Medintz, I. L.; Uyeda, H. T.; Goldman, E. R.; Mattoussi, H. Quantum Dot Bioconjugates for Imaging, Labelling and Sensing. *Nat. Mater.* **2005**, *4*, 435.

(29) Wu, X.; Liu, H.; Liu, J.; Haley, K. N.; Treadway, J. A.; Larson, J. P.; Ge, N.; Peale, F.; Bruchez, M. P. Immunofluorescent Labeling of Cancer Marker Her2 and other Cellular Targets with Semiconductor Quantum Dots. *Nat. Biotechnol.* **2003**, *21*, 41.

(30) Boutureira, O.; Bernardes, G. J. Advances in Chemical Protein Modification. *Chem. Rev.* **2015**, *115*, 2174-2195.

(31) Ruizendaal, L.; Pujari, S. P.; Gevaerts, V.; Paulusse, J. M.; Zuilhof, H. Biofunctional Silicon Nanoparticles by Means of Thiol–Ene Click Chemistry. *Chem. Asian J.* **2011**, *6*, 2776-2786.

(32) Wang, L.; Reipa, V.; Blasic, J. Silicon Nanoparticles as a Luminescent Label to DNA. *Bioconjugate Chem.* **2004**, *15*, 409-412.

(33) Choi, J.; Wang, N. S.; Reipa, V. Conjugation of the Photoluminescent Silicon Nanoparticles to Streptavidin. *Bioconjugate Chem.* **2008**, *19*, 680-685.

(34) Hessel, C. M.; Henderson, E. J.; Veinot, J. G. C. Hydrogen Silsesquioxane: A Molecular Precursor for Nanocrystalline Si− SiO_2 Composites and Freestanding Hydride-Surface-Terminated Silicon Nanoparticles. *Chem. Mater.* **2006**, *18*, 6139-6146.

(35) Clark, R. J.; Aghajamali, M.; Gonzalez, C. M.; Hadidi, L.; Islam, M. A.; Javadi, M.; Mobarok, M. H.; Purkait, T. K.; Robidillo, C. J. T.; Sinelnikov, R.; Thiessen, A. N.; Washington, J.; Yu, H.; Veinot, J. G. C. From Hydrogen Silsesquioxane to Functionalized Silicon Nanocrystals. *Chem. Mater.* **2016**, *29*, 80-89.

(36) Van Driel, A.; Nikolaev, I.; Vergeer, P.; Lodahl, P.; Vanmaekelbergh, D.; Vos, W. L. Statistical Analysis of Time-Resolved Emission from Ensembles of Semiconductor Quantum Dots: Interpretation of Exponential Decay Models. *Phys. Rev. B* **2007***, 75*, 035329.

(37) Nguyen, A.; Gonzalez, C. M.; Sinelnikov, R.; Newman, W.; Sun, S.; Lockwood, R.; Veinot, J. G. C.; Meldrum, A. Detection of Nitroaromatics in the Solid, Solution, and Vapor Phases Using Silicon Quantum Dot Sensors. *Nanotechnology* **2016***, 27*, 105501.

(38) Hessel, C. M.; Henderson, E. J.; Veinot, J. G. C. An Investigation of the Formation and Growth of Oxide-Embedded Silicon Nanocrystals in Hydrogen Silsesquioxane-Derived Nanocomposites. *J. Phys. Chem. C* **2007***, 111*, 6956-6961.

(39) Yang, Z.; Iqbal, M.; Dobbie, A. R.; Veinot, J. G. C. Surface-Induced Alkene Oligomerization: Does Thermal Hydrosilylation Really Lead to Monolayer Protected Silicon Nanocrystals? *J. Am. Chem. Soc.* **2013***, 135*, 17595-17601.

(40) Otsuka, H.; Nagasaki, Y.; Kataoka, K. PEGylated Nanoparticles for Biological and Pharmaceutical Applications. *Adv. Drug Deliv. Rev.* **2012***, 64*, 246-255.

(41) Wörz, A.; Berchtold, B.; Moosmann, K.; Prucker, O.; Rühe, J. Protein-Resistant Polymer Surfaces. *J. Mater. Chem.* **2012***, 22*, 19547-19561.

(42) Pelaz, B.; del Pino, P.; Maffre, P.; Hartmann, R.; Gallego, M.; Rivera-Fernandez, S.; de la Fuente, Jesus M; Nienhaus, G. U.; Parak, W. J. Surface Functionalization of Nanoparticles with Polyethylene Glycol: Effects on Protein Adsorption and Cellular Uptake. *ACS Nano* **2015***, 9*, 6996-7008.

(43) Dai, Q.; Walkey, C.; Chan, W. C. Polyethylene Glycol Backfilling Mitigates the Negative Impact of the Protein Corona on Nanoparticle Cell Targeting. *Angew. Chem., Int. Ed.* **2014***, 53*, 5093-5096.

(44) Clark, R. J.; Dang, M. K.; Veinot, J. G. C. Exploration of Organic Acid Chain Length on Water-Soluble Silicon Quantum Dot Surfaces. *Langmuir* **2010***, 26*, 15657-15664.

(45) Yang, L.; Heatley, F.; Blease, T. G.; Thompson, R. I. A Study of the Mechanism of the Oxidative Thermal Degradation of Poly(ethylene oxide) and Poly(propylene oxide) Using ^{1}H-and ^{13}C-NMR. *Eur. Polym. J.* **1996***, 32*, 535-547.

(46) Mkhatresh, O. A.; Heatley, F. A Study of the Products and Mechanism of the Thermal Oxidative Degradation of Poly(ethylene oxide) Using ^{1}H and ^{13}C 1-D and 2-D NMR. *Polym. Int.* **2004***, 53*, 1336-1342.

(47) Yang, Z.; Gonzalez, C. M.; Purkait, T. K.; Iqbal, M.; Meldrum, A.; Veinot, J. G. C. Radical Initiated Hydrosilylation on Silicon Nanocrystal Surfaces: An Evaluation of Functional Group Tolerance and Mechanistic Study. *Langmuir* **2015***, 31*, 10540-10548.

(48) Matsuura, H.; Miyazawa, T. Vibrational Analysis of Molten Poly(ethylene glycol). *J. Polym. Sci. Pol. Phys.* **1969***, 7*, 1735-1744.

(49) Huang, Y.; Tien, H.; Ma, C. M.; Yang, S.; Wu, S.; Liu, H.; Mai, Y. Effect of Extended Polymer Chains on Properties of Transparent Graphene Nanosheets Conductive Film. *J. Mater. Chem.* **2011***, 21*, 18236-18241.

(50) Campos, M. A. C.; Paulusse, J. M.; Zuilhof, H. Functional Monolayers on Oxide-Free Silicon Surfaces via Thiol–Ene Click Chemistry. *Chem. Commun.* **2010***, 46*, 5512-5514.

(51) Wu, E. C.; Park, J. H.; Park, J.; Segal, E.; Cunin, F.; Sailor, M. J. Oxidation-Triggered Release of Fluorescent Molecules or Drugs from Mesoporous Si Microparticles. *ACS Nano* **2008**, *2* (11), 2401–2409.

(52) Hecht, H.; Kalisz, H.; Hendle, J.; Schmid, R.; Schomburg, D. Crystal Structure of Glucose Oxidase from *Aspergillus niger* Refined at 2·3 Å Resolution. *J. Mol. Biol.* **1993***, 229*, 153-172.

(53) Pazur, J. H.; Kleppe, K. The Oxidation of Glucose and Related Compounds by Glucose Oxidase from *Aspergillus niger*. *Biochemistry* **1964***, 3*, 578-583.

(54) Magonet, E.; Hayen, P.; Delforge, D.; Delaive, E.; Remacle, J. Importance of the Structural Zinc Atom for the Stability of Yeast Alcohol Dehydrogenase. *Biochem. J.* **1992***, 287 (Pt 2)*, 361-365.

(55) Bennetzen, J. L.; Hall, B. D. The Primary Structure of the *Saccharomyces cerevisiae* Gene for Alcohol Dehydrogenase. *J. Biol. Chem.* **1982***, 257*, 3018-3025.

(56) Bühner, M.; Sund, H. Yeast Alcohol Dehydrogenase: –SH Groups, Disulfide Groups, Quaternary Structure, and Reactivation by Reductive Cleavage of Disulfide Groups. *FEBS J.* **1969***, 11*, 73-79.

(57) Tamm, L. K.; Tatulian, S. A. Infrared Spectroscopy of Proteins and Peptides in Lipid Bilayers. *Q. Rev. Biophys.* **1997***, 30*, 365-429.

(58) Jedlovszky-Hajdú, A.; Bombelli, F. B.; Monopoli, M. P.; Tombácz, E.; Dawson, K. A. Surface Coatings Shape the Protein Corona of SPIONs with Relevance to their Application in Vivo. *Langmuir* **2012***, 28*, 14983-14991.

(59) Ray, S.; Shard, A. G. Quantitative Analysis of Adsorbed Proteins by X-ray Photoelectron Spectroscopy. *Anal. Chem.* **2011***, 83*, 8659-8666.

(60) Buhl, M.; Vonhören, B.; Ravoo, B. J. Immobilization of Enzymes via Microcontact Printing and Thiol–Ene Click Chemistry. *Bioconjugate Chem.* **2015***, 26*, 1017-1020.

(61) Anderson, S. L.; Luber, E, J.; Olsen, B. C.; Buriak, J. M. Substance over Subjectivity: Moving beyond the Histogram. *Chem. Mater.* **2016**, *28*, 5973–5975.

(62) Sinelnikov, R.; Dasog, M.; Beamish, J.; Meldrum, A.; Veinot, J. G. C. Revisiting an Ongoing Debate: What Role Do Surface Groups Play in Silicon Nanocrystal Photoluminescence? *ACS Photonics* **2017***, 4*, 1920-1929.

(63) Hua, F.; Erogbogbo, F.; Swihart, M. T.; Ruckenstein, E. Organically Capped Silicon Nanoparticles with Blue Photoluminescence Prepared by Hydrosilylation Followed by Oxidation. *Langmuir* **2006***, 22*, 4363-4370.

(64) Dickinson, F.; Alsop, T.; Al-Sharif, N.; Berger, C.; Datta, H.; Šiller, L.; Chao, Y.; Tuite, E.; Houlton, A.; Horrocks, B. Dispersions of Alkyl-Capped Silicon Nanocrystals in Aqueous Media: Photoluminescence and Ageing. *Analyst* **2008***, 133*, 1573-1580.

(65) Lott, J. A.; Turner, K. Evaluation of Trinder's Glucose Oxidase Method for Measuring Glucose in Serum and Urine. *Clin. Chem.* **1975***, 21*, 1754-1760.

(66) Trinder, P. Determination of Glucose in Blood Using Glucose Oxidase with an Alternative Oxygen Acceptor. *Ann. Clin. Biochem.* **1969***, 6*, 24-27.

(67) Gregg, B. A.; Heller, A. Cross-Linked Redox Gels Containing Glucose Oxidase for Amperometric Biosensor Applications. *Anal. Chem.* **1990***, 62*, 258-263.

(68) Johnson, K. A.; Goody, R. S. The Original Michaelis Constant: Translation of the 1913 Michaelis–Menten paper. *Biochemistry* **2011***, 50*, 8264-8269.

(69) Menten, L.; Michaelis, M. Die Kinetik der Invertinwirkung. *Biochem. Z.* **1913***, 49*, 333-369.

(70) Lineweaver, H.; Burk, D. The Determination of Enzyme Dissociation Constants. *J. Am. Chem. Soc.* **1934***, 56*, 658-666.

(71) Pandey, P.; Singh, S. P.; Arya, S. K.; Gupta, V.; Datta, M.; Singh, S.; Malhotra, B. D. Application of Thiolated Gold Nanoparticles for the Enhancement of Glucose Oxidase Activity. *Langmuir* **2007***, 23*, 3333-3337.

(72) Rossi, L. M.; Quach, A. D.; Rosenzweig, Z. Glucose Oxidase–Magnetite Nanoparticle Bioconjugate for Glucose Sensing. *Anal. Bioanal. Chem.* **2004***, 380*, 606-613.

(73) Yi, Y.; Deng, J.; Zhang, Y.; Li, H.; Yao, S. Label-Free Si Quantum Dots as Photoluminescence Probes for Glucose Detection. *Chem. Commun.* **2013***, 49*, 612-614.

(74) Abe, K.; Matsuki, N. Measurement of Cellular 3-(4,5-Dimethylthiazol-2-yl)-2,5-Diphenyltetrazolium Bromide (MTT) Reduction Activity and Lactate Dehydrogenase Release Using MTT. *Neurosci. Res.* **2000***, 38*, 325-329.

(75) Zanon, J. P.; Peres, M. F.; Gattás, E. A. Colorimetric Assay of Ethanol Using Alcohol Dehydrogenase from Dry Baker's Yeast. *Enzyme Microb. Technol.* **2007***, 40*, 466-470.

(76) Taber, R. L. The Competitive Inhibition of Yeast Alcohol Dehydrogenase by 2,2,2-Trifluoroethanol. *Biochem. Mol. Biol. Edu.* **1998***, 26*, 239-242.

Chapter 3

Interfacing Enzymes with Silicon Nanocrystals through the Thiol–Ene Reaction[2]

3.1 Introduction

Semiconductor nanoparticles (i.e., quantum dots; QDs) are promising materials for bioimaging, medical diagnostics, and chemical sensing.[1–4] Their large absorption cross-section, intense photoluminescence, long excited-state lifetimes, large Stokes shifts, and photostability make them attractive alternatives to conventional organic fluorophores that are known to suffer from photobleaching as well as exhibit limitations related to comparatively short fluorescence lifetimes and small Stokes shifts.[5,6] Most QDs, however, contain cytotoxic cadmium that can leach under oxidative conditions and/or upon exposure to ultraviolet radiation.[7] While strategies have been explored to mitigate Cd^{2+} release,[8–10] this characteristic still hinders the widespread utilization of QDs in many biological applications, including medical diagnostics and therapy.[11,12] Silicon nanocrystals (SiNCs) or silicon QDs exhibit the favorable characteristics of their cadmium-containing QD counterparts while also being biocompatible.[13,14] As such, a number of research groups have employed SiNCs as prototype in vitro and in vivo bioimaging platforms[15–23] and as sensors for small molecules and ions.[24–26] SiNCs also have been conjugated with biological molecules, such as DNA[27,28] and the proteins streptavidin[29] and transferrin.[17]

Very recently, our group reported the first example of functional bioinorganic hybrids that combined the properties of luminescent silicon-based nanoparticles with active enzymes by exploiting the amide coupling reaction.[30] However, amide coupling, although widely reported throughout the literature, yields a number of unwanted side products (e.g., anhydrides, *N*-acylisourea) that can limit reaction yields greatly.[31] Also, owing to the presence of reactive amine and carboxylic acid groups in enzymes and proteins, in general, intra and intermolecular crosslinking of enzyme molecules is inevitable.[32] Thus, a more efficient and chemoselective

[2]The contents of this chapter have been copied and/or adapted from the following publication: Robidillo, C. J. T.; Aghajamali, M.; Faramus, A.; Sinelnikov, R.; Veinot, J. G. C. *Nanoscale* **2018**, *10*, 18706-18719. Copyright © 2018 Royal Society of Chemistry.

bioconjugate reaction strategy that overcomes the aforementioned limitations is of great interest and will facilitate the preparation of bioinorganic hybrids better.

Of late, the thiol–ene 'click' reaction has gained popularity among bioconjugate chemists, partly because of its high yield, compatibility with water, insensitivity to oxygen, and the chemical robustness of the resulting thioether bond.[33] In addition, this reaction tolerates a wide variety of functional groups, does not require metal-based catalysts,[33,34] and addresses challenges associated with biomolecule crosslinking (vide supra). The utility of the thiol–ene reaction and the related thiol–yne reaction in materials and polymer chemistry also has been demonstrated in the functionalization of iron oxide nanoparticles, nanodiamonds, microspheres, and bulk silicon surfaces with small molecules, polymers, and carbohydrates.[35–40] Moreover, the thiol–ene chemistry has been employed in covalently printing proteins (e.g., antibodies, enzymes, fluorescent proteins) and DNA onto bulk surfaces, such as alkene-terminated polymer films,[41] alkene-terminated glass,[42] thiol-functionalized glass,[43] and alkene-terminated silicon.[44] There are also limited examples where a thiol–ene reaction has been applied to the derivatization of SiNCs to introduce a variety of surface groups. Cheng and co-workers installed amine, carboxyl, and sulfonate moieties on SiNCs surfaces.[45] Similarly, Ruizendaal et al. used this strategy to functionalize alkene-terminated SiNCs with hydrophilic hydroxyl, poly(ethylene oxide), and carboxylic acid groups.[27] Su and co-workers also employed the thiol–ene reaction in conjugating SiNCs with DNA.[46] Clearly, the thiol–ene coupling reaction opens the door to a vast array of surface chemistries. However, these known examples of thiol–ene 'click' chemistry being applied to SiNCs only involve modification of surface-emitting blue SiNCs that exhibit short-lived excited state lifetimes not amenable to SiNC applications, such as gated imaging. In this context, the important question remains: will the thiol–ene coupling chemistry compromise the optical properties of SiNCs emitting from long-lived excited states via a band gap transition? Furthermore, the thiol–ene reaction has not been employed yet to prepare functional bioinorganic hybrids made up of a combination of enzymes and freestanding SiNCs. In this regard, we will demonstrate the preparation of water-dispersible photoluminescent enzyme-conjugated SiNCs through the photochemical thiol–ene reaction.

3.2 Experimental Section

3.2.1 Chemicals

Commercial hydrogen silsesquioxane (HSQ, trade name Fox-17) dissolved in methyl isobutyl ketone was purchased from Dow Corning Corporation; the solvent was removed in vacuo, and the resulting white solid was used without further purification. Electronics grade hydrofluoric acid (49% $HF_{(aq)}$) was obtained from J. T. Baker. Allyloxy poly(ethylene oxide) methyl ether (9–12 ethylene oxide units, MW ~ 450 g mol^{-1}, ρ = 1.076 g mL^{-1}) (Gelest), lactase (*Lse*, 3 kU, from *Escherichia coli*), urease (*Use*, 20 kU, from *Canavalia ensiformis*), alcohol dehydrogenase (*ADH*, 30 kU, from *Saccharomyces cerevisiae*), 2-hydroxy-4'-(2-hydroxyethoxy)-2-methylpropiophenone (HHMP), *o*-nitrophenyl-β-D-galactopyranoside, sodium nitroprusside, alkaline hypochlorite solution (0.2% sodium hypochlorite in alkali solution), phenol (Sigma Aldrich), and 1,7-octadiene (MW = 110.2 g mol^{-1}, ρ = 0.735 g mL^{-1}) (Alfa Aesar) were used as received without further purification. All other reagents and solvents used were of analytical grade, unless otherwise indicated.

3.2.2 Preparation of Oxide-Embedded Silicon Nanocrystals

Oxide-embedded silicon nanocrystals were prepared following a well-established procedure developed in the Veinot laboratory.[47,48] Briefly, four grams of HSQ were placed in a furnace (Sentro Tech. Corp.), heated to 1100 °C, and thermally processed at that temperature in an atmosphere of 5% H_2 and 95% Ar for 1 h. The resulting amber-coloured product is a composite consisting of 3 nm silicon nanocrystals embedded in an oxide matrix. This composite was wetted with ethanol and ground using an agate mortar and pestle. The mixture was transferred into a flask containing glass beads, shaken for 6 h, and filtered through a hydrophilic membrane filter. The finely ground composite was stored in a standard glass vial and used as needed.

3.2.3 Synthesis of Hydride-Terminated Silicon Nanocrystals (*H*-SiNCs)

Hydride-terminated silicon nanocrystals (*H*-SiNCs) were liberated from the oxide matrix through HF etching. Three hundred milligrams of the powdered composite were dispersed in a 9 mL solution consisting of 49% HF (**Note:** *HF is very corrosive. Handle it with extreme*

care and in accordance with local regulations.), 100% ethanol, and deionized water in a 1:1:1 volume ratio. The mixture was stirred for 40 min under ambient light and temperature conditions. The liberated *H*-SiNCs (ca. 30 mg) were isolated through multiple extractions with toluene (i.e., 3× 15 mL) and multiple centrifugation–decantation cycles in toluene (i.e., 3×, 3000 rpm, 5 min).

3.2.4 Synthesis of Alkene-Terminated Poly(ethylene oxide)-Coated Silicon Nanocrystals (*ene*-SiNCs)

Mixed surface alkene-terminated poly(ethylene oxide)-coated silicon nanocrystals (*ene*-SiNCs) were prepared through thermal hydrosilylation. *H*-SiNCs obtained from etching 300 mg of the composite were dispersed in a mixture of 1,7-octadiene (1.5 mL, 10.0 mmol) and allyloxy poly(ethylene oxide) methyl ether (4.5 mL, ~10.8 mmol) in a Schlenk flask equipped with a magnetic stir bar. This mixture was heated to 170 °C and stirred at that temperature for 12 h in an Ar atmosphere. The resulting water-dispersible silicon nanocrystals were purified by multiple centrifugation–decantation cycles in 5 mL absolute ethanol (i.e., 5×, 3000 rpm, 5 min) followed by multiple centrifugation–decantation cycles in 5 mL mQ water (i.e., 5×, 3000 rpm, 5 min). Finally, the pellet containing the *ene*-SiNCs was suspended in mQ water to form 12.0 mL of dispersion (1.3 mg Si mL^{-1}).

3.2.5 Preparation of Enzyme-Conjugated Silicon Nanocrystals (*enz*-SiNCs)

To a 1.0 mL mQ water dispersion of *ene*-SiNCs was added 2.0 mL of phosphate buffer (0.10 M, pH 7.0), 10 mg of 2-hydroxy-4'-(2-hydroxyethoxy)-2-methylpropiophenone (HHMP), and 100 µL of 1.2 kU/mL lactase (*Lse*) or 100 µL of 6.7 kU/mL urease (*Use*) or 10 µL of 15 kU/mL alcohol dehydrogenase (*ADH*) solution. The dispersion was exposed to ultraviolet (UV) light (365 nm) for 4 min using a handheld UV flashlight and then stirred for three hours at 25 °C. Afterwards, the mixture was centrifuged at 3000 rpm for 5 min, the supernatant collected, and the resulting pellet further subjected to multiple centrifugation–decantation cycles in 5 mL phosphate buffer (0.10 M, pH 7.0) (i.e., 5×, 3000 rpm, 5 min). Finally, the pellet containing the *enz*-SiNCs was suspended in phosphate buffer (0.10 M, pH 7.0) to form 2.0 mL of dispersion (ca. 0.7 mg Si mL^{-1}).

3.2.6 Desorption of Adsorbed Enzymes Using Hot Sodium Dodecyl Sulfate Solution

Aqueous sodium dodecyl sulfate (5% (*w/v*); 1 mL) was added to each of three vials containing 0.5 mL dispersions of *Lse*-SiNCs, *Use*-SiNCs, or *ADH*-SiNCs (ca. 0.7 mg Si mL^{-1}) in phosphate buffer (0.10 M, pH 7.0). The resulting mixtures were heated to 100 °C in an oil bath for 1 h, after which they were cooled to room temperature and centrifuged at 3000 rpm for 5 min. The supernatant was decanted and the resulting pellets subjected to multiple centrifugation–decantation cycles in 3 mL mQ water (i.e., 5×, 3000 rpm, 5 min). Finally, the pellets containing the *enz*-SiNCs were dispersed in 0.25 mL of mQ water.

3.2.7 Characterization of *ene*-SiNCs and *enz*-SiNCs

Fourier transform infrared (FTIR) spectra of *ene*-SiNCs and *enz*-SiNCs were obtained using a Nicolet Magna 750 IR spectrometer. X-ray photoelectron spectroscopy (XPS) analyses were carried out using a Kratos Axis Ultra instrument operating in energy spectrum mode at 210 W. Thin film samples for XPS were prepared by depositing the aqueous SiNC dispersion of choice onto a copper foil and drying in air. The instrument base and operating chamber pressures were kept at 10^{-7} Pa. A monochromatic Al Kα source (λ = 8.34 Å) was used to excite samples, and spectra were obtained with an electron takeoff angle of 90°. When necessary, the charge neutralizer filament was used to minimize charging. Survey XP spectra were acquired using an elliptical spot with major and minor axis lengths of 2 and 1 mm, respectively, and a 160-eV pass energy with a step of 0.33 eV. CasaXPS software (VAMAS) was used to process all high-resolution spectra. Spectra were calibrated to the C 1s emission (284.8 eV), and a Shirley-type background was applied to remove most of the extrinsic loss structure. The high-resolution Si 2p region was fitted to Si $2p_{3/2}$ and Si $2p_{1/2}$ components, with spin-orbit splitting fixed at 0.6 eV and the Si $2p_{3/2}$ / Si $2p_{1/2}$ intensity ratio set to 2/1.

Bright field transmission electron microscopy (TEM) imaging was performed using a JEOL 2010 TEM equipped with a LaB_6 filament operating at an accelerating voltage of 200 kV. SiNC specimens were prepared by depositing a drop of dilute dispersion containing the SiNCs of choice onto a carbon-coated copper grid (Ted Pella, Inc.). The nanocrystal size was determined for 300 particles using ImageJ software (version 1.51) and is reported as an average. Scanning electron microscopy (SEM) images were acquired using a ZEISS Sigma

300 VP-FESEM equipped with a back-scattered electron (BSE) detector and a Bruker energy dispersive X-ray (EDX) spectroscopy system operated at 10 kV. The SEM samples were prepared by drop-coating of dilute aqueous solutions of the enzyme-conjugated SiNCs onto double-sided carbon tapes attached onto aluminum stubs (Ted Pella, Inc.). Dynamic light scattering (DLS) analyses were performed using a Malvern Zetasizer Nano S series equipped with a 633-nm laser. Dilute buffer dispersions of *ene*-SiNCs and *enz*-SiNCs (*ca.* 0.03 mg Si mL^{-1}) were equilibrated to 25 °C prior to data acquisition and scanned three times.

Absorbance spectra of the samples were recorded using a SpectraMax® i3x multimode microplate reader. Photoluminescence (PL) spectra of the samples were obtained using a Varian Cary Eclipse fluorescence spectrometer (λ_{ex} = 350 nm). Photostability experiments were performed by exposing dispersions of *ene*-SiNCs and *enz*-SiNCs in phosphate buffer (0.10 M, pH 7.0) to UV light (UV Trans-illuminator; λ_{ex} = 365 nm) and covering them with a non-reflective enclosure. PL intensities were monitored after 0, 1, 2, 4, and 6 h using a SpectraMax® i3x multimode microplate reader (λ_{ex} = 350 nm). Photostability under ambient light conditions was monitored similarly but in the absence of UV light. PL intensities were recorded after 0, 1, 2, 3, and 4 days using a Varian Cary Eclipse fluorescence spectrometer (λ_e = 350 nm). Time-resolved PL spectroscopy was measured using an Argon ion laser with 351-nm emission wavelength, which was modulated by an acousto-optic modulator (response time ~50 ns) operated at a frequency of 200 Hz with a 50% duty cycle. The PL was fed into an optic fiber, passed through a 500 nm long-pass filter, and was then incident on a Hamamatsu H7422P-50 photomultiplier tube interfaced with a Becker-Hickl PMS-400A gated photon counter. The PL data were collected in 1 μs timesteps, and a total of 10,000 sweeps were collected to ensure an adequate signal-to-noise ratio. The luminescence decays were calculated using lognormal fitting of the data.[49,50] PL quantum yield measurements were performed using a home-built integrating sphere. A phosphate buffer (0.10 M, pH 7.0) blank and sample dispersions were placed in a quartz cuvette-housed integrating sphere, and light supplied by a 365 nm light-emitting diode was used as the excitation source. The PL and excitation intensities were captured through a fiber attached to the sphere and analyzed with a calibrated Ocean Optics spectrometer. Quantum yields (QY) were determined using the equation $QY = (I_{PL,sample} - I_{PL,blank})/(I_{ex,blank} - I_{ex,sample})$, where I_{PL} is the integrated photoluminescence intensity

and I_{ex} is the excitation intensity. The measured samples have an absorbance of 0.1 at 365 nm. All measurements were performed in quadruplicates.

3.2.8 Evaluation of Catalytic Activity of *enz*-SiNCs through Enzyme Activity Assays

3.2.8.1 *o*-Nitrophenyl-β-D-Galactopyranoside Assay for Lactase (*Lse*) Activity

Predefined volumes (i.e., 100 µL each) of 15 mM *o*-nitrophenyl-β-D-galactopyranoside$_{(aq)}$ and phosphate buffer (0.10 M, pH 7.0) were added to a series of different vials containing 100 µL of *Lse* (12 U/mL) in phosphate buffer (0.10 M, pH 7.0), 100 µL of supernatant obtained from the first round of centrifugation of *Lse*-SiNCs, 100 µL of *Lse*-SiNC dispersion (ca. 0.7 mg Si mL^{-1}) in phosphate buffer (0.10 M, pH 7.0), or 100 µL of phosphate buffer (0.10 M, pH 7.0). The vials were inspected qualitatively visually and analyzed spectroscopically for the formation of a yellow solution arising from the formation *o*-nitrophenolate ion (λ_{max} = 420 nm), which indicates lactase activity.[51,52]

3.2.8.2 Berthelot Assay for Urease (*Use*) Activity

Aqueous urea (3.3 M; 200 µL) and phosphate buffer (0.10 M, pH 7.0; 300 µL) were added to a series of different vials containing 100 µL of *Use* (67 U/mL), 100 µL of supernatant obtained from the first round of centrifugation of *Use*-SiNCs, 100 µL of dispersion of *Use*-SiNCs (ca. 0.7 mg Si mL^{-1}) in phosphate buffer (0.10 M, pH 7.0), or 100 µL of phosphate buffer (0.10 M, pH 7.0). Following stirring the vials for 1 h, aqueous phenol (44.1 mM; 250 µL), aqueous alkaline hypochlorite (0.2% sodium hypochlorite in alkali solution; 250 µL), and aqueous sodium nitroprusside (173 mM; 250 µL) were added to each. The vials were immersed in boiling water for 3 min, inspected qualitatively visually, and analyzed spectroscopically for the appearance of a blue solution[53] arising from the formation of indophenol (λ_{max} = 670 nm) as a result of urease activity.

3.2.9 Photoluminescence (PL) Quenching Experiments

3.2.9.1 Quenching of *Lse*-SiNC PL in the Presence of *o*-Nitrophenyl-β-D-Galactopyranoside

Aqueous *o*-nitrophenyl-β-D-galactopyranoside (15 mM; 0.15 mL) or phosphate buffer (0.10 M, pH 7.0; 0.15 mL) were added to two separate vials containing a dispersion of *Lse*-SiNCs (ca. 0.7 mg Si mL^{-1}) in phosphate buffer (0.10 M, pH 7.0; 0.15 mL). The PL and absorbance spectra of the resulting mixtures were acquired 10 min after mixing using a SpectraMax® i3x multimode microplate reader (λ_{ex} = 350 nm). The experiments were performed in triplicates.

3.2.9.2 Quenching of *Use*-SiNC Photoluminescence in the Presence of Urea

Aqueous urea (3.3 M; 0.5 mL) or phosphate buffer (0.10 M, pH 7.0; 0.5 mL) were added to two separate vials containing a dispersion of *Use*-SiNCs (ca. 0.7 mg Si mL^{-1}) in phosphate buffer (0.10 M, pH 7.0; 0.5 mL). Next, the PL spectra of the resulting mixtures were measured 0, 2.5, 6, 9, and 16 h after mixing using a Varian Cary Eclipse fluorescence spectrometer (λ_{ex} = 350 nm). The experiments were performed in triplicates.

3.3. Results and Discussion

The utility of thiol–ene 'click' chemistry in the immobilization of proteins on bulk surfaces has been reported widely in the literature. Weinrich et al. have used this reaction in the fabrication of protein microarrays through the reaction of farnesylated proteins with thiol-terminated glass slides.[43] Jeong and co-workers also have employed this strategy in immobilizing cysteine-containing antibodies, fluorescent proteins, and protein scaffolds on glass, paper, and polyethylene films.[41] Buhl et al. used this reaction in covalently printing glucose oxidase and lactase on alkene-terminated glass. In addition, it also has been used in bioconjugate reactions, such as glycosylation of proteins with thiolated carbohydrates[54] and oligomerization of the protein ubiquitin.[55] Encouraged by these reports, we set out to interface enzymes with freestanding silicon nanocrystals (SiNCs) through the thiol–ene 'click' reaction.

In this context, hydride-terminated SiNCs (*H*-SiNCs) were synthesized via thermally induced disproportionation of hydrogen silsesquioxane, followed by alcoholic HF etching.[47,48,56] Subsequently, *H*-SiNCs were functionalized with 1,7-octadiene and allyloxy poly(ethylene oxide) methyl ether moieties via thermal hydrosilylation (Figure 3-1A).[30,48] This mixture of surface ligands was identified because the poly(ethylene oxide) chains were expected to render the SiNCs hydrophilic and minimize nonspecific protein adsorption,[57–60] while the alkene groups provided the necessary platform for conjugation with enzymes.

Successful surface derivatization of SiNCs and the introduction of alkene moieties were confirmed by evaluating the Fourier transform infrared (FTIR) spectrum of alkene-terminated poly(ethylene oxide)-coated silicon nanocrystals (*ene*-SiNCs), which showed the expected spectral signatures (Figure 3-1B). The immediately obvious difference between the spectrum of *H*-SiNCs (Figure 3-2) and that of the *ene*-SiNCs is the diminished intensity of the feature routinely assigned to Si–H_x stretching at ca. 2100 cm^{-1} in the spectrum of the latter.[48] More detailed evaluation of the spectrum reveals a feature attributed to C=C stretching vibration at 1663 cm^{-1}.[61] We also note a broad absorption at ca. 1100 cm^{-1} that arises as a result of a combination of Si–O, C–O and C–C stretching vibrations as well as a peak at ca. 1470 cm^{-1} arising from aliphatic –CH_x– bending vibrations.[47,62,63] There also is a feature at ca. 1730 cm^{-1} that we assign to formate ester groups appended to the nanocrystal surface that form as a result of the thermal oxidation of poly(ethylene oxide).[20,64,65] X-ray photoelectron spectroscopy (XPS) analyses of *ene*-SiNCs show C 1s emissions characteristic of C=C, C–C and C–H carbons (284.8 eV), C–O carbons (286.5 eV), and carboxyl carbons (288.7 eV) arising from alkenyl and poly(ethylene oxide) ester chains (Figure 3-1C).[19,40,66] The Si 2p region of the XP spectrum of *ene*-SiNCs (Figure 3-1D) indicates the presence of Si(0) and oxidized silicon species – Si(I), Si(III), and Si(IV). These silicon suboxides result from the aqueous oxidation of silicon that most certainly occurs during purification and subsequent dispersion in water.[67,68]

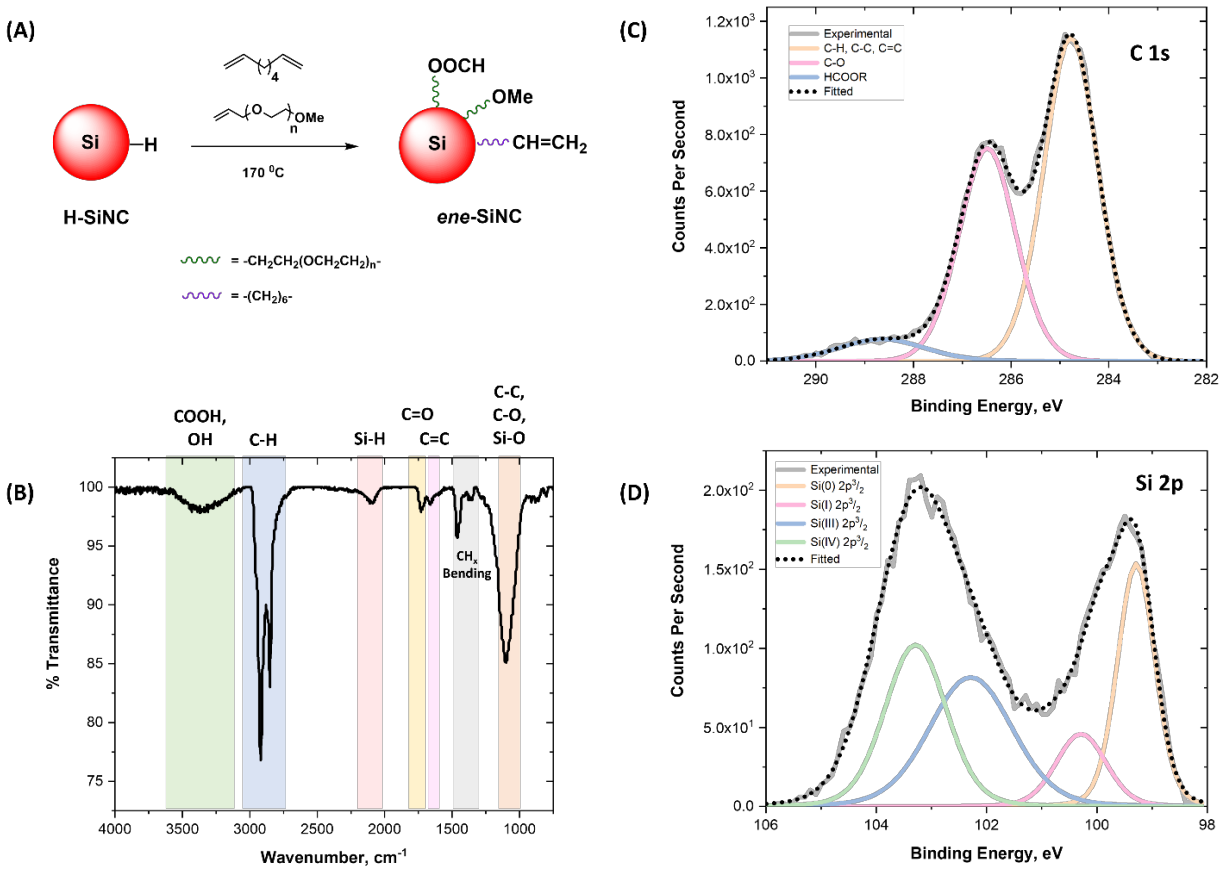

Figure 3-1. **(A)** Scheme showing thermally induced hydrosilylation of 1,7-octadiene and allyloxy poly(ethylene oxide) methyl ether with *H*-SiNCs (–OOCH is a formate ester group). **(B)** FTIR spectrum, **(C)** C 1s and **(D)** Si 2p spectral regions of the XP spectrum of *ene*-SiNCs (Si 2p1/2 peaks were omitted for clarity).

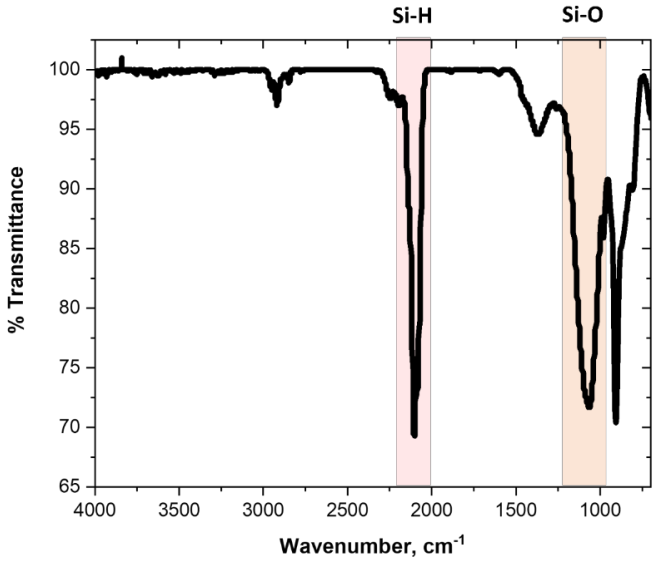

Figure 3-2. FTIR spectrum of hydride-terminated silicon nanocrystals (*H*-SiNCs).

With SiNCs bearing alkene moieties in hand, it was imperative to confirm whether the thiol–ene reaction of *ene*-SiNCs with enzymes would, in fact, proceed. Three cysteine-containing enzymes, lactase (*Lse*), urease (*Use*), and alcohol dehydrogenase (*ADH*), were chosen as representative enzymes and reacted with *ene*-SiNCs in the presence of 2-hydroxy-4'-(2-hydroxyethoxy)-2-methylpropiophenone (HHMP), as a water-soluble photoinitiator, and ultraviolet (UV) light (365 nm) (Scheme 3-1). The radicals that result from the dissociation of HHMP upon UV light exposure abstract hydrogen atoms from the thiol groups of cysteine residues, forming thiyl radicals. These radicals add across the alkene carbons in an anti-Markovnikov fashion,[42] leading to the attachment of the enzyme molecules to the nanocrystal surface. The resulting enzyme-conjugated SiNCs (*enz*-SiNCs) were purified through repeated centrifugation–decantation cycles, the reaction mixture was transferred into a test tube, and centrifuged multiple times in order to separate the hybrids from unbound enzyme molecules. The hybrids are centrifuged to yield a pellet, while the unbound enzyme molecules remain in the supernatant.

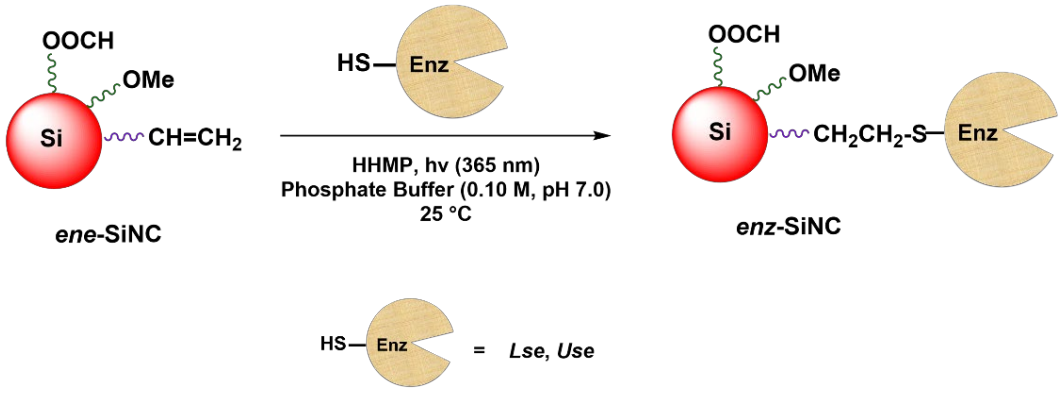

Scheme 3-1. Bioconjugation of *ene*-SiNCs with enzymes through the photochemical thiol–ene reaction.

The covalent attachment of the enzymes to the SiNCs was verified initially through desorption of potentially adsorbed proteins on the nanocrystals following an established literature procedure that uses a hot solution of sodium dodecyl sulfate (SDS) in water as a desorbing agent.[69–71] SDS is a powerful denaturant that unfolds and coats protein molecules through hydrophobic interactions and, in the process, breaking their nonspecific interactions with nanoparticle surfaces.[71,72] Heat also denatures proteins, causing them to lose their characteristic three-dimensional structures,[73] thereby weakening their interactions with

nanoparticle surface groups.[71] The resulting bioinorganic hybrids from the thiol–ene reaction were heated to 100 °C in 3.3% (*w/v*) SDS solution in phosphate buffer for 1 h. FTIR spectra of the bioinorganic hybrids before and after SDS treatment are shown in Figure 3-3. The peptide (i.e. amide) bond peaks at 1650–1500 cm^{-1}, characteristic of enzymes[74] (vide infra), persisted in *Lse*-SiNCs and *Use*-SiNCs, while the same peaks disappeared in *ADH*-SiNCs after treatment with a hot SDS solution. These observations are consistent with *Lse* and *Use* being covalently linked to the SiNCs, while *ADH* is adsorbed only physically on the nanocrystals. *Lse* and *Use* have approximately 43 and 36 exposed cysteine residues,[51,75–77] respectively, while *ADH* just contains 4 available cysteine residues at most for reaction.[78] These results suggest that a minimum number of cysteine residues is necessary for a succesful thiol–ene reaction between proteins and alkene-terminated nanoparticles.

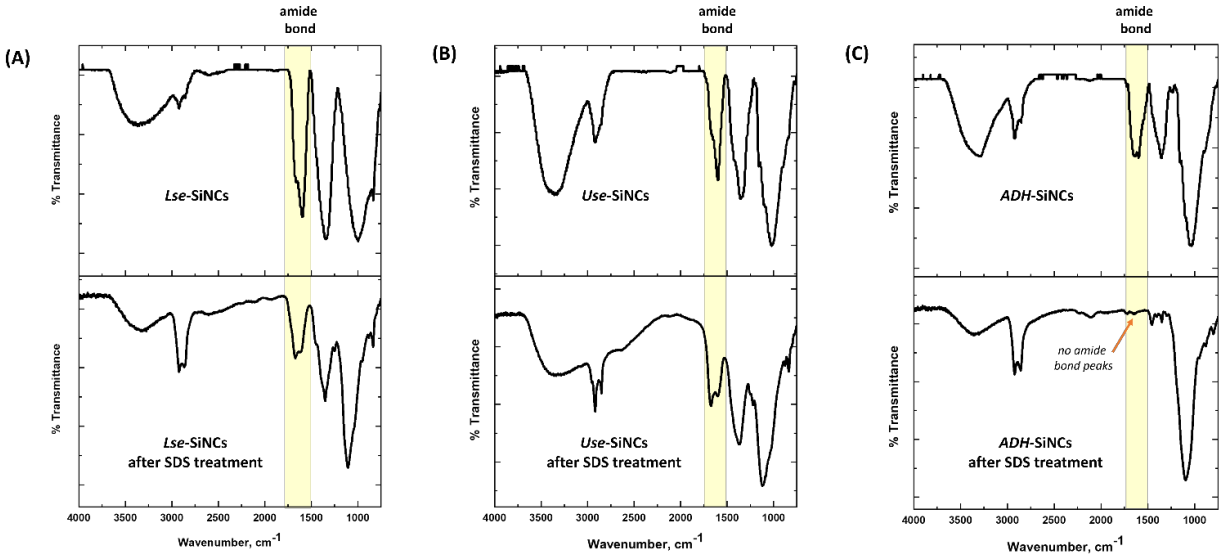

Figure 3-3. FTIR spectra of **(A)** *Lse*-SiNCs, **(B)** *Use*-SiNCs, and **(C)** *ADH*-SiNCs before (top) and after (bottom) treatment with hot SDS solution.

The covalent bioinorganic hybrids obtained from *Lse* or *Use* and *ene*-SiNCs were characterized using FTIR and XPS. As mentioned previously, successful bioconjugation of the enzymes with the *ene*-SiNCs was confirmed by the appearance of amide peaks in the 1650–1500 cm^{-1} region of the FTIR spectrum, characteristic of amide C=O stretching and N–H bending vibrations (Figures 3-4A and 3-4B).[74] The C 1s XP spectra of the *enz*-SiNCs (*Lse*-SiNCs and *Use*-SiNCs) also show peaks characteristic of the aliphatic carbon (*ca.* 284.8 eV

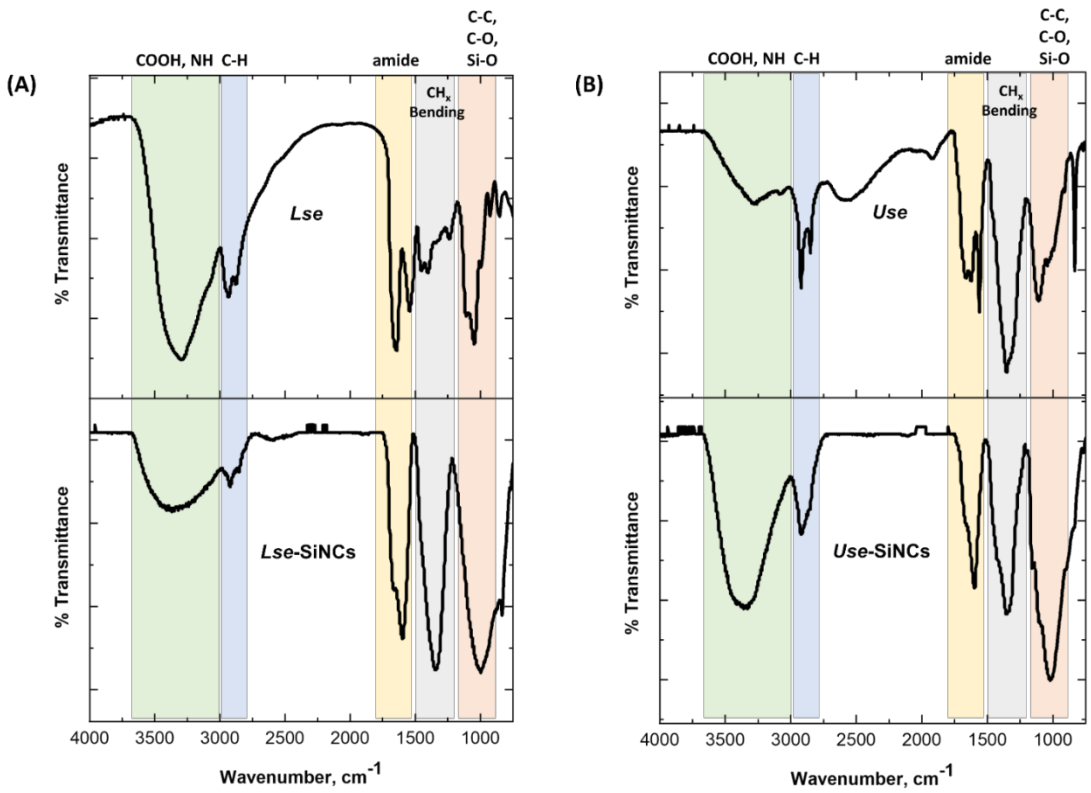

Figure 3-4. FTIR spectra of **(A)** *Lse* (top) and *Lse*-SiNCs (bottom), and **(B)** *Use* (top) and *Use*-SiNCs (bottom).

and 286.4 eV) and peptide bond (ca. 288.2 eV) framework of the enzymes (Figures 3-5A and 3-5D).[79] Furthermore, the nitrogen atoms of the enzymes, which show a peak at around 400.0 eV, also were detected in the N 1s XP spectra of the bioinorganic hybrids (Figures 3-5B and 3-5E).[42] As expected, survey XPS analysis did not detect the presence of N in the *ene*-SiNCs at the limit of detection of the XP spectrometer (Figure 3-6). We conclude that the appearance of N 1s XP emissions in the spectra of the hybrids arise as a result of the N atoms of the surface-tethered enzymes. In addition, the Si 2p XP spectra of *enz*-SiNCs (Figures 3-5C and 3-5F) show features consistent with the presence of Si(0) and silicon suboxides. Bright field transmission electron microscopy (TEM) and average shifted histogram[80] analyses of *ene*-SiNCs revealed a diameter of 4.6 ± 1.3 nm (Figure 3-7). Unfortunately, attempts to image the *enz*-SiNCs were unsuccessful and may be the result of particle-enzyme crosslinking (vide infra) and/or the presence of the enzyme. Backscattered scanning electron microscopy (BSE/SEM) imaging and energy-dispersive X-ray spectroscopy (EDX) mapping of the *enz*-SiNCs revealed aggregated silicon particles. Unfortunately, no useful size information

regarding the structure of the hybrids can be obtained at the limit of resolution of the SEM technique (Figure 3-8).

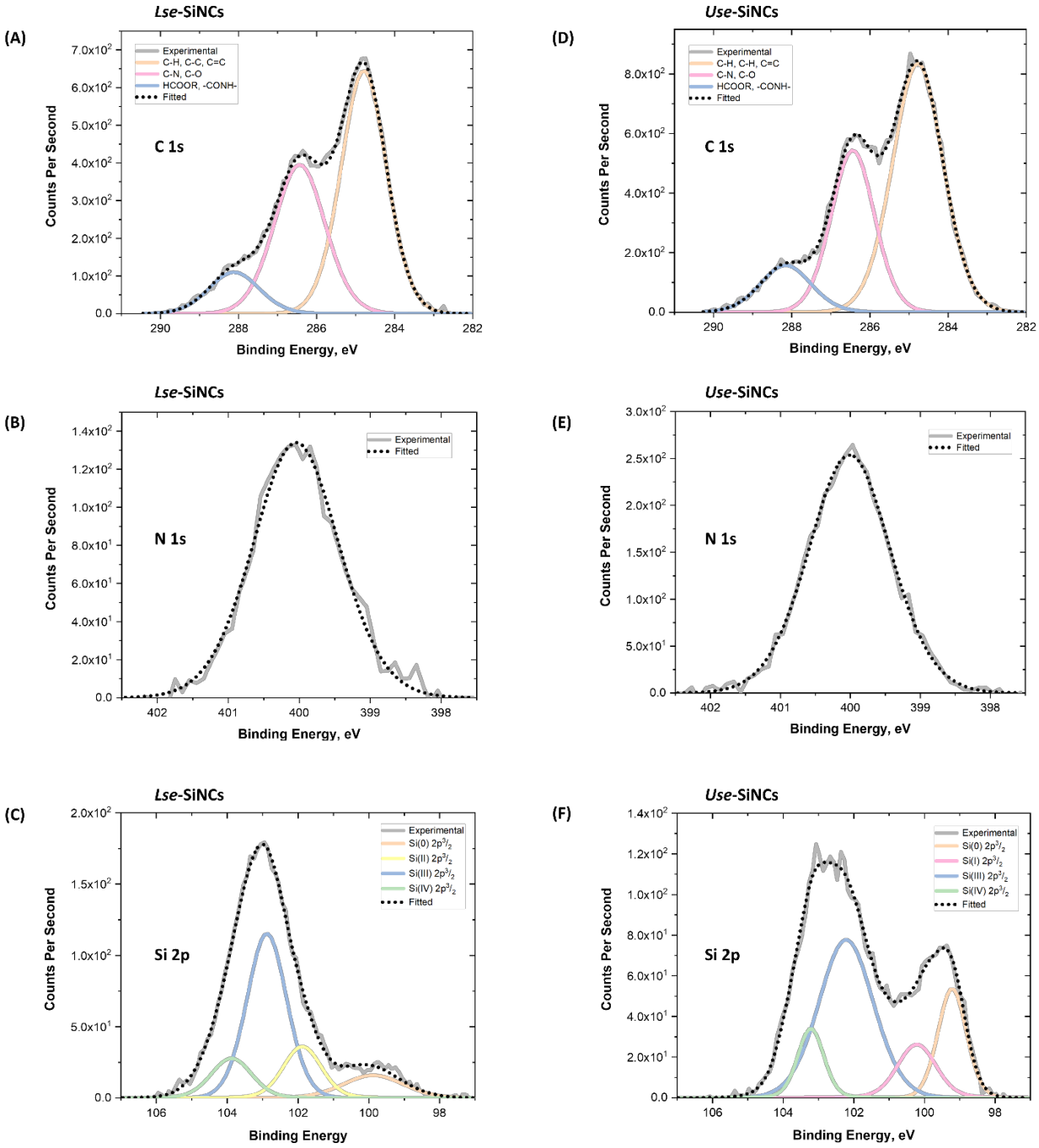

Figure 3-5. (A) C 1s, **(B)** N 1s, and **(C)** Si 2p XP spectra of *Lse*-SiNCs, and **(D)** C 1s, **(E)** N 1s, **(F)** Si 2p XP spectra of *Use*-SiNCs (Si 2p1/2 peaks were omitted for clarity).

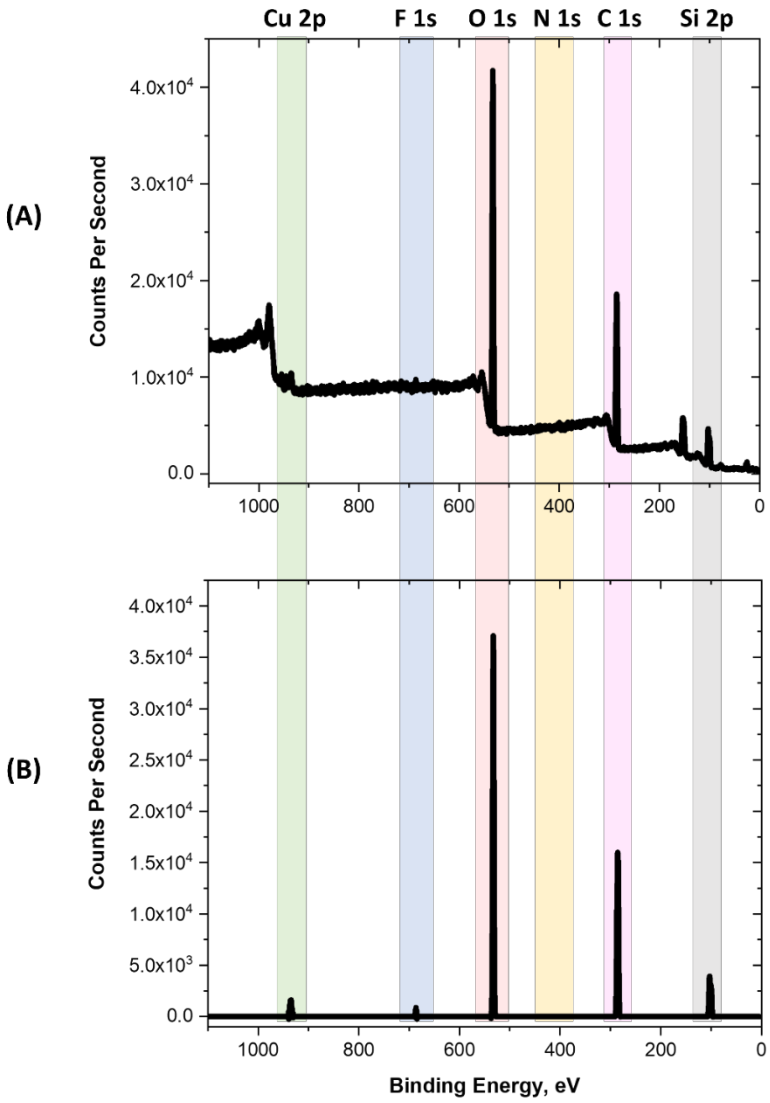

Figure 3-6. Survey XP spectra of *ene*-SiNCs **(A)** before and **(B)** after background correction. Notice that the material does not contain nitrogen (*i.e.*, absence of N 1s peak at ca. 400 eV), as expected.

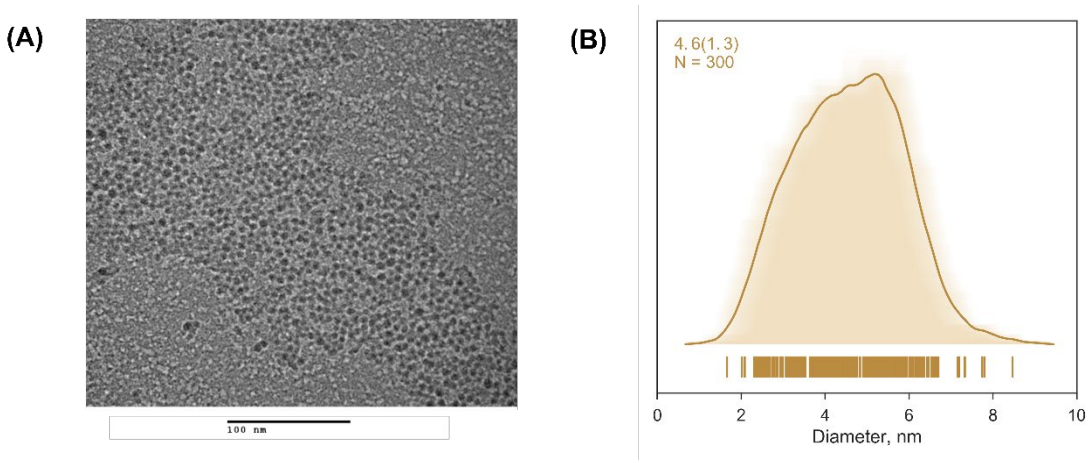

Figure 3-7. (A) Bright field TEM image of *ene*-SiNCs. **(B)** Average shifted histogram of 300 nanocrystals.

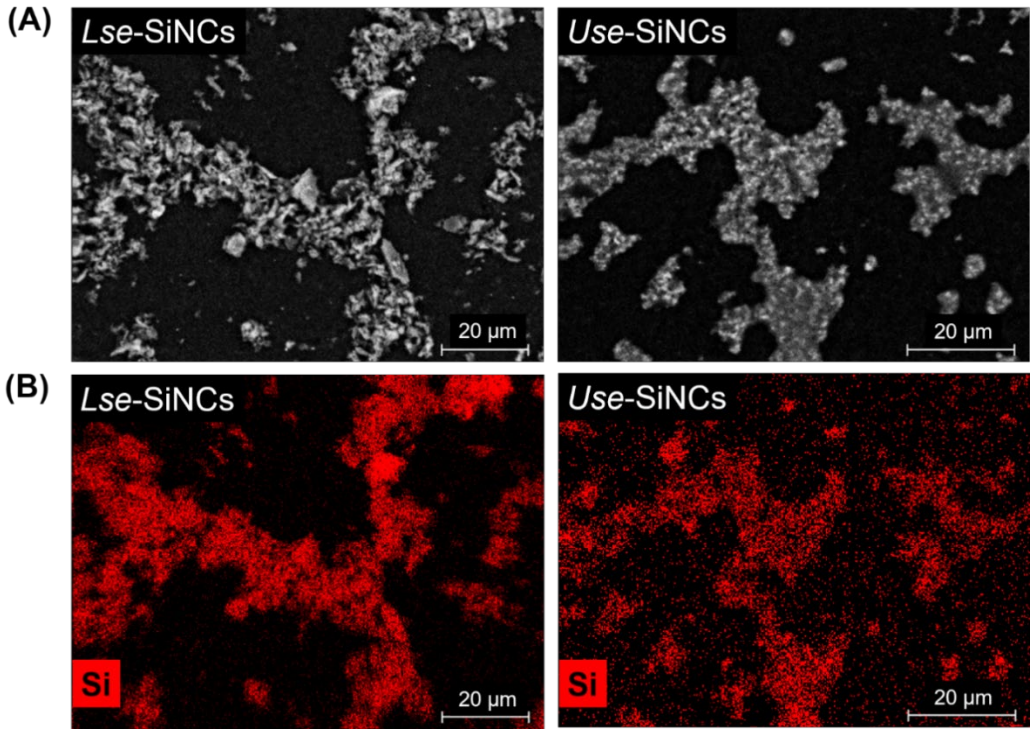

Figure 3-8. (A) BSE/SEM images and (B) EDX mapping of *Lse*-SiNCs and *Use*-SiNCs on a carbon tape. The brighter regions in the BSE/SEM images correspond to *enz*-SiNCs, as confirmed by EDX mapping.

Dynamic light scattering (DLS) analyses of *ene*-SiNCs and *enz*-SiNCs provides insight into the nature of the SiNCs in suspension. The enzyme-free *ene*-SiNCs showed a mean hydrodynamic diameter of approximately 620 nm (Figure 3-9), suggesting substantial agglomeration/aggregation. This agglomeration/aggregation may result from interactions

between the poly(ethylene oxide) and alkenyl chains on the nanocrystal surfaces, however, covalent linkages between nanocrystals via the diene are not unexpected and cannot be discounted. Despite the large particle sizes, the *ene*-SiNCs remain dispersible in water and remain suspended for up to 24 h, after which they begin to settle from suspension. Of important note, the *ene*-SiNCs are readily redispersed with mild aggitation.

DLS evaluation of *enz*-SiNCs showed aggregates having hydrodynamic sizes ranging from 80 to 140 nm (Figure 3-9). Not surprisingly, conjugation with enzymes renders *enz*-SiNCs more hydrophilic and compatible with aqueous media. The hydrodynamic dimensions of the *enz*-SiNC hybrids are larger than what is expected (i.e., 15–18 nm) for a SiNC-enzyme dimer (i.e., one nanocrystal bonded to one enzyme molecule). This estimate is based upon the knowledge that the hydrodynamic diameters of *Lse* and *Use* molecules are 12.2 ± 3.8 and 10.1 ± 2.7 nm, respectively, and that typical water-soluble SiNCs possess hydrodynamic diameters of *ca.* 5.5 nm. Considering that *Lse* and *Use* are estimated to have 43 and 36 total exposed cysteine residues per enzyme molecule,[51,75–77] respectively, and that crosslinking between polyenes and polythiols is known,[81] enzyme mediated cross-linking of *ene*-SiNCs is not unexpected.

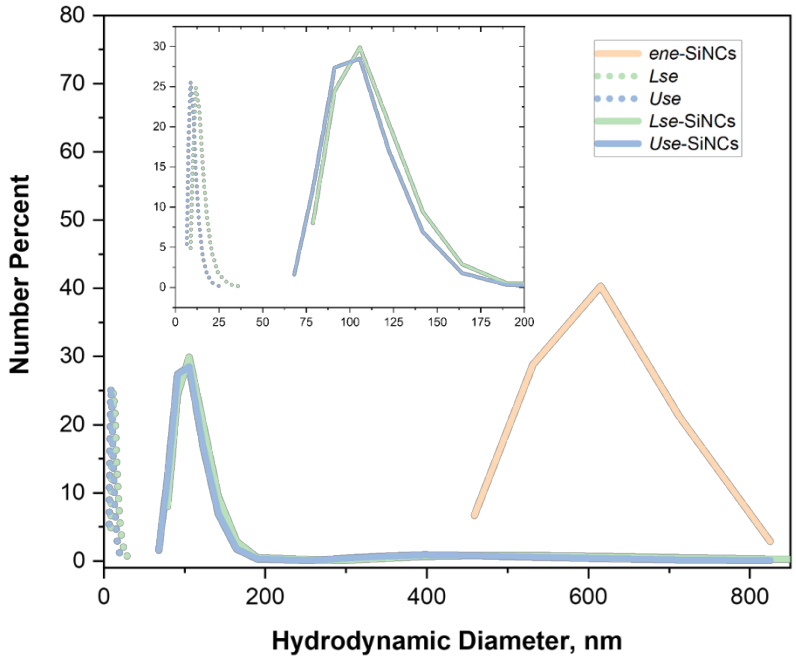

Figure 3-9. DLS size distribution analysis of *Lse*, *Use*, *ene*-SiNCs, *Lse*- SiNCs, and *Use*-SiNCs. The inset shows a magnified view of the 0–200 nm region.

Figure 3-10A and 3-10B show water-dispersible *ene*-SiNCs and *enz*-SiNCs that exhibit red PL (λ_{em} = 640 nm and 630 nm, respectively), quantum yields in the range of 39–47% (λ_{ex} = 365 nm; Table 3-1), and microsecond lifetimes (40–52 μs; Figure 3-11). Consistent with other reports, these SiNCs absorb strongly at wavelengths shorter than 400 nm (Figure 3-10C).[15,17,30,82,83] The *enz*-SiNCs obtained from the thiol–ene reaction have PL maxima that are slightly blue-shifted from that of the parent *ene*-SiNCs (ca. 10 nm) (Figure 3-10D). This spectral shift can be attributed to the influence of oxidation of the silicon nanocrystal surface upon conjugation with enzymes.[30] Oxide surface traps have been implicated in similarly blue-shifted SiNC photoluminescence.[82] The ratio of PL intensity after a given time period to the initial PL intensity at 640 nm (I/I_0) of *ene*-SiNCs and *enz*-SiNCs decreased with time upon continuous illumination with a 365-nm UV light (Figure 3-10E), consistent with the UV-induced oxidation of styrene-grafted silicon nanocrystals in toluene observed by Hua and co-workers.[84] The PL intensities of their SiNCs decreased by approximately 95% after 6 h, while that of the present systems decreased by 45–75% after the same time period. The greater resistance of our SiNCs to photobleaching is of note since the present nanocrystals were dispersed in an aqueous environment. Water molecules are known to cause decomposition of silicon.[68,85] In addition, the present bioinorganic hybrids exhibit comparable photostability to hybrids that we have prepared using the amide coupling reaction.[30] Figure 3-10F shows that the PL intensities of our SiNCs decreased by 15–70% of their original values after being dispersed in phosphate buffer for four days under ambient light and temperature conditions. Despite this loss in PL intensity, the *enz*-SiNCs remain photoluminescent in phosphate buffer even after being left to stand at room temperature and in ambient light for more than eight months. Also, both the *ene*-SiNCs and *enz*-SiNCs can be stored in a -20 °C freezer with no visibly observable change in PL intensity after one year. A similar observation was made by Dickinson et al. for a dispersion of undecyl-capped silicon nanocrystals in 1% (*v/v)* THF/phosphate buffer.[86] The relative photostability displayed by the present SiNCs in phosphate buffer, both under UV illumination and in ambient light and temperature conditions, is of note given the well-established degradation (i.e., dissolution) of silicon nanomaterials upon prolonged dispersion in aqueous environments.[68,85]

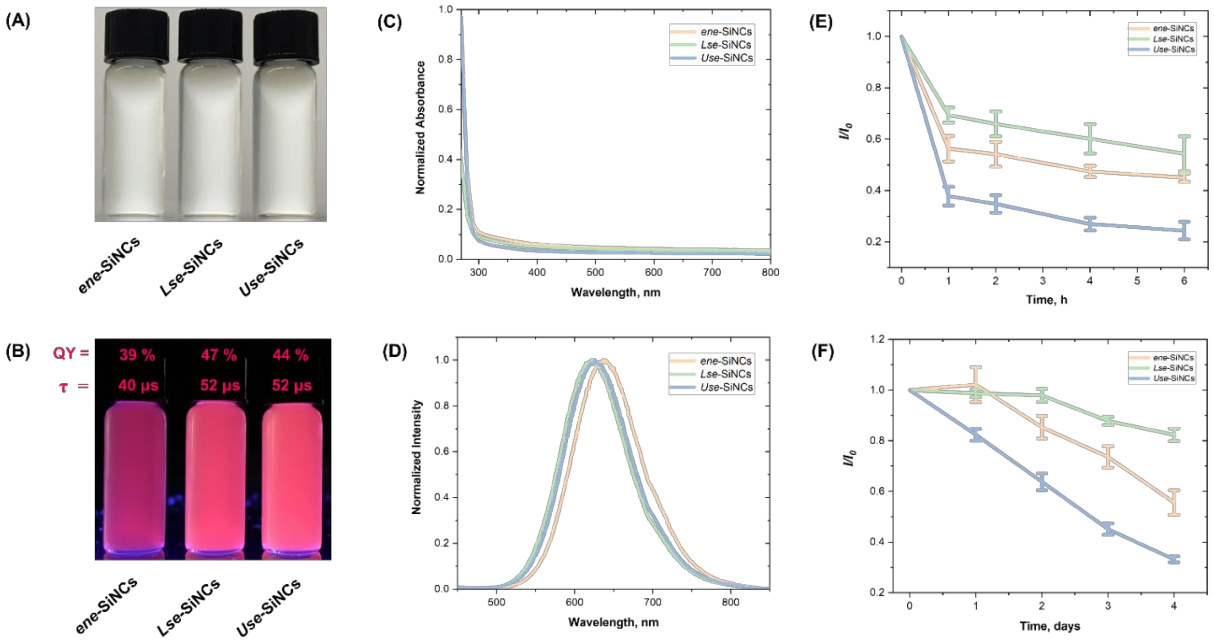

Figure 3-10. Photographs of *ene*-SiNCs, *Lse*-SiNCs, and *Use*-SiNCs in **(A)** ambient light and **(B)** under UV light (λ_{ex} = 365 nm) illumination. **(C)** Normalized UV-vis absorption and **(D)** normalized PL spectra of *ene*-SiNCs, *Lse*-SiNCs, and *Use*-SiNCs (λ_{ex} = 350 nm). Ratio of PL intensity after a given time period to the initial PL intensity at 640 nm (I/I_0) of *ene*-SiNCs, *Lse*-SiNCs, and *Use*-SiNCs as a function of time under **(E)** continuous UV light (λ_{ex} = 365 nm) illumination and **(F)** ambient light conditions.

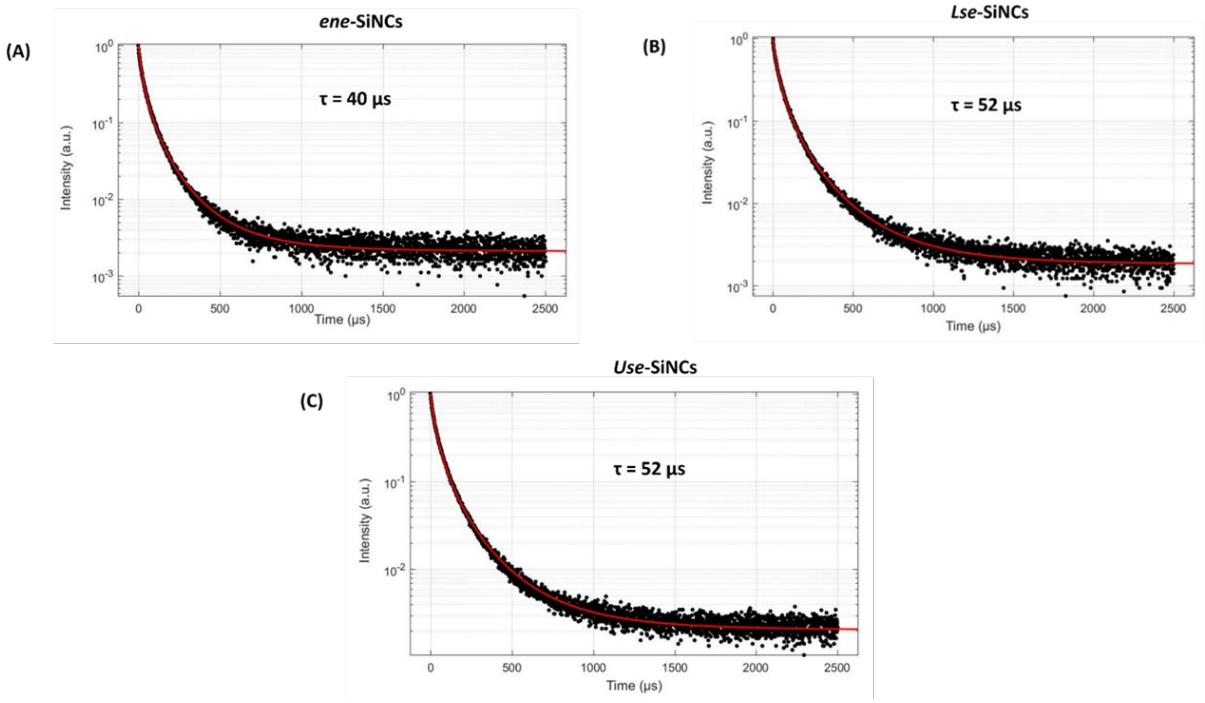

Figure 3-11. Photoluminescence decay plots of **(A)** *ene*-SiNCs, **(B)** *Lse*-SiNCs, and **(C)** *Use*-SiNCs. The lifetimes were calculated using lognormal fitting.

Table 3-1. Absolute Quantum Yields of *ene*-SiNCs, *Lse*-SiNCs, and *Use*-SiNCs (λ_{ex} = 365 nm)

Silicon Nanocrystal	Absolute Quantum Yield, %
ene-SiNC	39.1 ± 4.0
Lse-SiNC	47.1 ± 3.5
Use-SiNC	43.7 ± 1.0

Lactase is an enzyme that catalyzes the hydrolysis of lactose into galactose and glucose.[51] The catalytic activity of *Lse*-SiNCs were tested using the *o*-nitrophenyl-β-D-galactopyranoside (ONPG) assay (Figure 3-12A). In this assay, lactase hydrolyzes ONPG into galactose and nitrophenolate ion, which forms a yellow solution in water and absorbs at 420 nm.[51,52] Figures 3-12B and 3-12C illustrate that pure *Lse* and the *Lse*-SiNCs show a positive reponse (i.e., yellow colour) for the formation of the nitrophenolate ion. The enzymatic activity of the supernatant, which contains unbound *Lse*, is minimal compared to that of the *Lse*-SiNC pellet recovered during purification, consistent with most of the enzyme molecules being conjugated with the SiNCs. As expected, the phosphate buffer did not show any catalytic activity.

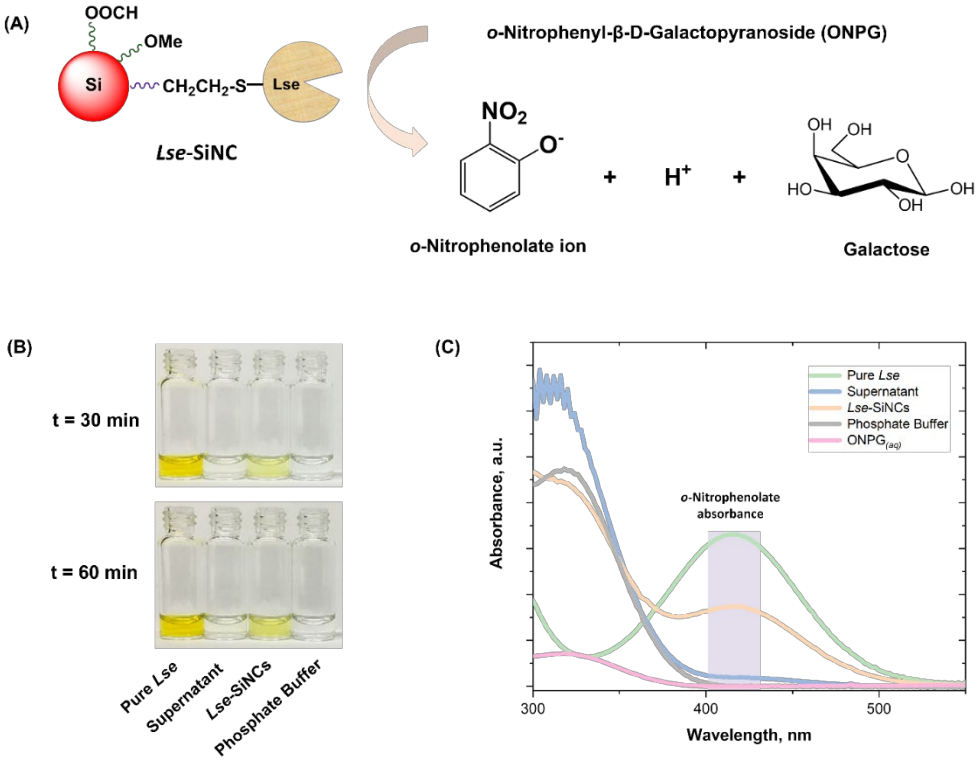

Figure 3-12. (A) *o*-Nitrophenyl-β-D-galactopyranoside (ONPG) assay for lactase activity. **(B)** Photographs and (C) absorbance spectra of vials containing the assay reagents and tested samples.

Le´tant and co-workers have reported the fabrication of a chemical sensor for *p*-nitrophenyl-β-D-galactopyranoside from porous silicon conjugated with the enzyme glucuronidase, an enzyme that shows catalytic activity similar to lactase. The *p*-nitrophenolate ion produced from the reaction is believed to quench the photoluminescence of porous silicon through a charge-transfer mechanism.[87] Based on this PL response, the same researchers have demonstrated that bulk porous silicon conjugated with organophosphorous acid anhydrolase can be used in the detection of the nerve agent surrogate *p*-nitrophenyl-soman.[88] Similarly, based upon the known response of functionalized SiNCs,[50,89] we anticipated *o*-nitrophenolate from the hydrolysis of ONPG to quench the PL of *Lse*-SiNCs. Figure 3-13A shows that the addition of ONPG to a dispersion of *Lse*-SiNCs in phosphate buffer caused its PL to disappear after 10 min. This quenching of PL is accompanied by formation of *o*-nitrophenolate ion, as suggested by both the resulting yellow dispersion and the characteristic absorption peak at 420 nm (Figures 3-13B and 3-13C).

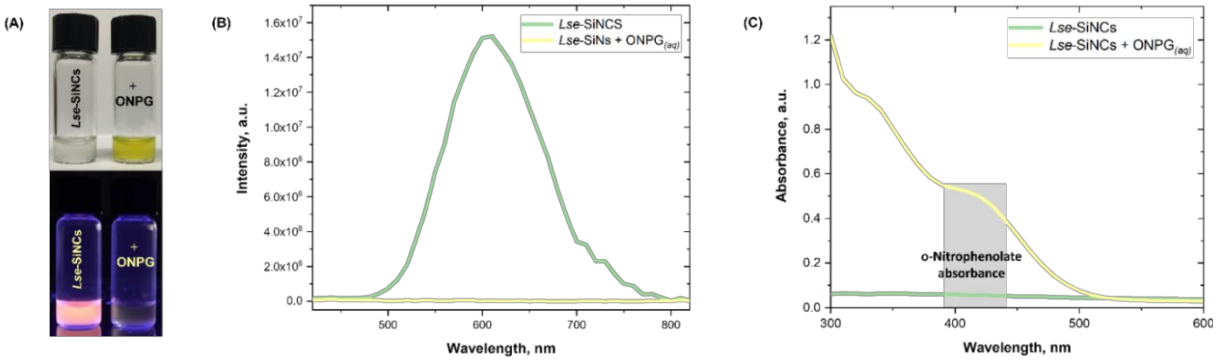

Figure 3-13. (A) Photographs of a vial containing only *Lse*-SiNCs and a vial containing *Lse*-SiNCs and 7.5 mM o-nitrophenyl-β-D-galactopyranoside (ONPG) in ambient light (top) and under UV light (λ_{ex} = 365 nm) illumination (bottom). **(B)** PL spectra of *Lse*-SiNCs in the presence and absence of 7.5 mM ONPG (λ_{ex} = 350 nm). **(C)** Absorbance spectra of Lse-SiNCs in the presence and absence of 7.5 mM ONPG.

As part of the present study, we also immobilized urease on SiNCs through the thiol–ene reaction. Urease, a Ni-containing multisubunit enzyme, catalyzes the hydrolysis of urea into ammonia and carbon dioxide.[90–92] The activity of *Use*-SiNCs was evaluated through the Berthelot assay, in which ammonia, hypochlorite, and phenol, in the presence of sodium nitroprusside as catalyst, form indophenol blue (Figure 3-14A).[53] Figure 3-14B shows that the test sample containing pure *Use* formed a blue solution, while the sample containing only phosphate buffer did not. The pellet and supernatant obtained from *Use*-SiNC purification,

containing the bioinorganic hybrids and the unconjugated *Use* molecules, respectively, also formed blue solutions. These results suggest that surface-immobilized *Use* molecules remain cataytically active upon bioconjugation. The absorbance spectra of the vials containing pure *Use*, *Use*-SiNCs, unbound *Use*, and the assay reagents showed an absorbance at 670 nm, consistent with the formation of indophenol. (Figure 3-14C).

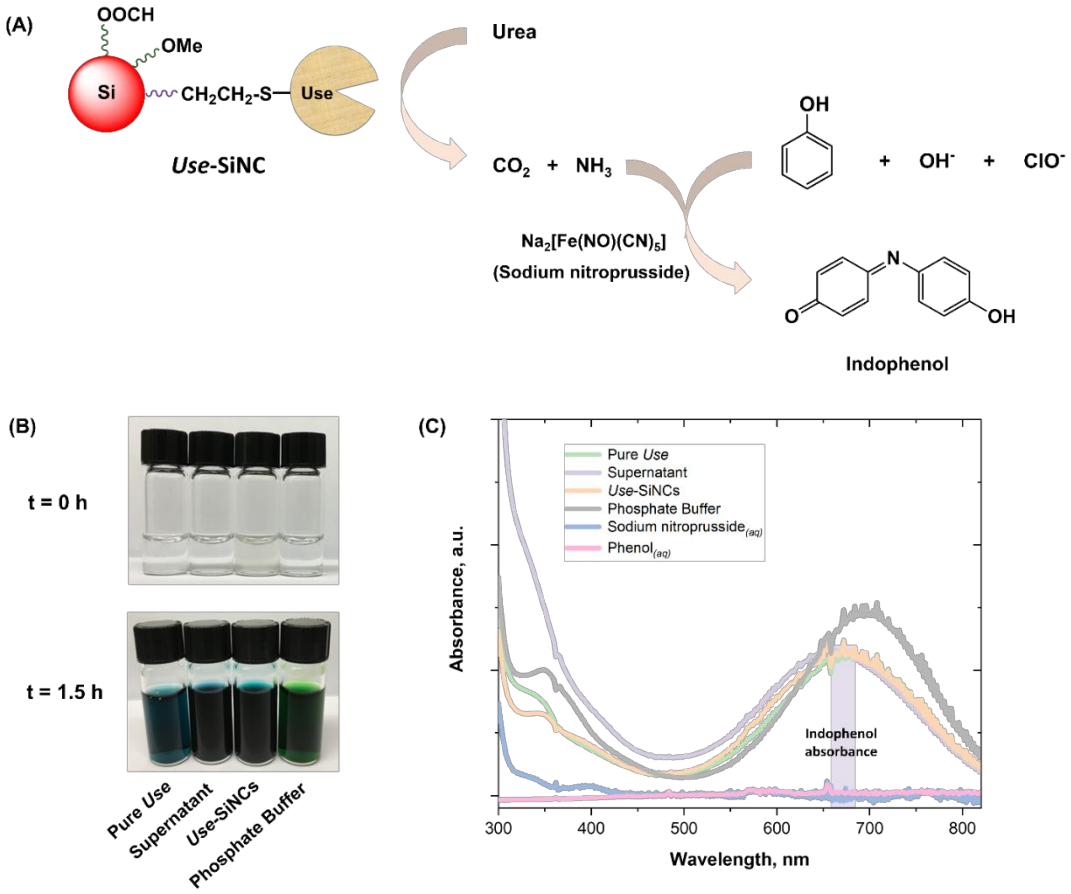

Figure 3-14. (A) Berthelot assay for urease activity. **(B)** Photographs and **(C)** absorbance spectra of vials containing the assay reagents and tested samples.

It is established that amines react with SiNCs and alter their PL properties (i.e., cause a shift in PL maximum or quench PL) through the formation of oxynitride species, the hydroxide ion-mediated silicon nanocrystal decomposition, or the dynamic quenching caused by the electron-donating nature of amines.[93–96] We envisaged then that the conjugation of urease with SiNCs could afford bioconjugate hybrids that can be used in detecting urea since ammonia, its hydrolysis product, potentially can quench SiNC PL. We have added an aqueous

solution of urea to a dispersion of Use-SiNCs in phosphate buffer and have indeed observed quenching of SiNC PL. Figure 3-15A shows two vials, one with urea and the other without, under UV illumination at different times after the addition of urea. A visually observable decrease in PL intensity can be seen after around 2.5 h. Figure 3-15B, however, shows that a significant drop (i.e., 30%) in PL intensity is realized immediately after addition of urea. This observation is consistent with the hydrolysis of urea into carbon dioxide and ammonia. It also suggests that the reaction between the SiNCs and ammonia (and/or hydroxide ions) occurs rapidly. Urea is the principal nitrogen-containing waste product of metabolism and is crucial for the diagnosis of a number of disorders (e.g., kidney failure, liver malfunction).[97] The present PL quenching observations with *Use*-SiNCs suggest that they could provide a convenient platform for urea quantification.

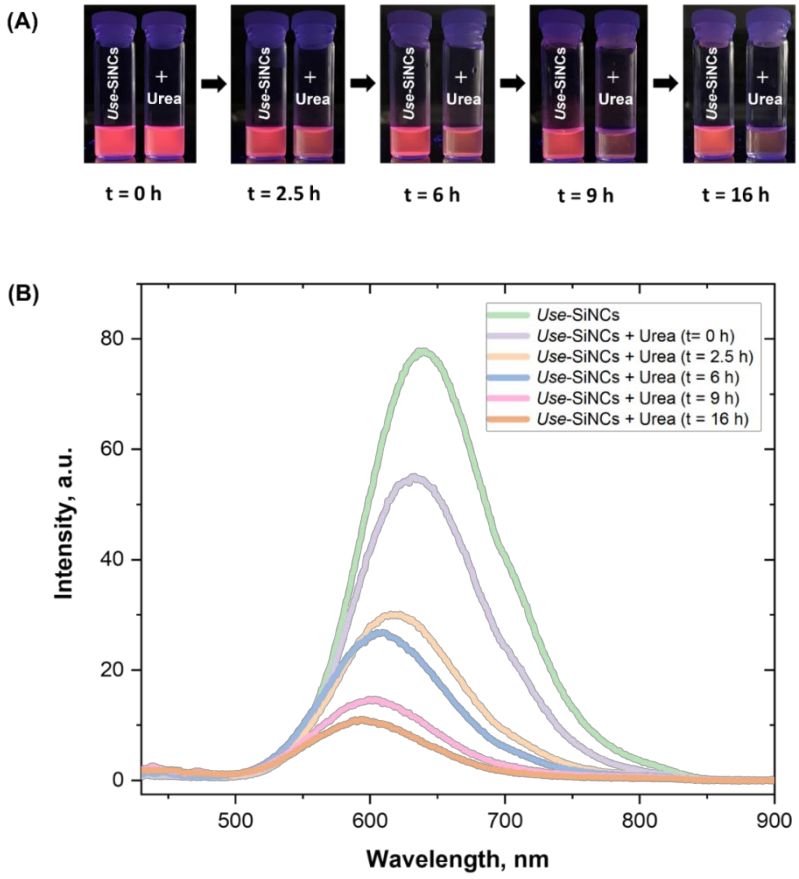

Figure 3-15. (A) Photographs of a vial containing only *Use*-SiNCs and a vial containing *Use*-SiNCs and 1.7 M urea under UV light (λ_{ex} = 365 nm) illumination at varying times after the addition of urea. **(B)** PL spectra of *Use*-SiNCs at varying times in the presence of 1.7 M urea (λ_{ex} = 350 nm).

3.4 Summary and Conclusions

We have prepared functional bioinorganic hybrids exhibiting long-lived red-photoluminescence and catalytic activity from freestanding silicon nanocrystals and enzymes through the thiol–ene 'click' reaction. Characterization of the hybrids through FTIR, XPS, TEM, DLS, steady-state and time-resolved PL spectroscopy, and pertinent enzymatic assays, confirmed the presence of groups characteristic of both silicon nanocrystals and enzymes. The hybrids prepared were dispersible and stable in water and phosphate buffer. We also have shown the potential use of these materials for the chemical detection *o*-nitrophenyl-β-D-galactopyranoside and urea. Lastly, aside from chemical detection, the bioinorganic hybrids synthesized here potentially offer an attractive platform for the simultaneous imaging and treatment of diseased tissues by taking advantage of the long-lived photoluminescence of silicon nanocrystals (i.e., time-gated imaging) and the substrate-specific activity of therapeutic enzymes.

3.5 References

(1) Kairdolf, B. A.; Smith, A. M.; Stokes, T. H.; Wang, M. D.; Young, A. N.; Nie, S. Semiconductor Quantum Dots for Bioimaging and Biodiagnostic Applications. *Annu. Rev. Anal. Chem.* **2013**, *6*, 143–162.

(2) Zrazhevskiy, P.; Sena, M.; Gao, X. Designing Multifunctional Quantum Dots for Bioimaging, Detection, and Drug Delivery. *Chem. Soc. Rev.* **2010**, *39* (11), 4326–4354.

(3) Michalet, X.; Pinaud, F. F.; Bentolila, L. A.; Tsay, J. M.; Doose, S.; Li, J. J.; Sundaresan, G.; Wu, A. M.; Gambhir, S. S.; Weiss, S. Quantum Dots for Live Cells, in Vivo Imaging, and Diagnostics. *Science* **2005**, *307* (5709), 538–544.

(4) Freeman, R.; Willner, I. Optical Molecular Sensing with Semiconductor Quantum Dots (QDs). *Chem. Soc. Rev.* **2012**, *41* (10), 4067–4085.

(5) Medintz, I. L.; Uyeda, H. T.; Goldman, E. R.; Mattoussi, H. Quantum Dot Bioconjugates for Imaging, Labelling and Sensing. *Nat. Mater.* **2005**, *4* (6), 435.

(6) Resch-Genger, U.; Grabolle, M.; Cavaliere-Jaricot, S.; Nitschke, R.; Nann, T. Quantum Dots versus Organic Dyes as Fluorescent Labels. *Nat. Methods* **2008**, *5* (9), 763.

(7) Derfus, A. M.; Chan, W. C.; Bhatia, S. N. Probing the Cytotoxicity of Semiconductor Quantum Dots. *Nano Lett.* **2004**, *4* (1), 11–18.

(8) Dabbousi, B. O.; Rodriguez-Viejo, J.; Mikulec, F. V.; Heine, J. R.; Mattoussi, H.; Ober, R.; Jensen, K. F.; Bawendi, M. G. (CdSe) ZnS Core- Shell Quantum Dots: Synthesis and Characterization of a Size Series of Highly Luminescent Nanocrystallites. *J. Phys. Chem. B* **1997**, *101* (46), 9463–9475.

(9) Gerion, D.; Pinaud, F.; Williams, S. C.; Parak, W. J.; Zanchet, D.; Weiss, S.; Alivisatos, A. P. Synthesis and Properties of Biocompatible Water-Soluble Silica-Coated CdSe/ZnS Semiconductor Quantum Dots. *J. Phys. Chem. B* **2001**, *105* (37), 8861–8871.

(10) Selvan, S. T.; Tan, T. T.; Ying, J. Y. Robust, Non-Cytotoxic, Silica-Coated CdSe Quantum Dots with Efficient Photoluminescence. *Adv. Mater.* **2005**, *17* (13), 1620–1625.

(11) Yong, K.-T.; Law, W.-C.; Hu, R.; Ye, L.; Liu, L.; Swihart, M. T.; Prasad, P. N. Nanotoxicity Assessment of Quantum Dots: From Cellular to Primate Studies. *Chem. Soc. Rev.* **2013**, *42* (3), 1236–1250.

(12) Tsoi, K. M.; Dai, Q.; Alman, B. A.; Chan, W. C. Are Quantum Dots Toxic? Exploring the Discrepancy between Cell Culture and Animal Studies. *Acc. Chem. Res.* **2012**, *46* (3), 662–671.

(13) Liu, J.; Erogbogbo, F.; Yong, K.-T.; Ye, L.; Liu, J.; Hu, R.; Chen, H.; Hu, Y.; Yang, Y.; Yang, J.; Roy, I.; Karker, N. A.; Swihart, M. T.; Prasad, P. N. Assessing Clinical Prospects of Silicon Quantum Dots: Studies in Mice and Monkeys. *ACS Nano* **2013**, *7* (8), 7303–7310.

(14) McVey, B. F.; Tilley, R. D. Solution Synthesis, Optical Properties, and Bioimaging Applications of Silicon Nanocrystals. *Acc. Chem. Res.* **2014**, *47* (10), 3045–3051.

(15) , J. H.; Hoshino, A.; Yamamoto, K.; Tilley, R. Water-Soluble Photoluminescent Silicon Quantum Dots. *Angew. Chem.* **2005**, *117* (29), 4626–4630.

(16) Fujioka, K.; Hiruoka, M.; Sato, K.; Manabe, N.; Miyasaka, R.; Hanada, S.; Hoshino, A.; Tilley, R. D.; Manome, Y.; Hirakuri, K. Luminescent Passive-Oxidized Silicon Quantum Dots as Biological Staining Labels and Their Cytotoxicity Effects at High Concentration. *Nanotechnology* **2008**, *19* (41), 415102.

(17) Erogbogbo, F.; Yong, K.-T.; Roy, I.; Xu, G.; Prasad, P. N.; Swihart, M. T. Biocompatible Luminescent Silicon Quantum Dots for Imaging of Cancer Cells. *ACS Nano* **2008**, *2* (5), 873–878.

(18) Osminkina, L. A.; Tamarov, K. P.; Sviridov, A. P.; Galkin, R. A.; Gongalsky, M. B.; Solovyev, V. V.; Kudryavtsev, A. A.; Timoshenko, V. Y. Photoluminescent Biocompatible Silicon Nanoparticles for Cancer Theranostic Applications. *J. Biophotonics* **2012**, *5* (7), 529–535.

(19) Li, Z. F.; Ruckenstein, E. Water-Soluble Poly (Acrylic Acid) Grafted Luminescent Silicon Nanoparticles and Their Use as Fluorescent Biological Staining Labels. *Nano Lett.* **2004**, *4* (8), 1463–1467.

(20) Zhai, Y.; Dasog, M.; Snitynsky, R. B.; Purkait, T. K.; Aghajamali, M.; Hahn, A. H.; Sturdy, C. B.; Lowary, T. L.; Veinot, J. G. Water-Soluble Photoluminescent D-Mannose and L-Alanine Functionalized Silicon Nanocrystals and Their Application to Cancer Cell Imaging. *J. Mater. Chem. B* **2014**, *2* (47), 8427–8433.

(21) Wu, S.; Zhong, Y.; Zhou, Y.; Song, B.; Chu, B.; Ji, X.; Wu, Y.; Su, Y.; He, Y. Biomimetic Preparation and Dual-Color Bioimaging of Fluorescent Silicon Nanoparticles. *J. Am. Chem. Soc.* **2015**, *137* (46), 14726–14732.

(22) Henderson, E. J.; Shuhendler, A. J.; Prasad, P.; Baumann, V.; Maier-Flaig, F.; Faulkner, D. O.; Lemmer, U.; Wu, X. Y.; Ozin, G. A. Colloidally Stable Silicon Nanocrystals with Near-Infrared Photoluminescence for Biological Fluorescence Imaging. *Small* **2011**, *7* (17), 2507–2516.

(23) Hessel, C. M.; Rasch, M. R.; Hueso, J. L.; Goodfellow, B. W.; Akhavan, V. A.; Puvanakrishnan, P.; Tunnel, J. W.; Korgel, B. A. Alkyl Passivation and Amphiphilic Polymer Coating of Silicon Nanocrystals for Diagnostic Imaging. *Small* **2010**, *6* (18), 2026–2034.

(24) Gonzalez, C. M.; Veinot, J. G. Silicon Nanocrystals for the Development of Sensing Platforms. *J. Mater. Chem. C* **2016**, *4* (22), 4836–4846.

(25) Lin, J.; Wang, Q. Role of Novel Silicon Nanoparticles in Luminescence Detection of a Family of Antibiotics. *RSC Adv.* **2015**, *5* (35), 27458–27463.

(26) Zhang, X.; Chen, X.; Kai, S.; Wang, H.-Y.; Yang, J.; Wu, F.-G.; Chen, Z. Highly Sensitive and Selective Detection of Dopamine Using One-Pot Synthesized Highly Photoluminescent Silicon Nanoparticles. *Anal. Chem.* **2015**, *87* (6), 3360–3365.

(27) Ruizendaal, L.; Pujari, S. P.; Gevaerts, V.; Paulusse, J. M.; Zuilhof, H. Biofunctional Silicon Nanoparticles by Means of Thiol–Ene Click Chemistry. *Chem. Asian J.* **2011**, *6* (10), 2776–2786.

(28) Wang, L.; Reipa, V.; Blasic, J. Silicon Nanoparticles as a Luminescent Label to DNA. *Bioconjugate Chem.* **2004**, *15* (2), 409–412.

(29) Choi, J.; Wang, N. S.; Reipa, V. Conjugation of the Photoluminescent Silicon Nanoparticles to Streptavidin. *Bioconjugate Chem.* **2008**, *19* (3), 680–685.

(30) Robidillo, C. J. T.; Islam, M. A.; Aghajamali, M.; Faramus, A.; Sinelnikov, R.; Zhang, X.; Boekhoven, J.; Veinot, J. G. C. Functional Bioinorganic Hybrids from Enzymes and Luminescent Silicon-Based Nanoparticles. *Langmuir* **2018**, *34* (22), 6556–6569.

(31) Totaro, K. A.; Liao, X.; Bhattacharya, K.; Finneman, J. I.; Sperry, J. B.; Massa, M. A.; Thorn, J.; Ho, S. V.; Pentelute, B. L. Systematic Investigation of EDC/SNHS-Mediated Bioconjugation Reactions for Carboxylated Peptide Substrates. *Bioconjugate Chem.* **2016**, *27* (4), 994–1004.

(32) Davis, M.-T. B.; Preston, J. F. A Simple Modified Carbodiimide Method for Conjugation of Small-Molecular-Weight Compounds to Immunoglobulin G with Minimal Protein Crosslinking. *Anal. Biochem.* **1981**, *116* (2), 402–407.

(33) Dondoni, A. The Emergence of Thiol–Ene Coupling as a Click Process for Materials and Bioorganic Chemistry. *Angew. Chem., Int. Ed.* **2008**, *47* (47), 8995–8997.

(34) Bertin, A.; Schlaad, H. Mild and Versatile (Bio-) Functionalization of Glass Surfaces via Thiol–Ene Photochemistry. *Chem. Mater.* **2009**, *21* (24), 5698–5700.

(35) Demay-Drouhard, P.; Nehlig, E.; Hardouin, J.; Motte, L.; Guénin, E. Nanoparticles under the Light: Click Functionalization by Photochemical Thiol–Yne Reaction, Towards Double Click Functionalization. *Chem.- Eur. J.* **2013**, *19* (26), 8388–8392.

(36) Huang, H.; Liu, M.; Tuo, X.; Chen, J.; Mao, L.; Wen, Y.; Tian, J.; Zhou, N.; Zhang, X.; Wei, Y. One-Step Fabrication of PEGylated Fluorescent Nanodiamonds through the Thiol–Ene Click Reaction and Their Potential for Biological Imaging. *Appl. Surf. Sci.* **2018**, *439*, 1143–1151.

(37) Gu, W.; Chen, G.; Stenzel, M. H. Synthesis of Glyco-Microspheres via a Thiol–Ene Coupling Reaction. *J. Polym. Sci. Part Polym. Chem.* **2009**, *47* (20), 5550–5556.

(38) Jones, M. W.; Gibson, M. I.; Mantovani, G.; Haddleton, D. M. Tunable Thermo-Responsive Polymer–Protein Conjugates via a Combination of Nucleophilic Thiol–Ene "Click" and SET-LRP. *Polym. Chem.* **2011**, *2* (3), 572–574.

(39) Bhairamadgi, N. S.; Gangarapu, S.; Caipa Campos, M. A.; Paulusse, J. M.; van Rijn, C. J.; Zuilhof, H. Efficient Functionalization of Oxide-Free Silicon (111) Surfaces: Thiol–Yne versus Thiol–Ene Click Chemistry. *Langmuir* **2013**, *29* (14), 4535–4542.

(40) Campos, M. A. C.; Paulusse, J. M.; Zuilhof, H. Functional Monolayers on Oxide-Free Silicon Surfaces via Thiol–Ene Click Chemistry. *Chem. Commun.* **2010**, *46* (30), 5512–5514.

(41) Jeong, G. M.; Seong, H.; Kim, Y. S.; Im, S. G.; Jeong, K. J. Site-Specific Immobilization of Proteins on Non-Conventional Substrates via Solvent-Free Initiated Chemical Vapour Deposition (ICVD) Process. *Polym. Chem.* **2014**, *5* (15), 4459–4465.

(42) Buhl, M.; Vonhören, B.; Ravoo, B. J. Immobilization of Enzymes via Microcontact Printing and Thiol–Ene Click Chemistry. *Bioconjugate. Chem.* **2015**, *26* (6), 1017–1020.

(43) Weinrich, D.; Lin, P.-C.; Jonkheijm, P.; Nguyen, U. T.; Schröder, H.; Niemeyer, C. M.; Alexandrov, K.; Goody, R.; Waldmann, H. Oriented Immobilization of Farnesylated Proteins by the Thiol–Ene Reaction. *Angew. Chem., Int. Ed.* **2010**, *49* (7), 1252–1257.

(44) Escorihuela, J.; Bañuls, M.-J.; Grijalvo, S.; Eritja, R.; Puchades, R.; Maquieira, Á. Direct Covalent Attachment of DNA Microarrays by Rapid Thiol–Ene "Click" Chemistry. *Bioconjugate Chem.* **2014**, *25* (3), 618–627.

(45) Cheng, X.; Gondosiswanto, R.; Ciampi, S.; Reece, P. J.; Gooding, J. J. One-Pot Synthesis of Colloidal Silicon Quantum Dots and Surface Functionalization via Thiol–Ene Click Chemistry. *Chem. Commun.* **2012**, *48* (97), 11874–11876.

(46) Su, X.; Kuang, L.; Battle, C.; Shaner, T.; Mitchell, B. S.; Fink, M. J.; Jayawickramarajah, J. Mild Two-Step Method to Construct DNA-Conjugated Silicon Nanoparticles: Scaffolds for the Detection of MicroRNA-21. *Bioconjugate Chem.* **2014**, *25* (10), 1739–1743.

(47) Hessel, C. M.; Henderson, E. J.; Veinot, J. G. Hydrogen Silsesquioxane: A Molecular Precursor for Nanocrystalline Si–SiO_2 Composites and Freestanding Hydride-Surface-Terminated Silicon Nanoparticles. *Chem. Mater.* **2006**, *18* (26), 6139–6146.

(48) Clark, R. J.; Aghajamali, M.; Gonzalez, C. M.; Hadidi, L.; Islam, M. A.; Javadi, M.; Mobarok, M. H.; Purkait, T. K.; Robidillo, C. J. T.; Sinelnikov, R. From Hydrogen Silsesquioxane to Functionalized Silicon Nanocrystals. *Chem. Mater.* **2016**, *29* (1), 80–89.

(49) Van Driel, A. F.; Nikolaev, I. S.; Vergeer, P.; Lodahl, P.; Vanmaekelbergh, D.; Vos, W. L. Statistical Analysis of Time-Resolved Emission from Ensembles of Semiconductor Quantum Dots: Interpretation of Exponential Decay Models. *Phys. Rev. B* **2007**, *75* (3), 035329.

(50) Nguyen, A.; Gonzalez, C. M.; Sinelnikov, R.; Newman, W.; Sun, S.; Lockwood, R.; Veinot, J. G.; Meldrum, A. Detection of Nitroaromatics in the Solid, Solution, and Vapor Phases Using Silicon Quantum Dot Sensors. *Nanotechnology* **2016**, *27* (10), 105501.

(51) Craven, G. R.; Steers, E.; Anfinsen, C. B. Purification, Composition, and Molecular Weight of the β-Galactosidase of Escherichia Coli K12. *J. Biol. Chem.* **1965**, *240* (6), 2468–2477.

(52) Kilian, M.; Bülo, P. Rapid Diagnosis of Enterobacteriaceae. *APMIS* **1976**, *84* (5), 245–251.

(53) Patton, C. J.; Crouch, S. R. Spectrophotometric and Kinetics Investigation of the Berthelot Reaction for the Determination of Ammonia. *Anal. Chem.* **1977**, *49* (3), 464–469.

(54) Dondoni, A.; Massi, A.; Nanni, P.; Roda, A. A New Ligation Strategy for Peptide and Protein Glycosylation: Photoinduced Thiol–Ene Coupling. *Chem.- Eur. J.* **2009**, *15* (43), 11444–11449.

(55) Valkevich, E. M.; Guenette, R. G.; Sanchez, N. A.; Chen, Y.; Ge, Y.; Strieter, E. R. Forging Isopeptide Bonds Using Thiol–Ene Chemistry: Site-Specific Coupling of Ubiquitin Molecules for Studying the Activity of Isopeptidases. *J. Am. Chem. Soc.* **2012**, *134* (16), 6916–6919.

(56) Hessel, C. M.; Henderson, E. J.; Veinot, J. G. An Investigation of the Formation and Growth of Oxide-Embedded Silicon Nanocrystals in Hydrogen Silsesquioxane-Derived Nanocomposites. *J. Phys. Chem. C* **2007**, *111* (19), 6956–6961.

(57) Otsuka, H.; Nagasaki, Y.; Kataoka, K. PEGylated Nanoparticles for Biological and Pharmaceutical Applications. *Adv. Drug Deliv. Rev.* **2012**, *64*, 246–255.

(58) Pelaz, B.; del Pino, P.; Maffre, P.; Hartmann, R.; Gallego, M.; Rivera-Fernandez, S.; de la Fuente, J. M.; Nienhaus, G. U.; Parak, W. J. Surface Functionalization of Nanoparticles with Polyethylene Glycol: Effects on Protein Adsorption and Cellular Uptake. *Acs Nano* **2015**, *9* (7), 6996–7008.

(59) Dai, Q.; Walkey, C.; Chan, W. C. Polyethylene Glycol Backfilling Mitigates the Negative Impact of the Protein Corona on Nanoparticle Cell Targeting. *Angew. Chem., Int. Ed.* **2014**, *53* (20), 5093–5096.

(60) Wörz, A.; Berchtold, B.; Moosmann, K.; Prucker, O.; Rühe, J. Protein-Resistant Polymer Surfaces. *J. Mater. Chem.* **2012**, *22* (37), 19547–19561.

(61) Mobarok, M. H.; Purkait, T. K.; Islam, M. A.; Miskolzie, M.; Veinot, J. G. Instantaneous Functionalization of Chemically Etched Silicon Nanocrystal Surfaces. *Angew. Chem.* **2017**, *129* (22), 6169–6173.

(62) Yang, Z.; Gonzalez, C. M.; Purkait, T. K.; Iqbal, M.; Meldrum, A.; Veinot, J. G. Radical Initiated Hydrosilylation on Silicon Nanocrystal Surfaces: An Evaluation of Functional Group Tolerance and Mechanistic Study. *Langmuir* **2015**, *31* (38), 10540–10548.

(63) Matsuura, H.; Miyazawa, T. Vibrational Analysis of Molten Poly (Ethylene Glycol). *J. Polym. Sci. Part B Polym. Phys.* **1969**, *7* (10), 1735–1744.

(64) Yang, L.; Heatley, F.; Blease, T. G.; Thompson, R. I. A Study of the Mechanism of the Oxidative Thermal Degradation of Poly (Ethylene Oxide) and Poly (Propylene Oxide) Using 1H-and 13C-NMR. *Eur. Polym. J.* **1996**, *32* (5), 535–547.

(65) Mkhatresh, O. A.; Heatley, F. A Study of the Products and Mechanism of the Thermal Oxidative Degradation of Poly (Ethylene Oxide) Using 1H and 13C 1-D and 2-D NMR. *Polym. Int.* **2004**, *53* (9), 1336–1342.

(66) Huang, Y.-L.; Tien, H.-W.; Ma, C.-C. M.; Yang, S.-Y.; Wu, S.-Y.; Liu, H.-Y.; Mai, Y.-W. Effect of Extended Polymer Chains on Properties of Transparent Graphene Nanosheets Conductive Film. *J. Mater. Chem.* **2011**, *21* (45), 18236–18241.

(67) Clark, R. J.; Dang, M. K.; Veinot, J. G. Exploration of Organic Acid Chain Length on Water-Soluble Silicon Quantum Dot Surfaces. *Langmuir* **2010**, *26* (19), 15657–15664.

(68) Doremus, R. H. Oxidation of Silicon by Water and Oxygen and Diffusion in Fused Silica. *J. Phys. Chem.* **1976**, *80* (16), 1773–1775.

(69) Amenitsch, H.; Caracciolo, G.; Foglia, P.; Fuscoletti, V.; Giansanti, P.; Marianecci, C.; Pozzi, D.; Laganà, A. Existence of Hybrid Structures in Cationic Liposome/DNA Complexes Revealed by Their Interaction with Plasma Proteins. *Colloids Surf. B Biointerfaces* **2011**, *82* (1), 141–146.

(70) Lundqvist, M.; Stigler, J.; Cedervall, T.; Berggård, T.; Flanagan, M. B.; Lynch, I.; Elia, G.; Dawson, K. The Evolution of the Protein Corona around Nanoparticles: A Test Study. *ACS Nano* **2011**, *5* (9), 7503–7509.

(71) Venerando, R.; Miotto, G.; Magro, M.; Dallan, M.; Baratella, D.; Bonaiuto, E.; Zboril, R.; Vianello, F. Magnetic Nanoparticles with Covalently Bound Self-Assembled Protein Corona for Advanced Biomedical Applications. *J. Phys. Chem. C* **2013**, *117* (39), 20320–20331.

(72) Reynolds, J. A.; Tanford, C. Binding of Dodecyl Sulfate to Proteins at High Binding Ratios. Possible Implications for the State of Proteins in Biological Membranes. *Proc. Natl. Acad. Sci.* **1970**, *66* (3), 1002–1007.

(73) Dill, K. A. Dominant Forces in Protein Folding. *Biochemistry* **1990**, *29* (31), 7133–7155.

(74) Tamm, L. K.; Tatulian, S. A. Infrared Spectroscopy of Proteins and Peptides in Lipid Bilayers. *Q. Rev. Biophys.* **1997**, *30* (4), 365–429.

(75) Takishima, K.; Suga, T.; Mamiya, G. The Structure of Jack Bean Urease. *FEBS J.* **1988**, *175* (1), 151–157.

(76) Krajewska, B.; Zaborska, W.; Chudy, M. Multi-Step Analysis of Hg2+ Ion Inhibition of Jack Bean Urease. *J. Inorg. Biochem.* **2004**, *98* (6), 1160–1168.

(77) Krajewska, B.; Zaborska, W. Jack Bean Urease: The Effect of Active-Site Binding Inhibitors on the Reactivity of Enzyme Thiol Groups. *Bioorganic Chem.* **2007**, *35* (5), 355–365.

(78) Magonet, E.; Hayen, P.; Delforge, D.; Delaive, E.; Remacle, J. Importance of the Structural Zinc Atom for the Stability of Yeast Alcohol Dehydrogenase. *Biochem. J.* **1992**, *287* (2), 361–365.

(79) Ray, S.; Shard, A. G. Quantitative Analysis of Adsorbed Proteins by X-Ray Photoelectron Spectroscopy. *Anal. Chem.* **2011**, *83* (22), 8659–8666.

(80) Anderson, S. L.; Luber, E. J.; Olsen, B. C.; Buriak, J. M. Substance over Subjectivity: Moving beyond the Histogram. *Chem. Mater.* **2016**, *28*, 5973–5975.

(81) McCall, J. D.; Anseth, K. S. Thiol–Ene Photopolymerizations Provide a Facile Method to Encapsulate Proteins and Maintain Their Bioactivity. *Biomacromolecules* **2012**, *13* (8), 2410–2417.

(82) Sinelnikov, R.; Dasog, M.; Beamish, J.; Meldrum, A.; Veinot, J. G. Revisiting an Ongoing Debate: What Role Do Surface Groups Play in Silicon Nanocrystal Photoluminescence? *ACS Photonics* **2017**, *4* (8), 1920–1929.

(83) Rosso-Vasic, M.; Spruijt, E.; Popović, Z.; Overgaag, K.; Van Lagen, B.; Grandidier, B.; Vanmaekelbergh, D.; Domínguez-Gutiérrez, D.; De Cola, L.; Zuilhof, H. Amine-Terminated Silicon Nanoparticles: Synthesis, Optical Properties and Their Use in Bioimaging. *J. Mater. Chem.* **2009**, *19* (33), 5926–5933.

(84) Hua, F.; Erogbogbo, F.; Swihart, M. T.; Ruckenstein, E. Organically Capped Silicon Nanoparticles with Blue Photoluminescence Prepared by Hydrosilylation Followed by Oxidation. *Langmuir* **2006**, *22* (9), 4363–4370.

(85) Park, J.-H.; Gu, L.; Von Maltzahn, G.; Ruoslahti, E.; Bhatia, S. N.; Sailor, M. J. Biodegradable Luminescent Porous Silicon Nanoparticles for in Vivo Applications. *Nat. Mater.* **2009**, *8* (4), 331.

(86) Dickinson, F. M.; Alsop, T. A.; Al-Sharif, N.; Berger, C. E. M.; Datta, H. K.; Šiller, L.; Chao, Y.; Tuite, E. M.; Houlton, A.; Horrocks, B. R. Dispersions of Alkyl-Capped Silicon Nanocrystals in Aqueous Media: Photoluminescence and Ageing. *Analyst* **2008**, *133* (11), 1573–1580.

(87) Letant, S. E.; Hart, B. R.; Kane, S. R.; Hadi, M. Z.; Shields, S. J.; Reynolds, J. G. Enzyme Immobilization on Porous Silicon Surfaces. *Adv. Mater.* **2004**, *16* (8), 689–693.

(88) Létant, S. E.; Kane, S. R.; Hart, B. R.; Hadi, M. Z.; Cheng, T.-C.; Rastogi, V. K.; Reynolds, J. G. Hydrolysis of Acetylcholinesterase Inhibitors–Organophosphorus Acid Anhydrolase Enzyme Immobilization on Photoluminescent Porous Silicon Platforms. *Chem. Commun.* **2005**, No. 7, 851–853.

(89) Gonzalez, C. M.; Iqbal, M.; Dasog, M.; Piercey, D. G.; Lockwood, R.; Klapötke, T. M.; Veinot, J. G. Detection of High-Energy Compounds Using Photoluminescent Silicon Nanocrystal Paper Based Sensors. *Nanoscale* **2014**, *6* (5), 2608–2612.

(90) Krajewska, B.; Ciurli, S. Jack Bean (Canavalia Ensiformis) Urease. Probing Acid–Base Groups of the Active Site by PH Variation. *Plant Physiol. Biochem.* **2005**, *43* (7), 651–658.

(91) Cesareo, S. D.; Langton, S. R. Kinetic Properties of Helicobacter Pylori Urease Compared with Jack Bean Urease. *FEMS Microbiol. Lett.* **1992**, *99* (1), 15–21.

(92) Norris, R.; Brocklehurst, K. A Convenient Method of Preparation of High-Activity Urease from Canavalia Ensiformis by Covalent Chromatography and an Investigation of Its Thiol Groups with 2, 2'-Dipyridyl Disulphide as a Thiol Titrant and Reactivity Probe. *Biochem. J.* **1976**, *159* (2), 245–257.

(93) Chiu, S.-K.; Manhat, B. A.; DeBenedetti, W. J.; Brown, A. L.; Fichter, K.; Vu, T.; Eastman, M.; Jiao, J.; Goforth, A. M. Aqueous Red-Emitting Silicon Nanoparticles for Cellular Imaging: Consequences of Protecting against Surface Passivation by Hydroxide and Water for Stable Red Emission. *J. Mater. Res.* **2013**, *28* (2), 216–230.

(94) Chandler-Henderson, R. R.; Sweryda-Krawiec, B.; Coffer, J. L. Steric Considerations in the Amine-Induced Quenching of Luminescent Porous Silicon. *J. Phys. Chem.* **1995**, *99* (21), 8851–8855.

(95) Sweryda-Krawiec, B.; Chandler-Henderson, R. R.; Coffer, J. L.; Rho, Y. G.; Pinizzotto, R. F. A Comparison of Porous Silicon and Silicon Nanocrystallite Photoluminescence Quenching with Amines. *J. Phys. Chem.* **1996**, *100* (32), 13776–13780.

(96) Dasog, M.; Yang, Z.; Regli, S.; Atkins, T. M.; Faramus, A.; Singh, M. P.; Muthuswamy, E.; Kauzlarich, S. M.; Tilley, R. D.; Veinot, J. G. Chemical Insight into the Origin of Red and Blue Photoluminescence Arising from Freestanding Silicon Nanocrystals. *ACS Nano* **2013**, *7* (3), 2676–2685.

(97) De Melo, J. V.; Cosnier, S.; Mousty, C.; Martelet, C.; Jaffrezic-Renault, N. Urea Biosensors Based on Immobilization of Urease into Two Oppositely Charged Clays (Laponite and Zn- Al Layered Double Hydroxides). *Anal. Chem.* **2002**, *74* (16), 4037–4043.

Chapter 4

Ratiometric Detection of Nerve Agents by Coupling Complementary Properties of Silicon-Based Quantum Dots and Green Fluorescent Protein[3]

4.1 Introduction

Nerve agents belong to a class of phosphorous-containing organic compounds broadly known as organophosphate esters (OPEs; organic esters of phosphoric acids). These reagents are potent inhibitors of the neurologically important enzyme acetylcholinesterase (AChE)[1,2] by a mechanism that involves phosphorylation of the catalytically important serine residue in the enzyme's active site.[1,2] The associated diminished activity of AChE leads to a dramatic increase in levels of acetylcholine (ACh), a neurotransmitter that is released at nerve synapses, which is important for normal nervous system function.[1,2] Accumulation of toxic levels of ACh causes impaired cholinergic synapse transmission, leading to respiratory depression, prolonged seizures, and death.[1,2] Nerve agents are toxic by all routes of exposure (e.g., inhalation, ingestion, contact with skin and eye) and are particularly potent percutaneous hazards.[1,2]

Paroxon (PX), a *p*-nitrophenyl-containing organophosphate ester, is one of the most potent organophosphate nerve agents.[3,4] As such, it is used rarely now as a pesticide in the agriculture industry. Unfortunately, the possibility of human exposure cannot be ignored because PX has been weaponized.[5] Parathion (PT), another extremely toxic *p*-nitrophenyl-containing organophosphate nerve agent, has been banned for use as a pesticide in many jurisdictions[6] (e.g., India, China, Japan, Thailand, New Zealand, Turkey, Sweden, United Kingdom, Russia).[7] Despite its limited availability, numerous reports have implicated it in poisonings and attempted suicides.[8] PT also has been employed in chemical warfare.[9]

Infrastructure-intensive methods for the selective and sensitive determination of OPEs involving gas and liquid chromatography as well as mass spectrometry have been reported in

[3]The contents of this chapter have been copied and/or adapted from the following publication: Robidillo, C. J. T.; Wandelt, S.; Dalangin, R.; Zhang, L.; Yu, H.; Meldrum, A.; Campbell, R. E.; Veinot, J. G. C. *ACS Appl. Mater. Interfaces* **2019**, *11*, 33478-33488. Copyright © 2019 American Chemical Society.

the literature.[10–13] While accurate and sensitive, these methods suffer from limiting drawbacks, such as the need for costly instrumentation and the necessity for highly trained technicians for operation; these two factors alone preclude the convenient implementation of these methods.[14] Recently, nanomaterial-based detection methods for OPEs have been developed.[14–17] These approaches rely on enzyme-substrate specificity[18] for selective detection and signal amplification resulting from the nanostructures' role as enzyme-carriers.[15] Adding to the material function, the catalytic action of the enzyme on OPEs produces an electrochemical signal or photoluminescence (PL) quenching species, among others, that provides a mode of detection.[14–16,18] In some instances, biosensor response is reliant upon the formation of an end-product (e.g., hydrogen peroxide) that arises from a cascade of chemical reactions catalyzed by multiple enzymes.[17,19] Though sensitive and selective, the dependence of these methods on the (combined) action of enzyme(s) adds complexity that could compromise biosensor performance (e.g., unwanted/unexpected denaturation and irreversible inactivation of enzymes). In addition, some reported fluorescent OPE sensors employ cytotoxic cadmium-based quantum dots (e.g., CdTe QDs)[17,20] or involve the use of toxic heavy metal ions, such as lead for detection.[21] This heavy metal reliance also potentially limits the utility of these systems in 'real-world' sensing applications.

Silicon-based quantum dots (SiQDs) are photoluminescent semiconductor nanoparticles that have attracted considerable interest as active materials in many applications, including bioimaging and biological and chemical sensing.[22–24] Their unique photophysical properties and biocompatibility make them an attractive alternative to commercially available cytotoxic CdSe and CdTe QDs.[25–28] Green fluorescent protein (GFP) is a naturally-occurring protein molecule that emits intense green fluorescence when excited with blue or ultraviolet (UV) light.[29] This biomolecule consists of a peptide-derived fluorophore that is encased within a 'barrel-like' protein structure.[30] Owing to their biocompatibility and tailorable fluorescence, GFP, its naturally occurring homologues, and engineered variants thereof, have been exploited for bioimaging and sensing.[31,32]

Ratiometric PL sensors have been demonstrated for fluorophore combinations consisting of nanomaterials such as CdSe or CdTe QDs and carbon dots, among others.[33–35] Compared to standard photoluminescence-based sensors that only employ one emitter, ratiometric sensors offer unique advantages of visual analyte detection and probe

concentration-independent response.[35] Although ratiometric sensing using porous silicon has been demonstrated already,[36] to our knowledge, no ratiometric sensors based upon freestanding SiQDs have been reported to date, presumably because the SiQD optical response typically is quenched or at least altered by most luminescent dye pairings. The complementary properties of SiQDs and GFPs, e.g., their complementary spectral response (red photoluminescence vs. green fluorescence), complementary chemical nature (inorganic vs. organic emitter), accessibility/non-accessibility of their emission centers (exposed SiQDs vs. isolated peptide-based fluorophore), and their biocompatibility provide near-ideal and convenient starting materials for developing a sensitive, cost effective, and toxic-metal-free ratiometric sensor platform. Here, we present a straightforward, convenient, biocompatible, paper-based ratiometric photoluminescent sensor for the nerve agents PX and PT that employs the long Stokes shift (LSS) GFP variant, mAmetrine1.2,[37] and red-emitting SiQDs, and where the SiQD PL is quenched selectively by the OPE in question. This new sensing platform provides a convenient and rapid visual detection system for OPEs via direct selective quenching and eliminates the need for heavy metals and intermediary biomolecules that could limit device utility.

4.2 Experimental Section

4.2.1 Chemicals

A methyl isobutyl ketone solution of hydrogen silsesquioxane (HSQ, trade name Fox-17, Dow Corning) was evaporated to dryness to yield a white solid. Aqueous electronics grade hydrofluoric acid (49%) was used as received from J. T. Baker. Allyloxy poly(ethylene oxide) methyl ether (9–12 ethylene oxide units, M ~ 450 g mol^{-1}, ρ = 1.076 g mL^{-1}, Gelest), 10-undecenoic acid (M = 184.28 g mol^{-1}, ρ = 0.912 g mL^{-1}), paraoxon (PX), parathion (PT), diazinon (DZ), malathion (MT), chlorpyrifos (CP) (**Caution:** *Organophosphate esters must be handled with extreme caution. Employ appropriate personal protective equipment as directed by local authorities and/or supplier.*), *p*-nitrophenol (PN), 4-(2-hydroxyethyl)-1-piperazineethanesulfonic acid (HEPES) (Millipore Sigma) were used as received. All other reagents and solvents used were of analytical grade, unless otherwise specified.

4.2.2 Preparation of Oxide-Embedded Silicon Nanoparticles

A composite of oxide-embedded silicon nanoparticles (SiNPs) was prepared following a well-established method developed in the Veinot laboratory.[38] One gram of HSQ was processed thermally by heating in a standard tube furnace to 1100 °C for 1 h in an atmosphere of 5% H_2 and 95% Ar. This procedure yielded silicon oxide-embedded inclusions of elemental silicon with dimensions of ca. 3 nm. This composite was annealed further for 1 h at 1200 °C in an Ar atmosphere to grow the inclusion dimensions to ca. 6 nm. The resulting '6 nm' composite was processed into a finely powdered stock material, as described previously.[39]

4.2.3 Synthesis of Hydride-Terminated Silicon Nanoparticles (*H*-SiNPs)

Hydride-terminated silicon nanoparticles (*H*-SiNPs) were liberated from their oxide matrix by ethanolic HF etching.[39]

4.2.4 Synthesis of Silicon-Based Quantum Dots (SiQDs)

Mixed surface acid-terminated poly(ethylene oxide)-coated silicon-based quantum dots (SiQDs) were prepared through thermally induced hydrosilylation.[40]

4.2.5 Expression and Purification of mAmetrine1.2 (mAm)

DNA encoding mAmetrine1.2[37] in pBAD/His B vector (Thermo Fisher Scientific) was transformed into electrocompetent *Escherichia coli* strain DH10B (Invitrogen). The transformed *E. coli* were cultured on Lennox Broth (LB) agar plates supplemented with 400 μg mL^{-1} ampicillin (Thermo Fisher) and 0.02% L-arabinose (Alfa Aesar) at 37 °C overnight. Single colonies from the transformed bacteria were used to inoculate 200 mL or 500 mL of LB supplemented with 100 μg mL^{-1} ampicillin and 0.02% L-arabinose and were cultured at 37 °C for 24 h. After culturing, bacteria were harvested by centrifugation at 8000 rpm for 10 min and resuspended in lysis buffer (50 mM Tris-HCl, 100 mM NaCl, 5% glycerol, 1 mM imidazole, pH 8.0). Cells were lysed using sonication and then clarified by centrifugation at 14000 rpm for 30 min. The cleared lysate was incubated with Ni-NTA beads (G Biosciences) on a rotary platform for at least 1 h. The lysate–bead mixture was transferred to a polypropylene centrifuge column and washed with 5-packed column volumes of wash buffer (lysis buffer with 20 mM

imidazole, pH 8.0) before elution using Ni-NTA elution buffer (lysis buffer with 250 mM imidazole, pH 8.0). Purified mAm was concentrated and buffer-exchanged into 20 mM HEPES (pH 7.0) using 10 kDa centrifugal filter units (Millipore). All steps were carried out at 4 °C or on ice. The protein concentration was measured by A_{280} using an extinction coefficient of 31,000 M^{-1} cm^{-1}.[37]

4.2.6 Characterization of SiQDs

The SiQDs were characterized using Fourier transform infrared spectroscopy (FTIR), X-ray photoelectron spectroscopy (XPS), bright-field transmission electron microscopy (TEM), dynamic light scattering analysis (DLS), and absorption spectroscopy, as described elsewhere.[39] Thermogravimetric analysis (TGA) was performed from 25 to 800 °C using a TGA/DSC 1 STARe System (Mettler Toledo) at a heating rate of 10 °C min^{-1} under Ar flow.

Photoluminescence excitation (PLE) and emission (PL) spectra of the samples were recorded using a SpectraMax® i3x multimode microplate reader. Time-resolved PL spectroscopy was performed as described previously.[39] The decay data were modeled using the stretched exponential function $I = A \cdot \exp[-(t/\tau)^{\beta}] + dc$, where the fitting parameters are A, τ, β, and the dc offset. For this intensity decay function, the mean time constant is given by $\langle\tau\rangle = \tau \cdot \Gamma(2/\beta)/\Gamma(1/\beta)$ and the mean decay time is $\langle t\rangle = \tau \cdot \Gamma(3/\beta)/\Gamma(2/\beta)$.[41] The fits were performed in Matlab using the trust region algorithm with unweighted minimization of the sum of the squares of the residuals. PL quantum yield measurements were performed as described previously.[40]

4.2.7 Effect of mAm on the PL of SiQDs

Solutions (V_{total} = 100 µL) containing 1.1 µM SiQDs and increasing concentrations (0, 0.5, 0.9, 1.8, 3.7 µM) of mAm were prepared by diluting stock SiQD and mAm solutions with 20 mM HEPES buffer (pH 7.0). The PL spectra of the solutions were measured at an excitation wavelength of 365 nm. The experiments were performed in triplicates.

4.2.8 Effect of SiQDs on the PL of mAm

Solutions (V_{total} = 100 µL) containing 1.8 µM mAm and increasing concentrations (0, 0.3, 0.6, 1.1, 2.2 µM) of SiQDs were prepared by diluting stock SiQD and mAm solutions with 20 mM

HEPES buffer (pH 7.0). The PL spectra of the solutions were measured at an excitation wavelength of 365 nm. The experiments were performed in triplicates.

4.2.9 Effect of Quenchers on SiQD Photoluminescence

Solutions (V_{total} = 100 μL) containing 1.1 μM SiQDs and increasing concentrations (0, 2.5, 5, 10, 20, 40 μM) of quencher in question (PX, PT, and PN) were prepared by diluting 50 μM quencher solution with 20 mM HEPES buffer (pH 7.0). The PL spectra of the solutions were acquired upon excitation at 365 nm. Stern–Volmer plots were constructed by plotting the ratio of PL intensities in the absence and presence of quencher at 635 nm, $I°/I$, against the concentration of quencher. Experiments were performed in triplicates. The ratio of PL lifetimes in the presence and absence of quencher, $\tau/\tau°$, was plotted also against the concentration of the quencher.

4.2.10 Effect of PX and PT on mAm Fluorescence

Solutions (V_{total} = 150 μL) containing 1.8 μM mAm and increasing concentrations (0, 5, 25, 100 μM) of quencher (PX, PT) were prepared by diluting 50 or 200 μM quencher solution with 20 mM HEPES buffer (pH 7.0). The PL spectra of the solutions were measured at an excitation wavelength of 365 nm. The experiments were performed in triplicates.

4.2.11 Effect of PX and PT on the Photoluminescence of Mixtures of SiQDs and mAm

Solutions (V_{total} = 150 μL) containing 1.1 μM SiQDs, 1.8 μM mAm, and increasing concentrations (i.e., 0, 2.5, 5.0, 10.0, 15.0, 20.0, 30.0, 40.0, 50.0, 75.0, 100.0 μM for PX; 0, 0.01, 0.1, 0.25, 0.5, 1.0, 2.5, 5.0, 10.0, 15.0, 20.0, 30.0, 40.0 μM for PT) of quencher were prepared by diluting 5, 50, or 200 μM quencher solution with 20 mM HEPES buffer (pH 7.0). The PL spectra of the solutions were measured at an excitation wavelength of 365 nm. The ratio of the PL intensity at 525 to the intensity at 635 nm, I_{525}/I_{635}, was plotted against the concentration of the quencher to obtain a straight line. This plot was used for the quantification of PX and PT. The experiments were performed in triplicates.

4.2.12 Analysis of Solutions with Known PX and PT Concentrations

Solutions (V_{total} = 150 µL) containing 1.1 µM SiQDs, 1.8 µM mAm, and 25.0 µM PX (or PT) were prepared by diluting 50 µM quencher solution with 20 mM HEPES buffer (pH 7.0). The PL intensities of the solutions at 525 and 635 nm were measured and the ratio I_{525}/I_{635} evaluated and used to determine the concentration of PX or PT from the linear calibration plots obtained above. The experiments were performed in triplicates.

4.2.13 Effect of Interferents on the Detection of PX and PT Using SiQDs and mAm

Solutions (V_{total} = 115 µL) containing 1.1 µM SiQDs, 0.9 µM mAm, and 0.30 mM of the interferents (Salts: KCl, KNO_2, KNO_3, K_2CO_3, K_3PO_4, Na_2SO_4, NaCl, NaF, NH_4Cl, $MgCl_2$, $Ca(NO_3)_2$; Organics: alanine (Ala), lysine (Lys), arginine (Arg), malonic acid (MA), sodium acetate (Acet), sodium citrate (Cit), glucose (Glc), sucrose (Suc)) were prepared by diluting the corresponding 1.0 mM solution with 20 mM HEPES buffer (pH 7.0). The PL intensities of the solutions were measured at an excitation wavelength of 365 nm, and the ratio I_{525}/I_{635} evaluated. Afterwards, 35 µL of 100 µM quencher solution were added to each solution, the PL intensities measured, and the ratio I_{525}/I_{635} after addition of the quencher evaluated. The value of the ratio $R = (I_{525}/I_{635})_{after}/(I_{525}/I_{635})_{before}$ for each solution was used to determine the effect of interferents on the analysis by comparing it to values obtained for positive (115 µL solution containing 1.1 µM SiQDs and 0.9 µM mAm in HEPES buffer + 35 µL 100 µM quencher solution) and negative (115 µL solution containing 1.1 µM SiQDs and 0.9 µM mAm in HEPES buffer + 35 µL mQ water) controls. The experiments were performed in triplicates.

4.2.14 Selectivity of the Detection Method for PX and PT

Solutions (V_{total} = 150 µL) containing 1.1 µM SiQDs, 1.8 µM mAm, and 20 µM organophosphate ester (PX, PT, DZ, MT, CP) or 20 µM PN were prepared by diluting the corresponding 100 µM organophosphate ester or PN solution with 20 mM HEPES buffer (pH 7.0). The PL spectra of the solutions were measured at an excitation wavelength of 365 nm. The experiments were performed in triplicates.

4.2.15 Detection of PX and PT Using Paper-Based Sensors Containing SiQDs and mAm

Paper-based sensors were prepared by dipping filter paper pieces (1.0 cm × 0.4 cm) in a solution containing 58 μM SiQDs and 36 μM mAm. After drying the papers in air for 30 min, 1 μL of organophosphate ester solution (5 and 100 μM; PX, PT, DZ, MT, CP), 1 μL of PN solution (5 and 100 μM), 1 μL of Edmonton municipal tap water, and 1 μL of mQ water were spotted on separate papers. After 1 min, the papers were exposed to a UV flashlight (λ = 365 nm) that was held 15 cm from the paper surface and photographs of the luminescence were acquired using a Canon Powershot SX730 HS camera with an ISO value of 3200 (Exposure time = $^{1}/_{200}$–$^{1}/_{500}$ s). The Color Picker app from Ratonera Inc. downloaded on an Android smartphone from the Google Play Store (2 April 2019) was used to analyze the image into its component red/green/blue (RGB) values. The green values were normalized to the corresponding red values to obtain green/red (G/R) ratios. Five points at the center of each image were evaluated to provide a statistical average corresponding to one experiment. The experiments were performed in five replicates.

4.3 Results and Discussion

Figure 4-1A describes the preparation of water-soluble Si-based quantum dots (SiQDs).[26,39,40] Briefly, 10-undecenoic acid and allyloxy poly(ethylene oxide) methyl ether were linked covalently to the surface of '6-nm' hydride-terminated silicon nanoparticles (SiNPs) via thermally induced hydrosilylation at 170 °C. The SiNPs were coated with poly(ethylene oxide) in order to render them water-soluble and resistant to nonspecific protein adsorption.[42–45] Successful surface functionalization was confirmed using Fourier transform infrared spectroscopy (FTIR) that shows the presence of aliphatic sp^3 C–H stretching peak at 3000–2800 cm^{-1} and characteristic carboxylic acid hydroxyl and carbonyl features centered at ca. 3000 and 1709 cm^{-1}, respectively (Figures 4-1B and 4-1C).[46] The diminished intensity of the peak at ca. 2100 cm^{-1}, routinely assigned to Si–H_x stretching (Figure 4-2), and the intense and broad peak at approximately 1100 cm^{-1}, characteristic of C–O and C–C stretches, are also consistent with successful covalent functionalization.[38] An additional carbonyl-based feature is noted at ca. 1734 cm^{-1} that arises from formate ester groups resulting from the thermal

oxidation of the polyethylene oxide moieties.[47,48] Poly(ethylene oxide) is believed to react with oxygen at elevated temperatures forming hydroperoxides that then undergo β-scission into formate esters and hemiacetals.[47] Characteristic bending –CH_x– vibrations resulting from both immobilized undecanoic acid and poly(ethylene oxide) moieties also are noted in the 1500–1300 cm^{-1} region of the FTIR spectrum.[49,50] X-ray photoelectron spectroscopy (XPS) revealed that the SiQDs used in this study are made up of silicon suboxides, as evidenced by the Si $2p_{3/2}$ peak at ca. 101.8 eV (Figure 4-1D).[40] It is reasonable that these suboxides result from exposure of the silicon core to water during aqueous workup (e.g., extraction, dialysis, centrifugal filtration) and subsequent storage.[46,51,52] The O 1s emission at ca. 532.3 eV corresponding to silicon-bonded oxygen atoms also supports the presence of silicon suboxides (Figure 4-1F).[53] Consistent with FTIR analyses, successful surface functionalization is confirmed further by the presence of C 1s peaks centered at ca. 284.8, 286.3, and 289.0 eV (Figure 4-1E) that correspond to aliphatic C–C/C–H, aliphatic C–O, and carboxyl groups, respectively.[54,55] We also note an O 1s associated emission at ca. 533.2 eV that corresponds to the O atoms of polyethylene oxide (Figure 4-1F).[56]

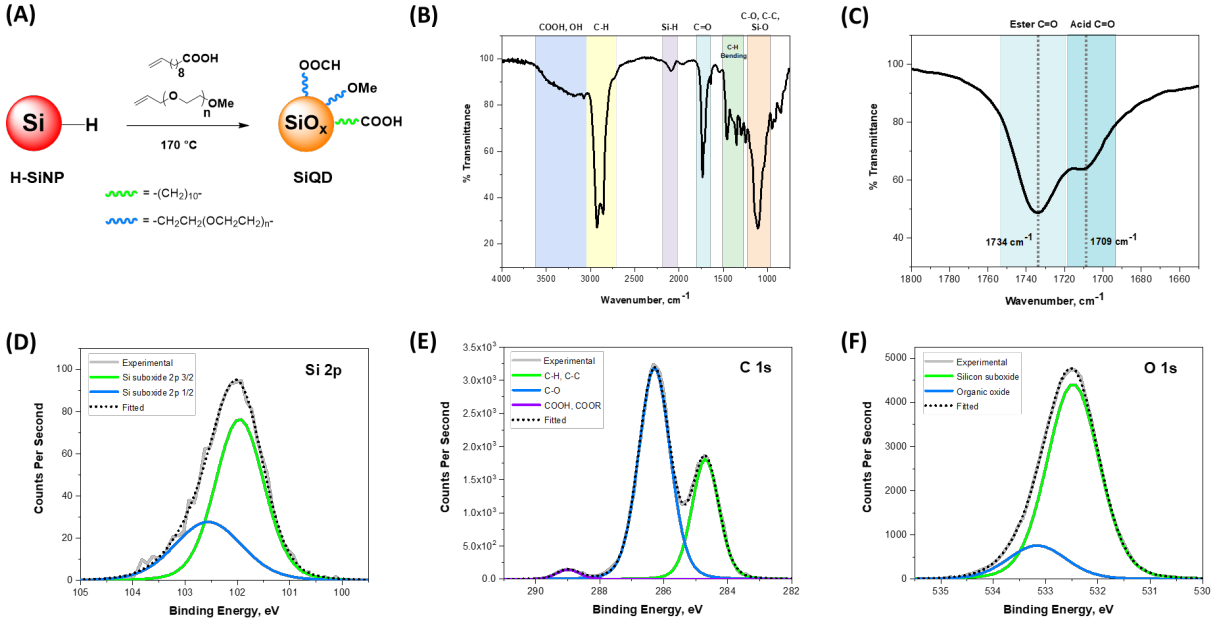

Figure 4-1. (A) Thermally induced hydrosilylation of 10-undecenoic acid and allyloxy poly(ethylene oxide) methyl ether with *H*-SiNPs (–OOCH is a formate ester group). **(B)** FTIR spectrum, **(C)** carbonyl region FTIR spectrum, **(D)** Si 2p, **(E)** C 1s, and **(F)** O 1s high resolution XP spectra of SiQDs.

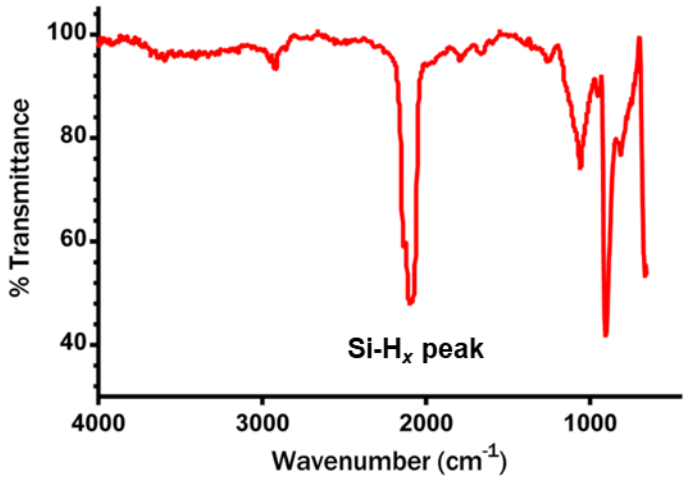

Figure 4-2. FTIR spectrum of hydride-terminated silicon nanoparticles.

Aqueous phase dynamic light scattering (DLS) analysis of the SiQDs revealed an average hydrodynamic diameter of 10.5 ± 2.1 nm (Figure 4-3A). This value is consistent with the core of the SiQDs being coated with hydrophilic poly(ethylene oxide) moieties and surrounded by a water solvation sphere.[26] Imaging the present water-soluble SiQDs using bright-field transmission electron microscopy (TEM) was unsuccessful because the particles were highly agglomerated; this is again consistent with the SiQDs being functionalized with poly(ethylene oxide). We also note a substantial and significant amount of organic content (i.e., 90%) in the present SiQDs, as indicated by the thermogravimetric profile (Figure 4-3C) that presumably arises from surface polymer functionalization and would be expected to preclude accurate determination of the particle core dimensions using electron microscopy. To better interrogate the dimensions of the particle core, we chose to prepare dodecyl-terminated SiQDs ($C_{12}H_{25}$-SiQDs) using *H*-SiNPs obtained from the identical composite batch and etching conditions used to prepare the present water-soluble SiQDs. The $C_{12}H_{25}$-SiQDs were analyzed with bright-field TEM and their resulting size distribution processed using an average shifted histogram;[57] their mean diameter (i.e., 5.0 ± 1.1 nm; Figure 4-3B) was assumed to provide a good approximation of the core dimensions of the water-soluble SiQDs. This value provided an estimated molar mass of the silicon core, which, when combined with the thermogravimetric analysis data, gave access to the solution concentration of the water-soluble SiQDs (See Appendix for the TEM image of $C_{12}H_{25}$-SiQDs and the estimation of the concentration of the SiQDs).

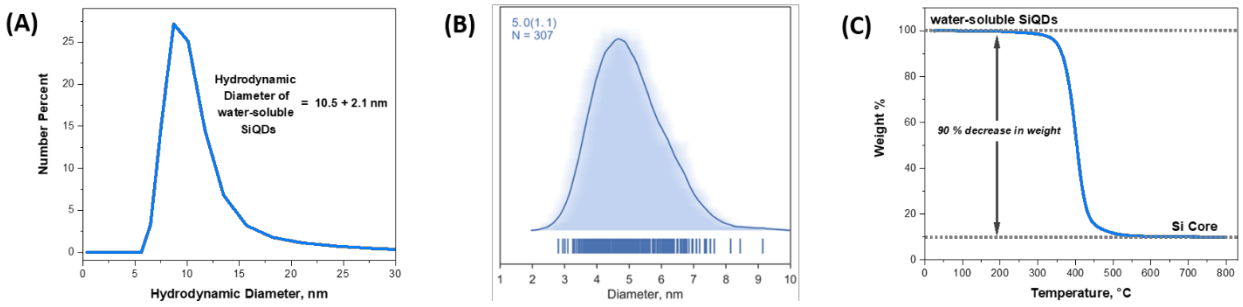

Figure 4-3. (A) DLS size distribution analysis of water-soluble SiQDs, **(B)** average shifted histogram (based on 300 quantum dots) of $C_{12}H_{25}$-SiQDs, and **(C)** thermogravimetric profile of water-soluble SiQDs.

Figure 4-4 shows the optical spectra of SiQDs, mAmetrine1.2 (mAm), and a mixture of SiQDs and mAm. The SiQDs exhibit strong absorption at wavelengths shorter than 400 nm, have a PLE maximum at ca. 365 nm, and a PL maximum at ca. 635 nm. They also have a PL quantum yield of 9.7% and a long-lived excited state lifetime of 58.4 μs; these observations are consistent with an indirect band gap silicon-based emitter. The inset in Figure 4-4A demonstrates that an aqueous solution of SiQDs exhibits visibly detectable orange PL. In contrast, the fluorescent protein employed in this study, mAm, shows absorbance and PLE maxima at ca. 410 nm and a green PL maximum at ca. 525 nm (Figure 4-4B inset). Figure 4-4C shows that a mixture of SiQDs and mAm appears yellow upon visible inspection and exhibits PL maxima at 635 and 525 nm (i.e., corresponding to each individual emitter and consistent with negligible interaction).

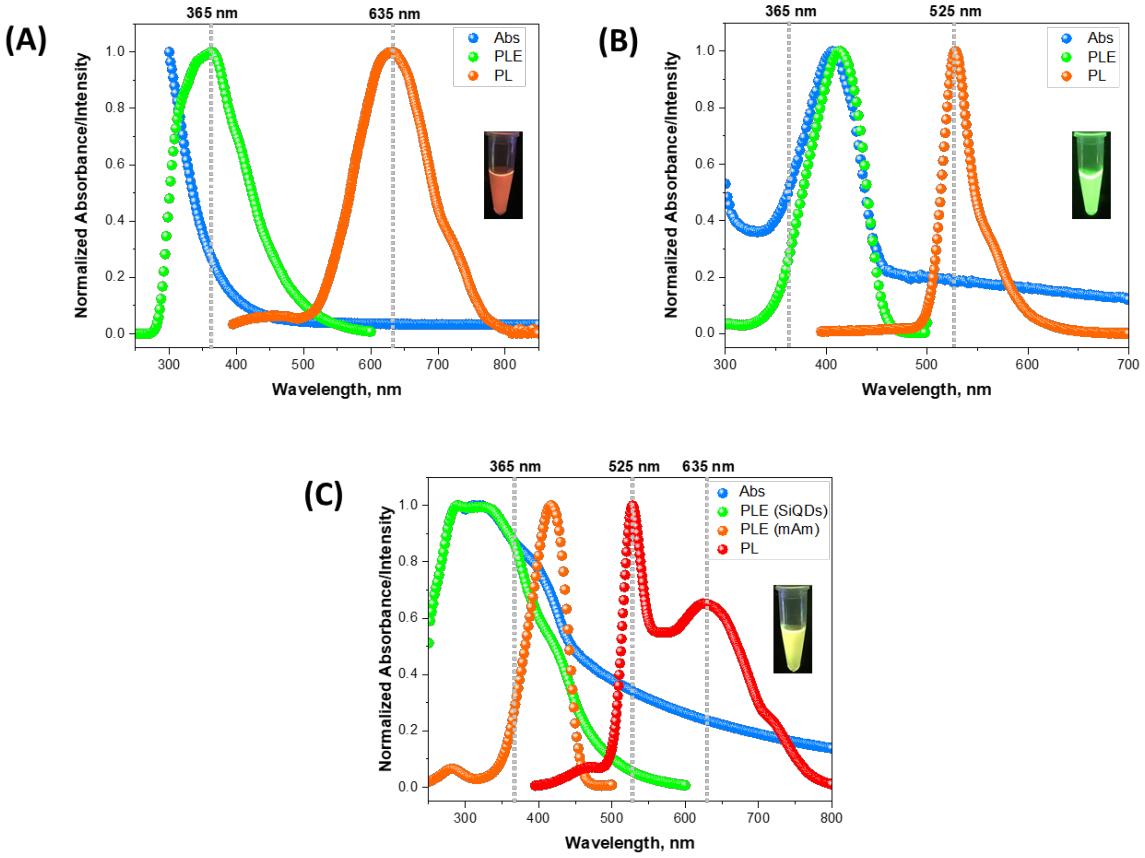

Figure 4-4. Absorbance (Abs), photoluminescence excitation (PLE), and photoluminescence emission (PL) spectra of **(A)** SiQDs, **(B)** mAm, and **(C)** a mixture consisting of SiQDs and mAm. Photographs of aqueous solutions of SiQDs, mAm, and their mixture under UV illumination (λ_{ex} = 365 nm) are shown as insets (C_{SiQDs} = 1.1 µM, C_{mAm} = 0.1 µM; SiQDs: PLE, λ_{em} = 635 nm; PL, λ_{ex} = 365 nm; mAm: PLE, λ_{em} = 525 nm; PL, λ_{ex} = 365 nm; mixture: PLE, λ_{em} = 635 nm (SiQDs), λ_{em} = 525 nm (mAm); PL, λ_{ex} = 365 nm).

Subsequently, we investigated the behavior of each emitter in the presence of the other through a rational concentration variation of one while maintaining the concentration of the other constant. Figure 4-5A shows that the PL intensity of the SiQDs decreased with increasing mAm concentration. Similarly, the mAm PL intensity decreased in the presence of increasing SiQD concentration (Figure 4-5B). This phenomenon has been observed for fluorophore mixtures[34] and is attributed reasonably to the overlap of the PLE spectra of the two emitters and a resulting 'competition' for incident excitation photons (i.e., an inner-filter effect).

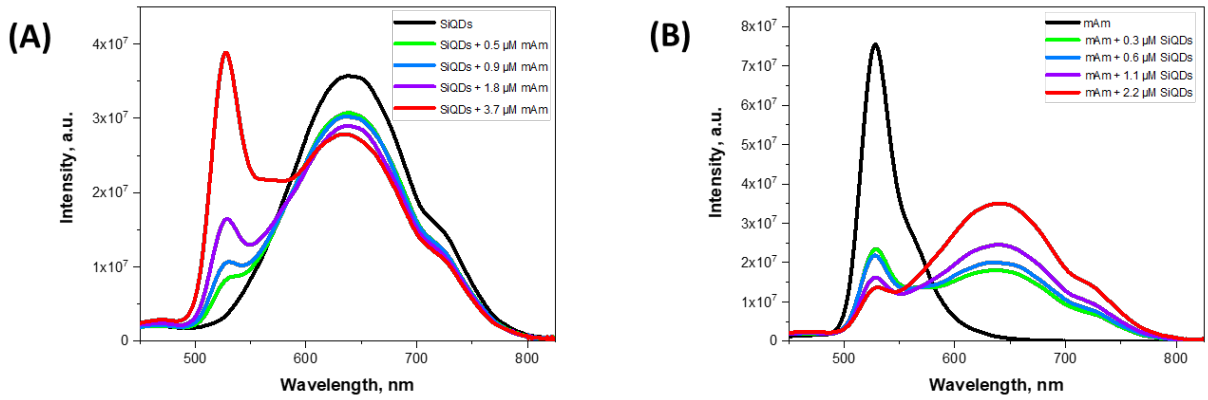

Figure 4-5. (A) PL spectra of SiQDs (1.1 μM) in the presence of increasing concentrations of mAm and **(B)** PL spectra of mAm (1.8 μM) in the presence of increasing concentrations of SiQDs (λ_{ex} = 365 nm).

Photoluminescent sensors offering detection of high-energy nitro-containing explosives based upon freestanding SiQDs as well as porous silicon nanocrystallites have been reported.[24,58] In this study, we extended the SiQD sensing repertoire by taking advantage of the tendency of nitroaromatic organic compounds to quench their PL and fabricated a ratiometric sensor based upon SiQD and mAm for *p*-nitrophenyl-containing organophosphate ester (OPE) nerve agents paraoxon (PX) and parathion (PT) (Scheme 4-1). To do so effectively, it was first necessary to determine the effect of PX and PT on the PL response of each emitter independently. Subsequently, we determined the effect of addition of PX and PT on the PL of SiQD/mAm mixtures (vide infra). Figures 4-6A and 4-6B show that PX and PT quench SiQD PL, while Figures 4-6C and 4-6D show that mAm PL is comparatively unaffected by their presence.

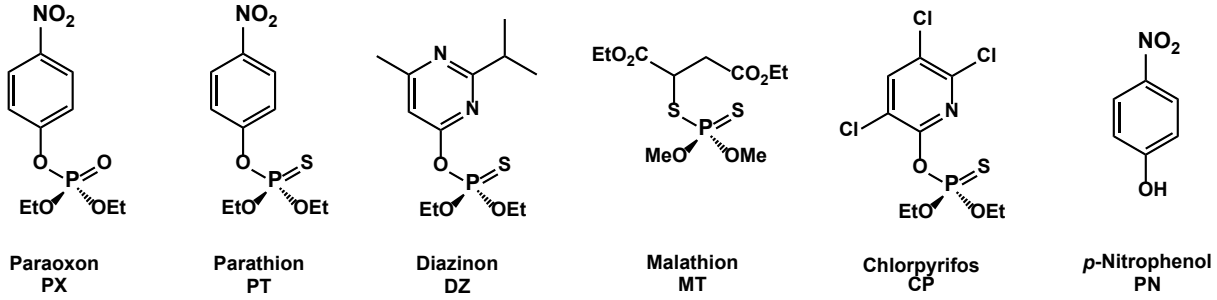

Scheme 4-1. Chemical structures of organophosphate nerve agents and *p*-nitrophenol used in this study.

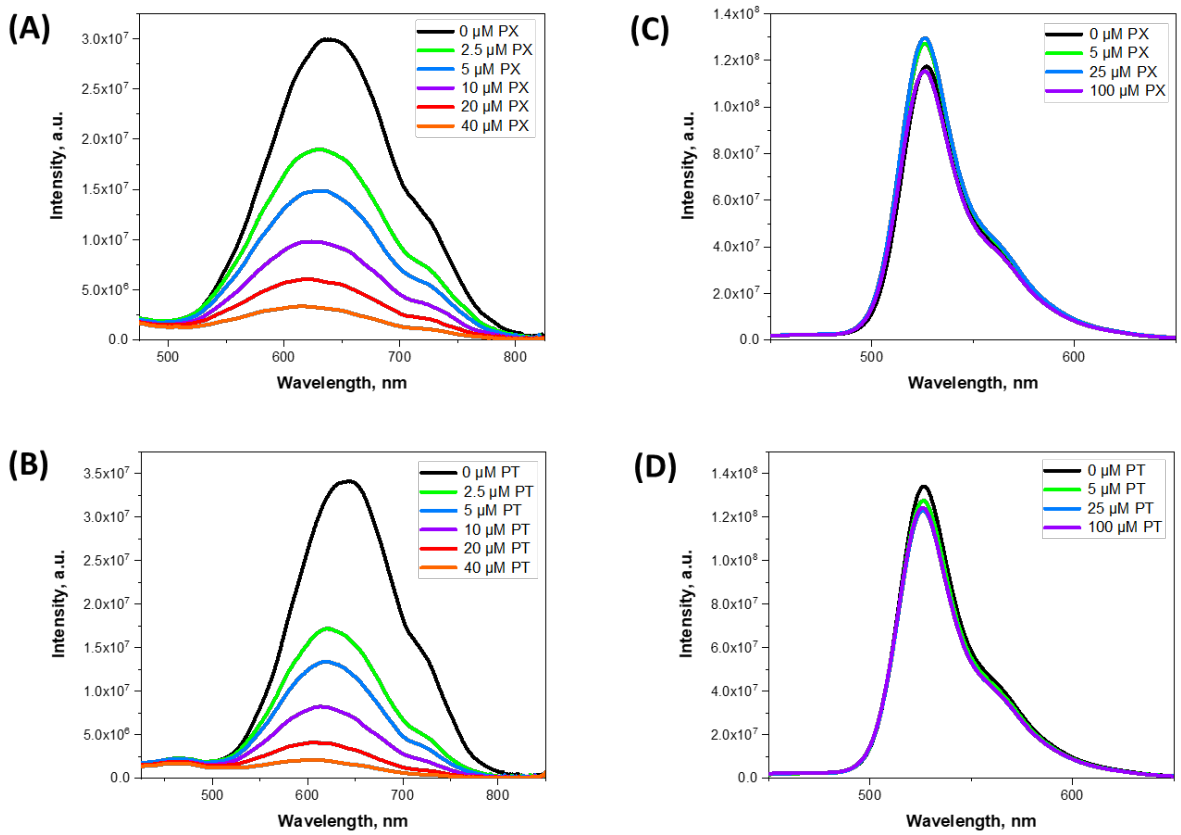

Figure 4-6. PL spectra of SiQDs in the presence of increasing concentrations of **(A)** PX and **(B)** PT and PL spectra of mAm in the presence of increasing concentrations of **(C)** PX and **(D)** PT (C_{SiQDs} = 1.1 μM, C_{mAm} = 1.8 μM, λ_{ex} = 365 nm).

To understand the response of the present sensing motif better, we determined the mechanism by which PX, PT, and *p*-nitrophenol (PN) quench the SiQD PL through steady-state and time-resolved PL measurements. Corresponding Stern–Volmer plots ($I°/I$ vs. [Quencher]) for PX, PT, and PN shown in Figure 4-7A yielded linear relationships with Stern–Volmer constants (K_{SV} = slope) of 0.21, 0.46, and 0.03, respectively. These values suggest that PT is a more effective quencher than PX, which, in turn, is a much more effective quencher than PN. Plots of $\tau/\tau°$ vs. [Quencher] indicate that the excited-state lifetimes of the SiQDs decrease with increasing quencher concentration (Figure 4-7B). The diminished SiQD lifetimes are consistent with PX, PT, and PN acting as dynamic quenchers by providing alternative relaxation pathways for the excited SiQDs; based upon past reports it is reasonable that they are acting as electron acceptors.[24,58]

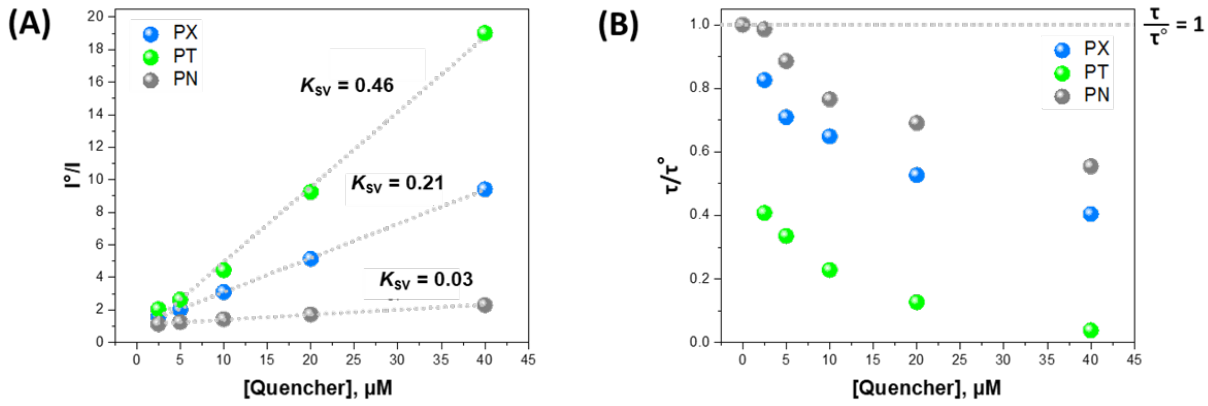

Figure 4-7. (A) Stern–Volmer plots (λ_{ex} = 365 nm) and (B) plots of τ/τ° vs. [Quencher] for PX, PT, and PN.

Figure 4-8A describes the general approach to sensing of the *p*-nitrophenyl-containing OPE nerve agents through the selective quenching of SiQD PL. Figure 4-8B shows the influence of increasing PX concentration on SiQD PL alone; no visually detectable change in PL intensity is noted until the PX concentration reaches 250 μM. Also, Figure 4-8C shows that PX does not quench the PL of mAm. In contrast (Figure 4-8D), when a mixture of SiQDs and mAm are exposed to varied PX concentrations, the changes in optical response are striking. The PL arising from a solution containing SiQDs and mAm clearly changes from yellow to green with increasing concentration of PX.

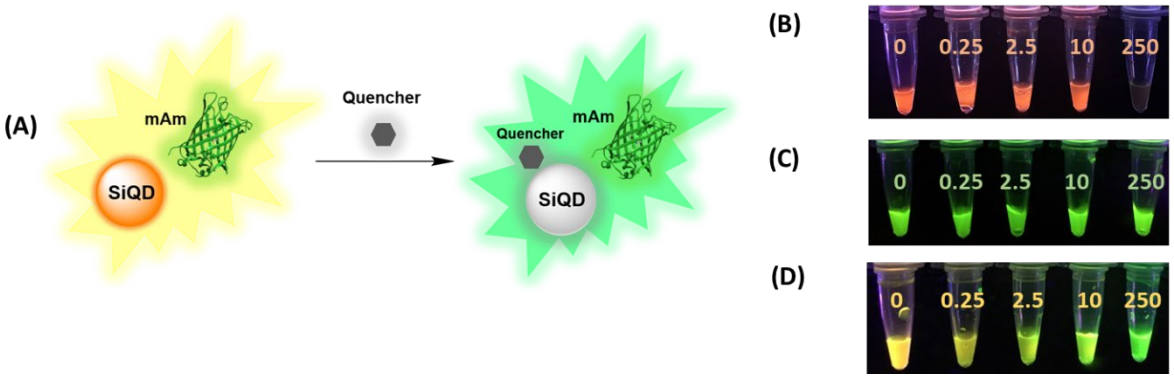

Figure 4-8. (A) Sensing motif that exploits the combined PL of SiQDs and mAm upon addition of quencher. Photographs showing a series of solutions containing **(B)** only SiQDs, **(C)** only mAm, and **(D)** SiQDs and mAm in the presence of increasing micromolar concentrations of PX under UV illumination (λ_{ex} = 365 nm).

Figures 4-9A and 4-9C show the evolution of PL spectra of aqueous solutions of SiQDs and mAm mixtures (i.e., C_{SiQDs} = 1.1 μM, C_{mAm} = 1.8 μM) containing increasing concentrations of PX and PT, respectively. The SiQD PL intensity (λ_{max} = 635 nm) is diminished significantly

with increasing quencher concentrations, while that of mAm (λ_{max} = 525 nm) remains unchanged. A plot of the ratio of PL intensities at 525 nm and 635 nm (i.e., I_{525}/I_{635}) versus the concentrations of PX or PT, yielded a straight line (Figures 4-9B and 4-9D), which points to the potential utility of SiQDs/mAm pairing in the analytical determination of PX and PT. To explore this possibility, we evaluated two solutions, one containing 25.0 µM PX and the other 25.0 µM PT; the presented calibration plots provided concentrations of 25.1 µM PX (0.26% error) and 25.1 µM PT (0.21% error), respectively. The limits of detection (LODs) of the present biocompatible toxic-metal-free SiQDs (LOD = 3.3σ/slope, σ = standard deviation of the blank),[24] 4.9 µM (1.3 µg mL^{-1}) for PX and 1.3 µM (0.4 µg mL^{-1}) for PT, obtained from the plots are in the range of the reported amount of PX that causes death of Sprague–Dawley rats in 6–8 min (4 mg kg^{-1})[3] and the median lethal dose (LD_{50}) of PT for human adults (20–100 mg)[59] and mammals (e.g., mice, cats, dogs) (1–12 mg kg^{-1}).[60–62]

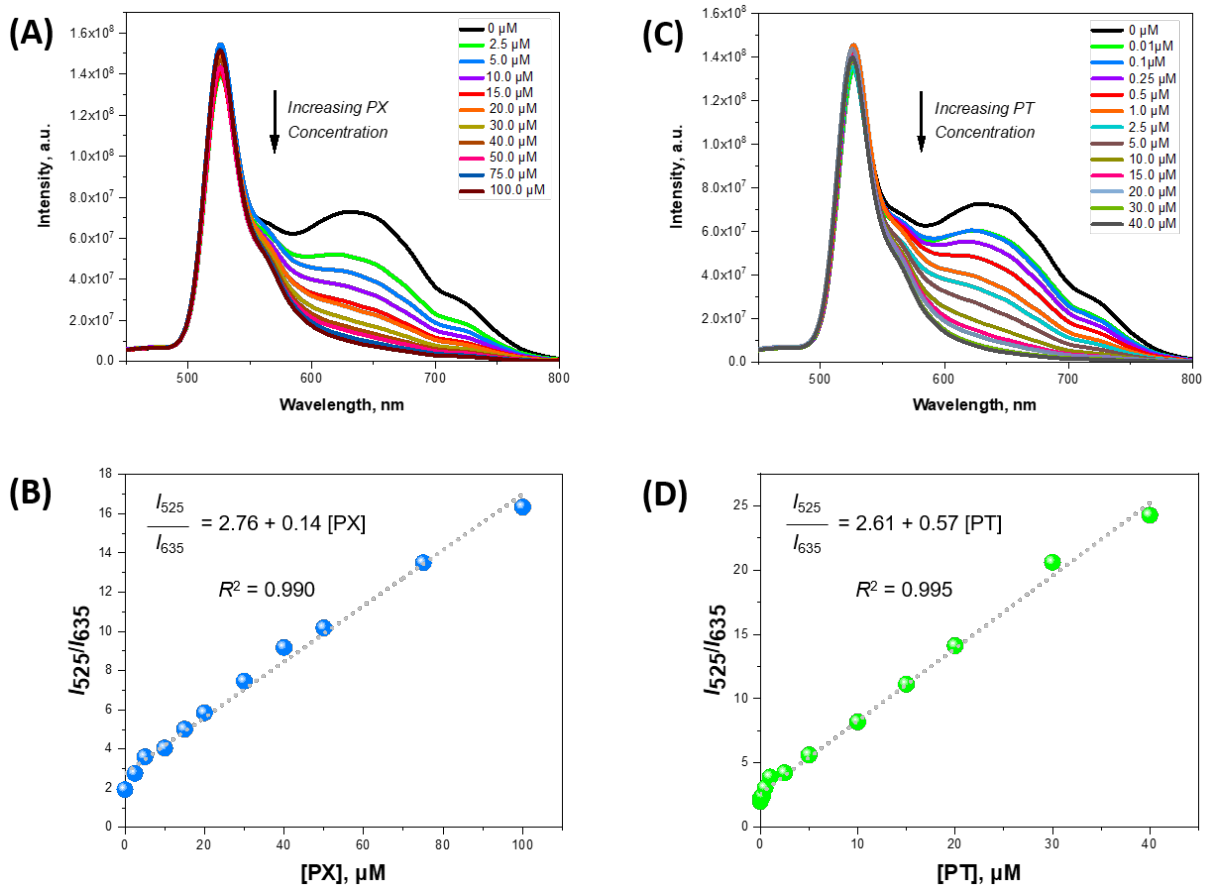

Figure 4-9. PL spectra of solutions containing SiQDs and mAm in the presence of increasing concentrations of **(A)** PX and **(C)** PT. Linear calibration plots for **(B)** PX and **(D)** PT obtained by plotting I_{525}/I_{635} against [Quencher] (C_{SiQDs} = 1.1 µM, C_{mAm} = 1.8 µM, λ_{ex} = 365 nm). The plotted values have relative standard deviations of 2–17%.

Yi and co-workers reported a detection strategy that has a sub-nanomolar detection limit for PT (LOD = 0.23 nM).[19] Their strategy is reliant upon the combined biological activities of two enzymes (acetylcholine esterase and choline oxidase), the use of acetylcholine as substrate, and the formation of choline and its subsequent oxidation that leads to the production of H_2O_2, which ultimately quenches the PL of blue-photoluminescent SiQDs. Therefore, PT and other OPE nerve agents are detected by their ability to inhibit acetylcholine esterase activity, leading to a decrease in the concentration of H_2O_2 and an increase in PL intensity. Compared to their system, the ratiometric sensing platform using mAm and red-photoluminescent SiQDs reported here offers the advantage of operational simplicity, as it does not depend on a cascade of chemical reactions catalyzed by enzymes for signal generation. Also, our detection strategy is straightforward and is, therefore, less likely to suffer from complications that might compromise sensor performance (e.g., unwanted/unexpected loss of activity of enzymes due to denaturation or the presence of unknown inhibitors). Lastly, the mAm/SiQD sensor allows for discrimination between nitrophenyl-based OPE nerve agents (e.g., parathion) and non-nitrophenyl-containing ones (e.g., diazinon) (vide infra), whereas the bienzyme-SiQD system mentioned above does not.

Zheng and colleagues developed a nanostructured sensor film that exhibits picomolar detection limits for PX (LOD = 11 pM) and PT (LOD = 4.5 pM) from a layer-by-layer assembly of acetylcholine esterase, poly(allylamine hydrochloride), sodium polystyrenesulfonate, and CdTe QDs.[20] Their sensor response relies on the acetylcholine esterase-catalyzed hydrolysis of acetylthiocholine to acetate and thiocholine and the tendency of the resulting thiocholine to quench the PL of CdTe QDs. PX and PT are detected through their ability to inhibit acetylcholine esterase activity that leads to a decrease in the PL quenching rate. Compared to their sensor, our mAm/SiQD ratiometric detection system is, again, much simpler and more robust (i.e., a solution consisting of fluorescent/photoluminescent molecules and nanoparticles compared to a film comprised of alternating layers of enzymes, polymers, and quantum dots). Moreover, our sensor does not employ cytotoxic Cd-based QDs.

In an effort to evaluate the utility of the present sensing platform, we investigated the effects of different ions and organic species that are common interferents. This was achieved for response to the presence of PX and PT by determining the ratios (R) of I_{525}/I_{635} before and

after addition of the quenchers to an aqueous solution containing the interfering species (Figures 4-10A to 4-10D). All solutions yielded *R* values that differed significantly from the negative control (i.e., pure mQ water) and were comparable to those of the corresponding positive controls (i.e., PX or PT in HEPES buffer). These observations indicate that PX and PT detection is relatively unaffected by the presence of inorganic and organic species. The values of *R* obtained for PT in the presence of divalent cations (i.e., Ca^{2+} and Mg^{2+}) and malonic acid (MA) differ slightly from the (+) control. mAm, which has a pK_a of 5.8 and is known to exhibit diminished fluorescence intensity under acidic conditions as a result of the protonation of its peptide-based fluorophore.[37] This may explain why the *R* value of PT in the presence of MA differs slightly from that of the (+) control. The cause of the slight variations of PT *R* values in the presence of Ca^{2+} and Mg^{2+} ions compared to that of the (+) control is the subject of an ongoing investigation. These variations do not preclude the present sensing application.

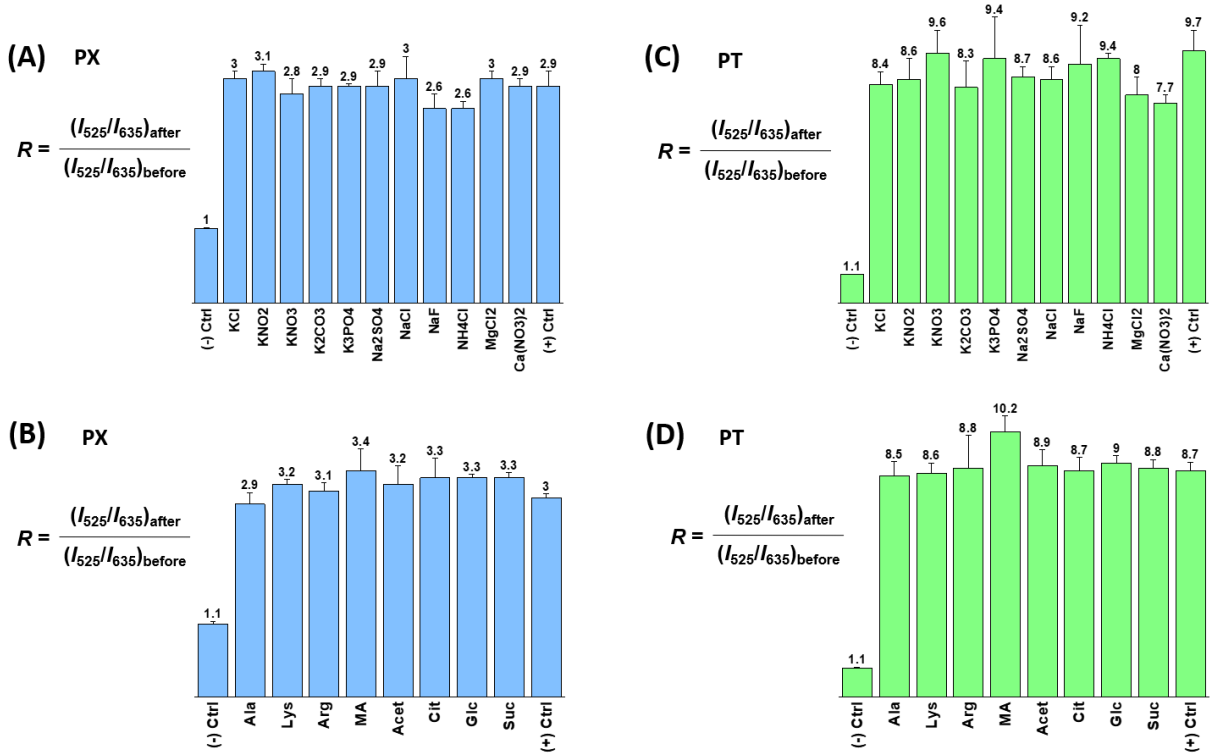

Figure 4-10. Plots of the effects of common interferents on the detection of **(A,B)** PX and **(C,D)** PT (C_{SiQDs} = 1.1 μM, C_{mAm} = 0.9 μM, λ_{ex} = 365 nm).

Figure 4-11 shows that the ratiometric sensor is selective for PX, PT, and PN. The figure also shows that, consistent with the Stern–Volmer plots, PT quenches the PL of the SiQDs best, followed by PX, and then by PN. The other organophosphate esters, diazinon (DZ), malathion (MT), and chlorpyrifos (CP), did not quench the PL of the SiQDs, presumably because they do not contain nitroaromatic groups.

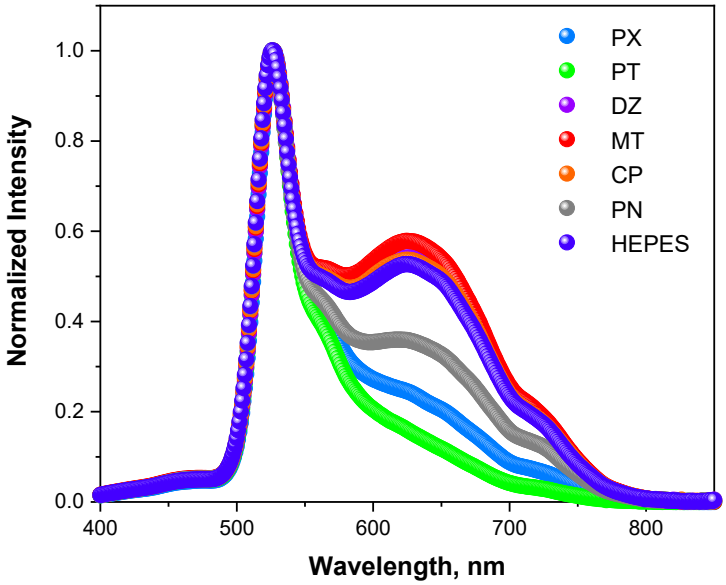

Figure 4-11. PL spectra of solutions containing SiQDs and mAm in the presence of PX, PT, DZ, MT, CP, and PN (C_{SiQDs} = 1.1 μM, C_{mAm} = 1.8 μM, λ_{ex} = 365 nm).

To expand the utility of the present sensing platform, we prepared paper-based sensors from SiQDs and mAm and used them in detecting PX and PT. The papers were allowed to dry fully prior to use. Figure 4-12A shows photographs of the paper-based sensors spotted with: 100 μM of different organophosphate esters, 100 μM of PN, tap water, and mQ water under UV light illumination (λ = 365 nm). The PL arising from spots exposed to PX, PT, and PN are qualitatively (visual inspection) more green than those of the other samples. To quantify these findings better, the emission from the spots was partitioned into red, green, and blue channels using a commerically available smart phone application (i.e., Color Picker), and the ratio of green and red components was evaluated. The ratios obtained for PX and PT (Figure 4-12B) were 4.4 and 1.9, respectively, and are significantly larger compared to those obtained for mQ water (1.2) and tap water (1.1). We also note that the ratios obtained for spots arising from DZ, MT, and CP spots are close to that of mQ water, consistent with their inability to quench SiQD

PL. Interestingly, PX appears to quench SiQD PL more strongly on paper than PT. This may have arisen from the relatively lower polarity of PT,[63] which hinders it from effectively accessing the SiQDs that are supported in the hydrophilic cellulose network of the paper. Figure 4-12C reveals that PX and PT can be detected and distinguished from water and other organophosphate esters even at solution concentrations as low as 5 µM, corresponding to 1.4 ng and 1.5 ng of PX and PT, respectively, spotted on the paper. Also, PN can be detected at a concentration of 100 µM but not at 5 µM. These results support the implementation of the paper-based sensors developed here as a quick and convenient litmus test for the detection of PX and PT.

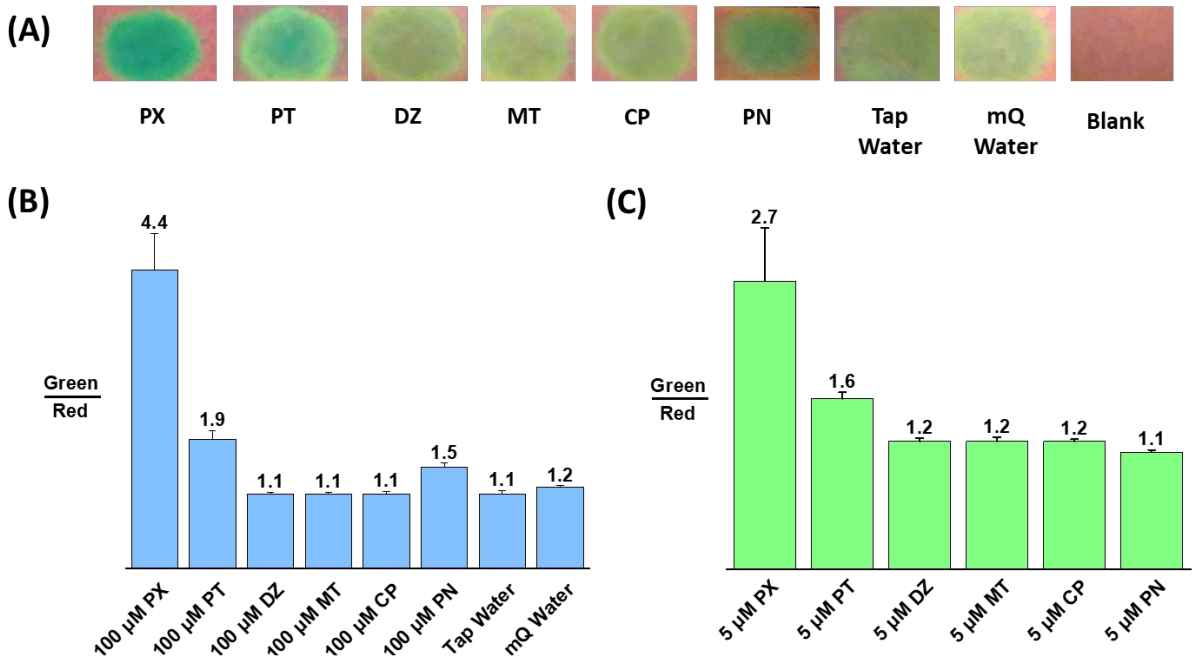

Figure 4-12. (A) Unprocessed photographs of paper-based sensors spotted with PX, PT, DZ, MT, CP, PN, tap water, and mQ water under UV light illumination (λ_{ex} = 365 nm). Green/Red ratios obtained for each sample at concentrations of **(B)** 100 µM and **(C)** 5 µM.

4.4 Summary and Conclusions

The present investigation reports the preparation of a convenient and biocompatible ratiometric photoluminescent sensor for paraoxon (PX) and parathion (PT) that is based upon mAmetrine1.2 and silicon quantum dots. PX and PT selectively quench SiQD photoluminescence by acting as dynamic quenchers. The ratiometric sensor developed has

micromolar detection limits for PX and PT, is unaffected by inorganic and organic species, and is selective for PX and PT. Paper-based sensors containing mAm and SiQDs also have been used for detecting PX and PT at low concentrations. This sensing platform provides a straightforward and cost-effective means for direct detection of PX and PT by eliminating the need for intermediary biomolecules, such as enzymes for signal generation, specificity, and selectivity.

4.5 References

(1) Sidell, F. R.; Borak, J. Chemical Warfare Agents: II. Nerve Agents. *Ann. Emerg. Med.* **1992**, *21* (7), 865–871.

(2) Holstege, C. P.; Kirk, M.; Sidell, F. R. Chemical Warfare: Nerve Agent Poisoning. *Crit. Care Clin.* **1997**, *13* (4), 923–942.

(3) Deshpande, L. S.; Carter, D. S.; Phillips, K. F.; Blair, R. E.; DeLorenzo, R. J. Development of Status Epilepticus, Sustained Calcium Elevations and Neuronal Injury in a Rat Survival Model of Lethal Paraoxon Intoxication. *Neurotoxicology* **2014**, *44*, 17–26.

(4) Deshpande, L. S.; Phillips, K.; Huang, B.; DeLorenzo, R. J. Chronic Behavioral and Cognitive Deficits in a Rat Survival Model of Paraoxon Toxicity. *Neurotoxicology* **2014**, *44*, 352–357.

(5) Gould, C.; Folb, P. The Role of Professionals in the South African Chemical and Biological Warfare Programme. *Minerva* **2002**, *40* (1), 77–91.

(6) Truelsen, J. B. Developments in Toxics in 2004: The Ratification of the Stockholm Convention and the Rotterdam Convention. *Colo. J. Int. Environ. Law Pol.* **2005**, *16*, 217–230.

(7) Parathion Health and Safety Guide. IPCS International Programme on Chemical Safety, 1992, http://www.inchem.org/documents/hsg/hsg/hsg74.htm (accessed Jun 23, 2019).

(8) Litchfield, M. H. Estimates of Acute Pesticide Poisoning in Agricultural Workers in Less Developed Countries. *Toxicol. Rev.* **2005**, *24* (4), 271–278.

(9) Cross, G. *Dirty War: Rhodesia and Chemical Biological Warfare 1975-1980*; Helion and Company: Solihull, England, 2017; p. 80.

(10) Zaugg, S. D.; Sandstrom, M. W.; Smith, S. G.; Fehlberg, K. M. Methods of Analysis by the US Geological Survey National Water Quality Laboratory; Determination of Pesticides in Water by C-18 Solid-Phase Extraction and Capillary-Column Gas Chromatography/Mass Spectrometry with Selected-Ion Monitoring. US Geological Survey, 1995. https://nwql.usgs.gov/Public/pubs/WRIR/WRIR-01-4098.pdf (accessed Jun 19, 2019)

(11) Lee, J.; Lee, H. K. Fully Automated Dynamic In-Syringe Liquid-Phase Microextraction and on-Column Derivatization of Carbamate Pesticides with Gas Chromatography/Mass Spectrometric Analysis. *Anal. Chem.* **2011**, *83* (17), 6856–6861.

(12) Mothes, S.; Popp, P.; Wennrich, R. Analysis of Organophosphorus Insecticides in Natural Waters by Use of Stir-Bar-Sorptive Extraction Then Gas Chromatography with Atomic Emission Detection. *Chromatographia* **2003**, *57* (1), S249–S252.

(13) Buonasera, K.; D'Orazio, G.; Fanali, S.; Dugo, P.; Mondello, L. Separation of Organophosphorus Pesticides by Using Nano-Liquid Chromatography. *J. Chromatogr. A* **2009**, *1216* (18), 3970–3976.

(14) Walker, J. P.; Asher, S. A. Acetylcholinesterase-Based Organophosphate Nerve Agent Sensing Photonic Crystal. *Anal. Chem.* **2005**, *77* (6), 1596–1600.

(15) Du, D.; Chen, W.; Zhang, W.; Liu, D.; Li, H.; Lin, Y. Covalent Coupling of Organophosphorus Hydrolase Loaded Quantum Dots to Carbon Nanotube/Au Nanocomposite for Enhanced Detection of Methyl Parathion. *Biosens. Bioelectron.* **2010**, *25* (6), 1370–1375.

(16) Hou, J.; Dong, J.; Zhu, H.; Teng, X.; Ai, S.; Mang, M. A Simple and Sensitive Fluorescent Sensor for Methyl Parathion Based on L-Tyrosine Methyl Ester Functionalized Carbon Dots. *Biosens. Bioelectron.* **2015**, *68*, 20–26.

(17) Meng, X.; Wei, J.; Ren, X.; Ren, J.; Tang, F. A Simple and Sensitive Fluorescence Biosensor for Detection of Organophosphorus Pesticides Using H_2O_2-Sensitive Quantum Dots/Bi-Enzyme. *Biosens. Bioelectron.* **2013**, *47*, 402–407.

(18) Ji, X.; Zheng, J.; Xu, J.; Rastogi, V. K.; Cheng, T.-C.; DeFrank, J. J.; Leblanc, R. M. (CdSe) ZnS Quantum Dots and Organophosphorus Hydrolase Bioconjugate as Biosensors for Detection of Paraoxon. *J. Phys. Chem. B* **2005**, *109* (9), 3793–3799.

(19) Yi, Y.; Zhu, G.; Liu, C.; Huang, Y.; Zhang, Y.; Li, H.; Zhao, J.; Yao, S. A Label-Free Silicon Quantum Dots-Based Photoluminescence Sensor for Ultrasensitive Detection of Pesticides. *Anal. Chem.* **2013**, *85* (23), 11464–11470.

(20) Zheng, Z.; Zhou, Y.; Li, X.; Liu, S.; Tang, Z. Highly-Sensitive Organophosphorous Pesticide Biosensors Based on Nanostructured Films of Acetylcholinesterase and CdTe Quantum Dots. *Biosens. Bioelectron.* **2011**, *26* (6), 3081–3085.

(21) Yan, X.; Li, H.; Yan, Y.; Su, X. Selective Detection of Parathion-Methyl Based on near-Infrared CuInS2 Quantum Dots. *Food Chem.* **2015**, *173*, 179–184.

(22) McVey, B. F.; Tilley, R. D. Solution Synthesis, Optical Properties, and Bioimaging Applications of Silicon Nanocrystals. *Acc. Chem. Res.* **2014**, *47* (10), 3045–3051.

(23) Zhai, Y.; Dasog, M.; Snitynsky, R. B.; Purkait, T. K.; Aghajamali, M.; Hahn, A. H.; Sturdy, C. B.; Lowary, T. L.; Veinot, J. G. C. Water-Soluble Photoluminescent D-Mannose and L-Alanine Functionalized Silicon Nanocrystals and Their Application to Cancer Cell Imaging. *J. Mater. Chem. B* **2014**, *2* (47), 8427–8433.

(24) Gonzalez, C. M.; Iqbal, M.; Dasog, M.; Piercey, D. G.; Lockwood, R.; Klapötke, T. M.; Veinot, J. G. C. Detection of High-Energy Compounds Using Photoluminescent Silicon Nanocrystal Paper Based Sensors. *Nanoscale* **2014**, *6* (5), 2608–2612.

(25) Sinelnikov, R.; Dasog, M.; Beamish, J.; Meldrum, A.; Veinot, J. G. C. Revisiting an Ongoing Debate: What Role Do Surface Groups Play in Silicon Nanocrystal Photoluminescence? *ACS Photonics* **2017**, *4* (8), 1920–1929.

(26) Islam, M. A.; Sinelnikov, R.; Howlader, M. A.; Faramus, A.; Veinot, J. G. C. Mixed Surface Chemistry: An Approach to Highly Luminescent Biocompatible Amphiphilic Silicon Nanocrystals. *Chem. Mater.* **2018**, *30* (24), 8925–8931.

(27) Liu, J.; Erogbogbo, F.; Yong, K.-T.; Ye, L.; Liu, J.; Hu, R.; Chen, H.; Hu, Y.; Yang, Y.; Yang, J. Assessing Clinical Prospects of Silicon Quantum Dots: Studies in Mice and Monkeys. *ACS Nano* **2013**, *7* (8), 7303–7310.

(28) Chen, N.; He, Y.; Su, Y.; Li, X.; Huang, Q.; Wang, H.; Zhang, X.; Tai, R.; Fan, C. The Cytotoxicity of Cadmium-Based Quantum Dots. *Biomaterials* **2012**, *33* (5), 1238–1244.

(29) Cubitt, A. B.; Heim, R.; Adams, S. R.; Boyd, A. E.; Gross, L. A.; Tsien, R. Y. Understanding, Improving and Using Green Fluorescent Proteins. *Trends Biochem. Sci.* **1995**, *20* (11), 448–455.

(30) Ormö, M.; Cubitt, A. B.; Kallio, K.; Gross, L. A.; Tsien, R. Y.; Remington, S. J. Crystal Structure of the Aequorea Victoria Green Fluorescent Protein. *Science* **1996**, *273* (5280), 1392–1395.

(31) Miyawaki, A.; Llopis, J.; Heim, R.; McCaffery, J. M.; Adams, J. A.; Ikura, M.; Tsien, R. Y. Fluorescent Indicators for Ca^{2+} Based on Green Fluorescent Proteins and Calmodulin. *Nature* **1997**, *388* (6645), 882–887.

(32) Miyawaki, A.; Niino, Y. Molecular Spies for Bioimaging—Fluorescent Protein-Based Probes. *Mol. Cell* **2015**, *58* (4), 632–643.

(33) Zhu, A.; Qu, Q.; Shao, X.; Kong, B.; Tian, Y. Carbon-Dot-Based Dual-Emission Nanohybrid Produces a Ratiometric Fluorescent Sensor for in Vivo Imaging of Cellular Copper Ions. *Angew. Chem., Int. Ed.* **2012**, *51* (29), 7185–7189.

(34) Cao, B.; Yuan, C.; Liu, B.; Jiang, C.; Guan, G.; Han, M.-Y. Ratiometric Fluorescence Detection of Mercuric Ion Based on the Nanohybrid of Fluorescence Carbon Dots and Quantum Dots. *Anal. Chim. Acta* **2013**, *786*, 146–152.

(35) Zhang, K.; Zhou, H.; Mei, Q.; Wang, S.; Guan, G.; Liu, R.; Zhang, J.; Zhang, Z. Instant Visual Detection of Trinitrotoluene Particulates on Various Surfaces by Ratiometric Fluorescence of Dual-Emission Quantum Dots Hybrid. *J. Am. Chem. Soc.* **2011**, *133* (22), 8424–8427.

(36) Chen, X.; Wo, F.; Jin, Y.; Tan, J.; Lai, Y.; Wu, J. Drug-Porous Silicon Dual Luminescent System for Monitoring and Inhibition of Wound Infection. *ACS Nano* **2017**, *11*, 7938–7949.

(37) Ding, Y.; Ai, H.; Hoi, H.; Campbell, R. E. Förster Resonance Energy Transfer-Based Biosensors for Multiparameter Ratiometric Imaging of Ca^{2+} Dynamics and Caspase-3 Activity in Single Cells. *Anal. Chem.* **2011**, *83* (24), 9687–9693.

(38) Hessel, C. M.; Henderson, E. J.; Veinot, J. G. C. Hydrogen Silsesquioxane: A Molecular Precursor for Nanocrystalline Si- SiO2 Composites and Freestanding Hydride-Surface-Terminated Silicon Nanoparticles. *Chem. Mater.* **2006**, *18* (26), 6139–6146.

(39) Robidillo, C. J. T.; Aghajamali, M.; Faramus, A.; Sinelnikov, R.; Veinot, J. G. C. Interfacing Enzymes with Silicon Nanocrystals through the Thiol–Ene Reaction. *Nanoscale* **2018**, *10* (39), 18706–18719.

(40) Robidillo, C. J. T.; Islam, M. A.; Aghajamali, M.; Faramus, A.; Sinelnikov, R.; Zhang, X.; Boekhoven, J.; Veinot, J. G. C. Functional Bioinorganic Hybrids from Enzymes and Luminescent Silicon-Based Nanoparticles. *Langmuir* **2018**, *34* (22), 6556–6569.

(41) Jakob, M.; Aissiou, A.; Morrish, W.; Marsiglio, F.; Islam, M.; Kartouzian, A.; Meldrum, A. Reappraising the Luminescence Lifetime Distributions in Silicon Nanocrystals. *Nanoscale Res. Lett.* **2018**, *13* (1), 383–394.

(42) Otsuka, H.; Nagasaki, Y.; Kataoka, K. PEGylated Nanoparticles for Biological and Pharmaceutical Applications. *Adv. Drug Delivery Rev.* **2012**, *64*, 246–255.

(43) Pelaz, B.; del Pino, P.; Maffre, P.; Hartmann, R.; Gallego, M.; Rivera-Fernandez, S.; de la Fuente, J. M.; Nienhaus, G. U.; Parak, W. J. Surface Functionalization of Nanoparticles with Polyethylene Glycol: Effects on Protein Adsorption and Cellular Uptake. *ACS Nano* **2015**, *9* (7), 6996–7008.

(44) Dai, Q.; Walkey, C.; Chan, W. C. Polyethylene Glycol Backfilling Mitigates the Negative Impact of the Protein Corona on Nanoparticle Cell Targeting. *Angew. Chem., Int. Ed.* **2014**, *53* (20), 5093–5096.

(45) Wörz, A.; Berchtold, B.; Moosmann, K.; Prucker, O.; Rühe, J. Protein-Resistant Polymer Surfaces. *J. Mater. Chem.* **2012**, *22* (37), 19547–19561.

(46) Clark, R. J.; Dang, M. K.; Veinot, J. G. C. Exploration of Organic Acid Chain Length on Water-Soluble Silicon Quantum Dot Surfaces. *Langmuir* **2010**, *26* (19), 15657–15664.

(47) Mkhatresh, O. A.; Heatley, F. A Study of the Products and Mechanism of the Thermal Oxidative Degradation of Poly (Ethylene Oxide) Using 1H and 13C 1-D and 2-D NMR. *Polym. Int.* **2004**, *53* (9), 1336–1342.

(48) Yang, L.; Heatley, F.; Blease, T. G.; Thompson, R. I. A Study of the Mechanism of the Oxidative Thermal Degradation of Poly (Ethylene Oxide) and Poly (Propylene Oxide) Using 1H-and 13C-NMR. *Eur. Polym. J.* **1996**, *32* (5), 535–547.

(49) Matsuura, H.; Miyazawa, T. Vibrational Analysis of Molten Poly (Ethylene Glycol). *J. Polym. Sci., Polym. Phys.* **1969**, *7* (10), 1735–1744.

(50) Yang, Z.; Gonzalez, C. M.; Purkait, T. K.; Iqbal, M.; Meldrum, A.; Veinot, J. G. C. Radical Initiated Hydrosilylation on Silicon Nanocrystal Surfaces: An Evaluation of Functional Group Tolerance and Mechanistic Study. *Langmuir* **2015**, *31* (38), 10540–10548.

(51) Doremus, R. H. Oxidation of Silicon by Water and Oxygen and Diffusion in Fused Silica. *J. Phys. Chem.* **1976**, *80* (16), 1773–1775.

(52) Wu, E. C.; Park, J. H.; Park, J.; Segal, E.; Cunin, F.; Sailor, M. J. Oxidation-Triggered Release of Fluorescent Molecules or Drugs from Mesoporous Si Microparticles. *ACS Nano* **2008**, *2* (11), 2401–2409.

(53) Flitsch, R.; Raider, S. I. Electron Mean Escape Depths from X- Ray Photoelectron Spectra of Thermally Oxidized Silicon Dioxide Films on Silicon. *J. Vac. Sci. Technol.* **1975**, *12* (1), 305–308.

(54) Damodaran, V. B.; Fee, C. J.; Ruckh, T.; Popat, K. C. Conformational Studies of Covalently Grafted Poly (Ethylene Glycol) on Modified Solid Matrices Using X-Ray Photoelectron Spectroscopy. *Langmuir* **2010**, *26* (10), 7299–7306.

(55) Briggs, D.; Beamson, G. Primary and Secondary Oxygen-Induced C1s Binding Energy Shifts in x-Ray Photoelectron Spectroscopy of Polymers. *Anal. Chem.* **1992**, *64* (15), 1729–1736.

(56) Thomas, H. R.; O'Malley, J. J. Surface Studies on Multicomponent Polymer Systems by X-Ray Photoelectron Spectroscopy. Polystyrene/Poly (Ethylene Oxide) Diblock Copolymers. *Macromolecules* **1979**, *12* (2), 323–329.

(57) Anderson, S. L.; Luber, E. J.; Olsen, B. C.; Buriak, J. M. Substance over Subjectivity: Moving beyond the Histogram. *Chem. Mater.* **2016**, *28*, 5973–5975.

(58) Content, S.; Trogler, W. C.; Sailor, M. J. Detection of Nitrobenzene, DNT, and TNT Vapors by Quenching of Porous Silicon Photoluminescence. *Chem. Eur. J.* **2000**, *6* (12), 2205–2213.

(59) Eyer, F.; Meischner, V.; Kiderlen, D.; Thiermann, H.; Worek, F.; Haberkorn, M.; Felgenhauer, N.; Zilker, T.; Eyer, P. Human Parathion Poisoning. *Toxicol. Rev.* **2003**, *22* (3), 143–163.

(60) Eto, M.; Kishimoto, K.; Matsumura, K.; Ohshita, N.; Oshima, Y. Studies on Saligenin Cyclic Phosphorus Esters with Insecticidal Activity Part IX. *Agric. Biol. Chem.* **1966**, *30* (2), 181–185.

(61) Nishizawa, Y.; Fujii, K.; Kadota, T.; Miyamoto, J.; Sakamoto, H. Studies on the Organophosphorus Insecticides: Part VII. Chemical and Biological Properties of New Low Toxic Organophosphorus Insecticide. O, O-Dimethyl-O-(3-Methyl-4-Nitrophenyl) Phosphorothioate. *Agric. Biol. Chem.* **1961**, *25* (8), 605–610.

(62) DuBois, K.P.; Doull, J.; Salerno, P.R.; Coon, J.M. Studies on the Toxicity and Mechanism of Action of *p*-Nitrophenyl Diethyl Thionophosphate (Parathion). *J. Pharmacol. Exp. Ther.* **1949**, *95* (1), 79-91.

(63) Koivistoinen, P.; Meriläinen, M. Paper Chromatographic Studies on the Effect of Ultraviolet Light on Parathion and Its Derivatives. *Acta Agr. Scand.* **1962**, *12* (4), 267–276.

Chapter 5

Conclusions and Future Work

5.1 Conclusions

Silicon-based quantum dots (SiQDs) offer advantages of nontoxicity,[1] biocompatibility,[2] and long photoluminescence (PL) lifetimes[3] for applications geared at biological imaging,[2,4] theranostics,[5] and chemical sensing.[6–9] Recent synthetic advances made in the area of preparation of water-soluble SiQDs[4,10] have made possible the implementation of these nanoparticles in bioimaging and chemical detection in aqueous environments.[4,6,7] This thesis shows examples where water-soluble SiQDs have been interfaced covalently with enzymes or used in conjunction with a fluorescent protein for possible applications in theranostics and chemical sensing, respectively.

Chapter 1 discusses the preparation of functional bioinorganic hybrids from enzymes and SiQDs that preserve the photoluminescent properties characteristic of SiQDs and the catalytic activity of enzymes. This is accomplished through the amide coupling reaction between carboxylic acid groups on acid-terminated SiQDs and the amine groups in enzymes (Scheme 5-1).[10] Notably, the orange PL of the SiQDs is not altered or quenched by the nitrogen-containing coupling agents employed for the reaction. The affinity of the enzymes for their substrates is diminished upon conjugation with the SiQDs. This can be attributed reasonably to the partial deformation of immobilised enzymes, their reduced mobility, and the potentially reduced accessibility of the enzymes' active site to the substrates. Furthermore, the amount by which the enzyme's affinity for its substrate is diminished may be dependent on the size, shape, and surface composition of the nanoparticles to which they are linked covalently. Despite the reduction in catalytic activity, the immobilised enzymes remain sufficiently active to perform their intended catalytic function.

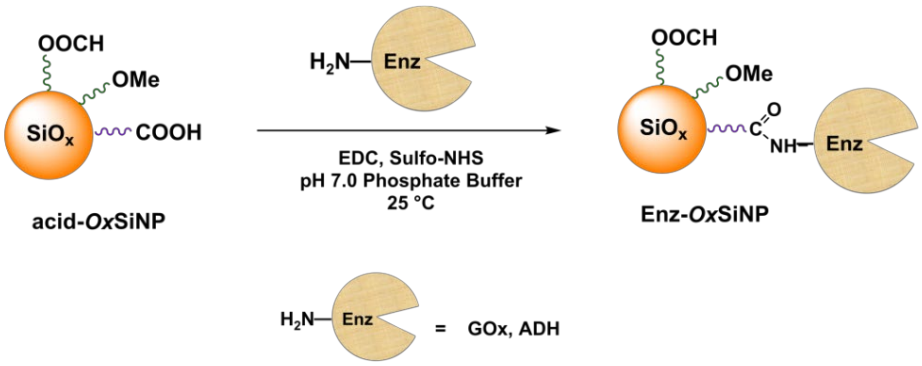

Scheme 5-1. Bioconjugation of acid-*Ox*SiNPs with enzymes through the amide coupling reaction (see Chapter 2 for details).

Chapter 2 details the use of the thiol–ene 'click' reaction as a convenient and quick method for conjugating enzymes with SiQDs.[7] This reaction mitigates the formation of unwanted side products and covalent multimerization of enzymes (and proteins, in general) typically encountered in amide coupling reactions. Alkene-terminated SiQDs were reacted with cysteine-containing enzymes through the thiol–ene reaction in the presence of a photochemical initiator and ultraviolet light (Scheme 5-2). The bioinorganic hybrids thus obtained exhibited the photoluminescent properties characteristic of SiQDs and the catalytic activity of the enzymes. Furthermore, the PL of the hybrids were quenched by the products of the enzyme-catalysed reactions (e.g., *o*-nitrophenolate ion, ammonia), potentially affording a sensing platform for the substrates (e.g., *o*-nitrophenyl-β-D-galactopyranoside, urea).

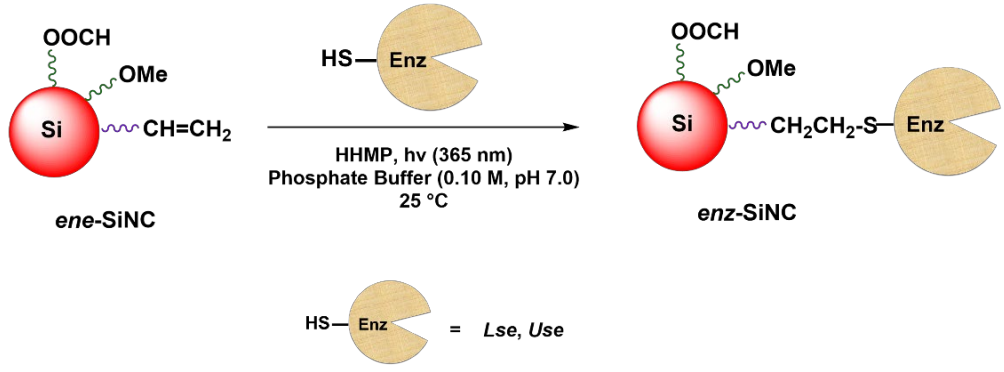

Scheme 5-2. Bioconjugation of *ene*-SiNCs with enzymes through the photochemical thiol–ene reaction (see Chapter 3 for details).

Chapter 4 demonstrates the utility of SiQDs and green fluorescent protein (GFP) in the ratiometric detection of the organophosphate nerve agents paraoxon (PX) and parathion (PT).[6] PX and PT selectively quench SiQD PL (Figure 5-1A) through a dynamic quenching mechanism by potentially accepting electrons from the excited SiQDs, thereby preventing radiative relaxation. The reported ratiometric sensor platform based upon SiQDs and GFP allowed for visual analyte detection (Figure 5-1B) and afforded micromolar limits of detection for PX and PT. Moreover, the sensor is unaffected by common inorganic and organic interferents and is specific for nitro-containing organophosphate nerve agents. Lastly, paper-based sensors for PX and PT have been fabricated from SiQDs and GFP, which further supports their implementation for the convenient and straightforward detection of PX and PT in 'real-world' samples.

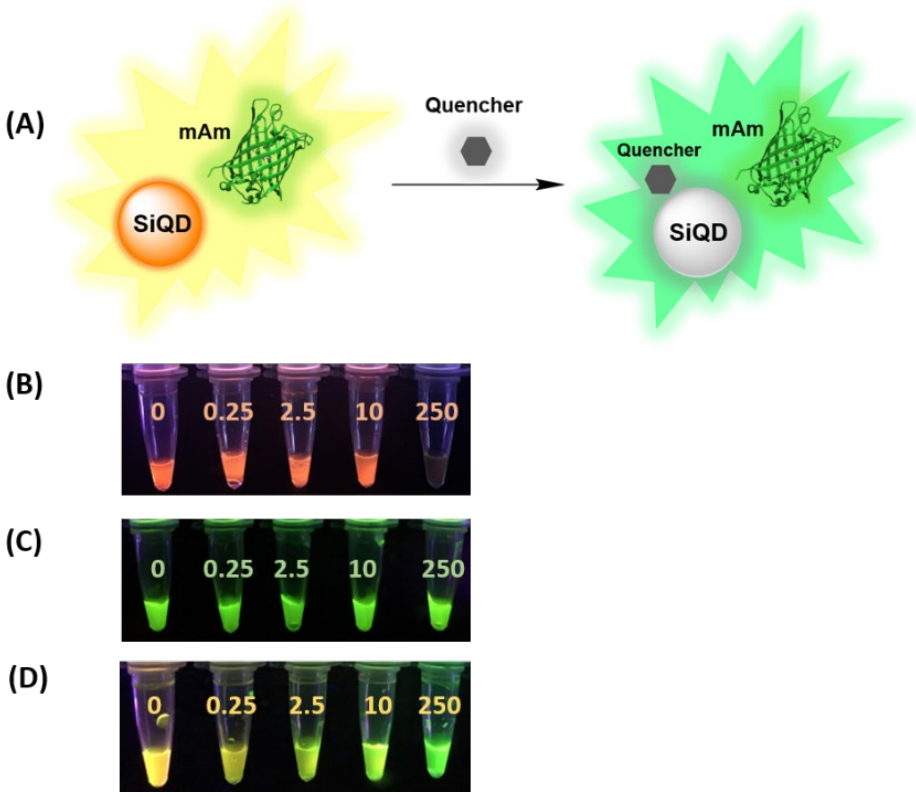

Figure 5-1. (A) Sensing motif that exploits the combined PL of SiQDs and mAm upon addition of a quencher. Photographs showing a series of solutions containing **(B)** only SiQDs, **(C)** only mAm, and **(D)** SiQDs and mAm in the presence of increasing micromolar concentrations of PX under UV illumination (λ_{ex} = 365 nm) (see Chapter 4 for details).

5.2 Future Work

5.2.1 Thermally Responsive Photoluminescent Hybrids from Elastin-Like Polypeptides and Silicon-Based Quantum Dots

Elastin-like polypeptides (ELPs) are genetically engineered elastomeric proteins that undergo reversible phase transition as a result of changes in temperature, pH, and ionic strength.[11,12] They are comprised of the repeating pentapeptide sequence Valine-Proline-Glycine-*X*-Glycine, where *X* refers to a variable amino acid, which can be any amino acid except proline.[11,12] ELPs are soluble in water at temperatures below their inverse transition temperature (T_t) but insoluble at temperatures higher than T_t. The value of T_t depends on the chemical properties of the variable amino acid, the molecular weight of the ELP, and its concentration in solution.[11,12]

Bioinorganic hybrids can be prepared from ELPs and acid-terminated SiQDs through the amide coupling reaction (Scheme 5-3). These hybrids are expected to retain the thermal responsiveness of the ELPs and the characteristic photoluminescence (PL) of the SiQDs (Scheme 5-4). Furthermore, the values of T_t of these hybrids are expected to be affected significantly by the hydrophilic nature of the poly(ethylene oxide) coating of the SiQDs. Thus, experiments must be performed in order to optimize the conditions under which the hybrids will show reversible phase transition (e.g., pH, ionic strength, buffer system employed). These photoluminescent and thermally responsive hybrids may find utility in the design of smart materials for theranostics, drug delivery, and other biomedical applications.

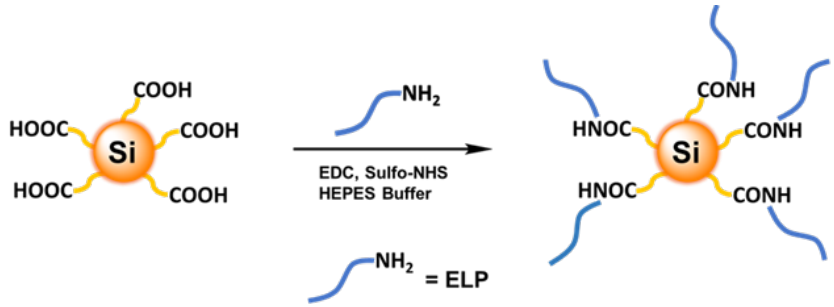

Scheme 5-3. Conjugation of ELP with acid-terminated SiQDs through the amide coupling reaction.

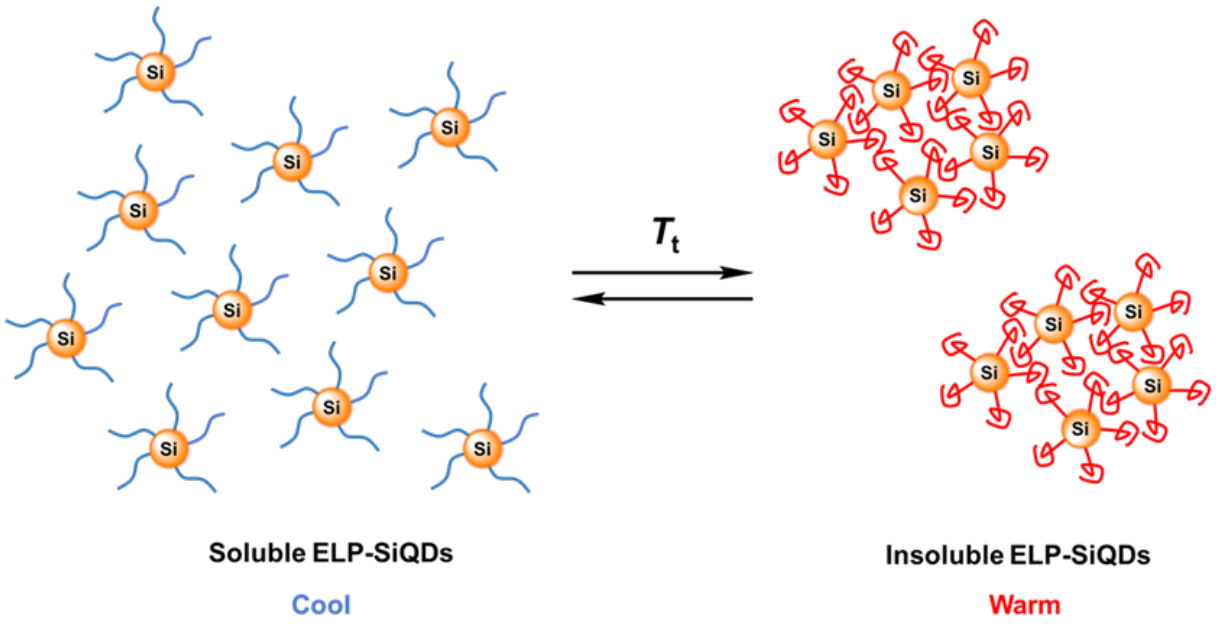

Scheme 5-4. Thermally responsive photoluminescent bioinorganic hybrids from ELPs and SiQDs.

5.2.2 Intracellular pH Sensing Using Fluorescent Protein–Silicon Quantum Dot Hybrids

The proper maintenance of intracellular pH is crucial for the normal operation of cells.[13] Many important cellular processes are associated intimately with intracellular pH; processes like cell signalling, activation, growth, and proliferation, to name a few, depend critically on tightly regulated pH within cells.[13,14] Furthermore, abnormal intracellular pH values are linked to pathophysiological conditions, like cancer[15] and Alzheimer's disease.[16] Thus, tools that enable monitoring of pH within cells are important for probing cellular processes, physiology, and associated pathologies.

Measurement of intracellular pH can be accomplished using microelectrodes and spectroscopic techniques, such as nuclear magnetic resonance spectroscopy (NMR) and absorption and fluorescence spectroscopy.[14,17,18] Recently, ratiometric sensors based upon a combination of fluorophores (e.g., organic dyes, quantum dots, fluorescent proteins) have been designed and implemented for measurement of intracellular pH.[19–22] Sensing motifs based upon this design take advantage of the pH-dependent energy transfer between covalently linked fluorophores.[19] Dennis and co-workers, for instance, reported a sensing platform consisting of green-emitting Cd-based quantum dots (Cd QDs) conjugated with orange fluorescent proteins

as tools for imaging cells and cellular compartments through pH-dependent Förster Resonance Energy Transfer (FRET).[19] The known toxicity of Cd and the tendency of Cd^{2+} to leach out of Cd QDs,[23] however, limits the potential utility of this probe in real life applications.

Green fluorescent proteins (GFPs) consist of a peptide-based fluorophore that is housed in a barrel-like protein structure.[24,25] Thus, the fluorophore is protected from quenchers, except for small ions like H^+. A long Stokes' shift GFP variant, mAmetrine1.2 (mAm), has a pK_a of 5.8 and exhibits significantly diminished PL at pH lower than this value.[26] On the contrary, nontoxic red-emitting SiQDs show relatively stable PL at pH values ranging from 5.0 to 7.0.

We thus envision the preparation of biocompatible dual-emitting covalent hybrids from mAm and SiQDs through the amide coupling reaction, which can be used as a pH sensor for intracellular imaging (Scheme 5-5). The hybrids are expected to glow red at relatively acidic pH (e.g., pH 5.0) and yellow (i.e., a combination of green mAm fluorescence and red SiQD emission) at neutral pH. We hypothesize that these hybrids could be used in imaging and discriminating between cellular compartments, such as the cytoplasm, endosome, and lysosome. These compartments differ significantly in their pH, with the lysosome being acidic, the cytoplasm neutral, and the endosome having a pH intermediate between the two.[19] Furthermore, the resulting hybrids can be used for discriminating cancer cells from healthy cells, as the former typically has a more acidic intracellular pH compared to the other.[15]

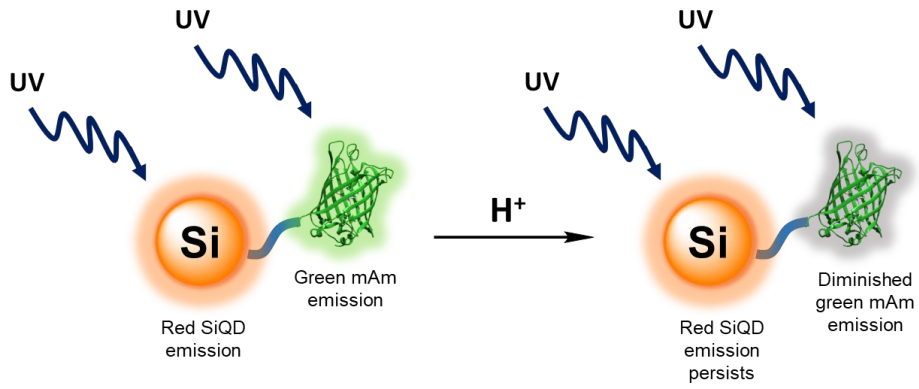

Scheme 5-5. Ratiometric pH sensing motif for cellular imaging using mAm-SiQD hybrids.

5.2.3 Tuning Enzyme Activity of Enzyme–Silicon Quantum Dot Hybrids through Dissipative Self-Assembly

Dissipative self-assembly (DSA) of molecules and nanoparticles fueled by chemical reaction networks provides a means for preparing novel materials with unique properties.[27,28] DSA involves the conversion of precursors into building blocks, which then associate into supramolecular assemblies[27] through consumption of a chemical fuel, such as *N*-(3-dimethylaminopropyl)-*N′*-ethylcarbodiimide (EDC).[29] Because the building blocks are kinetically labile, they spontaneously decompose back into the precursors.[27] The interplay between the rates of precursor activation, building block assembly, building block deactivation, and disassembly imparts a finite lifetime on the supramolecular assemblies, which is directly dependent on the kinetic characteristics of the reaction network that supports their formation.[30]

This project is geared at the preparation of a biologically active material from enzyme-conjugated silicon quantum dots (*enz*-SiQDs) and acid-terminated SiQDs (*acid*-SiQDs), which exhibits time-dependent enzymatic activity through DSA. This will be accomplished through the conversion of *acid*-SiQDs (precursors) into self-assembling *N*-hydroxysuccinimide-functionalized SiQDs (*OSu*-SiQDs; building blocks) using EDC as fuel (Scheme 5-6). As shown in Scheme 5-7, we expect the *enz*-SiQDs embedded within the self-assembled Osu-SiQDs to exhibit diminished activity compared to non-assembled *enz*-SiQDs, as a result of the reduced accessibility of the enzyme for its substrate. Furthermore, we expect the *enz*-SiQDs to recover their catalytic activity fully upon complete hydrolysis of *Osu*-SiQDs and disassembly. Thus, DSA allows for the design and preparation of smart and responsive biological materials by exerting spatio-temporal control over material properties (e.g., catalytic activity) through a rational variation in fuel concentration.

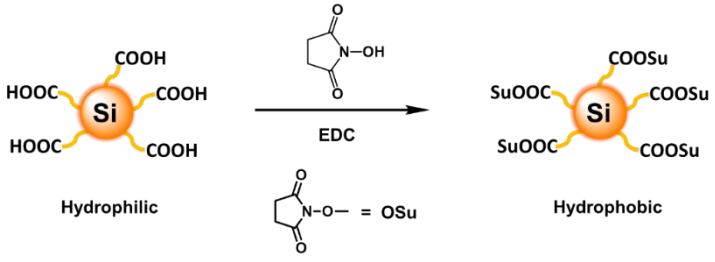

Scheme 5-6. Conversion of hydrophilic *acid*-SiQDs (precursors) into hydrophobic *Osu*-SiQDs (building blocks) using EDC as fuel.

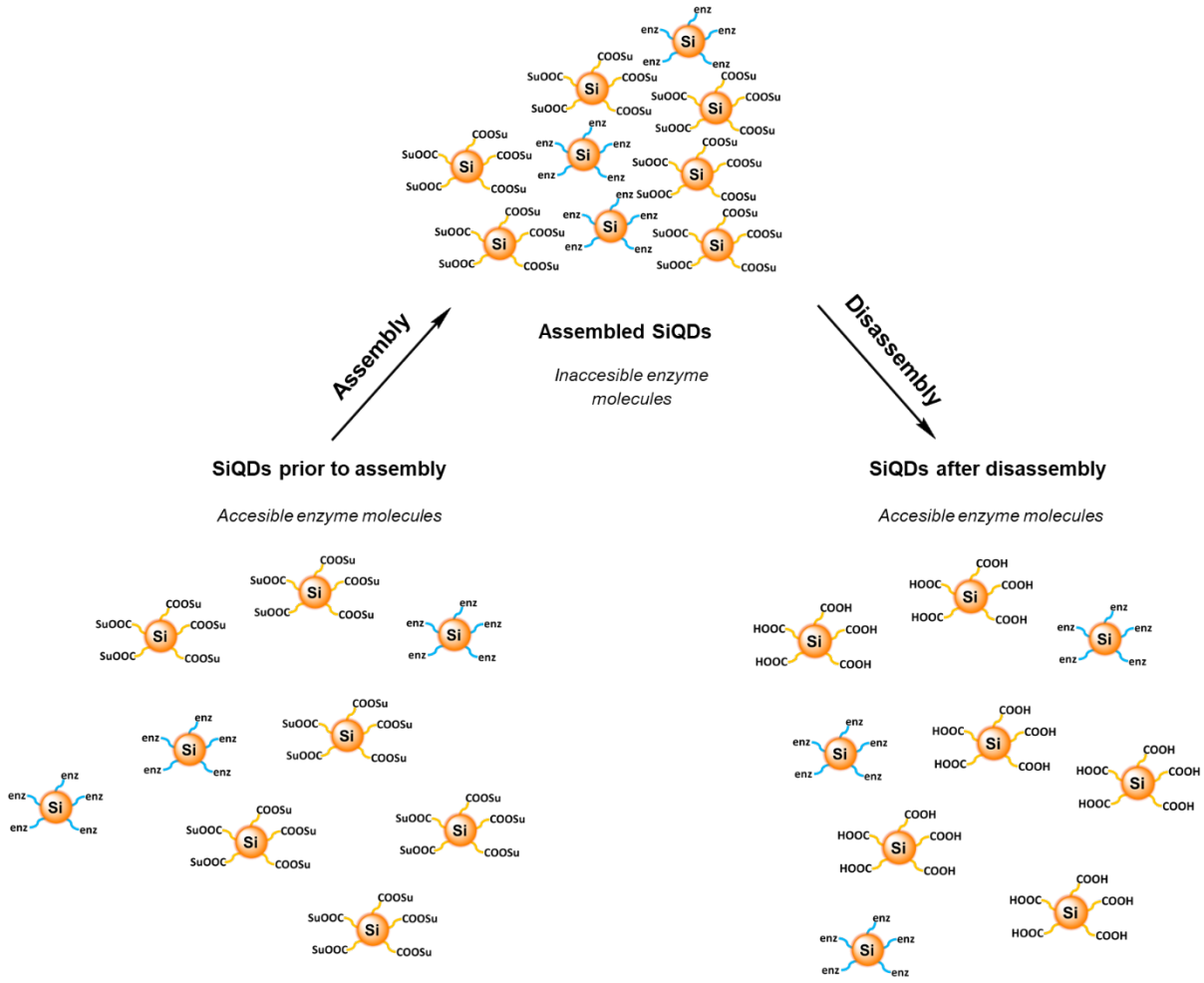

Scheme 5-7. Dissipative self-assembly of a mixture of *OSu*-SiQDs and *enz*-SiQDs. The hydrophobic *Osu*-SiQDs form assemblies, which then undergo disassembly upon hydrolysis into *acid*-SiQDs. The enzyme molecules bound to the *enz*-SiQDs become buried within the assemblies, resulting in diminished catalytic activity. This catalytic activity is recovered upon complete disassembly.

5.2.4 Silicon Nanocrystals as Selective Photoluminescent Dual Sensors for Tetrahydrocannabinol and Fentanyl

Tetrahydrocannabinol (THC) is the principal psychoactive compound found in marijuana. It is responsible for the characteristic 'high' and temporary cognitive and physical impairments associated with cannabis usage.[31] Canada legalised recreational marijuana in 2018. However, there is no rapid and straightforward method, equivalent to the alcohol breathalyzer, for detecting or evaluating impairment. In this context, criminal offences associated with marijuana consumption (e.g., impaired driving) remain of paramount public concern.

Fentanyl (FTY), a powerful opioid pain medication, is also a serious public health concern;[32] it is a popular illicit recreational drug. While useful when employed under a physician's supervision, FTY is extremely dangerous and, as little as 2 mg, is lethal to most individuals.[33] As a direct result of illegal FTY use and the associated deaths (over 8,000 Canadian deaths since 2016),[34] an ongoing public health crisis was declared in Canada in 2015.[35] In addition, there have been reports of fentanyl-laced marijuana in the United Kingdom[36] and the United States.[37] Clearly, FTY and THC pose serious public health and safety threats in Canada and the world.

Reports describing the use of gold nanoparticles/nanorods, AuNP(R)s, for biomedical applications abound in the literature.[38–41] Of relevance to this future work is the ability of AuNP(R)s to quench the photoluminescence (PL) of dyes[42,43] and cytotoxic cadmium-based quantum dots (Cd QDs) efficiently.[23,44] While not demonstrated to date, it is anticipated that QDs based upon biocompatible silicon (SiQDs)[45] will behave similarly. Highlighting the potential of SiQDs, their biocompatibility combined with their surface tailorability already have opened the door to possible applications in biological imaging[46] and chemical sensing.[47] Recently, we reported functional hybrids from SiNCs and catalytic protein molecules, and we demonstrated their potential utility in chemical sensing and the simultaneous detection and treatment of diseases.[7,10]

This work will target the preparation of new hybrid structures made up of AuNP(R)s and SiQDs held together by DNA interactions that do not photoluminesce when assembled. Upon dissociation of these hybrids in the presence of THC and/or FTY, a characteristic bright SiQD PL appears, thus providing a sensor. The PL intensity of the liberated SiQDs will be proportional to the concentration of the target in question and can be used for its selective quantification. To realize these advanced sensors, red and blue-photoluminescent DNA-coated SiQDs (*red*-DNA-SiNCs and *blue*-DNA-SiNCs) will be prepared using established procedures developed in the Veinot laboratory.[10] Similarly, DNA-coated AuNP(R)s, DNA-AuNP(R)s, will be synthesized using known methods.[48] The DNA on the *red*-DNA-SiNCs and *blue*-DNA-SiQDs will be designed specifically to have stronger interactions with THC and FTY, respectively, compared to the DNA on DNA-AuNP(R)s. These differing strengths of interactions will allow displacement of DNA-AuNP(R)s from the hybrids, resulting in red (THC), blue (FTY), or purple (combination of THC and FTY) PL and providing a sensitive,

rapid, and convenient means for qualitatively detecting THC, FTY, and fentanyl-laced marijuana (Scheme 5-8). The PL intensities and colour related to the specific concentrations of THC and FTY in the samples also can be evaluated using a portable fluorescence detector, thus providing a quick and cost-effective method for their quantification. Once established, the general sensor design and methods can be extended readily to the detection and quantification of other opioids and illicit drug cocktails (e.g., fentanyl-laced heroin).

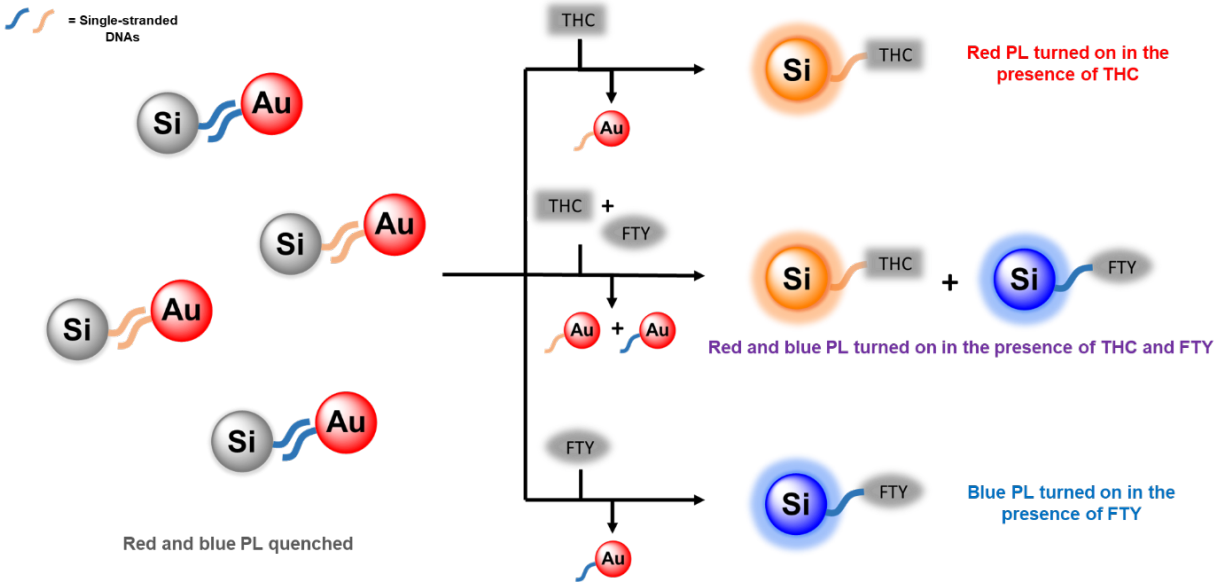

Scheme 5-8. Detection of tetrahydrocannabinol (THC) and fentanyl (FTY) using red- and blue-emitting SiQDs.

Success in this work will afford a rapid and straightforward detection system for THC and FTY that potentially can be employed by law enforcers in prosecuting cases of marijuana-related criminal offences and curbing the illegal drug trade involving fentanyl and fentanyl-laced opioids in Canada and around the world.

5.3 References

(1) Liu, J.; Erogbogbo, F.; Yong, K.-T.; Ye, L.; Liu, J.; Hu, R.; Chen, H.; Hu, Y.; Yang, Y.; Yang, J.; Roy, I.; Karker, N. A.; Swihart, M. T.; Prasad, P. N. Assessing Clinical Prospects of Silicon Quantum Dots: Studies in Mice and Monkeys. *ACS Nano* **2013**, *7* (8), 7303–7310.

(2) Erogbogbo, F.; Yong, K.-T.; Roy, I.; Xu, G.; Prasad, P. N.; Swihart, M. T. Biocompatible Luminescent Silicon Quantum Dots for Imaging of Cancer Cells. *ACS Nano* **2008**, *2* (5), 873–878.

(3) Sinelnikov, R.; Dasog, M.; Beamish, J.; Meldrum, A.; Veinot, J. G. C. Revisiting an Ongoing Debate: What Role Do Surface Groups Play in Silicon Nanocrystal Photoluminescence? *ACS Photonics* **2017**, *4* (8), 1920–1929.

(4) Islam, M. A.; Sinelnikov, R.; Howlader, M. A.; Faramus, A.; Veinot, J. G. C. Mixed Surface Chemistry: An Approach to Highly Luminescent Biocompatible Amphiphilic Silicon Nanocrystals. *Chem. Mater.* **2018**, *30* (24), 8925–8931.

(5) Erogbogbo, F.; May, J.; Swihart, M.; Prasad, P. N.; Smart, K.; Jack, S. E.; Korcyk, D.; Webster, M.; Stewart, R.; Zeng, I.; Jullig, M.; Bakeev, K.; Jamieson, M.; Kasabov, N.; Gopalan, B.; Liang, L.; Hu, R.; Schliebs, S.; Villas-Boas, S.; Gladding, P. Bioengineering Silicon Quantum Dot Theranostics Using a Network Analysis of Metabolomic and Proteomic Data in Cardiac Ischemia. *Theranostics* **2013**, *3* (9), 719–728.

(6) Robidillo, C. J. T.; Wandelt, S.; Dalangin, R.; Zhang, L.; Yu, H.; Meldrum, A.; Campbell, R. E.; Veinot, J. G. C. Ratiometric Detection of Nerve Agents by Coupling Complementary Properties of Silicon-Based Quantum Dots and Green Fluorescent Protein. *ACS Appl. Mater. Interfaces* **2019**, *11* (36), 33478–33488.

(7) Robidillo, C. J. T.; Aghajamali, M.; Faramus, A.; Sinelnikov, R.; Veinot, J. G. C. Interfacing Enzymes with Silicon Nanocrystals through the Thiol–Ene Reaction. *Nanoscale* **2018**, *10* (39), 18706–18719.

(8) Gonzalez, C.; Iqbal, M.; Dasog, M.; G. Piercey, D.; Lockwood, R.; M. Klapötke, T.; C. Veinot, J. G. C. Detection of High-Energy Compounds Using Photoluminescent Silicon Nanocrystal Paper Based Sensors. *Nanoscale* **2014**, *6* (5), 2608–2612.

(9) Gonzalez, C.; C. Veinot, J. G. C. Silicon Nanocrystals for the Development of Sensing Platforms. *J. Mater. Chem. C* **2016**, *4* (22), 4836–4846.

(10) Robidillo, C. J. T.; Islam, M. A.; Aghajamali, M.; Faramus, A.; Sinelnikov, R.; Zhang, X.; Boekhoven, J.; Veinot, J. G. C. Functional Bioinorganic Hybrids from Enzymes and Luminescent Silicon-Based Nanoparticles. *Langmuir* **2018**, *34* (22), 6556–6569.

(11) Kowalczyk, T.; Hnatuszko-Konka, K.; Gerszberg, A.; Kononowicz, A. K. Elastin-like Polypeptides as a Promising Family of Genetically Engineered Protein Based Polymers. *World J. Microbiol. Biotechnol.* **2014**, *30* (8), 2141–2152.

(12) Nettles, D. L.; Chilkoti, A.; Setton, L. A. Applications of Elastin-like Polypeptides in Tissue Engineering. *Adv. Drug Deliv. Rev.* **2010**, *62* (15), 1479–1485.

(13) Busa, W. B.; Nuccitelli, R. Metabolic Regulation via Intracellular pH. *Am. J. Physiol. Regul. Integr. Comp. Physiol.* **1984**, *246* (4), R409–R438.

(14) Loiselle, F. B.; Casey, J. R. Measurement of Intracellular pH in Membrane Transporters: Methods and Protocols; Yan, Q., Ed.; Methods in Molecular Biology; Humana Press: Totowa, NJ, 2003; pp 259–280.

(15) Izumi, H.; Torigoe, T.; Ishiguchi, H.; Uramoto, H.; Yoshida, Y.; Tanabe, M.; Ise, T.; Murakami, T.; Yoshida, T.; Nomoto, M.; et al. Cellular PH Regulators: Potentially Promising Molecular Targets for Cancer Chemotherapy. *Cancer Treat. Rev.* **2003**, *29* (6), 541–549.

(16) Davies, T. A.; Fine, R. E.; Johnson, R. J.; Levesque, C. A.; Rathbun, W. H.; Seetoo, K. F.; Smith, S. J.; Strohmeier, G.; Volicer, L.; Delva, L.; Simons, E. R. Non-Age Related Differences in Thrombin Responses by Platelets from Male Patients with Advanced Alzheimer′s Disease. *Biochem. Biophys. Res. Commun.* **1993**, *194* (1), 537–543.

(17) Wray, S. Smooth Muscle Intracellular pH: Measurement, Regulation, and Function. *Am. J. Physiol. Cell Physiol.* **1988**, *254* (2), C213–C225.

(18) Kotyk, A.; Slavik, J. Intracellular PH and Its Measurement; CRC Press: Boca Raton, FL, 1989.

(19) Dennis, A. M.; Rhee, W. J.; Sotto, D.; Dublin, S. N.; Bao, G. Quantum Dot–Fluorescent Protein FRET Probes for Sensing Intracellular pH. *ACS Nano* **2012**, *6* (4), 2917–2924.

(20) Awaji, T.; Hirasawa, A.; Shirakawa, H.; Tsujimoto, G.; Miyazaki, S. Novel Green Fluorescent Protein-Based Ratiometric Indicators for Monitoring PH in Defined Intracellular Microdomains. *Biochem. Biophys. Res. Commun.* **2001**, *289* (2), 457–462.

(21) Tantama, M.; Hung, Y. P.; Yellen, G. Imaging Intracellular PH in Live Cells with a Genetically Encoded Red Fluorescent Protein Sensor. *J. Am. Chem. Soc.* **2011**, *133* (26), 10034–10037.

(22) Shi, W.; Li, X.; Ma, H. A Tunable Ratiometric PH Sensor Based on Carbon Nanodots for the Quantitative Measurement of the Intracellular pH of Whole Cells. *Angew. Chem., Int. Ed.* **2012**, *51* (26), 6432–6435.

(23) Chen, N.; He, Y.; Su, Y.; Li, X.; Huang, Q.; Wang, H.; Zhang, X.; Tai, R.; Fan, C. The Cytotoxicity of Cadmium-Based Quantum Dots. *Biomaterials* **2012**, *33* (5), 1238–1244.

(24) Ormö, M.; Cubitt, A. B.; Kallio, K.; Gross, L. A.; Tsien, R. Y.; Remington, S. J. Crystal Structure of the Aequorea Victoria Green Fluorescent Protein. *Science* **1996**, *273* (5280), 1392–1395.

(25) Cubitt, A. B.; Heim, R.; Adams, S. R.; Boyd, A. E.; Gross, L. A.; Tsien, R. Y. Understanding, Improving and Using Green Fluorescent Proteins. *Trends Biochem. Sci.* **1995**, *20* (11), 448–455.

(26) Ding, Y.; Ai, H.; Hoi, H.; Campbell, R. E. Förster Resonance Energy Transfer-Based Biosensors for Multiparameter Ratiometric Imaging of Ca2+ Dynamics and Caspase-3 Activity in Single Cells. *Anal. Chem.* **2011**, *83* (24), 9687–9693.

(27) van Rossum, S. A. P.; Tena-Solsona, M.; Esch, J. H. van; Eelkema, R.; Boekhoven, J. Dissipative Out-of-Equilibrium Assembly of Man-Made Supramolecular Materials. *Chem. Soc. Rev.* **2017**, *46* (18), 5519–5535.

(28) Boekhoven, J.; Hendriksen, W. E.; Koper, G. J. M.; Eelkema, R.; Esch, J. H. van. Transient Assembly of Active Materials Fueled by a Chemical Reaction. *Science* **2015**, *349* (6252), 1075–1079.

(29) Boekhoven, J.; Brizard, A. M.; Kowlgi, K. N. K.; Koper, G. J. M.; Eelkema, R.; van Esch, J. H. Dissipative Self-Assembly of a Molecular Gelator by Using a Chemical Fuel. *Angew. Chem. Int., Ed.* **2010**, *49* (28), 4825–4828.

(30) Tena-Solsona, M.; Rieß, B.; Grötsch, R. K.; Löhrer, F. C.; Wanzke, C.; Käsdorf, B.; Bausch, A. R.; Müller-Buschbaum, P.; Lieleg, O.; Boekhoven, J. Non-Equilibrium Dissipative Supramolecular Materials with a Tunable Lifetime. *Nat. Commun.* **2017**, *8* (1), 1–8.

(31) Carlini, E. A. The Good and the Bad Effects of (-) Trans-Delta-9-Tetrahydrocannabinol (Δ9-THC) on Humans. *Toxicon* **2004**, *44* (4), 461–467.

(32) Payne, R.; Mathias, S. D.; Pasta, D. J.; Wanke, L. A.; Williams, R.; Mahmoud, R. Quality of Life and Cancer Pain: Satisfaction and Side Effects with Transdermal Fentanyl versus Oral Morphine. *J. Clin. Oncol.* **1998**, *16* (4), 1588–1593.

(33) Fentanyl | DEA https://www.dea.gov/galleries/drug-images/fentanyl (accessed Jan 14, 2019).

(34) MPs debate how Canada should approach fighting fentanyl, opioid crises | Globalnews.ca https://globalnews.ca/news/4748497/fentanyl-opioid-crisis-debate-house-of-commons/ (accessed Jan 14, 2019).

(35) Fentanyl Overdose https://www.huffingtonpost.ca/news/fentanyl-overdose/ (accessed Jan 14, 2019).

(36) Mackie stands behind fentanyl-in-pot warning, despite "spirited" backlash | CBC News https://www.cbc.ca/news/canada/london/fentanyl-marijuana-warning-backlash-1.4240332 (accessed Jan 14, 2019).

(37) Police Say Some of Synthetic Marijuana Was Laced with Fentanyl | Watch News Videos Online. Global News. https://globalnews.ca/video/4391863/police-say-some-of-synthetic-marijuana-was-laced-with-fentanyl (accessed Jan 14, 2019).

(38) Huang, X.; Jain, P. K.; El-Sayed, I. H.; El-Sayed, M. A. Gold Nanoparticles: Interesting Optical Properties and Recent Applications in Cancer Diagnostics and Therapy. *Nanomedicine (Lond.)* **2007**, *2* (5) 681-693.

(39) Eustis, S.; El-Sayed, M. A. Why Gold Nanoparticles Are More Precious than Pretty Gold: Noble Metal Surface Plasmon Resonance and Its Enhancement of the Radiative and Nonradiative Properties of Nanocrystals of Different Shapes. *Chem. Soc. Rev.* **2006**, *35* (3), 209–217.

(40) Tsunoyama, H.; Sakurai, H.; Ichikuni, N.; Negishi, Y.; Tsukuda, T. Colloidal Gold Nanoparticles as Catalyst for Carbon- Carbon Bond Formation: Application to Aerobic Homocoupling of Phenylboronic Acid in Water. *Langmuir* **2004**, *20* (26), 11293–11296.

(41) Daniel, M.-C.; Astruc, D. Gold Nanoparticles: Assembly, Supramolecular Chemistry, Quantum-Size-Related Properties, and Applications toward Biology, Catalysis, and Nanotechnology. *Chem. Rev.* **2004**, *104* (1), 293–346.

(42) Fan, C.; Wang, S.; Hong, J. W.; Bazan, G. C.; Plaxco, K. W.; Heeger, A. J. Beyond Superquenching: Hyper-Efficient Energy Transfer from Conjugated Polymers to Gold Nanoparticles. *Proc. Natl. Acad. Sci.* **2003**, *100* (11), 6297–6301.

(43) Dulkeith, E.; Ringler, M.; Klar, T. A.; Feldmann, J.; Munoz Javier, A.; Parak, W. J. Gold Nanoparticles Quench Fluorescence by Phase Induced Radiative Rate Suppression. *Nano Lett.* **2005**, *5* (4), 585–589.

(44) Pons, T.; Medintz, I. L.; Sapsford, K. E.; Higashiya, S.; Grimes, A. F.; English, D. S.; Mattoussi, H. On the Quenching of Semiconductor Quantum Dot Photoluminescence by Proximal Gold Nanoparticles. *Nano Lett.* **2007**, *7* (10), 3157–3164.

(45) Liu, J.; Erogbogbo, F.; Yong, K.-T.; Ye, L.; Liu, J.; Hu, R.; Chen, H.; Hu, Y.; Yang, Y.; Yang, J. Assessing Clinical Prospects of Silicon Quantum Dots: Studies in Mice and Monkeys. *ACS Nano* **2013**, *7* (8), 7303–7310.

(46) McVey, B. F.; Tilley, R. D. Solution Synthesis, Optical Properties, and Bioimaging Applications of Silicon Nanocrystals. *Acc. Chem. Res.* **2014**, *47* (10), 3045–3051.

(47) Gonzalez, C. M.; Veinot, J. G. Silicon Nanocrystals for the Development of Sensing Platforms. *J. Mater. Chem. C* **2016**, *4* (22), 4836–4846.

(48) Wijaya, A.; Hamad-Schifferli, K. Ligand Customization and DNA Functionalization of Gold Nanorods via Round-Trip Phase Transfer Ligand Exchange. *Langmuir* **2008**, *24* (18), 9966–9969.

Bibliography

Chapter 1

(1) Alivisatos, A. P. Semiconductor Clusters, Nanocrystals, and Quantum Dots. *Science* **1996**, *271* (5251), 933–937.

(2) Brus, L. Quantum Crystallites and Nonlinear Optics. *Appl. Phys. A* **1991**, *53* (6), 465–474.

(3) Wang, Y.; Herron, N. Nanometer-Sized Semiconductor Clusters: Materials Synthesis, Quantum Size Effects, and Photophysical Properties. *J. Phys. Chem.* **1991**, *95* (2), 525–532.

(4) Weller, H. Colloidal Semiconductor Q-Particles: Chemistry in the Transition Region Between Solid State and Molecules. *Angew. Chem., Int. Ed.* **1993**, *32* (1), 41–53.

(5) Resch-Genger, U.; Grabolle, M.; Cavaliere-Jaricot, S.; Nitschke, R.; Nann, T. Quantum Dots versus Organic Dyes as Fluorescent Labels. *Nat. Methods* **2008**, *5* (9), 763–775.

(6) Peng, X.; Manna, L.; Yang, W.; Wickham, J.; Scher, E.; Kadavanich, A.; Alivisatos, A. P. Shape Control of CdSe Nanocrystals. *Nature* **2000**, *404* (6773), 59–61.

(7) Gerion, D.; Pinaud, F.; Williams, S. C.; Parak, W. J.; Zanchet, D.; Weiss, S.; Alivisatos, A. P. Synthesis and Properties of Biocompatible Water-Soluble Silica-Coated CdSe/ZnS Semiconductor Quantum Dots. *J. Phys. Chem. B* **2001**, *105* (37), 8861–8871.

(8) Rajh, T.; Micic, O. I.; Nozik, A. J. Synthesis and Characterization of Surface-Modified Colloidal Cadmium Telluride Quantum Dots. *J. Phys. Chem.* **1993**, *97* (46), 11999–12003.

(9) Semonin, O. E.; Johnson, J. C.; Luther, J. M.; Midgett, A. G.; Nozik, A. J.; Beard, M. C. Absolute Photoluminescence Quantum Yields of IR-26 Dye, PbS, and PbSe Quantum Dots. *J. Phys. Chem. Lett.* **2010**, *1* (16), 2445–2450.

(10) Zhang, J.; Gao, J.; Miller, E. M.; Luther, J. M.; Beard, M. C. Diffusion-Controlled Synthesis of PbS and PbSe Quantum Dots with In Situ Halide Passivation for Quantum Dot Solar Cells. *ACS Nano* **2014**, *8* (1), 614–622.

(11) Micic, O. I.; Sprague, J. R.; Curtis, C. J.; Jones, K. M.; Machol, J. L.; Nozik, A. J.; Giessen, H.; Fluegel, B.; Mohs, G.; Peyghambarian, N. Synthesis and Characterization of InP, GaP, and $GaInP_2$ Quantum Dots. *J. Phys. Chem.* **1995**, *99* (19), 7754–7759.

(12) Medintz, I. L.; Uyeda, H. T.; Goldman, E. R.; Mattoussi, H. Quantum Dot Bioconjugates for Imaging, Labelling and Sensing. *Nat. Mater.* **2005**, *4* (6), 435–446.

(13) Chen, N.; He, Y.; Su, Y.; Li, X.; Huang, Q.; Wang, H.; Zhang, X.; Tai, R.; Fan, C. The Cytotoxicity of Cadmium-Based Quantum Dots. *Biomaterials* **2012**, *33* (5), 1238–1244.

(14) Wani, A. L.; Ara, A.; Usmani, J. A. Lead Toxicity: A Review. *Interdiscip. Toxicol.* **2015**, *8* (2), 55–64.

(15) Martelli, A.; Rousselet, E.; Dycke, C.; Bouron, A.; Moulis, J.-M. Cadmium Toxicity in Animal Cells by Interference with Essential Metals. *Biochimie* **2006**, *88* (11), 1807–1814.

(16) Liu, J.; Erogbogbo, F.; Yong, K.-T.; Ye, L.; Liu, J.; Hu, R.; Chen, H.; Hu, Y.; Yang, Y.; Yang, J.; et al. Assessing Clinical Prospects of Silicon Quantum Dots: Studies in Mice and Monkeys. *ACS Nano* **2013**, *7* (8), 7303–7310.

(17) Meinardi, F.; Ehrenberg, S.; Dhamo, L.; Carulli, F.; Mauri, M.; Bruni, F.; Simonutti, R.; Kortshagen, U.; Brovelli, S. Highly Efficient Luminescent Solar Concentrators Based on Earth-Abundant Indirect-Bandgap Silicon Quantum Dots. *Nat. Photonics* **2017**, *11* (3), 177–185.

(18) Park, J.-H.; Gu, L.; Maltzahn, G. von; Ruoslahti, E.; Bhatia, S. N.; Sailor, M. J. Biodegradable Luminescent Porous Silicon Nanoparticles for in Vivo Applications. *Nat. Mater.* **2009**, *8* (4), 331–336.

(19) Dasog, M.; Yang, Z.; Regli, S.; Atkins, T. M.; Faramus, A.; Singh, M. P.; Muthuswamy, E.; Kauzlarich, S. M.; Tilley, R. D.; Veinot, J. G. C. Chemical Insight into the Origin of Red and Blue Photoluminescence Arising from Freestanding Silicon Nanocrystals. *ACS Nano* **2013**, *7* (3), 2676–2685.

(20) Sinelnikov, R.; Dasog, M.; Beamish, J.; Meldrum, A.; Veinot, J. G. C. Revisiting an Ongoing Debate: What Role Do Surface Groups Play in Silicon Nanocrystal Photoluminescence? *ACS Photonics* **2017**, *4* (8), 1920–1929.

(21) Dasog, M.; De los Reyes, G. B.; Titova, L. V.; Hegmann, F. A.; Veinot, J. G. C. Size vs Surface: Tuning the Photoluminescence of Freestanding Silicon Nanocrystals Across the Visible Spectrum via Surface Groups. *ACS Nano* **2014**, *8* (9), 9636–9648.

(22) Tilley, R. D.; Yamamoto, K. The Microemulsion Synthesis of Hydrophobic and Hydrophilic Silicon Nanocrystals. *Adv. Mater.* **2006**, *18* (15), 2053–2056.

(23) Manhat, B. A.; Brown, A. L.; Black, L. A.; Ross, J. B. A.; Fichter, K.; Vu, T.; Richman, E.; Goforth, A. M. One-Step Melt Synthesis of Water-Soluble, Photoluminescent, Surface-Oxidized Silicon Nanoparticles for Cellular Imaging Applications. *Chem. Mater.* **2011**, *23* (9), 2407–2418.

(24) Pettigrew, K. A.; Liu, Q.; Power, P. P.; Kauzlarich, S. M. Solution Synthesis of Alkyl- and Alkyl/Alkoxy-Capped Silicon Nanoparticles via Oxidation of Mg_2Si. *Chem. Mater.* **2003**, *15* (21), 4005–4011.

(25) Yang, C.-S.; Bley, R. A.; Kauzlarich, S. M.; Lee, H. W. H.; Delgado, G. R. Synthesis of Alkyl-Terminated Silicon Nanoclusters by a Solution Route. *J. Am. Chem. Soc.* **1999**, *121* (22), 5191–5195.

(26) Erogbogbo, F.; Yong, K.-T.; Roy, I.; Xu, G.; Prasad, P. N.; Swihart, M. T. Biocompatible Luminescent Silicon Quantum Dots for Imaging of Cancer Cells. *ACS Nano* **2008**, *2* (5), 873–878.

(27) Erogbogbo, F.; Tien, C.-A.; Chang, C.-W.; Yong, K.-T.; Law, W.-C.; Ding, H.; Roy, I.; Swihart, M. T.; Prasad, P. N. Bioconjugation of Luminescent Silicon Quantum Dots for Selective Uptake by Cancer Cells. *Bioconjugate Chem.* **2011**, *22* (6), 1081–1088.

(28) May, J. L.; Erogbogbo, F.; Yong, K.; Ding, H.; Law, W.; Swihart, T.; Prasad, P. N. *J. Solid Tumors* **2012**, *2* (3), 24–37.

(29) Hessel, C. M.; Henderson, E. J.; Veinot, J. G. C. Hydrogen Silsesquioxane: A Molecular Precursor for Nanocrystalline Si−SiO2 Composites and Freestanding Hydride-Surface-Terminated Silicon Nanoparticles. *Chem. Mater.* **2006**, *18* (26), 6139–6146.

(30) Clark, R. J.; Aghajamali, M.; Gonzalez, C. M.; Hadidi, L.; Islam, M. A.; Javadi, M.; Mobarok, M. H.; Purkait, T. K.; Robidillo, C. J. T.; Sinelnikov, R.; et al. From Hydrogen Silsesquioxane to Functionalized Silicon Nanocrystals. *Chem. Mater.* **2017**, *29* (1), 80–89.

(31) Veinot, J. G. C. Synthesis, Surface Functionalization, and Properties of Freestanding Silicon Nanocrystals. *Chem. Commun.* **2006**, *40*, 4160–4168.

(32) McVey, B. F. P.; Tilley, R. D. Solution Synthesis, Optical Properties, and Bioimaging Applications of Silicon Nanocrystals. *Acc. Chem. Res.* **2014**, *47* (10), 3045–3051.

(33) Cheng, X.; B. Lowe, S.; J. Reece, P.; Justin Gooding, J. Colloidal Silicon Quantum Dots: From Preparation to the Modification of Self-Assembled Monolayers (SAMs) for Bio-Applications. *Chem. Soc. Rev.* **2014**, *43* (8), 2680–2700.

(34) Buriak, J. M. Organometallic Chemistry on Silicon and Germanium Surfaces. *Chem. Rev.* **2002**, *102* (5), 1271–1308.

(35) Doremus, R. H. Oxidation of Silicon by Water and Oxygen and Diffusion in Fused Silica. *J. Phys. Chem.* **1976**, *80* (16), 1773–1775.

(36) Das, P.; Saha, A.; Ranjan Maity, A.; C. Ray, S.; R. Jana, N. Silicon Nanoparticle Based Fluorescent Biological Label via Low Temperature Thermal Degradation of Chloroalkylsilane. *Nanoscale* **2013**, *5* (13), 5732–5737.

(37) Islam, M. A.; Sinelnikov, R.; Howlader, M. A.; Faramus, A.; Veinot, J. G. C. Mixed Surface Chemistry: An Approach to Highly Luminescent Biocompatible Amphiphilic Silicon Nanocrystals. Chem. Mater. **2018**, *30* (24), 8925–8931.

(38) Choi, J.; Wang, N. S.; Reipa, V. Conjugation of the Photoluminescent Silicon Nanoparticles to Streptavidin. *Bioconjugate Chem.* **2008**, *19* (3), 680–685.

(39) Zhong, Y.; Peng, F.; Bao, F.; Wang, S.; Ji, X.; Yang, L.; Su, Y.; Lee, S.-T.; He, Y. Large-Scale Aqueous Synthesis of Fluorescent and Biocompatible Silicon Nanoparticles and Their Use as Highly Photostable Biological Probes. *J. Am. Chem. Soc.* **2013**, *135* (22), 8350–8356.

(40) Oliinyk, B. V.; Korytko, D.; Lysenko, V.; Alekseev, S. Are Fluorescent Silicon Nanoparticles Formed in a One-Pot Aqueous Synthesis? *Chem. Mater.* **2019**, *31* (18), 7167–7172.

(41) L.Z. Ddungu, J.; Silvestrini, S.; Tassoni, A.; Cola, L. D. Shedding Light on the Aqueous Synthesis of Silicon Nanoparticles by Reduction of Silanes with Citrates. Faraday Discuss. **2020**, doi.org/10.1039/C9FD00127A.

(42) Zhong, Y.; Sun, X.; Wang, S.; Peng, F.; Bao, F.; Su, Y.; Li, Y.; Lee, S.-T.; He, Y. Facile, Large-Quantity Synthesis of Stable, Tunable-Color Silicon Nanoparticles and Their Application for Long-Term Cellular Imaging. *ACS Nano* **2015**, *9* (6), 5958–5967.

(43) Yanagawa, H.; Inoue, A.; Sugimoto, H.; Shioi, M.; Fujii, M. Antibody-Conjugated near-Infrared Luminescent Silicon Quantum Dots for Biosensing. *MRS Commun.* **2019**, *9* (3), 1079–1086.

(44) Wang, L.; Reipa, V.; Blasic, J. Silicon Nanoparticles as a Luminescent Label to DNA. *Bioconjugate Chem.* **2004**, *15* (2), 409–412.

(45) Ruizendaal, L.; Pujari, S. P.; Gevaerts, V.; Paulusse, J. M. J.; Zuilhof, H. Biofunctional Silicon Nanoparticles by Means of Thiol-Ene Click Chemistry. *Chem. Asian J.* **2011**, *6* (10), 2776–2786.

(46) Lai, C.-H.; Hütter, J.; Hsu, C.-W.; Tanaka, H.; Varela-Aramburu, S.; De Cola, L.; Lepenies, B.; Seeberger, P. H. Analysis of Carbohydrate–Carbohydrate Interactions Using Sugar-Functionalized Silicon Nanoparticles for Cell Imaging. *Nano Lett.* **2016**, *16* (1), 807–811.

(47) Ahire, J. H.; Wang, Q.; Coxon, P. R.; Malhotra, G.; Brydson, R.; Chen, R.; Chao, Y. Highly Luminescent and Nontoxic Amine-Capped Nanoparticles from Porous Silicon: Synthesis and Their Use in Biomedical Imaging. *ACS Appl. Mater. Interfaces* **2012**, *4* (6), 3285–3292.

(48) Ahire, J. H.; Behray, M.; Webster, C. A.; Wang, Q.; Sherwood, V.; Saengkrit, N.; Ruktanonchai, U.; Woramongkolchai, N.; Chao, Y. Synthesis of Carbohydrate Capped Silicon Nanoparticles and Their Reduced Cytotoxicity, In Vivo Toxicity, and Cellular Uptake. *Adv. Healthc. Mater.* **2015**, *4* (12), 1877–1886.

(49) Ahire, J. H.; Chambrier, I.; Mueller, A.; Bao, Y.; Chao, Y. Synthesis of D-Mannose Capped Silicon Nanoparticles and Their Interactions with MCF-7 Human Breast Cancerous Cells. *ACS Appl. Mater. Interfaces* **2013**, *5* (15), 7384–7391.

(50) Dondoni, A. The Emergence of Thiol–Ene Coupling as a Click Process for Materials and Bioorganic Chemistry. *Angew. Chem., Int. Ed.* **2008**, *47* (47), 8995–8997.

(51) Bertin, A.; Schlaad, H. Mild and Versatile (Bio-)Functionalization of Glass Surfaces via Thiol−Ene Photochemistry. *Chem. Mater.* **2009**, *21* (24), 5698–5700.

(52) Su, X.; Kuang, L.; Battle, C.; Shaner, T.; Mitchell, B. S.; Fink, M. J.; Jayawickramarajah, J. Mild Two-Step Method to Construct DNA-Conjugated Silicon Nanoparticles: Scaffolds for the Detection of MicroRNA-21. *Bioconjugate Chem.* **2014**, *25* (10), 1739–1743.

(53) Zhai, Y.; Dasog, M.; B. Snitynsky, R.; K. Purkait, T.; Aghajamali, M.; H. Hahn, A.; B. Sturdy, C.; L. Lowary, T.; C. Veinot, J. G. C. Water-Soluble Photoluminescent d -Mannose and l -Alanine Functionalized Silicon Nanocrystals and Their Application to Cancer Cell Imaging. *J. Mater. Chem. B* **2014**, *2* (47), 8427–8433.

(54) Zhong, Y.; Peng, F.; Wei, X.; Zhou, Y.; Wang, J.; Jiang, X.; Su, Y.; Su, S.; Lee, S.-T.; He, Y. Microwave-Assisted Synthesis of Biofunctional and Fluorescent Silicon Nanoparticles Using Proteins as Hydrophilic Ligands. *Angew. Chem., Int. Ed.* **2012**, *51* (34), 8485–8489.

(55) Bagga, K.; Barchanski, A.; Intartaglia, R.; Dante, S.; Marotta, R.; Diaspro, A.; Sajti, C. L.; Brandi, F. Laser-Assisted Synthesis OfStaphylococcus Aureusprotein-Capped Silicon Quantum Dots as Bio-Functional Nanoprobes. Laser *Phys. Lett.* **2013**, *10* (6), 065603.

(56) Intartaglia, R.; Barchanski, A.; Bagga, K.; Genovese, A.; Das, G.; Wagener, P.; Fabrizio, E. D.; Diaspro, A.; Brandi, F.; Barcikowski, S. Bioconjugated Silicon Quantum Dots from One-Step Green Synthesis. *Nanoscale* **2012**, *4* (4), 1271–1274.

(57) M. Gonzalez, C.; C. Veinot, J. G. C. Silicon Nanocrystals for the Development of Sensing Platforms. *J. Mater. Chem. C* **2016**, *4* (22), 4836–4846.

(58) Murphy, C. J. Peer Reviewed: Optical Sensing with Quantum Dots. *Anal. Chem.* **2002**, *74* (19), 520 A-526 A.

(59) Lin, C.-A. J.; Liedl, T.; Sperling, R. A.; Fernández-Argüelles, M. T.; Costa-Fernández, J. M.; Pereiro, R.; Sanz-Medel, A.; Chang, W. H.; Parak, W. J. Bioanalytics and Biolabeling with Semiconductor Nanoparticles (Quantum Dots). *J. Mater. Chem.* **2007**, *17* (14), 1343–1346.

(60) Lou, Y.; Zhao, Y.; Chen, J.; Zhu, J.-J. Metal Ions Optical Sensing by Semiconductor Quantum Dots. *J. Mater. Chem. C* **2014**, *2* (4), 595–613.

(61) Freeman, R.; Girsh, J.; Willner, I. Nucleic Acid/Quantum Dots (QDs) Hybrid Systems for Optical and Photoelectrochemical Sensing. *ACS Appl. Mater. Interfaces* **2013**, *5* (8), 2815–2834.

(62) Freeman, R.; Willner, I. Optical Molecular Sensing with Semiconductor Quantum Dots (QDs). *Chem. Soc. Rev.* **2012**, *41* (10), 4067–4085.

(63) Silvi, S.; Credi, A. Luminescent Sensors Based on Quantum Dot–Molecule Conjugates. *Chem. Soc. Rev.* **2015**, *44* (13), 4275–4289.

(64) Amelia, M.; Impellizzeri, S.; Monaco, S.; Yildiz, I.; Silvi, S.; Raymo, F. M.; Credi, A. Structural and Size Effects on the Spectroscopic and Redox Properties of CdSe Nanocrystals in Solution: The Role of Defect States. *ChemPhysChem* **2011**, *12* (12), 2280–2288.

(65) Fraiji, L. K.; Hayes, D. M.; Werner, T. C. Static and Dynamic Fluorescence Quenching Experiments for the Physical Chemistry Laboratory. *J. Chem. Educ.* **1992**, *69* (5), 424.

(66) Selvin, P. R. The Renaissance of Fluorescence Resonance Energy Transfer. *Nat. Struct. Biol.* **2000**, *7* (9), 730–734.

(67) Yue, Z.; Lisdat, F.; Parak, W. J.; Hickey, S. G.; Tu, L.; Sabir, N.; Dorfs, D.; Bigall, N. C. Quantum-Dot-Based Photoelectrochemical Sensors for Chemical and Biological Detection. *ACS Appl. Mater. Interfaces* **2013**, *5* (8), 2800–2814.

(68) Zhang, J.; Yu, S.-H. Highly Photoluminescent Silicon Nanocrystals for Rapid, Label-Free and Recyclable Detection of Mercuric Ions. *Nanoscale* **2014**, *6* (8), 4096–4101.

(69) Liao, B.; Wang, W.; Deng, X.; He, B.; Zeng, W.; Tang, Z.; Liu, Q. A Facile One-Step Synthesis of Fluorescent Silicon Quantum Dots and Their Application for Detecting Cu^{2+}. *RSC Adv.* **2016**, *6* (18), 14465–14467.

(70) Zhao, J.; Deng, J.; Yi, Y.; Li, H.; Zhang, Y.; Yao, S. Label-Free Silicon Quantum Dots as Fluorescent Probe for Selective and Sensitive Detection of Copper Ions. *Talanta* **2014**, *125*, 372–377.

(71) Campos, B. B.; Algarra, M.; Alonso, B.; Casado, C. M.; Jiménez-Jiménez, J.; Rodríguez-Castellón, E.; Esteves da Silva, J. C. G. Fluorescent Sensor for Cr(VI) Based in Functionalized Silicon Quantum Dots with Dendrimers. *Talanta* **2015**, *144*, 862–867.

(72) Content, S.; Trogler, W. C.; Sailor, M. J. Detection of Nitrobenzene, DNT, and TNT Vapors by Quenching of Porous Silicon Photoluminescence. *Chem. Eur. J.* **2000**, *6* (12), 2205–2213.

(73) Germanenko, I. N.; Li, S.; El-Shall, M. S. Decay Dynamics and Quenching of Photoluminescence from Silicon Nanocrystals by Aromatic Nitro Compounds. *J. Phys. Chem. B* **2001**, *105* (1), 59–66.

(74) M. Gonzalez, C.; Iqbal, M.; Dasog, M.; G. Piercey, D.; Lockwood, R.; M. Klapötke, T.; C. Veinot, J. G. C. Detection of High-Energy Compounds Using Photoluminescent Silicon Nanocrystal Paper Based Sensors. *Nanoscale* **2014**, *6* (5), 2608–2612.

(75) Ban, R.; Zheng, F.; Zhang, J. A Highly Sensitive Fluorescence Assay for 2,4,6-Trinitrotoluene Using Amine-Capped Silicon Quantum Dots as a Probe. *Anal. Methods* **2015**, *7* (5), 1732–1737.

(76) Nguyen, A.; Gonzalez, C. M.; Sinelnikov, R.; Newman, W.; Sun, S.; Lockwood, R.; Veinot, J. G. C.; Meldrum, A. Detection of Nitroaromatics in the Solid, Solution, and Vapor Phases Using Silicon Quantum Dot Sensors. *Nanotechnology* **2016**, *27* (10), 105501.

(77) Zhang, Z. H.; Lockwood, R.; Veinot, J. G. C.; Meldrum, A. Detection of Ethanol and Water Vapor with Silicon Quantum Dots Coupled to an Optical Fiber. *Sens. Actuators B Chem.* **2013**, *181*, 523–528.

(78) Yi, Y.; Deng, J.; Zhang, Y.; Li, H.; Yao, S. Label-Free Si Quantum Dots as Photoluminescence Probes for Glucose Detection. *Chem. Commun.* **2013**, *49* (6), 612–614.

(79) Chen, Q.; Liu, M.; Zhao, J.; Peng, X.; Chen, X.; Mi, N.; Yin, B.; Li, H.; Zhang, Y.; Yao, S. Water-Dispersible Silicon Dots as a Peroxidase Mimetic for the Highly-Sensitive Colorimetric Detection of Glucose. *Chem. Commun.* **2014**, *50* (51), 6771–6774.

(80) Zhang, X.; Chen, X.; Kai, S.; Wang, H.-Y.; Yang, J.; Wu, F.-G.; Chen, Z. Highly Sensitive and Selective Detection of Dopamine Using One-Pot Synthesized Highly Photoluminescent Silicon Nanoparticles. *Anal. Chem.* **2015**, *87* (6), 3360–3365.

(81) Lin, J.; Wang, Q. Role of Novel Silicon Nanoparticles in Luminescence Detection of a Family of Antibiotics. *RSC Adv.* **2015**, *5* (35), 27458–27463.

(82) Yi, Y.; Zhu, G.; Liu, C.; Huang, Y.; Zhang, Y.; Li, H.; Zhao, J.; Yao, S. A Label-Free Silicon Quantum Dots-Based Photoluminescence Sensor for Ultrasensitive Detection of Pesticides. *Anal. Chem.* **2013**, *85* (23), 11464–11470.

Chapter 2

(1) Warner, J. H.; Hoshino, A.; Yamamoto, K.; Tilley, R. Water-Soluble Photoluminescent Silicon Quantum Dots. *Angew. Chem.* **2005***, 117*, 4626-4630.

(2) Murray, C.; Norris, D. J.; Bawendi, M. G. Synthesis and Characterization of Nearly Monodisperse CdE (E = Sulfur, Selenium, Tellurium) Semiconductor Nanocrystallites. *J. Am. Chem. Soc.* **1993***, 115*, 8706-8715.

(3) Fujioka, K.; Hiruoka, M.; Sato, K.; Manabe, N.; Miyasaka, R.; Hanada, S.; Hoshino, A.; Tilley, R. D.; Manome, Y.; Hirakuri, K. Luminescent Passive-Oxidized Silicon Quantum Dots as Biological Staining Labels and Their Cytotoxicity Effects at High Concentration. *Nanotechnology* **2008***, 19*, 415102.

(4) Resch-Genger, U.; Grabolle, M.; Cavaliere-Jaricot, S.; Nitschke, R.; Nann, T. Quantum Dots versus Organic Dyes as Fluorescent Labels. *Nat. Methods* **2008***, 5*, 763.

(5) Derfus, A. M.; Chan, W. C.; Bhatia, S. N. Probing the Cytotoxicity of Semiconductor Quantum Dots. *Nano Lett.* **2004***, 4*, 11-18.

(6) Park, J.; Gu, L.; Von Maltzahn, G.; Ruoslahti, E.; Bhatia, S. N.; Sailor, M. J. Biodegradable Luminescent Porous Silicon Nanoparticles for in Vivo Applications. *Nat. Mater.* **2009***, 8*, 331.

(7) Zhong, Y.; Peng, F.; Bao, F.; Wang, S.; Ji, X.; Yang, L.; Su, Y.; Lee, S.; He, Y. Large-Scale Aqueous Synthesis of Fluorescent and Biocompatible Silicon Nanoparticles and Their Use as Highly Photostable Biological Probes. *J. Am. Chem. Soc.* **2013***, 135*, 8350-8356.

(8) Erogbogbo, F.; Yong, K.; Roy, I.; Xu, G.; Prasad, P. N.; Swihart, M. T. Biocompatible Luminescent Silicon Quantum Dots for Imaging of Cancer Cells. *ACS Nano* **2008***, 2*, 873-878.

(9) Osminkina, L. A.; Tamarov, K. P.; Sviridov, A. P.; Galkin, R. A.; Gongalsky, M. B.; Solovyev, V. V.; Kudryavtsev, A. A.; Timoshenko, V. Y. Photoluminescent Biocompatible Silicon Nanoparticles for Cancer Theranostic Applications. *J Biophotonics* **2012***, 5*, 529-535.

(10) Bhattacharjee, S.; Rietjens, I. M.; Singh, M. P.; Atkins, T. M.; Purkait, T. K.; Xu, Z.; Regli, S.; Shukaliak, A.; Clark, R. J.; Mitchell, B. S.; Alink, G. M.; Marcelis, A. T. M.; Fink, M. J.; Veinot, J. G. C.; Kauzlarich, S. M.; Zuilhof, H. Cytotoxicity of Surface-Functionalized Silicon and Germanium Nanoparticles: The Dominant Role of Surface Charges. *Nanoscale* **2013***, 5*, 4870-4883.

(11) Holmes, J. D.; Ziegler, K. J.; Doty, R. C.; Pell, L. E.; Johnston, K. P.; Korgel, B. A. Highly Luminescent Silicon Nanocrystals with Discrete Optical Transitions. *J. Am. Chem. Soc.* **2001***, 123*, 3743-3748.

(12) Wilcoxon, J.; Samara, G.; Provencio, P. Optical and Electronic Properties of Si Nanoclusters Synthesized in Inverse Micelles. *Phys. Rev. B* **1999***, 60*, 2704.

(13) Zhou, Z.; Brus, L.; Friesner, R. Electronic Structure and Luminescence of 1.1- and 1.4-nm Silicon Nanocrystals: Oxide Shell versus Hydrogen Passivation. *Nano Lett.* **2003***, 3*, 163-167.

(14) Kang, Z.; Liu, Y.; Tsang, C. H. A.; Ma, D. D. D.; Fan, X.; Wong, N.; Lee, S. Water-Soluble Silicon Quantum Dots with Wavelength-Tunable Photoluminescence. *Adv. Mater.* **2009***, 21*, 661-664.

(15) Dasog, M.; De los Reyes, Glenda B; Titova, L. V.; Hegmann, F. A.; Veinot, J. G. C. Size vs Surface: Tuning the Photoluminescence of Freestanding Silicon Nanocrystals Across the Visible Spectrum via Surface Groups. *ACS Nano* **2014***, 8*, 9636-9648.

(16) Hessel, C. M.; Reid, D.; Panthani, M. G.; Rasch, M. R.; Goodfellow, B. W.; Wei, J.; Fujii, H.; Akhavan, V.; Korgel, B. A. Synthesis of Ligand-Stabilized Silicon Nanocrystals with Size-Dependent Photoluminescence Spanning Visible to Near-Infrared Wavelengths. *Chem. Mater.* **2011***, 24*, 393-401.

(17) Veinot, J. G. C. Synthesis, Surface Functionalization, and Properties of Freestanding Silicon Nanocrystals. *Chem. Commun.* **2006**, 4160-4168.

(18) Maier-Flaig, F.; Rinck, J.; Stephan, M.; Bocksrocker, T.; Bruns, M.; Kübel, C.; Powell, A. K.; Ozin, G. A.; Lemmer, U. Multicolor Silicon Light-Emitting Diodes (SiLEDs). *Nano Lett.* **2013***, 13*, 475-480.

(19) Zou, J.; Baldwin, R. K.; Pettigrew, K. A.; Kauzlarich, S. M. Solution Synthesis of Ultrastable Luminescent Siloxane-Coated Silicon Nanoparticles. *Nano Lett.* **2004***, 4*, 1181-1186.

(20) Dasog, M.; Yang, Z.; Regli, S.; Atkins, T. M.; Faramus, A.; Singh, M. P.; Muthuswamy, E.; Kauzlarich, S. M.; Tilley, R. D.; Veinot, J. G. C. Chemical Insight into the Origin of Red and Blue Photoluminescence Arising from Freestanding Silicon Nanocrystals. *ACS Nano* **2013***, 7*, 2676-2685.

(21) Li, Z.; Ruckenstein, E. Water-Soluble Poly(acrylic acid) Grafted Luminescent Silicon Nanoparticles and Their Use as Fluorescent Biological Staining Labels. *Nano Lett.* **2004***, 4*, 1463-1467.

(22) Zhai, Y.; Dasog, M.; Snitynsky, R. B.; Purkait, T. K.; Aghajamali, M.; Hahn, A. H.; Sturdy, C. B.; Lowary, T. L.; Veinot, J. G. C. Water-Soluble Photoluminescent D-Mannose and L-Alanine Functionalized Silicon Nanocrystals and Their Application to Cancer Cell Imaging. *J. Mater. Chem. B* **2014***, 2*, 8427-8433.

(23) Wu, S.; Zhong, Y.; Zhou, Y.; Song, B.; Chu, B.; Ji, X.; Wu, Y.; Su, Y.; He, Y. Biomimetic Preparation and Dual-Color Bioimaging of Fluorescent Silicon Nanoparticles. *J. Am. Chem. Soc.* 2015*, 137*, 14726-14732.

(24) Henderson, E. J.; Shuhendler, A. J.; Prasad, P.; Baumann, V.; Maier-Flaig, F.; Faulkner, D. O.; Lemmer, U.; Wu, X. Y.; Ozin, G. A. Colloidally Stable Silicon Nanocrystals with Near-Infrared Photoluminescence for Biological Fluorescence Imaging. *Small* **2011***, 7*, 2507-2516.

(25) McVey, B. F.; Tilley, R. D. Solution Synthesis, Optical Properties, and Bioimaging Applications of Silicon Nanocrystals. *Acc. Chem. Res.* **2014***, 47*, 3045-3051.

(26) Hessel, C. M.; Rasch, M. R.; Hueso, J. L.; Goodfellow, B. W.; Akhavan, V. A.; Puvanakrishnan, P.; Tunnel, J. W.; Korgel, B. A. Alkyl Passivation and Amphiphilic Polymer Coating of Silicon Nanocrystals for Diagnostic Imaging. *Small* **2010***, 6*, 2026-2034.

(27) Wu, P.; He, Y.; Wang, H.; Yan, X. Conjugation of Glucose Oxidase onto Mn-Doped ZnS Quantum Dots for Phosphorescent Sensing of Glucose in Biological Fluids. *Anal. Chem.* **2010***, 82*, 1427-1433.

(28) Medintz, I. L.; Uyeda, H. T.; Goldman, E. R.; Mattoussi, H. Quantum Dot Bioconjugates for Imaging, Labelling and Sensing. *Nat. Mater.* **2005***, 4*, 435.

(29) Wu, X.; Liu, H.; Liu, J.; Haley, K. N.; Treadway, J. A.; Larson, J. P.; Ge, N.; Peale, F.; Bruchez, M. P. Immunofluorescent Labeling of Cancer Marker Her2 and other Cellular Targets with Semiconductor Quantum Dots. *Nat. Biotechnol.* **2003***, 21*, 41.

(30) Boutureira, O.; Bernardes, G. J. Advances in Chemical Protein Modification. *Chem. Rev.* **2015***, 115*, 2174-2195.

(31) Ruizendaal, L.; Pujari, S. P.; Gevaerts, V.; Paulusse, J. M.; Zuilhof, H. Biofunctional Silicon Nanoparticles by Means of Thiol–Ene Click Chemistry. *Chem. Asian J.* **2011***, 6*, 2776-2786.

(32) Wang, L.; Reipa, V.; Blasic, J. Silicon Nanoparticles as a Luminescent Label to DNA. *Bioconjugate Chem.* **2004***, 15*, 409-412.

(33) Choi, J.; Wang, N. S.; Reipa, V. Conjugation of the Photoluminescent Silicon Nanoparticles to Streptavidin. *Bioconjugate Chem.* **2008***, 19*, 680-685.

(34) Hessel, C. M.; Henderson, E. J.; Veinot, J. G. C. Hydrogen Silsesquioxane: A Molecular Precursor for Nanocrystalline Si− SiO_2 Composites and Freestanding Hydride-Surface-Terminated Silicon Nanoparticles. *Chem. Mater.* **2006***, 18*, 6139-6146.

(35) Clark, R. J.; Aghajamali, M.; Gonzalez, C. M.; Hadidi, L.; Islam, M. A.; Javadi, M.; Mobarok, M. H.; Purkait, T. K.; Robidillo, C. J. T.; Sinelnikov, R.; Thiessen, A. N.; Washington, J.; Yu, H.; Veinot, J. G.

C. From Hydrogen Silsesquioxane to Functionalized Silicon Nanocrystals. *Chem. Mater.* **2016**, *29*, 80-89.

(36) Van Driel, A.; Nikolaev, I.; Vergeer, P.; Lodahl, P.; Vanmaekelbergh, D.; Vos, W. L. Statistical Analysis of Time-Resolved Emission from Ensembles of Semiconductor Quantum Dots: Interpretation of Exponential Decay Models. *Phys. Rev. B* **2007**, *75*, 035329.

(37) Nguyen, A.; Gonzalez, C. M.; Sinelnikov, R.; Newman, W.; Sun, S.; Lockwood, R.; Veinot, J. G. C.; Meldrum, A. Detection of Nitroaromatics in the Solid, Solution, and Vapor Phases Using Silicon Quantum Dot Sensors. *Nanotechnology* **2016**, *27*, 105501.

(38) Hessel, C. M.; Henderson, E. J.; Veinot, J. G. C. An Investigation of the Formation and Growth of Oxide-Embedded Silicon Nanocrystals in Hydrogen Silsesquioxane-Derived Nanocomposites. *J. Phys. Chem. C* **2007**, *111*, 6956-6961.

(39) Yang, Z.; Iqbal, M.; Dobbie, A. R.; Veinot, J. G. C. Surface-Induced Alkene Oligomerization: Does Thermal Hydrosilylation Really Lead to Monolayer Protected Silicon Nanocrystals? *J. Am. Chem. Soc.* **2013**, *135*, 17595-17601.

(40) Otsuka, H.; Nagasaki, Y.; Kataoka, K. PEGylated Nanoparticles for Biological and Pharmaceutical Applications. *Adv. Drug Deliv. Rev.* **2012**, *64*, 246-255.

(41) Wörz, A.; Berchtold, B.; Moosmann, K.; Prucker, O.; Rühe, J. Protein-Resistant Polymer Surfaces. *J. Mater. Chem.* **2012**, *22*, 19547-19561.

(42) Pelaz, B.; del Pino, P.; Maffre, P.; Hartmann, R.; Gallego, M.; Rivera-Fernandez, S.; de la Fuente, Jesus M; Nienhaus, G. U.; Parak, W. J. Surface Functionalization of Nanoparticles with Polyethylene Glycol: Effects on Protein Adsorption and Cellular Uptake. *ACS Nano* **2015**, *9*, 6996-7008.

(43) Dai, Q.; Walkey, C.; Chan, W. C. Polyethylene Glycol Backfilling Mitigates the Negative Impact of the Protein Corona on Nanoparticle Cell Targeting. *Angew. Chem., Int. Ed.* **2014**, *53*, 5093-5096.

(44) Clark, R. J.; Dang, M. K.; Veinot, J. G. C. Exploration of Organic Acid Chain Length on Water-Soluble Silicon Quantum Dot Surfaces. *Langmuir* **2010**, *26*, 15657-15664.

(45) Yang, L.; Heatley, F.; Blease, T. G.; Thompson, R. I. A Study of the Mechanism of the Oxidative Thermal Degradation of Poly(ethylene oxide) and Poly(propylene oxide) Using ^{1}H-and ^{13}C-NMR. *Eur. Polym. J.* **1996**, *32*, 535-547.

(46) Mkhatresh, O. A.; Heatley, F. A Study of the Products and Mechanism of the Thermal Oxidative Degradation of Poly(ethylene oxide) Using ^{1}H and ^{13}C 1-D and 2-D NMR. *Polym. Int.* **2004**, *53*, 1336-1342.

(47) Yang, Z.; Gonzalez, C. M.; Purkait, T. K.; Iqbal, M.; Meldrum, A.; Veinot, J. G. C. Radical Initiated Hydrosilylation on Silicon Nanocrystal Surfaces: An Evaluation of Functional Group Tolerance and Mechanistic Study. *Langmuir* **2015**, *31*, 10540-10548.

(48) Matsuura, H.; Miyazawa, T. Vibrational Analysis of Molten Poly(ethylene glycol). *J. Polym. Sci. Pol. Phys.* **1969**, *7*, 1735-1744.

(49) Huang, Y.; Tien, H.; Ma, C. M.; Yang, S.; Wu, S.; Liu, H.; Mai, Y. Effect of Extended Polymer Chains on Properties of Transparent Graphene Nanosheets Conductive Film. *J. Mater. Chem.* **2011***, 21*, 18236-18241.

(50) Campos, M. A. C.; Paulusse, J. M.; Zuilhof, H. Functional Monolayers on Oxide-Free Silicon Surfaces via Thiol–Ene Click Chemistry. *Chem. Commun.* **2010***, 46*, 5512-5514.

(51) Wu, E. C.; Park, J. H.; Park, J.; Segal, E.; Cunin, F.; Sailor, M. J. Oxidation-Triggered Release of Fluorescent Molecules or Drugs from Mesoporous Si Microparticles. *ACS Nano* **2008**, *11*, 2401-2409.

(52) Hecht, H.; Kalisz, H.; Hendle, J.; Schmid, R.; Schomburg, D. Crystal Structure of Glucose Oxidase from *Aspergillus niger* Refined at 2·3 Å Resolution. *J. Mol. Biol.* **1993***, 229*, 153-172.

(53) Pazur, J. H.; Kleppe, K. The Oxidation of Glucose and Related Compounds by Glucose Oxidase from *Aspergillus niger*. *Biochemistry* **1964***, 3*, 578-583.

(54) Magonet, E.; Hayen, P.; Delforge, D.; Delaive, E.; Remacle, J. Importance of the Structural Zinc Atom for the Stability of Yeast Alcohol Dehydrogenase. *Biochem. J.* **1992***, 287 (Pt 2)*, 361-365.

(55) Bennetzen, J. L.; Hall, B. D. The Primary Structure of the *Saccharomyces cerevisiae* Gene for Alcohol Dehydrogenase. *J. Biol. Chem.* **1982***, 257*, 3018-3025.

(56) Bühner, M.; Sund, H. Yeast Alcohol Dehydrogenase: –SH Groups, Disulfide Groups, Quaternary Structure, and Reactivation by Reductive Cleavage of Disulfide Groups. *FEBS J.* **1969***, 11*, 73-79.

(57) Tamm, L. K.; Tatulian, S. A. Infrared Spectroscopy of Proteins and Peptides in Lipid Bilayers. *Q. Rev. Biophys.* **1997***, 30*, 365-429.

(58) Jedlovszky-Hajdú, A.; Bombelli, F. B.; Monopoli, M. P.; Tombácz, E.; Dawson, K. A. Surface Coatings Shape the Protein Corona of SPIONs with Relevance to their Application in Vivo. *Langmuir* **2012***, 28*, 14983-14991.

(59) Ray, S.; Shard, A. G. Quantitative Analysis of Adsorbed Proteins by X-ray Photoelectron Spectroscopy. *Anal. Chem.* **2011***, 83*, 8659-8666.

(60) Buhl, M.; Vonhören, B.; Ravoo, B. J. Immobilization of Enzymes via Microcontact Printing and Thiol–Ene Click Chemistry. *Bioconjugate Chem.* **2015***, 26*, 1017-1020.

(61) Anderson, S. L.; Luber, E, J.; Olsen, B. C.; Buriak, J. M. Substance over Subjectivity: Moving beyond the Histogram. *Chem. Mater.* **2016**, *28*, 5973-5975.

(62) Sinelnikov, R.; Dasog, M.; Beamish, J.; Meldrum, A.; Veinot, J. G. C. Revisiting an Ongoing Debate: What Role Do Surface Groups Play in Silicon Nanocrystal Photoluminescence? *ACS Photonics* **2017***, 4*, 1920-1929.

(63) Hua, F.; Erogbogbo, F.; Swihart, M. T.; Ruckenstein, E. Organically Capped Silicon Nanoparticles with Blue Photoluminescence Prepared by Hydrosilylation Followed by Oxidation. *Langmuir* **2006***, 22*, 4363-4370.

(64) Dickinson, F.; Alsop, T.; Al-Sharif, N.; Berger, C.; Datta, H.; Šiller, L.; Chao, Y.; Tuite, E.; Houlton, A.; Horrocks, B. Dispersions of Alkyl-Capped Silicon Nanocrystals in Aqueous Media: Photoluminescence and Ageing. *Analyst* **2008***, 133*, 1573-1580.

(65) Lott, J. A.; Turner, K. Evaluation of Trinder's Glucose Oxidase Method for Measuring Glucose in Serum and Urine. *Clin. Chem.* **1975***, 21*, 1754-1760.

(66) Trinder, P. Determination of Glucose in Blood Using Glucose Oxidase with an Alternative Oxygen Acceptor. *Ann. Clin. Biochem.* **1969***, 6*, 24-27.

(67) Gregg, B. A.; Heller, A. Cross-Linked Redox Gels Containing Glucose Oxidase for Amperometric Biosensor Applications. *Anal. Chem.* **1990***, 62*, 258-263.

(68) Johnson, K. A.; Goody, R. S. The Original Michaelis Constant: Translation of the 1913 Michaelis–Menten paper. *Biochemistry* **2011***, 50*, 8264-8269.

(69) Menten, L.; Michaelis, M. Die Kinetik der Invertinwirkung. *Biochem. Z.* **1913***, 49*, 333-369.

(70) Lineweaver, H.; Burk, D. The Determination of Enzyme Dissociation Constants. *J. Am. Chem. Soc.* **1934***, 56*, 658-666.

(71) Pandey, P.; Singh, S. P.; Arya, S. K.; Gupta, V.; Datta, M.; Singh, S.; Malhotra, B. D. Application of Thiolated Gold Nanoparticles for the Enhancement of Glucose Oxidase Activity. *Langmuir* **2007***, 23*, 3333-3337.

(72) Rossi, L. M.; Quach, A. D.; Rosenzweig, Z. Glucose Oxidase–Magnetite Nanoparticle Bioconjugate for Glucose Sensing. *Anal. Bioanal. Chem.* **2004***, 380*, 606-613.

(73) Yi, Y.; Deng, J.; Zhang, Y.; Li, H.; Yao, S. Label-Free Si Quantum Dots as Photoluminescence Probes for Glucose Detection. *Chem. Commun.* **2013***, 49*, 612-614.

(74) Abe, K.; Matsuki, N. Measurement of Cellular 3-(4,5-Dimethylthiazol-2-yl)-2,5-Diphenyltetrazolium Bromide (MTT) Reduction Activity and Lactate Dehydrogenase Release Using MTT. *Neurosci. Res.* **2000***, 38*, 325-329.

(75) Zanon, J. P.; Peres, M. F.; Gattás, E. A. Colorimetric Assay of Ethanol Using Alcohol Dehydrogenase from Dry Baker's Yeast. *Enzyme Microb. Technol.* **2007***, 40*, 466-470.

(76) Taber, R. L. The Competitive Inhibition of Yeast Alcohol Dehydrogenase by 2,2,2-Trifluoroethanol. *Biochem. Mol. Biol. Edu.* **1998***, 26*, 239-242.

Chapter 3

(1) Kairdolf, B. A.; Smith, A. M.; Stokes, T. H.; Wang, M. D.; Young, A. N.; Nie, S. Semiconductor Quantum Dots for Bioimaging and Biodiagnostic Applications. *Annu. Rev. Anal. Chem.* **2013**, *6*, 143–162.

(2) Zrazhevskiy, P.; Sena, M.; Gao, X. Designing Multifunctional Quantum Dots for Bioimaging, Detection, and Drug Delivery. *Chem. Soc. Rev.* **2010**, *39* (11), 4326–4354.

(3) Michalet, X.; Pinaud, F. F.; Bentolila, L. A.; Tsay, J. M.; Doose, S.; Li, J. J.; Sundaresan, G.; Wu, A. M.; Gambhir, S. S.; Weiss, S. Quantum Dots for Live Cells, in Vivo Imaging, and Diagnostics. *Science* **2005**, *307* (5709), 538–544.

(4) Freeman, R.; Willner, I. Optical Molecular Sensing with Semiconductor Quantum Dots (QDs). *Chem. Soc. Rev.* **2012**, *41* (10), 4067–4085.

(5) Medintz, I. L.; Uyeda, H. T.; Goldman, E. R.; Mattoussi, H. Quantum Dot Bioconjugates for Imaging, Labelling and Sensing. *Nat. Mater.* **2005**, *4* (6), 435.

(6) Resch-Genger, U.; Grabolle, M.; Cavaliere-Jaricot, S.; Nitschke, R.; Nann, T. Quantum Dots versus Organic Dyes as Fluorescent Labels. *Nat. Methods* **2008**, *5* (9), 763.

(7) Derfus, A. M.; Chan, W. C.; Bhatia, S. N. Probing the Cytotoxicity of Semiconductor Quantum Dots. *Nano Lett.* **2004**, *4* (1), 11–18.

(8) Dabbousi, B. O.; Rodriguez-Viejo, J.; Mikulec, F. V.; Heine, J. R.; Mattoussi, H.; Ober, R.; Jensen, K. F.; Bawendi, M. G. (CdSe) ZnS Core- Shell Quantum Dots: Synthesis and Characterization of a Size Series of Highly Luminescent Nanocrystallites. *J. Phys. Chem. B* **1997**, *101* (46), 9463–9475.

(9) Gerion, D.; Pinaud, F.; Williams, S. C.; Parak, W. J.; Zanchet, D.; Weiss, S.; Alivisatos, A. P. Synthesis and Properties of Biocompatible Water-Soluble Silica-Coated CdSe/ZnS Semiconductor Quantum Dots. *J. Phys. Chem. B* **2001**, *105* (37), 8861–8871.

(10) Selvan, S. T.; Tan, T. T.; Ying, J. Y. Robust, Non-Cytotoxic, Silica-Coated CdSe Quantum Dots with Efficient Photoluminescence. *Adv. Mater.* **2005**, *17* (13), 1620–1625.

(11) Yong, K.-T.; Law, W.-C.; Hu, R.; Ye, L.; Liu, L.; Swihart, M. T.; Prasad, P. N. Nanotoxicity Assessment of Quantum Dots: From Cellular to Primate Studies. *Chem. Soc. Rev.* **2013**, *42* (3), 1236–1250.

(12) Tsoi, K. M.; Dai, Q.; Alman, B. A.; Chan, W. C. Are Quantum Dots Toxic? Exploring the Discrepancy between Cell Culture and Animal Studies. *Acc. Chem. Res.* **2012**, *46* (3), 662–671.

(13) Liu, J.; Erogbogbo, F.; Yong, K.-T.; Ye, L.; Liu, J.; Hu, R.; Chen, H.; Hu, Y.; Yang, Y.; Yang, J.; Roy, I.; Karker, N. A.; Swihart, M. T.; Prasad, P. N. Assessing Clinical Prospects of Silicon Quantum Dots: Studies in Mice and Monkeys. *ACS Nano* **2013**, *7* (8), 7303–7310.

(14) McVey, B. F.; Tilley, R. D. Solution Synthesis, Optical Properties, and Bioimaging Applications of Silicon Nanocrystals. *Acc. Chem. Res.* **2014**, *47* (10), 3045–3051.

(15) , J. H.; Hoshino, A.; Yamamoto, K.; Tilley, R. Water-Soluble Photoluminescent Silicon Quantum Dots. *Angew. Chem.* **2005**, *117* (29), 4626–4630.

(16) Fujioka, K.; Hiruoka, M.; Sato, K.; Manabe, N.; Miyasaka, R.; Hanada, S.; Hoshino, A.; Tilley, R. D.; Manome, Y.; Hirakuri, K. Luminescent Passive-Oxidized Silicon Quantum Dots as Biological Staining Labels and Their Cytotoxicity Effects at High Concentration. *Nanotechnology* **2008**, *19* (41), 415102.

(17) Erogbogbo, F.; Yong, K.-T.; Roy, I.; Xu, G.; Prasad, P. N.; Swihart, M. T. Biocompatible Luminescent Silicon Quantum Dots for Imaging of Cancer Cells. *ACS Nano* **2008**, *2* (5), 873–878.

(18) Osminkina, L. A.; Tamarov, K. P.; Sviridov, A. P.; Galkin, R. A.; Gongalsky, M. B.; Solovyev, V. V.; Kudryavtsev, A. A.; Timoshenko, V. Y. Photoluminescent Biocompatible Silicon Nanoparticles for Cancer Theranostic Applications. *J. Biophotonics* **2012**, *5* (7), 529–535.

(19) Li, Z. F.; Ruckenstein, E. Water-Soluble Poly (Acrylic Acid) Grafted Luminescent Silicon Nanoparticles and Their Use as Fluorescent Biological Staining Labels. *Nano Lett.* **2004**, *4* (8), 1463–1467.

(20) Zhai, Y.; Dasog, M.; Snitynsky, R. B.; Purkait, T. K.; Aghajamali, M.; Hahn, A. H.; Sturdy, C. B.; Lowary, T. L.; Veinot, J. G. Water-Soluble Photoluminescent D-Mannose and L-Alanine Functionalized

Silicon Nanocrystals and Their Application to Cancer Cell Imaging. *J. Mater. Chem. B* **2014**, *2* (47), 8427–8433.

(21) Wu, S.; Zhong, Y.; Zhou, Y.; Song, B.; Chu, B.; Ji, X.; Wu, Y.; Su, Y.; He, Y. Biomimetic Preparation and Dual-Color Bioimaging of Fluorescent Silicon Nanoparticles. *J. Am. Chem. Soc.* **2015**, *137* (46), 14726–14732.

(22) Henderson, E. J.; Shuhendler, A. J.; Prasad, P.; Baumann, V.; Maier-Flaig, F.; Faulkner, D. O.; Lemmer, U.; Wu, X. Y.; Ozin, G. A. Colloidally Stable Silicon Nanocrystals with Near-Infrared Photoluminescence for Biological Fluorescence Imaging. *Small* **2011**, *7* (17), 2507–2516.

(23) Hessel, C. M.; Rasch, M. R.; Hueso, J. L.; Goodfellow, B. W.; Akhavan, V. A.; Puvanakrishnan, P.; Tunnel, J. W.; Korgel, B. A. Alkyl Passivation and Amphiphilic Polymer Coating of Silicon Nanocrystals for Diagnostic Imaging. *Small* **2010**, *6* (18), 2026–2034.

(24) Gonzalez, C. M.; Veinot, J. G. Silicon Nanocrystals for the Development of Sensing Platforms. *J. Mater. Chem. C* **2016**, *4* (22), 4836–4846.

(25) Lin, J.; Wang, Q. Role of Novel Silicon Nanoparticles in Luminescence Detection of a Family of Antibiotics. *RSC Adv.* **2015**, *5* (35), 27458–27463.

(26) Zhang, X.; Chen, X.; Kai, S.; Wang, H.-Y.; Yang, J.; Wu, F.-G.; Chen, Z. Highly Sensitive and Selective Detection of Dopamine Using One-Pot Synthesized Highly Photoluminescent Silicon Nanoparticles. *Anal. Chem.* **2015**, *87* (6), 3360–3365.

(27) Ruizendaal, L.; Pujari, S. P.; Gevaerts, V.; Paulusse, J. M.; Zuilhof, H. Biofunctional Silicon Nanoparticles by Means of Thiol–Ene Click Chemistry. *Chem. Asian J.* **2011**, *6* (10), 2776–2786.

(28) Wang, L.; Reipa, V.; Blasic, J. Silicon Nanoparticles as a Luminescent Label to DNA. *Bioconjugate Chem.* **2004**, *15* (2), 409–412.

(29) Choi, J.; Wang, N. S.; Reipa, V. Conjugation of the Photoluminescent Silicon Nanoparticles to Streptavidin. *Bioconjugate Chem.* **2008**, *19* (3), 680–685.

(30) Robidillo, C. J. T.; Islam, M. A.; Aghajamali, M.; Faramus, A.; Sinelnikov, R.; Zhang, X.; Boekhoven, J.; Veinot, J. G. C. Functional Bioinorganic Hybrids from Enzymes and Luminescent Silicon-Based Nanoparticles. *Langmuir* **2018**, *34* (22), 6556–6569.

(31) Totaro, K. A.; Liao, X.; Bhattacharya, K.; Finneman, J. I.; Sperry, J. B.; Massa, M. A.; Thorn, J.; Ho, S. V.; Pentelute, B. L. Systematic Investigation of EDC/SNHS-Mediated Bioconjugation Reactions for Carboxylated Peptide Substrates. *Bioconjugate Chem.* **2016**, *27* (4), 994–1004.

(32) Davis, M.-T. B.; Preston, J. F. A Simple Modified Carbodiimide Method for Conjugation of Small-Molecular-Weight Compounds to Immunoglobulin G with Minimal Protein Crosslinking. *Anal. Biochem.* **1981**, *116* (2), 402–407.

(33) Dondoni, A. The Emergence of Thiol–Ene Coupling as a Click Process for Materials and Bioorganic Chemistry. *Angew. Chem., Int. Ed.* **2008**, *47* (47), 8995–8997.

(34) Bertin, A.; Schlaad, H. Mild and Versatile (Bio-) Functionalization of Glass Surfaces via Thiol–Ene Photochemistry. *Chem. Mater.* **2009**, *21* (24), 5698–5700.

(35) Demay-Drouhard, P.; Nehlig, E.; Hardouin, J.; Motte, L.; Guénin, E. Nanoparticles under the Light: Click Functionalization by Photochemical Thiol–Yne Reaction, Towards Double Click Functionalization. *Chem.- Eur. J.* **2013**, *19* (26), 8388–8392.

(36) Huang, H.; Liu, M.; Tuo, X.; Chen, J.; Mao, L.; Wen, Y.; Tian, J.; Zhou, N.; Zhang, X.; Wei, Y. One-Step Fabrication of PEGylated Fluorescent Nanodiamonds through the Thiol–Ene Click Reaction and Their Potential for Biological Imaging. *Appl. Surf. Sci.* **2018**, *439*, 1143–1151.

(37) Gu, W.; Chen, G.; Stenzel, M. H. Synthesis of Glyco-Microspheres via a Thiol–Ene Coupling Reaction. *J. Polym. Sci. Part Polym. Chem.* **2009**, *47* (20), 5550–5556.

(38) Jones, M. W.; Gibson, M. I.; Mantovani, G.; Haddleton, D. M. Tunable Thermo-Responsive Polymer–Protein Conjugates via a Combination of Nucleophilic Thiol–Ene "Click" and SET-LRP. *Polym. Chem.* **2011**, *2* (3), 572–574.

(39) Bhairamadgi, N. S.; Gangarapu, S.; Caipa Campos, M. A.; Paulusse, J. M.; van Rijn, C. J.; Zuilhof, H. Efficient Functionalization of Oxide-Free Silicon (111) Surfaces: Thiol–Yne versus Thiol–Ene Click Chemistry. *Langmuir* **2013**, *29* (14), 4535–4542.

(40) Campos, M. A. C.; Paulusse, J. M.; Zuilhof, H. Functional Monolayers on Oxide-Free Silicon Surfaces via Thiol–Ene Click Chemistry. *Chem. Commun.* **2010**, *46* (30), 5512–5514.

(41) Jeong, G. M.; Seong, H.; Kim, Y. S.; Im, S. G.; Jeong, K. J. Site-Specific Immobilization of Proteins on Non-Conventional Substrates via Solvent-Free Initiated Chemical Vapour Deposition (ICVD) Process. *Polym. Chem.* **2014**, *5* (15), 4459–4465.

(42) Buhl, M.; Vonhören, B.; Ravoo, B. J. Immobilization of Enzymes via Microcontact Printing and Thiol–Ene Click Chemistry. *Bioconjugate. Chem.* **2015**, *26* (6), 1017–1020.

(43) Weinrich, D.; Lin, P.-C.; Jonkheijm, P.; Nguyen, U. T.; Schröder, H.; Niemeyer, C. M.; Alexandrov, K.; Goody, R.; Waldmann, H. Oriented Immobilization of Farnesylated Proteins by the Thiol–Ene Reaction. *Angew. Chem., Int. Ed.* **2010**, *49* (7), 1252–1257.

(44) Escorihuela, J.; Bañuls, M.-J.; Grijalvo, S.; Eritja, R.; Puchades, R.; Maquieira, Á. Direct Covalent Attachment of DNA Microarrays by Rapid Thiol–Ene "Click" Chemistry. *Bioconjugate Chem.* **2014**, *25* (3), 618–627.

(45) Cheng, X.; Gondosiswanto, R.; Ciampi, S.; Reece, P. J.; Gooding, J. J. One-Pot Synthesis of Colloidal Silicon Quantum Dots and Surface Functionalization via Thiol–Ene Click Chemistry. *Chem. Commun.* **2012**, *48* (97), 11874–11876.

(46) Su, X.; Kuang, L.; Battle, C.; Shaner, T.; Mitchell, B. S.; Fink, M. J.; Jayawickramarajah, J. Mild Two-Step Method to Construct DNA-Conjugated Silicon Nanoparticles: Scaffolds for the Detection of MicroRNA-21. *Bioconjugate Chem.* **2014**, *25* (10), 1739–1743.

(47) Hessel, C. M.; Henderson, E. J.; Veinot, J. G. Hydrogen Silsesquioxane: A Molecular Precursor for Nanocrystalline Si–SiO_2 Composites and Freestanding Hydride-Surface-Terminated Silicon Nanoparticles. *Chem. Mater.* **2006**, *18* (26), 6139–6146.

(48) Clark, R. J.; Aghajamali, M.; Gonzalez, C. M.; Hadidi, L.; Islam, M. A.; Javadi, M.; Mobarok, M. H.; Purkait, T. K.; Robidillo, C. J. T.; Sinelnikov, R. From Hydrogen Silsesquioxane to Functionalized Silicon Nanocrystals. *Chem. Mater.* **2016**, *29* (1), 80–89.

(49) Van Driel, A. F.; Nikolaev, I. S.; Vergeer, P.; Lodahl, P.; Vanmaekelbergh, D.; Vos, W. L. Statistical Analysis of Time-Resolved Emission from Ensembles of Semiconductor Quantum Dots: Interpretation of Exponential Decay Models. *Phys. Rev. B* **2007**, *75* (3), 035329.

(50) Nguyen, A.; Gonzalez, C. M.; Sinelnikov, R.; Newman, W.; Sun, S.; Lockwood, R.; Veinot, J. G.; Meldrum, A. Detection of Nitroaromatics in the Solid, Solution, and Vapor Phases Using Silicon Quantum Dot Sensors. *Nanotechnology* **2016**, *27* (10), 105501.

(51) Craven, G. R.; Steers, E.; Anfinsen, C. B. Purification, Composition, and Molecular Weight of the β-Galactosidase of Escherichia Coli K12. *J. Biol. Chem.* **1965**, *240* (6), 2468–2477.

(52) Kilian, M.; Bülo, P. Rapid Diagnosis of Enterobacteriaceae. *APMIS* **1976**, *84* (5), 245–251.

(53) Patton, C. J.; Crouch, S. R. Spectrophotometric and Kinetics Investigation of the Berthelot Reaction for the Determination of Ammonia. *Anal. Chem.* **1977**, *49* (3), 464–469.

(54) Dondoni, A.; Massi, A.; Nanni, P.; Roda, A. A New Ligation Strategy for Peptide and Protein Glycosylation: Photoinduced Thiol–Ene Coupling. *Chem.- Eur. J.* **2009**, *15* (43), 11444–11449.

(55) Valkevich, E. M.; Guenette, R. G.; Sanchez, N. A.; Chen, Y.; Ge, Y.; Strieter, E. R. Forging Isopeptide Bonds Using Thiol–Ene Chemistry: Site-Specific Coupling of Ubiquitin Molecules for Studying the Activity of Isopeptidases. *J. Am. Chem. Soc.* **2012**, *134* (16), 6916–6919.

(56) Hessel, C. M.; Henderson, E. J.; Veinot, J. G. An Investigation of the Formation and Growth of Oxide-Embedded Silicon Nanocrystals in Hydrogen Silsesquioxane-Derived Nanocomposites. *J. Phys. Chem. C* **2007**, *111* (19), 6956–6961.

(57) Otsuka, H.; Nagasaki, Y.; Kataoka, K. PEGylated Nanoparticles for Biological and Pharmaceutical Applications. *Adv. Drug Deliv. Rev.* **2012**, *64*, 246–255.

(58) Pelaz, B.; del Pino, P.; Maffre, P.; Hartmann, R.; Gallego, M.; Rivera-Fernandez, S.; de la Fuente, J. M.; Nienhaus, G. U.; Parak, W. J. Surface Functionalization of Nanoparticles with Polyethylene Glycol: Effects on Protein Adsorption and Cellular Uptake. *Acs Nano* **2015**, *9* (7), 6996–7008.

(59) Dai, Q.; Walkey, C.; Chan, W. C. Polyethylene Glycol Backfilling Mitigates the Negative Impact of the Protein Corona on Nanoparticle Cell Targeting. *Angew. Chem., Int. Ed.* **2014**, *53* (20), 5093–5096.

(60) Wörz, A.; Berchtold, B.; Moosmann, K.; Prucker, O.; Rühe, J. Protein-Resistant Polymer Surfaces. *J. Mater. Chem.* **2012**, *22* (37), 19547–19561.

(61) Mobarok, M. H.; Purkait, T. K.; Islam, M. A.; Miskolzie, M.; Veinot, J. G. Instantaneous Functionalization of Chemically Etched Silicon Nanocrystal Surfaces. *Angew. Chem.* **2017**, *129* (22), 6169–6173.

(62) Yang, Z.; Gonzalez, C. M.; Purkait, T. K.; Iqbal, M.; Meldrum, A.; Veinot, J. G. Radical Initiated Hydrosilylation on Silicon Nanocrystal Surfaces: An Evaluation of Functional Group Tolerance and Mechanistic Study. *Langmuir* **2015**, *31* (38), 10540–10548.

(63) Matsuura, H.; Miyazawa, T. Vibrational Analysis of Molten Poly (Ethylene Glycol). *J. Polym. Sci. Part B Polym. Phys.* **1969**, *7* (10), 1735–1744.

(64) Yang, L.; Heatley, F.; Blease, T. G.; Thompson, R. I. A Study of the Mechanism of the Oxidative Thermal Degradation of Poly (Ethylene Oxide) and Poly (Propylene Oxide) Using 1H-and 13C-NMR. *Eur. Polym. J.* **1996**, *32* (5), 535–547.

(65) Mkhatresh, O. A.; Heatley, F. A Study of the Products and Mechanism of the Thermal Oxidative Degradation of Poly (Ethylene Oxide) Using 1H and 13C 1-D and 2-D NMR. *Polym. Int.* **2004**, *53* (9), 1336–1342.

(66) Huang, Y.-L.; Tien, H.-W.; Ma, C.-C. M.; Yang, S.-Y.; Wu, S.-Y.; Liu, H.-Y.; Mai, Y.-W. Effect of Extended Polymer Chains on Properties of Transparent Graphene Nanosheets Conductive Film. *J. Mater. Chem.* **2011**, *21* (45), 18236–18241.

(67) Clark, R. J.; Dang, M. K.; Veinot, J. G. Exploration of Organic Acid Chain Length on Water-Soluble Silicon Quantum Dot Surfaces. *Langmuir* **2010**, *26* (19), 15657–15664.

(68) Doremus, R. H. Oxidation of Silicon by Water and Oxygen and Diffusion in Fused Silica. *J. Phys. Chem.* **1976**, *80* (16), 1773–1775.

(69) Amenitsch, H.; Caracciolo, G.; Foglia, P.; Fuscoletti, V.; Giansanti, P.; Marianecci, C.; Pozzi, D.; Laganà, A. Existence of Hybrid Structures in Cationic Liposome/DNA Complexes Revealed by Their Interaction with Plasma Proteins. *Colloids Surf. B Biointerfaces* **2011**, *82* (1), 141–146.

(70) Lundqvist, M.; Stigler, J.; Cedervall, T.; Berggård, T.; Flanagan, M. B.; Lynch, I.; Elia, G.; Dawson, K. The Evolution of the Protein Corona around Nanoparticles: A Test Study. *ACS Nano* **2011**, *5* (9), 7503–7509.

(71) Venerando, R.; Miotto, G.; Magro, M.; Dallan, M.; Baratella, D.; Bonaiuto, E.; Zboril, R.; Vianello, F. Magnetic Nanoparticles with Covalently Bound Self-Assembled Protein Corona for Advanced Biomedical Applications. *J. Phys. Chem. C* **2013**, *117* (39), 20320–20331.

(72) Reynolds, J. A.; Tanford, C. Binding of Dodecyl Sulfate to Proteins at High Binding Ratios. Possible Implications for the State of Proteins in Biological Membranes. *Proc. Natl. Acad. Sci.* **1970**, *66* (3), 1002–1007.

(73) Dill, K. A. Dominant Forces in Protein Folding. *Biochemistry* **1990**, *29* (31), 7133–7155.

(74) Tamm, L. K.; Tatulian, S. A. Infrared Spectroscopy of Proteins and Peptides in Lipid Bilayers. *Q. Rev. Biophys.* **1997**, *30* (4), 365–429.

(75) Takishima, K.; Suga, T.; Mamiya, G. The Structure of Jack Bean Urease. *FEBS J.* **1988**, *175* (1), 151–157.

(76) Krajewska, B.; Zaborska, W.; Chudy, M. Multi-Step Analysis of Hg2+ Ion Inhibition of Jack Bean Urease. *J. Inorg. Biochem.* **2004**, *98* (6), 1160–1168.

(77) Krajewska, B.; Zaborska, W. Jack Bean Urease: The Effect of Active-Site Binding Inhibitors on the Reactivity of Enzyme Thiol Groups. *Bioorganic Chem.* **2007**, *35* (5), 355–365.

(78) Magonet, E.; Hayen, P.; Delforge, D.; Delaive, E.; Remacle, J. Importance of the Structural Zinc Atom for the Stability of Yeast Alcohol Dehydrogenase. *Biochem. J.* **1992**, *287* (2), 361–365.

(79) Ray, S.; Shard, A. G. Quantitative Analysis of Adsorbed Proteins by X-Ray Photoelectron Spectroscopy. *Anal. Chem.* **2011**, *83* (22), 8659–8666.

(80) Anderson, S. L.; Luber, E. J.; Olsen, B. C.; Buriak, J. M. Substance over Subjectivity: Moving beyond the Histogram. *Chem. Mater.* **2016**, *28*, 5973–5975.

(81) McCall, J. D.; Anseth, K. S. Thiol–Ene Photopolymerizations Provide a Facile Method to Encapsulate Proteins and Maintain Their Bioactivity. *Biomacromolecules* **2012**, *13* (8), 2410–2417.

(82) Sinelnikov, R.; Dasog, M.; Beamish, J.; Meldrum, A.; Veinot, J. G. Revisiting an Ongoing Debate: What Role Do Surface Groups Play in Silicon Nanocrystal Photoluminescence? *ACS Photonics* **2017**, *4* (8), 1920–1929.

(83) Rosso-Vasic, M.; Spruijt, E.; Popović, Z.; Overgaag, K.; Van Lagen, B.; Grandidier, B.; Vanmaekelbergh, D.; Domínguez-Gutiérrez, D.; De Cola, L.; Zuilhof, H. Amine-Terminated Silicon Nanoparticles: Synthesis, Optical Properties and Their Use in Bioimaging. *J. Mater. Chem.* **2009**, *19* (33), 5926–5933.

(84) Hua, F.; Erogbogbo, F.; Swihart, M. T.; Ruckenstein, E. Organically Capped Silicon Nanoparticles with Blue Photoluminescence Prepared by Hydrosilylation Followed by Oxidation. *Langmuir* **2006**, *22* (9), 4363–4370.

(85) Park, J.-H.; Gu, L.; Von Maltzahn, G.; Ruoslahti, E.; Bhatia, S. N.; Sailor, M. J. Biodegradable Luminescent Porous Silicon Nanoparticles for in Vivo Applications. *Nat. Mater.* **2009**, *8* (4), 331.

(86) Dickinson, F. M.; Alsop, T. A.; Al-Sharif, N.; Berger, C. E. M.; Datta, H. K.; Šiller, L.; Chao, Y.; Tuite, E. M.; Houlton, A.; Horrocks, B. R. Dispersions of Alkyl-Capped Silicon Nanocrystals in Aqueous Media: Photoluminescence and Ageing. *Analyst* **2008**, *133* (11), 1573–1580.

(87) Letant, S. E.; Hart, B. R.; Kane, S. R.; Hadi, M. Z.; Shields, S. J.; Reynolds, J. G. Enzyme Immobilization on Porous Silicon Surfaces. *Adv. Mater.* **2004**, *16* (8), 689–693.

(88) Létant, S. E.; Kane, S. R.; Hart, B. R.; Hadi, M. Z.; Cheng, T.-C.; Rastogi, V. K.; Reynolds, J. G. Hydrolysis of Acetylcholinesterase Inhibitors–Organophosphorus Acid Anhydrolase Enzyme Immobilization on Photoluminescent Porous Silicon Platforms. *Chem. Commun.* **2005**, No. 7, 851–853.

(89) Gonzalez, C. M.; Iqbal, M.; Dasog, M.; Piercey, D. G.; Lockwood, R.; Klapötke, T. M.; Veinot, J. G. Detection of High-Energy Compounds Using Photoluminescent Silicon Nanocrystal Paper Based Sensors. *Nanoscale* **2014**, *6* (5), 2608–2612.

(90) Krajewska, B.; Ciurli, S. Jack Bean (Canavalia Ensiformis) Urease. Probing Acid–Base Groups of the Active Site by PH Variation. *Plant Physiol. Biochem.* **2005**, *43* (7), 651–658.

(91) Cesareo, S. D.; Langton, S. R. Kinetic Properties of Helicobacter Pylori Urease Compared with Jack Bean Urease. *FEMS Microbiol. Lett.* **1992**, *99* (1), 15–21.

(92) Norris, R.; Brocklehurst, K. A Convenient Method of Preparation of High-Activity Urease from Canavalia Ensiformis by Covalent Chromatography and an Investigation of Its Thiol Groups with 2, 2'-Dipyridyl Disulphide as a Thiol Titrant and Reactivity Probe. *Biochem. J.* **1976**, *159* (2), 245–257.

(93) Chiu, S.-K.; Manhat, B. A.; DeBenedetti, W. J.; Brown, A. L.; Fichter, K.; Vu, T.; Eastman, M.; Jiao, J.; Goforth, A. M. Aqueous Red-Emitting Silicon Nanoparticles for Cellular Imaging: Consequences of Protecting against Surface Passivation by Hydroxide and Water for Stable Red Emission. *J. Mater. Res.* **2013**, *28* (2), 216–230.

(94) Chandler-Henderson, R. R.; Sweryda-Krawiec, B.; Coffer, J. L. Steric Considerations in the Amine-Induced Quenching of Luminescent Porous Silicon. *J. Phys. Chem.* **1995**, *99* (21), 8851–8855.

(95) Sweryda-Krawiec, B.; Chandler-Henderson, R. R.; Coffer, J. L.; Rho, Y. G.; Pinizzotto, R. F. A Comparison of Porous Silicon and Silicon Nanocrystallite Photoluminescence Quenching with Amines. *J. Phys. Chem.* **1996**, *100* (32), 13776–13780.

(96) Dasog, M.; Yang, Z.; Regli, S.; Atkins, T. M.; Faramus, A.; Singh, M. P.; Muthuswamy, E.; Kauzlarich, S. M.; Tilley, R. D.; Veinot, J. G. Chemical Insight into the Origin of Red and Blue Photoluminescence Arising from Freestanding Silicon Nanocrystals. *ACS Nano* **2013**, *7* (3), 2676–2685.

(97) De Melo, J. V.; Cosnier, S.; Mousty, C.; Martelet, C.; Jaffrezic-Renault, N. Urea Biosensors Based on Immobilization of Urease into Two Oppositely Charged Clays (Laponite and Zn- Al Layered Double Hydroxides). *Anal. Chem.* **2002**, *74* (16), 4037–4043.

Chapter 4

(1) Sidell, F. R.; Borak, J. Chemical Warfare Agents: II. Nerve Agents. *Ann. Emerg. Med.* **1992**, *21* (7), 865–871.

(2) Holstege, C. P.; Kirk, M.; Sidell, F. R. Chemical Warfare: Nerve Agent Poisoning. *Crit. Care Clin.* **1997**, *13* (4), 923–942.

(3) Deshpande, L. S.; Carter, D. S.; Phillips, K. F.; Blair, R. E.; DeLorenzo, R. J. Development of Status Epilepticus, Sustained Calcium Elevations and Neuronal Injury in a Rat Survival Model of Lethal Paraoxon Intoxication. *Neurotoxicology* **2014**, *44*, 17–26.

(4) Deshpande, L. S.; Phillips, K.; Huang, B.; DeLorenzo, R. J. Chronic Behavioral and Cognitive Deficits in a Rat Survival Model of Paraoxon Toxicity. *Neurotoxicology* **2014**, *44*, 352–357.

(5) Gould, C.; Folb, P. The Role of Professionals in the South African Chemical and Biological Warfare Programme. *Minerva* **2002**, *40* (1), 77–91.

(6) Truelsen, J. B. Developments in Toxics in 2004: The Ratification of the Stockholm Convention and the Rotterdam Convention. *Colo. J. Int. Environ. Law Pol.* **2005**, *16*, 217–230.

(7) Parathion Health and Safety Guide. IPCS International Programme on Chemical Safety, 1992, http://www.inchem.org/documents/hsg/hsg/hsg74.htm (accessed Jun 23, 2019).

(8) Litchfield, M. H. Estimates of Acute Pesticide Poisoning in Agricultural Workers in Less Developed Countries. *Toxicol. Rev.* **2005**, *24* (4), 271–278.

(9) Cross, G. *Dirty War: Rhodesia and Chemical Biological Warfare 1975-1980*; Helion and Company: Solihull, England, 2017; p. 80.

(10) Zaugg, S. D.; Sandstrom, M. W.; Smith, S. G.; Fehlberg, K. M. Methods of Analysis by the US Geological Survey National Water Quality Laboratory; Determination of Pesticides in Water by C-18 Solid-Phase Extraction and Capillary-Column Gas Chromatography/Mass Spectrometry with Selected-Ion Monitoring. US Geological Survey, 1995. https://nwql.usgs.gov/Public/pubs/WRIR/WRIR-01-4098.pdf (accessed Jun 19, 2019)

(11) Lee, J.; Lee, H. K. Fully Automated Dynamic In-Syringe Liquid-Phase Microextraction and on-Column Derivatization of Carbamate Pesticides with Gas Chromatography/Mass Spectrometric Analysis. *Anal. Chem.* **2011**, *83* (17), 6856–6861.

(12) Mothes, S.; Popp, P.; Wennrich, R. Analysis of Organophosphorus Insecticides in Natural Waters by Use of Stir-Bar-Sorptive Extraction Then Gas Chromatography with Atomic Emission Detection. *Chromatographia* **2003**, *57* (1), S249–S252.

(13) Buonasera, K.; D'Orazio, G.; Fanali, S.; Dugo, P.; Mondello, L. Separation of Organophosphorus Pesticides by Using Nano-Liquid Chromatography. *J. Chromatogr. A* **2009**, *1216* (18), 3970–3976.

(14) Walker, J. P.; Asher, S. A. Acetylcholinesterase-Based Organophosphate Nerve Agent Sensing Photonic Crystal. *Anal. Chem.* **2005**, *77* (6), 1596–1600.

(15) Du, D.; Chen, W.; Zhang, W.; Liu, D.; Li, H.; Lin, Y. Covalent Coupling of Organophosphorus Hydrolase Loaded Quantum Dots to Carbon Nanotube/Au Nanocomposite for Enhanced Detection of Methyl Parathion. *Biosens. Bioelectron.* **2010**, *25* (6), 1370–1375.

(16) Hou, J.; Dong, J.; Zhu, H.; Teng, X.; Ai, S.; Mang, M. A Simple and Sensitive Fluorescent Sensor for Methyl Parathion Based on L-Tyrosine Methyl Ester Functionalized Carbon Dots. *Biosens. Bioelectron.* **2015**, *68*, 20–26.

(17) Meng, X.; Wei, J.; Ren, X.; Ren, J.; Tang, F. A Simple and Sensitive Fluorescence Biosensor for Detection of Organophosphorus Pesticides Using H_2O_2-Sensitive Quantum Dots/Bi-Enzyme. *Biosens. Bioelectron.* **2013**, *47*, 402–407.

(18) Ji, X.; Zheng, J.; Xu, J.; Rastogi, V. K.; Cheng, T.-C.; DeFrank, J. J.; Leblanc, R. M. (CdSe) ZnS Quantum Dots and Organophosphorus Hydrolase Bioconjugate as Biosensors for Detection of Paraoxon. *J. Phys. Chem. B* **2005**, *109* (9), 3793–3799.

(19) Yi, Y.; Zhu, G.; Liu, C.; Huang, Y.; Zhang, Y.; Li, H.; Zhao, J.; Yao, S. A Label-Free Silicon Quantum Dots-Based Photoluminescence Sensor for Ultrasensitive Detection of Pesticides. *Anal. Chem.* **2013**, *85* (23), 11464–11470.

(20) Zheng, Z.; Zhou, Y.; Li, X.; Liu, S.; Tang, Z. Highly-Sensitive Organophosphorous Pesticide Biosensors Based on Nanostructured Films of Acetylcholinesterase and CdTe Quantum Dots. *Biosens. Bioelectron.* **2011**, *26* (6), 3081–3085.

(21) Yan, X.; Li, H.; Yan, Y.; Su, X. Selective Detection of Parathion-Methyl Based on near-Infrared CuInS2 Quantum Dots. *Food Chem.* **2015**, *173*, 179–184.

(22) McVey, B. F.; Tilley, R. D. Solution Synthesis, Optical Properties, and Bioimaging Applications of Silicon Nanocrystals. *Acc. Chem. Res.* **2014**, *47* (10), 3045–3051.

(23) Zhai, Y.; Dasog, M.; Snitynsky, R. B.; Purkait, T. K.; Aghajamali, M.; Hahn, A. H.; Sturdy, C. B.; Lowary, T. L.; Veinot, J. G. C. Water-Soluble Photoluminescent D-Mannose and L-Alanine Functionalized Silicon Nanocrystals and Their Application to Cancer Cell Imaging. *J. Mater. Chem. B* **2014**, *2* (47), 8427–8433.

(24) Gonzalez, C. M.; Iqbal, M.; Dasog, M.; Piercey, D. G.; Lockwood, R.; Klapötke, T. M.; Veinot, J. G. C. Detection of High-Energy Compounds Using Photoluminescent Silicon Nanocrystal Paper Based Sensors. *Nanoscale* **2014**, *6* (5), 2608–2612.

(25) Sinelnikov, R.; Dasog, M.; Beamish, J.; Meldrum, A.; Veinot, J. G. C. Revisiting an Ongoing Debate: What Role Do Surface Groups Play in Silicon Nanocrystal Photoluminescence? *ACS Photonics* **2017**, *4* (8), 1920–1929.

(26) Islam, M. A.; Sinelnikov, R.; Howlader, M. A.; Faramus, A.; Veinot, J. G. C. Mixed Surface Chemistry: An Approach to Highly Luminescent Biocompatible Amphiphilic Silicon Nanocrystals. *Chem. Mater.* **2018**, *30* (24), 8925–8931.

(27) Liu, J.; Erogbogbo, F.; Yong, K.-T.; Ye, L.; Liu, J.; Hu, R.; Chen, H.; Hu, Y.; Yang, Y.; Yang, J. Assessing Clinical Prospects of Silicon Quantum Dots: Studies in Mice and Monkeys. *ACS Nano* **2013**, *7* (8), 7303–7310.

(28) Chen, N.; He, Y.; Su, Y.; Li, X.; Huang, Q.; Wang, H.; Zhang, X.; Tai, R.; Fan, C. The Cytotoxicity of Cadmium-Based Quantum Dots. *Biomaterials* **2012**, *33* (5), 1238–1244.

(29) Cubitt, A. B.; Heim, R.; Adams, S. R.; Boyd, A. E.; Gross, L. A.; Tsien, R. Y. Understanding, Improving and Using Green Fluorescent Proteins. *Trends Biochem. Sci.* **1995**, *20* (11), 448–455.

(30) Ormö, M.; Cubitt, A. B.; Kallio, K.; Gross, L. A.; Tsien, R. Y.; Remington, S. J. Crystal Structure of the Aequorea Victoria Green Fluorescent Protein. *Science* **1996**, *273* (5280), 1392–1395.

(31) Miyawaki, A.; Llopis, J.; Heim, R.; McCaffery, J. M.; Adams, J. A.; Ikura, M.; Tsien, R. Y. Fluorescent Indicators for Ca^{2+} Based on Green Fluorescent Proteins and Calmodulin. *Nature* **1997**, *388* (6645), 882–887.

(32) Miyawaki, A.; Niino, Y. Molecular Spies for Bioimaging—Fluorescent Protein-Based Probes. *Mol. Cell* **2015**, *58* (4), 632–643.

(33) Zhu, A.; Qu, Q.; Shao, X.; Kong, B.; Tian, Y. Carbon-Dot-Based Dual-Emission Nanohybrid Produces a Ratiometric Fluorescent Sensor for in Vivo Imaging of Cellular Copper Ions. *Angew. Chem., Int. Ed.* **2012**, *51* (29), 7185–7189.

(34) Cao, B.; Yuan, C.; Liu, B.; Jiang, C.; Guan, G.; Han, M.-Y. Ratiometric Fluorescence Detection of Mercuric Ion Based on the Nanohybrid of Fluorescence Carbon Dots and Quantum Dots. *Anal. Chim. Acta* **2013**, *786*, 146–152.

(35) Zhang, K.; Zhou, H.; Mei, Q.; Wang, S.; Guan, G.; Liu, R.; Zhang, J.; Zhang, Z. Instant Visual Detection of Trinitrotoluene Particulates on Various Surfaces by Ratiometric Fluorescence of Dual-Emission Quantum Dots Hybrid. *J. Am. Chem. Soc.* **2011**, *133* (22), 8424–8427.

(36) Chen, X.; Wo, F.; Jin, Y.; Tan, J.; Lai, Y.; Wu, J. Drug-Porous Silicon Dual Luminescent System for Monitoring and Inhibition of Wound Infection. *ACS Nano* **2017**, *11*, 7938–7949.

(37) Ding, Y.; Ai, H.; Hoi, H.; Campbell, R. E. Förster Resonance Energy Transfer-Based Biosensors for Multiparameter Ratiometric Imaging of Ca^{2+} Dynamics and Caspase-3 Activity in Single Cells. *Anal. Chem.* **2011**, *83* (24), 9687–9693.

(38) Hessel, C. M.; Henderson, E. J.; Veinot, J. G. C. Hydrogen Silsesquioxane: A Molecular Precursor for Nanocrystalline Si- SiO2 Composites and Freestanding Hydride-Surface-Terminated Silicon Nanoparticles. *Chem. Mater.* **2006**, *18* (26), 6139–6146.

(39) Robidillo, C. J. T.; Aghajamali, M.; Faramus, A.; Sinelnikov, R.; Veinot, J. G. C. Interfacing Enzymes with Silicon Nanocrystals through the Thiol–Ene Reaction. *Nanoscale* **2018**, *10* (39), 18706–18719.

(40) Robidillo, C. J. T.; Islam, M. A.; Aghajamali, M.; Faramus, A.; Sinelnikov, R.; Zhang, X.; Boekhoven, J.; Veinot, J. G. C. Functional Bioinorganic Hybrids from Enzymes and Luminescent Silicon-Based Nanoparticles. *Langmuir* **2018**, *34* (22), 6556–6569.

(41) Jakob, M.; Aissiou, A.; Morrish, W.; Marsiglio, F.; Islam, M.; Kartouzian, A.; Meldrum, A. Reappraising the Luminescence Lifetime Distributions in Silicon Nanocrystals. *Nanoscale Res. Lett.* **2018**, *13* (1), 383–394.

(42) Otsuka, H.; Nagasaki, Y.; Kataoka, K. PEGylated Nanoparticles for Biological and Pharmaceutical Applications. *Adv. Drug Delivery Rev.* **2012**, *64*, 246–255.

(43) Pelaz, B.; del Pino, P.; Maffre, P.; Hartmann, R.; Gallego, M.; Rivera-Fernandez, S.; de la Fuente, J. M.; Nienhaus, G. U.; Parak, W. J. Surface Functionalization of Nanoparticles with Polyethylene Glycol: Effects on Protein Adsorption and Cellular Uptake. *ACS Nano* **2015**, *9* (7), 6996–7008.

(44) Dai, Q.; Walkey, C.; Chan, W. C. Polyethylene Glycol Backfilling Mitigates the Negative Impact of the Protein Corona on Nanoparticle Cell Targeting. *Angew. Chem., Int. Ed.* **2014**, *53* (20), 5093–5096.

(45) Wörz, A.; Berchtold, B.; Moosmann, K.; Prucker, O.; Rühe, J. Protein-Resistant Polymer Surfaces. *J. Mater. Chem.* **2012**, *22* (37), 19547–19561.

(46) Clark, R. J.; Dang, M. K.; Veinot, J. G. C. Exploration of Organic Acid Chain Length on Water-Soluble Silicon Quantum Dot Surfaces. *Langmuir* **2010**, *26* (19), 15657–15664.

(47) Mkhatresh, O. A.; Heatley, F. A Study of the Products and Mechanism of the Thermal Oxidative Degradation of Poly (Ethylene Oxide) Using 1H and 13C 1-D and 2-D NMR. *Polym. Int.* **2004**, *53* (9), 1336–1342.

(48) Yang, L.; Heatley, F.; Blease, T. G.; Thompson, R. I. A Study of the Mechanism of the Oxidative Thermal Degradation of Poly (Ethylene Oxide) and Poly (Propylene Oxide) Using 1H-and 13C-NMR. *Eur. Polym. J.* **1996**, *32* (5), 535–547.

(49) Matsuura, H.; Miyazawa, T. Vibrational Analysis of Molten Poly (Ethylene Glycol). *J. Polym. Sci., Polym. Phys.* **1969**, *7* (10), 1735–1744.

(50) Yang, Z.; Gonzalez, C. M.; Purkait, T. K.; Iqbal, M.; Meldrum, A.; Veinot, J. G. C. Radical Initiated Hydrosilylation on Silicon Nanocrystal Surfaces: An Evaluation of Functional Group Tolerance and Mechanistic Study. *Langmuir* **2015**, *31* (38), 10540–10548.

(51) Doremus, R. H. Oxidation of Silicon by Water and Oxygen and Diffusion in Fused Silica. *J. Phys. Chem.* **1976**, *80* (16), 1773–1775.

(52) Wu, E. C.; Park, J. H.; Park, J.; Segal, E.; Cunin, F.; Sailor, M. J. Oxidation-Triggered Release of Fluorescent Molecules or Drugs from Mesoporous Si Microparticles. *ACS Nano* **2008**, *2* (11), 2401–2409.

(53) Flitsch, R.; Raider, S. I. Electron Mean Escape Depths from X- Ray Photoelectron Spectra of Thermally Oxidized Silicon Dioxide Films on Silicon. *J. Vac. Sci. Technol.* **1975**, *12* (1), 305–308.

(54) Damodaran, V. B.; Fee, C. J.; Ruckh, T.; Popat, K. C. Conformational Studies of Covalently Grafted Poly (Ethylene Glycol) on Modified Solid Matrices Using X-Ray Photoelectron Spectroscopy. *Langmuir* **2010**, *26* (10), 7299–7306.

(55) Briggs, D.; Beamson, G. Primary and Secondary Oxygen-Induced C1s Binding Energy Shifts in x-Ray Photoelectron Spectroscopy of Polymers. *Anal. Chem.* **1992**, *64* (15), 1729–1736.

(56) Thomas, H. R.; O'Malley, J. J. Surface Studies on Multicomponent Polymer Systems by X-Ray Photoelectron Spectroscopy. Polystyrene/Poly (Ethylene Oxide) Diblock Copolymers. *Macromolecules* **1979**, *12* (2), 323–329.

(57) Anderson, S. L.; Luber, E. J.; Olsen, B. C.; Buriak, J. M. Substance over Subjectivity: Moving beyond the Histogram. *Chem. Mater.* **2016**, *28*, 5973–5975.

(58) Content, S.; Trogler, W. C.; Sailor, M. J. Detection of Nitrobenzene, DNT, and TNT Vapors by Quenching of Porous Silicon Photoluminescence. *Chem. Eur. J.* **2000**, *6* (12), 2205–2213.

(59) Eyer, F.; Meischner, V.; Kiderlen, D.; Thiermann, H.; Worek, F.; Haberkorn, M.; Felgenhauer, N.; Zilker, T.; Eyer, P. Human Parathion Poisoning. *Toxicol. Rev.* **2003**, *22* (3), 143–163.

(60) Eto, M.; Kishimoto, K.; Matsumura, K.; Ohshita, N.; Oshima, Y. Studies on Saligenin Cyclic Phosphorus Esters with Insecticidal Activity Part IX. *Agric. Biol. Chem.* **1966**, *30* (2), 181–185.

(61) Nishizawa, Y.; Fujii, K.; Kadota, T.; Miyamoto, J.; Sakamoto, H. Studies on the Organophosphorus Insecticides: Part VII. Chemical and Biological Properties of New Low Toxic Organophosphorus Insecticide. O, O-Dimethyl-O-(3-Methyl-4-Nitrophenyl) Phosphorothioate. *Agric. Biol. Chem.* **1961**, *25* (8), 605–610.

(62) DuBois, K.P.; Doull, J.; Salerno, P.R.; Coon, J.M. Studies on the Toxicity and Mechanism of Action of *p*-Nitrophenyl Diethyl Thionophosphate (Parathion). *J. Pharmacol. Exp. Ther.* **1949**, *95* (1), 79-91.

(63) Koivistoinen, P.; Meriläinen, M. Paper Chromatographic Studies on the Effect of Ultraviolet Light on Parathion and Its Derivatives. *Acta Agr. Scand.* **1962**, *12* (4), 267–276.

Chapter 5

(1) Liu, J.; Erogbogbo, F.; Yong, K.-T.; Ye, L.; Liu, J.; Hu, R.; Chen, H.; Hu, Y.; Yang, Y.; Yang, J.; Roy, I.; Karker, N. A.; Swihart, M. T.; Prasad, P. N. Assessing Clinical Prospects of Silicon Quantum Dots: Studies in Mice and Monkeys. *ACS Nano* **2013**, *7* (8), 7303–7310.

(2) Erogbogbo, F.; Yong, K.-T.; Roy, I.; Xu, G.; Prasad, P. N.; Swihart, M. T. Biocompatible Luminescent Silicon Quantum Dots for Imaging of Cancer Cells. *ACS Nano* **2008**, *2* (5), 873–878.

(3) Sinelnikov, R.; Dasog, M.; Beamish, J.; Meldrum, A.; Veinot, J. G. C. Revisiting an Ongoing Debate: What Role Do Surface Groups Play in Silicon Nanocrystal Photoluminescence? *ACS Photonics* **2017**, *4* (8), 1920–1929.

(4) Islam, M. A.; Sinelnikov, R.; Howlader, M. A.; Faramus, A.; Veinot, J. G. C. Mixed Surface Chemistry: An Approach to Highly Luminescent Biocompatible Amphiphilic Silicon Nanocrystals. *Chem. Mater.* **2018**, *30* (24), 8925–8931.

(5) Erogbogbo, F.; May, J.; Swihart, M.; Prasad, P. N.; Smart, K.; Jack, S. E.; Korcyk, D.; Webster, M.; Stewart, R.; Zeng, I.; Jullig, M.; Bakeev, K.; Jamieson, M.; Kasabov, N.; Gopalan, B.; Liang, L.; Hu, R.; Schliebs, S.; Villas-Boas, S.; Gladding, P. Bioengineering Silicon Quantum Dot Theranostics Using a Network Analysis of Metabolomic and Proteomic Data in Cardiac Ischemia. *Theranostics* **2013**, *3* (9), 719–728.

(6) Robidillo, C. J. T.; Wandelt, S.; Dalangin, R.; Zhang, L.; Yu, H.; Meldrum, A.; Campbell, R. E.; Veinot, J. G. C. Ratiometric Detection of Nerve Agents by Coupling Complementary Properties of Silicon-Based Quantum Dots and Green Fluorescent Protein. *ACS Appl. Mater. Interfaces* **2019**, *11* (36), 33478–33488.

(7) Robidillo, C. J. T.; Aghajamali, M.; Faramus, A.; Sinelnikov, R.; Veinot, J. G. C. Interfacing Enzymes with Silicon Nanocrystals through the Thiol–Ene Reaction. *Nanoscale* **2018**, *10* (39), 18706–18719.

(8) Gonzalez, C.; Iqbal, M.; Dasog, M.; G. Piercey, D.; Lockwood, R.; M. Klapötke, T.; C. Veinot, J. G. C. Detection of High-Energy Compounds Using Photoluminescent Silicon Nanocrystal Paper Based Sensors. *Nanoscale* **2014**, *6* (5), 2608–2612.

(9) Gonzalez, C.; C. Veinot, J. G. C. Silicon Nanocrystals for the Development of Sensing Platforms. *J. Mater. Chem. C* **2016**, *4* (22), 4836–4846.

(10) Robidillo, C. J. T.; Islam, M. A.; Aghajamali, M.; Faramus, A.; Sinelnikov, R.; Zhang, X.; Boekhoven, J.; Veinot, J. G. C. Functional Bioinorganic Hybrids from Enzymes and Luminescent Silicon-Based Nanoparticles. *Langmuir* **2018**, *34* (22), 6556–6569.

(11) Kowalczyk, T.; Hnatuszko-Konka, K.; Gerszberg, A.; Kononowicz, A. K. Elastin-like Polypeptides as a Promising Family of Genetically Engineered Protein Based Polymers. *World J. Microbiol. Biotechnol.* **2014**, *30* (8), 2141–2152.

(12) Nettles, D. L.; Chilkoti, A.; Setton, L. A. Applications of Elastin-like Polypeptides in Tissue Engineering. *Adv. Drug Deliv. Rev.* **2010**, *62* (15), 1479–1485.

(13) Busa, W. B.; Nuccitelli, R. Metabolic Regulation via Intracellular pH. *Am. J. Physiol. Regul. Integr. Comp. Physiol.* **1984**, *246* (4), R409–R438.

(14) Loiselle, F. B.; Casey, J. R. Measurement of Intracellular pH in Membrane Transporters: Methods and Protocols; Yan, Q., Ed.; Methods in Molecular Biology; Humana Press: Totowa, NJ, 2003; pp 259–280.

(15) Izumi, H.; Torigoe, T.; Ishiguchi, H.; Uramoto, H.; Yoshida, Y.; Tanabe, M.; Ise, T.; Murakami, T.; Yoshida, T.; Nomoto, M.; et al. Cellular PH Regulators: Potentially Promising Molecular Targets for Cancer Chemotherapy. *Cancer Treat. Rev.* **2003**, *29* (6), 541–549.

(16) Davies, T. A.; Fine, R. E.; Johnson, R. J.; Levesque, C. A.; Rathbun, W. H.; Seetoo, K. F.; Smith, S. J.; Strohmeier, G.; Volicer, L.; Delva, L.; Simons, E. R. Non-Age Related Differences in Thrombin Responses by Platelets from Male Patients with Advanced Alzheimer′s Disease. *Biochem. Biophys. Res. Commun.* **1993**, *194* (1), 537–543.

(17) Wray, S. Smooth Muscle Intracellular pH: Measurement, Regulation, and Function. *Am. J. Physiol. Cell Physiol.* **1988**, *254* (2), C213–C225.

(18) Kotyk, A.; Slavik, J. Intracellular PH and Its Measurement; CRC Press: Boca Raton, FL, 1989.

(19) Dennis, A. M.; Rhee, W. J.; Sotto, D.; Dublin, S. N.; Bao, G. Quantum Dot–Fluorescent Protein FRET Probes for Sensing Intracellular pH. *ACS Nano* **2012**, *6* (4), 2917–2924.

(20) Awaji, T.; Hirasawa, A.; Shirakawa, H.; Tsujimoto, G.; Miyazaki, S. Novel Green Fluorescent Protein-Based Ratiometric Indicators for Monitoring PH in Defined Intracellular Microdomains. *Biochem. Biophys. Res. Commun.* **2001**, *289* (2), 457–462.

(21) Tantama, M.; Hung, Y. P.; Yellen, G. Imaging Intracellular PH in Live Cells with a Genetically Encoded Red Fluorescent Protein Sensor. *J. Am. Chem. Soc.* **2011**, *133* (26), 10034–10037.

(22) Shi, W.; Li, X.; Ma, H. A Tunable Ratiometric PH Sensor Based on Carbon Nanodots for the Quantitative Measurement of the Intracellular pH of Whole Cells. *Angew. Chem., Int. Ed.* **2012**, *51* (26), 6432–6435.

(23) Chen, N.; He, Y.; Su, Y.; Li, X.; Huang, Q.; Wang, H.; Zhang, X.; Tai, R.; Fan, C. The Cytotoxicity of Cadmium-Based Quantum Dots. *Biomaterials* **2012**, *33* (5), 1238–1244.

(24) Ormö, M.; Cubitt, A. B.; Kallio, K.; Gross, L. A.; Tsien, R. Y.; Remington, S. J. Crystal Structure of the Aequorea Victoria Green Fluorescent Protein. *Science* **1996**, *273* (5280), 1392–1395.

(25) Cubitt, A. B.; Heim, R.; Adams, S. R.; Boyd, A. E.; Gross, L. A.; Tsien, R. Y. Understanding, Improving and Using Green Fluorescent Proteins. *Trends Biochem. Sci.* **1995**, *20* (11), 448–455.

(26) Ding, Y.; Ai, H.; Hoi, H.; Campbell, R. E. Förster Resonance Energy Transfer-Based Biosensors for Multiparameter Ratiometric Imaging of Ca2+ Dynamics and Caspase-3 Activity in Single Cells. *Anal. Chem.* **2011**, *83* (24), 9687–9693.

(27) van Rossum, S. A. P.; Tena-Solsona, M.; Esch, J. H. van; Eelkema, R.; Boekhoven, J. Dissipative Out-of-Equilibrium Assembly of Man-Made Supramolecular Materials. *Chem. Soc. Rev.* **2017**, *46* (18), 5519–5535.

(28) Boekhoven, J.; Hendriksen, W. E.; Koper, G. J. M.; Eelkema, R.; Esch, J. H. van. Transient Assembly of Active Materials Fueled by a Chemical Reaction. *Science* **2015**, *349* (6252), 1075–1079.

(29) Boekhoven, J.; Brizard, A. M.; Kowlgi, K. N. K.; Koper, G. J. M.; Eelkema, R.; van Esch, J. H. Dissipative Self-Assembly of a Molecular Gelator by Using a Chemical Fuel. *Angew. Chem. Int., Ed.* **2010**, *49* (28), 4825–4828.

(30) Tena-Solsona, M.; Rieß, B.; Grötsch, R. K.; Löhrer, F. C.; Wanzke, C.; Käsdorf, B.; Bausch, A. R.; Müller-Buschbaum, P.; Lieleg, O.; Boekhoven, J. Non-Equilibrium Dissipative Supramolecular Materials with a Tunable Lifetime. *Nat. Commun.* **2017**, *8* (1), 1–8.

(31) Carlini, E. A. The Good and the Bad Effects of (-) Trans-Delta-9-Tetrahydrocannabinol (Δ9-THC) on Humans. *Toxicon* **2004**, *44* (4), 461–467.

(32) Payne, R.; Mathias, S. D.; Pasta, D. J.; Wanke, L. A.; Williams, R.; Mahmoud, R. Quality of Life and Cancer Pain: Satisfaction and Side Effects with Transdermal Fentanyl versus Oral Morphine. *J. Clin. Oncol.* **1998**, *16* (4), 1588–1593.

(33) Fentanyl | DEA https://www.dea.gov/galleries/drug-images/fentanyl (accessed Jan 14, 2019).

(34) MPs debate how Canada should approach fighting fentanyl, opioid crises | Globalnews.ca https://globalnews.ca/news/4748497/fentanyl-opioid-crisis-debate-house-of-commons/ (accessed Jan 14, 2019).

(35) Fentanyl Overdose https://www.huffingtonpost.ca/news/fentanyl-overdose/ (accessed Jan 14, 2019).

(36) Mackie stands behind fentanyl-in-pot warning, despite "spirited" backlash | CBC News https://www.cbc.ca/news/canada/london/fentanyl-marijuana-warning-backlash-1.4240332 (accessed Jan 14, 2019).

(37) Police Say Some of Synthetic Marijuana Was Laced with Fentanyl | Watch News Videos Online. Global News. https://globalnews.ca/video/4391863/police-say-some-of-synthetic-marijuana-was-laced-with-fentanyl (accessed Jan 14, 2019).

(38) Huang, X.; Jain, P. K.; El-Sayed, I. H.; El-Sayed, M. A. Gold Nanoparticles: Interesting Optical Properties and Recent Applications in Cancer Diagnostics and Therapy. *Nanomedicine (Lond.)* **2007**, *2* (5) 681-693.

(39) Eustis, S.; El-Sayed, M. A. Why Gold Nanoparticles Are More Precious than Pretty Gold: Noble Metal Surface Plasmon Resonance and Its Enhancement of the Radiative and Nonradiative Properties of Nanocrystals of Different Shapes. *Chem. Soc. Rev.* **2006**, *35* (3), 209–217.

(40) Tsunoyama, H.; Sakurai, H.; Ichikuni, N.; Negishi, Y.; Tsukuda, T. Colloidal Gold Nanoparticles as Catalyst for Carbon- Carbon Bond Formation: Application to Aerobic Homocoupling of Phenylboronic Acid in Water. *Langmuir* **2004**, *20* (26), 11293–11296.

(41) Daniel, M.-C.; Astruc, D. Gold Nanoparticles: Assembly, Supramolecular Chemistry, Quantum-Size-Related Properties, and Applications toward Biology, Catalysis, and Nanotechnology. *Chem. Rev.* **2004**, *104* (1), 293–346.

(42) Fan, C.; Wang, S.; Hong, J. W.; Bazan, G. C.; Plaxco, K. W.; Heeger, A. J. Beyond Superquenching: Hyper-Efficient Energy Transfer from Conjugated Polymers to Gold Nanoparticles. *Proc. Natl. Acad. Sci.* **2003**, *100* (11), 6297–6301.

(43) Dulkeith, E.; Ringler, M.; Klar, T. A.; Feldmann, J.; Munoz Javier, A.; Parak, W. J. Gold Nanoparticles Quench Fluorescence by Phase Induced Radiative Rate Suppression. *Nano Lett.* **2005**, *5* (4), 585–589.

(44) Pons, T.; Medintz, I. L.; Sapsford, K. E.; Higashiya, S.; Grimes, A. F.; English, D. S.; Mattoussi, H. On the Quenching of Semiconductor Quantum Dot Photoluminescence by Proximal Gold Nanoparticles. *Nano Lett.* **2007**, *7* (10), 3157–3164.

(45) Liu, J.; Erogbogbo, F.; Yong, K.-T.; Ye, L.; Liu, J.; Hu, R.; Chen, H.; Hu, Y.; Yang, Y.; Yang, J. Assessing Clinical Prospects of Silicon Quantum Dots: Studies in Mice and Monkeys. *ACS Nano* **2013**, *7* (8), 7303–7310.

(46) McVey, B. F.; Tilley, R. D. Solution Synthesis, Optical Properties, and Bioimaging Applications of Silicon Nanocrystals. *Acc. Chem. Res.* **2014**, *47* (10), 3045–3051.

(47) Gonzalez, C. M.; Veinot, J. G. Silicon Nanocrystals for the Development of Sensing Platforms. *J. Mater. Chem. C* **2016**, *4* (22), 4836–4846.

(48) Wijaya, A.; Hamad-Schifferli, K. Ligand Customization and DNA Functionalization of Gold Nanorods via Round-Trip Phase Transfer Ligand Exchange. *Langmuir* **2008**, *24* (18), 9966–9969.

Appendix

Estimation of the Concentration of Silicon-Based Quantum Dots Presented in Chapter 4

The average molar mass (M) of the particle core of the water-soluble SiQDs has been assumed to be equal to that of the silicon core of dodecyl-terminated SiQDs ($C_{12}H_{25}$-SiQDs) (Figure A-1) which was obtained as follows:

$M = (4/3)\,\pi\,(d/2)^3\,\rho\,N_A = 4/3\,\pi\,(5.0/2\text{ nm})^3\,(2.3\text{ g cm}^{-3})\,(6.023\text{x}10^{23}\text{ mol}^{-1})\,(1\text{x}10^{-21}\text{ cm}^3\text{ nm}^{-3})$
$= 9.07\text{x}10^4\text{ g mol}^{-1}$

where ρ = density of silicon, d = diameter of the silicon core, N_A = Avogadro's number

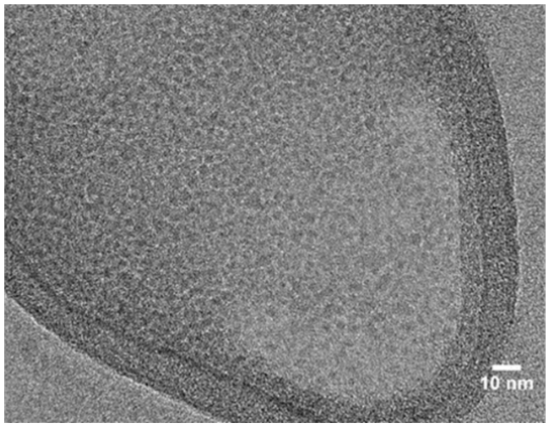

Figure A-1. Bright field transmission electron micrograph of $C_{12}H_{25}$-SiQDs.

The concentration (C) of the stock solution of water-soluble SiQDs, on a per particle core basis, in μM, has been computed as follows:

$C = 10.0\text{ mg Si mL}^{-1} / 9.07\text{x}10^4\text{ mg Si mmol}^{-1}\,(1\text{x}10^6\,\mu\text{M M}^{-1}) = 1.10\text{x}10^2\,\mu\text{M}$